Optical Resonators Integrated into a Hollow Core Photonic Crystal Fiber for Enhanced Light-Matter Interactions

by

Jeremy Flannery

A thesis
presented to the University of Waterloo
in fulfillment of the
thesis requirement for the degree of
Doctor of Philosophy
in
Physics (Quantum Information)

Waterloo, Ontario, Canada, 2019

Examining Committee Membership

The following served on the Examining Committee for this thesis. The decision of the Examining Committee is by majority vote.

External Examiner:	Aephraim Steinberg Professor, Dept. of Physics, University of Toronto
Supervisor(s):	Michal Bajcsy Assistant Professor, Dept. of Electrical and Computer Engineering, University of Waterloo
Internal Member:	Thomas Jennewein Associate Professor, Dept. of Physics and Astronomy, University of Waterloo
Internal Member:	Kyung Soo Choi Assistant Professor, Dept. of Physics and Astronomy, University of Waterloo
Internal-External Member:	Chris Wilson Professor, Dept. of Electrical and Computer Engineering, University of Waterloo
Other Member(s):	James Martin Associate Professor, Dept. of Physics and Astronomy, University of Waterloo

I hereby declare that I am the sole author of this thesis. This is a true copy of the thesis, including any required final revisions, as accepted by my examiners.

I understand that my thesis may be made electronically available to the public.

Abstract

The focus of this thesis is to investigate and fabricate a platform that can facilitate the enhancement of light-matter interactions. By tightly confining the photons and atoms to the same region of space, the probability of interaction is drastically increased as compared to free space interactions. Specifically, we focus on forming an optical cavity (or resonator) incorporated into a hollow-core photonic crystal fiber (HCPCF) using two distinct types of reflective mirrors along the axis of the fiber while still permitting atoms to be loaded into the region of high field confinement.

One means of pursuing this goal that we explored was to propose and numerically simulate two methods for implementing Bragg gratings in a HCPCF. These two methods leave the hollow-core unobstructed and are both based on controlled selective injection of photosensitive polymers into the photonic-crystal region of the hollow-core fiber, followed by interference photolithography. We report the results of numerical simulations for the hollow core fiber with Bragg gratings formed by the two methods. We find that a reflectivity of $> 99.99\%$ should be achievable from such fiber-integrated mirrors. Such a device could support high cooperativity and strong coupling regimes to be achieved.

We also demonstrate a fiber-integrated Fabry-Pérot cavity formed by attaching a pair of dielectric metasurfaces to the ends of a hollow-core photonic-crystal fiber segment. The metasurfaces consist of perforated membranes designed as photonic-crystal slabs that act as planar mirrors but can potentially allow injection of gases through their holes into the hollow core of the fiber. We have so far observed cavities with finesse of 11 and Q-factors of $\sim 4.5 \times 10^5$, but much higher values should be achievable with improved fabrication procedures. We expect this device to enable the advancement of new fiber lasers, enhanced gas spectroscopy, and studies of fundamental light-matter interactions and nonlinear optics. These mirrors can be designed to be polarization dichroic — transparent for one polarization and reflective for another. This unique property can be exploited to allow for all signals to be directed along the high optical depth axis of the cavity and may provide a excellent platform for applications such as optical switching.

Finally, we develop a novel protocol for a single photon all-optical transistor and how it may be implemented in the above mentioned fiber cavity systems. This unique scheme utilizes a far off-resonant vacuum cavity mode to stimulate a Raman absorption process of a source photon which may be switched off by the insertion of a single gate photon into the cavity mode. Relatively high switching contrasts and ratios for the source photon transmission can be obtained in our system.

Acknowledgements

I would like to acknowledge the many people that have influenced and encouraged me throughout my educational pursuits. My graduate studies have been both a challenging and fulfilling time period in my life with many obstacles that I only managed to overcome with the support of the many individuals around me.

Firstly, it must be mentioned that my research could not have been completed without the guidance of my PhD supervisor, Michal Bajcsy. I have been fortunate enough to learn a great deal about the scientific process from him both inside and outside of the laboratory. Through the use of his many anecdotes/allegories that at first seem a bit peculiar, he seems to always be able to inject a life lesson that becomes memorable despite the initial confusion. His mentorship has been invaluable and I thank him for the chance to learn and grow under his leadership.

I was privileged to have directly worked with many outstanding members of our research group over the years. In particular, in the initial few years of my PhD program I closely worked with our postdoc Chris Haapamaki, who was patient enough to teach me some of the basic skills I needed to survive my graduate studies. Our other postdoc, Taehyun Yoon, also provided me with many technical skills while working in our laboratory.

In the later portion of my degree, I had the opportunity to collaborate with another postdoc in our group, Behrooz Semnani. I am very proud of the work we accomplished together. I was lucky enough to be a part of a project involving the fabrication of chiral-dependent PC membranes, for which Behrooz worked on the simulation and design of the mirrors, as well as the reflectivity measurements. He also took the measurements of the linearly polarized PC mirror reflectivities in Section 5.7.1. I am very grateful for the deep insights into the physics involved in these nanophotonic structures that Behrooz provided me with. He was one of the most knowledgeable people that I was able to work with, and the value of the experience I gained from this collaboration with him cannot be overstated.

I would also like to thank the many graduate students that have been a part of our group including Paul Anderson, Golam Bappi, Rubayet Al Maruf, Andy Ding, Cameron Vickers, Sai Sreesh Venuturumilli, Fereshteh Rajabi, Brian Duong, and Jackson Qiu. I thank my office mates, Rubayet Al Maruf and Andy Ding, for providing an environment that made me feel excited to come to work every day and for the many stimulating conversations. In addition, my neighbouring office mates Cameron Vickers and Jérémy Béjanin were vital in making my studies not only an intellectually stimulating one but an enjoyable experience as well.

During my studies I was also able to volunteer for various scientific outreach programs to educate and inspire the public. There were various demonstrations, lab tours, activities and lectures that I was involved in to educate or display the physics of some of the work being done at the university to high school students and teachers, undergraduate students, as well as the general public. Most of these opportunities were because of the work done by Scientific Outreach Manager Martin Laforest. These experiences provided me with a well rounded graduate education that taught me the value of scientific awareness for the public, as well as the opportunity to sharpen my communication and explanatory skills. These are attributes that I believe all graduate students should attempt to include in their learnings during their studies. These are lessons not strictly part of the graduate school package, but that I consider as vitally important as any other part of the process.

I must also thank my family for the unconditional support that they have provided me with, not only during my graduate studies but during my entire educational career. My mother and father, Laurie and Tim, and brothers, Bryan and Dylan, have always allowed me to follow my interests no matter where they have taken me. My aunt and uncle, Diana and Manny, have been encouraging me ever since I was young. I will always be grateful for their amazing home cooked meals that kept me going as an under-funded student.

And finally, I would like to thank all of my friends that surrounded me over the years with a sense of belonging and relief from the stresses of student life. There are an innumerable amount of fellow students and friends I have met at the Institute for Quantum Computing (IQC) that have helped me through my studies and, by solidarity, endure the pressures that come with obtaining a graduate degree. One of the best parts about working at IQC, without a doubt, are the people that I was lucky enough to work with and the sense of community that it provides.

I have also been lucky enough to have stayed close friends with many people that I have grown up with, some of which I have known almost my entire life. In particular, I would like to thank the 'Lakeshore Boys' (LSB) including Craig Rance, Duncan Smith, Danny Reiner, Alexander Spanopoulos, Anthony Caiazzo, Matt Shantz, Tim Reitzel, Will Demaiter, Dan Graul, Joel Bradley, Kevin Fielding, Nick Giardina, James Balcarras and Andrew Vincent. There have been countless people in my life that have allowed me to become the person I am today, and I look forward to this next stage of my life.

Dedication

This thesis is dedicated to my friends and family who have encouraged and supported me throughout the entirety of my educational pursuits. They have allowed me to persevere through all obstacles I faced in the writing of this thesis.

Previously Published Work

Most of the theoretical results presented in Chapter 4 have been published in:

Flannery, J., Bappi, G., Bhaskara, V., Alshehri, O., & Bajcsy, M. (2017). Implementing Bragg mirrors in a hollow-core photonic-crystal fiber. *Optical Materials Express*, 7(4), 1198-1210.

The experimental results described in Chapter 5 have been published in:

Flannery, J., Al Maruf, R., Yoon, T., & Bajcsy, M. (2017). Fabry-prot cavity formed with dielectric metasurfaces in a hollow-core fiber. *ACS Photonics*, 5(2), 337-341.

Parts of Chapter 4 and 5 also appear in:

Haapamaki, C. M., Flannery, J., Bappi, G., Al Maruf, R., Bhaskara, S. V., Alshehri, O., Yoon,T., & Bajcsy, M. (2016). Mesoscale cavities in hollow-core waveguides for quantum optics with atomic ensembles. Nanophotonics, 5(3), 392-408.

Other published work that I was involved in during my PhD studies that are not directly presented in this thesis are:

Bappi, G., Flannery, J., Al Maruf, R., & Bajcsy, M. (2017). Prospects and limitations of bottom-up fabricated hollow-core waveguides. Optical Materials Express, 7(1), 148-157.

Yoon, T., Ding, Z., Flannery, J., Rajabi, F., & Bajcsy, M. (2019). Monitoring Raman emission through state population in cold atoms confined inside a hollow-core fiber. Optics Express, 27(13), 17592-17600.

Table of Contents

List of Figures **xiii**

1 Introduction **1**

1.1 Motivations 2

1.2 Outline of Thesis 4

2 Nanophotonics and Optics **5**

2.1 Fabry-Pérot Cavity 5

2.2 Bragg Reflection 10

2.2.1 Band Structure 14

2.2.2 2D Photonic Crystal Bandgap Effect 18

2.3 Photonic Crystal Membranes 21

2.3.1 Fano Resonance in PC slabs 23

3 Light-Matter Interactions **28**

3.1 Light-Matter Interaction in Free Space 28

3.1.1 Two Level Atom 31

3.1.2 Three Level Atom 36

3.1.3 Resonant Control ($\Delta_c = 0$): Electromagnetically Induced Transparency (EIT) 39

3.1.4 Off-Resonant Control ($\Delta_c \neq 0$): Two Photon Absorption 43

3.2 Cavity Quantum Electrodynamics . . . 46
3.2.1 Jaynes-Cummings Hamiltonian . . . 47
3.2.2 Dissipation . . . 48
3.3 Coupling Regimes and Figures of Merit . . . 49
3.3.1 Strong Coupling . . . 50
3.3.2 High Cooperativity . . . 52
3.3.3 Weak Coupling Regime . . . 54
3.4 Atomic Ensemble in a Cavity . . . 56
3.5 Vacuum Induced Transparency (VIT) . . . 59
3.5.1 Hamiltonian and Master Equation . . . 60
3.5.2 Transmission Spectrum . . . 63
3.5.3 Group Velocity and Pulse Width . . . 65
3.6 Validity of Approximations . . . 68

4 Implementing Bragg Mirrors in a Hollow-Core Photonic-Crystal Fiber 69
4.1 HCPCF Simulation Model . . . 71
4.2 Theoretical Calculation of Bragg Reflectivity . . . 74
4.3 Bragg Mirror Reflectivity Results . . . 77
4.3.1 Coating Hollow Core Walls . . . 77
4.3.2 Selective Filling of Outer PC Holes . . . 79
4.4 Fiber Bragg Mirror Performance . . . 83
4.5 Fiber Bragg Cavity . . . 85
4.6 Conclusions and Outlook . . . 88

5 Fiber-integrated cavity based on photonic-crystal slab mirrors 89
5.1 Photonic Crystal Membrane Simulations . . . 91
5.2 Fabrication of Fiber Cavity . . . 94
5.2.1 PC Membrane Fabrication . . . 94

5.2.2 Mounting Technique . . . 97
5.3 PC Membrane Reflectivity Measurements . . . 98
5.4 Fiber-Integrated Cavity Measurements . . . 102
5.5 Cavity Tuning . . . 104
5.6 PC Membrane-Based Cavity Regimes . . . 106
5.7 Polarization-Selective Membranes . . . 108
5.7.1 Polarization Dependent Reflectivity Measurements . . . 110
5.7.2 Mounting Polarization-Selective Mirrors . . . 112
5.7.3 Preliminary Polarization-Selective Fiber-Cavity . . . 114
5.8 Conclusion and Future Work . . . 115

6 All-Optical Single Photon Switching **117**
6.1 Four-Level Optical Switching Scheme . . . 118
6.1.1 Resonant Case . . . 120
6.2 Semiclassical: Continuous Probe and Control Switch . . . 124
6.2.1 Quasi-Continuous Wave Switch . . . 127
6.3 Pulsed Probe and Control Switch . . . 130
6.3.1 M-Scheme Group Velocity Matching . . . 131
6.3.2 Bragg Grating Slow Light . . . 134
6.4 Three-Level Switching Scheme . . . 137
6.4.1 On-Resonance Cavity Mode: VIT Switch . . . 138
6.4.2 Off-Resonance Cavity Mode: VIRA Switch . . . 143
6.5 Conclusion . . . 148

7 Conclusions and Outlook **149**
7.1 Summary . . . 149
7.2 Future Directions . . . 150

References **153**

APPENDICES 165

A Fabrication Variants of Photonic Crystal Membranes 166

List of Figures

2.1 (a) A Fabry-Pérot cavity, which is comprised of two parallel mirrors separated a distance, d, apart with reflectivities r_1 and r_2 and transmissivities t_1 and t_2, respectively. (b) Cavity transmission spectrum caused by the build-up of field that is transmitted through the cavity after each round trip. Multiple cavity decay rates (linewidths), κ, are plotted showing large finesse cavities possessing well resolved peaks with narrow linewidths. . . . 6

2.2 A Bragg medium consisting of two periodic layers with refractive indices n_1 and n_2 with thicknesses a and b, respectively. The unit-cell that repeated n times and has a period of $\Lambda = a + b$. The field amplitudes moving in the forward (backward) z direction in layer 1 and 2 are a_n (b_n) and c_n (d_n), respectively. 11

2.3 (a) Band diagram of a periodically layered medium comprised of two layers with index n_1 and n_2. The optical stop band is found at the Bragg condition of $\mathrm{Re}\{K\} = \pi/\Lambda$ with a center frequency of w_0 and bandwidth $\Delta\omega$ for the first stop band. 16

2.4 A 2D photonic crystal with a hexagonal (or triangular) pattern of holes in a dielectric material with lattice constant, a, and hole radius, r. The pattern is repeated for any linear combination of the primitive lattice vectors a_1 and a_2. Bandgaps (or stop bands) can occur in the dispersion relation for in-plane guided modes and thus can act as a reflective mirror allowing only evanescent waves to exist within the photonic crystal structure. 19

2.5 (a) The band diagram of TE modes for a hexagonal lattice PC membrane with $\epsilon = 13$, $\frac{r}{a} = 0.48$ and $K_z = 0$ (found using Lumerical Mode Solutions software). The photonic bandgap is shown in the shaded area and the inset depicts the Bloch vector directions for the irreducible Brillouin zone. (b) An SEM image of a hollow core photonic crystal fiber (HCPCF) with a hexagonal PC pattern in the cladding that confines light to the center hollow core. 21

2.6 Incident light perpendicular to the plane of the PC membrane can be completely reflected for a PC membrane with a certain material index, lattice constant, a, hole diameter, d, (or radius, r) and membrane thickness, t. . . 22

2.7 (a) Band diagram (for TE modes) of a silicon membrane with a square lattice PC pattern of hole radius, $r = 0.2a$, and film thickness, $t = 0.5a$, for Bloch vector directions in the irreducible Brillouin zone depicted in the inset. The yellow shaded region represents the radiation modes above the light cone ($\omega = ck$) where leaky modes (guided resonances) are possible. The non-shaded region are in-plane guided modes below the light cone. (b) Reflection spectrum of the 2D PC silicon membrane (solid blue line). The dashed green line shows the spectrum for a uniform film without PC holes with a refractive index found by averaging the holes and silicon material of the PC film. The dotted red circles in (a) and (b) represent the same low Q guided resonant mode. Both plots are produced by numerical simulations of the described PC membrane using Lumerical Solutions software. 24

2.8 The first resonant peak of the silicon PC membrane simulated in Fig. 2.7b (circled in a red dotted line). The simulation results (shown as a solid blue line here) are fitted to Eq. 2.64 (using Eq. 2.68 and Eq. 2.67). This theoretical fit (shown as a dotted green line) uses fitting parameters of $\gamma = 1.122 \times 10^{-3} \times \frac{2\pi c}{a}$ and $\omega_0 = 0.3816 \times \frac{2\pi c}{a}$. 27

3.1 A two level atom excited by a weak external probe field with Rabi frequency, Ω_p, at a frequency detuning, Δ. The separation between the ground and excited state is ω_{eg}, and the spontaneous emission rate (natural linewidth) is Γ. 32

3.2 (a) Normalized values for the real (solid blue line) and imaginary (dashed red line) parts of the susceptibility of a two level atom with a weak probe field (Eq. 3.29), representing the index of refraction and the attenuation, respectively. The absorption Lorentzian peak has a full-width half maximum of Γ. (b) Transmission of a weak probe field through a two level atomic medium (Eq. 3.32) with $OD = 10$. 36

3.3 A three-level Λ scheme, with coupling probe and control Rabi frequencies, Ω_p and Ω_c, and detunings, Δ_p and Δ_c, respectively. Decay rates from the excited state to $|g\rangle$ and $|s\rangle$ are Γ_{eg} and Γ_{es}, respectively, while the metastable ground state decay is Γ_{sg}. 37

3.4 (a) The normalized real and imaginary parts of the susceptibility of a two level atom ($\Omega_c = 0$) and three level atom ($\Omega_c = \frac{\Gamma_e}{2}$). (b) Transmission of a two and three level atom, with $OD = 10$. 40

3.5 Comparison of a two level system and a three level system with $\Delta_c = 2\Gamma_e$ and $\Omega_c = \frac{\Gamma_e}{2}$. (a) The normalized imaginary part of the susceptibility and the (b) transmission with $OD = 10$. The EIT resonance with large transmission is found at $\Delta_p^{EIT} = \Delta_c$, and the TPA resonance is found at $\Delta_p^{2ph} = \Delta_c + \frac{\Omega_c^2}{4\Delta_c}$. 44

3.6 A two level atom interacting with a field in a cavity. The rate at which the atom coherently interacts with the cavity photons is the vacuum Rabi frequency, g. The two damping process are the atomic decay rate, Γ, which characterizes emission of photons into modes other than the cavity mode, and rate at which photons are leaked from the cavity, κ. 49

3.7 The left most ladders are the uncoupled bare states for a detuning between the atom and cavity frequencies, $\Delta = \omega_c - \omega_{eg}$. When the atom and cavity are strongly coupled, the new eigenstates are instead the dressed states. . . 51

3.8 The single excitation manifold scheme for a three-level atomic ensemble in a cavity consists of the bipartite states $|E, 0\rangle$, $|G, 0\rangle$ and $|S, 1\rangle$. A weak probe field with Rabi frequency Ω_p is coupled through free space to the $|E\rangle$-$|G\rangle$ atomic transition. The cavity mode is coupled to the $|S\rangle$-$|G\rangle$ with an effective vacuum Rabi frequency, g_{eff}, for the atomic ensemble, with cavity photons leaking at a rate κ. 61

3.9 Transmission of the probe field at a cavity frequency resonant with the $|E\rangle$ - $|S\rangle$ transition ($\Delta_c = 0$) for various cooperativities resulting in vacuum induced transparency (VIT). The resonance probe transmission peak at $\Delta_p = 0$ increases in both amplitude and width for larger coupling strengths, in accordance with the behaviours of Eq. 3.122 and Eq. 3.123, respectively. The optical depth is set to $OD = 10$ and cavity decay rate as $\kappa = 0.1\Gamma_e$. . 66

4.1 Bragg mirror formed in a hollow core photonic crystal fiber (HCPCF) by periodically altering the effective index along the optical axis of the fiber. The interference of a particular wavelength (Bragg condition) light reflected from each interface of the Bragg layers can cause for near unity reflection. 70

4.2 The two proposed methods for integrating Bragg gratings into HCPCFs: (a) the cross section and (b) cutout of a HCPCF with a thin film of resist coating the hollow core. The (c) cross section and (d) cutout of a HCPCF with a UV-curable polymer selectively filled in the first layer of the photonic crystal holes. 71

4.3 HCPCF cross sections: The (a) SEM picture of the HC-800-02 fiber. (b) The circular hole model and (c) hexagonal hole model [60] implemented to simulate the fiber structure (optimized lattice pitch, PC hole size and hollow core diameter not drawn to scale). Propagation attenuation in HCPCFs: (d) The manufacturer specification for HC-800-02 and the numerically simulated losses for the (e) circular hole model and (f) hexagonal hole model. 73

4.4 (a) The penetration depth method (PDM) method finds the reflectivity by accounting for the attenuation associated with propagation of the light into the lossy Bragg mirror to an average penetration depth, z_p. (b) The method of single expression (MSE) iteratively solves the coupled differential equations in Eq. 4.5 - 4.7 to find the reflectivity. The Bragg layers are discretized into Δx step sizes and the fields are solved for at the transmitted side and iterated towards the illuminated side. 75

4.5 Simulation results for (a) attenuation and (b) effective refractive index in the fiber with a varying layer thickness of photoresist coating the inside walls of its hollow core, as shown in the inset. Results are obtained for the hexagonal hole model at a wavelength of 851 nm. Three different indices for the resist material were used: 1.61, 1.45 and 1.30. Simulations were done using a custom mesh size of $\sim$ 1.6 nm$\times$1.6 nm$\times$1.6 nm for the resist film in order to accurately model the relatively thin layer. 78

4.6 Maximum reflectivities for a Bragg mirror formed by periodic films of resist coating the hollow core. The three different material refractive indices used are (a) 1.61, (b) 1.45, and (c) 1.3 for the hexagonal hole model (note that 1-Reflectivity is plotted). The penetration depth method (PDM) calculates the reflectivity using Eq. 4.1 by accounting for the attenuation acquired as the light propagates an average penetration depth (Eq. 4.2) into the Bragg gratings. The method of single expression (MSE) is also used to analyze the grating reflectivity. Some of the reflectivity data points are absent for MSE because the numerical algorithm did not always converge to a finite value. 79

4.7 Simulation results for attenuation and effective refractive index in the fiber with the first or second layer of PC holes filled with epoxy: (a) and (b) show the simulation results for the filled first layer of PC holes using the hexagonal hole model. (c) and (d) show results for the filled second layer of PC holes. All simulations are performed at a wavelength of 851 nm. The 'hole number' signifies the number of filled holes in a clockwise direction. Three different indices for the uncured polymer material were used: 1.62 (representative of Norland NOA162 optical adhesive), 1.45 and 1.30. 81

4.8 Maximum reflectivities for a Bragg mirror formed by periodic exposure of UV-curable epoxy selectively injected into the photonic crystal region. Hexagonal hole model is used for simulation when the (a) first and (b) second layers in the PC region are filled with modulated material. The three different material indices used for the uncured epoxy are 1.62, 1.45, and 1.30, while the cured epoxy indices are 1.64, 1.47, and 1.32. Both PDM and MSE reflectivity results are plotted. 82

4.9 Maximum reflectivity of a lossy Bragg mirror for a range of effective refractive index contrast between layer pairs and average loss per unit length of the structure for the hexagonal hole model. Resist layer thicknesses that produced the highest reflectivities in the core coating method are marked in the plot (black circles), together with the points corresponding to the largest reflectivity predicted for the hole filling method (purple diamonds) for the corresponding number of holes filled. The reflectivity produced by Bragg layers formed by modulating the fiber silica material is also plotted (white dot). 83

4.10 (a) The simulated spectrum of a fiber Bragg grating using a 700nm thick resist (1.61 index) coating the hollow core walls for 100,000 periods. The maximum reflectivity is $\sim 99.9969\%$. (b) Estimated reflectivity bandwidth of the Bragg mirror (dashed blue, Eq. (4.11)) and corresponding penetration depth (solid orange, Eq. (4.2)) plotted against refractive index contrast between the layer pairs forming the mirror. 85

4.11 (a) A Fabry-Pérot cavity integrated into a HCPCF using two Bragg mirrors placed a distance L_{spacer} apart. The field along the optical axis of the fiber is shown as the black line, which experiences exponential decay when entering the Bragg layers with an average penetration depth of z_p, producing an effective length of the cavity as $L_{eff} = L_{spacer} + 2z_p$. (b) Cooperativity at varying effective index contrasts between Bragg layers and average attenuation per period. The thicknesses resulting in the largest cooperativity by coating the hollow core with resist (for each resist index) are plotted as black dots. The black line distinguishes the high and low cooperativity regimes. Bragg mirrors formed by modulating the fiber silica material is plotted as a white dot. 86

4.12 The thicknesses of the resist coating the inner walls of the hollow core that produce the highest reflectivity and cooperativity are again plotted here for each resist index discussed (for $n = 1.30, 1.45, 1.61$ we use resist thickness, $t =$ 700nm, 400nm, 700nm, respectively). The strong coupling regime is defined as $\frac{g}{\kappa} > 1$ (since $g > \Gamma_\perp$ is the less stringent inequality). Forming Bragg layers by modulating the fiber silica material results in $\frac{g}{\kappa} \ll 1$ and so is not plotted. 87

5.1 The HCPCF-integrated Fabry-Pérot cavity. The fiber serves as the cavity medium and confines light in the transverse direction, while a pair of dielectric metasurfaces (PC membranes) mounted on the ends of the fiber segment confine light longitudinally. 90

5.2 A magneto optical trap (MOT) would be used to load atoms into the fiber cavity. Atoms can be gravity-loaded by turning off the MOT system and letting the atoms be funnelled into the hollow core of the fiber using a magic wavelength dipole trap (blue beam) [Image credit: Chris Haapamaki]. . . . 91

5.3 (a) FDTD simulation results of the reflectivity produced for light incident perpendicularly on a PC membrane with lattice constant a=819 nm, hole radius r=347 nm, and film thickness t=500 nm. A plane wave and a Gaussian beam (with 2.75 μm waist radius) experience significantly different reflectivities. (b) The simulated reflectivity spectra for plane wave and Gaussian beam with membrane parameters chosen to optimize the reflectivity for the 2.75 μm-waist Gaussian source with a=680 nm, r=297 nm, t=369 nm (material index used was 2.26). 93

5.4 (a) Summary of the PC membrane fabrication process. E-beam lithography is used to create a pattern in ZEP520A resist, which is transfer to an Al hard mask followed by a SiN etch using RIE. The film is left free standing by undercutting the Si using a KOH wet etch. (b) The fabricated mirror template with the PC pattern that will be mounted onto the HCPCF tips to form a cavity. The inset shows a scanning electron microscope (SEM) image of the inner square of photonic crystal holes at the desired dimensions to produce maximum reflectivity at ∼852 nm. 95

5.5 A diagram of the mounting technique, as described in the text. 97

5.6 SEM image of the PC membrane attached to the tip face of a HCPCF segment. The centre square lattice of PC holes in the membrane covers the entire PC region of the underlying HCPCF. 99

5.7 (a) Image of one of the versions of the reflectivity measurement optical setup. (b) Optical setup used to measure the transmission and reflectivity of the PC mirrors using power measurements and cavity measurements (shown in the dotted black boxes). Imaging of the sample is done using flip mirrors to introduce a white light source to illuminate the sample and a CCD camera is positioned to collect the reflected output light. 100

5.8 (a) Reflectivity of a PC pattern consisting of a square lattice of circular holes on Norcada samples (index 2.11) with thickness, t = 500 nm, lattice constant, a = 817 nm, radius, r = 383 nm using power measurements. The cavity measurements using a metallic mirror found a reflectivity of ∼ 92% at 852 nm wavelength. Due to fluctuations in the laser power, the calibration is not stable and acts to create the noise seen in these reflectivity measurements. 101

5.9 (a) Optical setup used to measure the transmission and reflectivity spectrum of the fiber-cavity. (b) The transmission spectrum of the fiber-cavity found by scanning the input light frequency at a centre wavelength of 852nm. The normalized transmission data (purple dotted line) is fitted to Eq. 5.1 (orange solid line). 103

5.10 (a) The reflectivity of the individual PC mirrors on the fiber tips extracted from the transmission spectrum fit. The parameters of the PC membrane measured from its SEM image were $a \approx$680 nm, $r \approx$260 nm, and $t \approx$363 nm. (b) Finesse (orange triangles) and Q factor (blue squares) of the fiber-cavity for a range of wavelengths. The finesse and FSR are found by fitting Eq. 5.1 to the cavity transmission spectrum and the Q factor is then found using the relationship $Q = \frac{\mathscr{F}}{FSR}\nu$. 105

5.11 (a) A temperature stage is used to tune the temperature of the fiber cavity which acts to shift the resonant Fabry-Péro peaks. The red arrows represent the coupling input light from the objective into the fiber cavity. (b) Normalized transmission spectrum of the cavity at varying temperatures. The resonant peaks are shifted ~ 0.2 GHz per °C. 106

5.12 (a) Single atom cooperativity for the fiber cavities discussed in this chapter with varying lengths. High cooperativity occurs for $\frac{4g^2}{\kappa\Gamma} > 1$. (b) Plot showing the relationship between g, κ, and Γ at varying cavity lengths for cesium atoms in a fiber cavity. Strong coupling regime occurs for $g > \kappa, \Gamma$, which is depicted as the shaded blue region for a mirror reflectivity of 0.998. Mirror reflectivities lower than this cannot reach the strong coupling regime, regardless of cavity length. [44] 107

5.13 Previous cavity systems require the free space and cavity illumination signals to be perpendicular to each other, resulting in side illumination of the atomic cloud along the low optical depth axis [Image source: [21]]. The co-linear illumination scheme provided by the polarization dependent fiber-integrated cavity can allow for both the free space and cavity sources to be sent along the high optical depth axis of the atomic ensemble by setting the correct polarization of the each signal. 108

5.14 (a) Unit cell of a polarization-selective photonic crystal pattern. The linear symmetry is broken by using a rectangular lattice and elliptical holes. (b) FDTD simulations show complete transmission and complete reflectivity at orthogonal linear polarizations using a plane wave source ($a_x = 781$ nm, $a_y = 560$ nm, $d_x = 504$ nm, $d_y = 396$ nm). 109

5.15 (a) Optical setup used to measure the four Jones matrix elements in Eq. 5.5. Half-wave plate A is used to set the polarization of the input light and half-wave plate B sets the polarization of the measured reflected light. (b) A summary table of the four settings of the half-wave plates A and B and the corresponding Jones matrix element that is measured. 111

5.16 (a) SEM image of a rectangular lattice of elliptical PC pattern resulting in a polarization selective mirror (with pattern dimensions $t = 342$ nm, $a_x = 676$ nm, $a_y = 444$ nm, $d_x \approx 396$ nm, and $d_y \approx 352$ nm). (b) Jones matrix elements for the fabricated polarization dependent PC mirrors. The largest extinction ratio was found to be $\frac{R_{yy}}{R_{xx}} \approx 23$ at 820 nm (with $R_{yy} \approx 93$ and $R_{xx} \approx 4$). 112

5.17 Optical setup used to measure the birefringent axis of the HCPCF. Both half-wave plates A and B are set to an angle of θ with respect to the horizontal and rotated until the power at the photodiode is minimized, thereby determining the angle of either the slow or fast axis in the fiber. 113

5.18 Spectrum of a polarization-selective fiber-integrated cavity using asymmetric PC patterned membranes acting as mirrors. Background noise is still included as the signal is not filtered through a single mode fiber. 114

5.19 Plot of the attractive Casimir-Polder potential across a single photonic crystal hole of radius 250 nm. The walls of the silicon nitride membrane are shown as the blued shaded region. We use a $-\frac{C_4}{r^4}$ potential from the dielectric surface with $C_4 = 8.2 \times 10^{-56} Jm^4$ from [63, 120]. 116

6.1 (a) Four level scheme used for optical switching of the weak probe field, Ω_p, by controlling the switching field, Ω_s. A cavity mode is set to near resonance to $|s\rangle$ and $|e\rangle$ transition with a coupling constant, g_{eff}, eliminating the need for biasing the switch with a strong control field. The decay rate between states $|i\rangle$ to $|j\rangle$ is Γ_{ij}. (b) Transmission of the probe field at different switch field powers. ($OD = 10$, $2g_{eff} = \Gamma_e$, $\Delta_p = \Delta_c = \Delta_s = 0$, $\Gamma_h = \Gamma_e$) 119

6.2 Transmission switch ratio as a function of the switch Rabi frequency normalized to the cavity vacuum Rabi frequency (Eq. 6.14). We use the D_2 cesium transition ($\mu = 1.7138 \times 10^{-29}$ Cm) at a wavelength of 852 nm. Varying cavity decay rates, κ, shown with the resulting mirror reflectivity required to produce the given decay rate. The number of atoms are set to 10^4 corresponding to an optical depth of 36.9. The fiber loss is ~ 150 dB/m with a core radius of 3.5 μm and Gaussian mode radius of 2.75 μm, and the length of the fiber is set to 1 cm. $\Gamma_e = \Gamma_d = 2\pi \times 5.2$ MHz. 124

6.3 Transmission contrast at varying optical depths. The maximum contrast occurs at a particular optical depth for each given switch power (given in both units of photons per second and MHz). The decay rate is set to $\kappa = \gamma_e$ and $L = 1$cm, $\Gamma_e = \Gamma_d = 2\pi \times 5.2$ MHz. 125

6.4 (a) Optimal optical depth that allows for the (b) maximum contrast between on and off switch states for a range of switch field powers. Each are plotted at different cavity decay rates and respective mirror reflectivities ($L = 1$cm, $\Gamma_e = \Gamma_d = 2\pi \times 5.2$ MHz). 126

6.5 (a) Optical depth required to produce the (b) maximum contrast at varying cavity decay rates, κ, and switch field strengths, Ω_s. 127

6.6 (a) Group velocity of the probe pulse as a function of the switch field and cavity decay rate. It should be noted that we plot the magnitude of the group velocity, as the dispersion relation for large switch powers creates a negative group velocity. (b) Number of switch photons required for a quasi-continuous source that is assumed to be turned on for only as long as the transit time of the probe pulse of the atomic cloud. (c) Frequency width of the switch field square pulse with a width in time equal to the transit time of the probe pulse. 129

6.7 A five level M-type scheme that can be used to tune the group velocity of the switch field, Ω_s, by altering the detuning of the tuner cavity mode, Δ_t. ($\Gamma_d \equiv \Gamma_{dg} + \Gamma_{ds} + \Gamma_{df}$, $\Gamma_e \equiv \Gamma_{eg} + \Gamma_{es} + \Gamma_{eg}$, $\Gamma_f \equiv \Gamma_{fs} + \Gamma_{fg}$) 131

6.8 Group velocities of the probe and switch pulses when altering the tuner cavity detuning, Δ_t, while keep $\Delta_p = \Delta_c = \Delta_s = 0$. The D_2 and D_1 lines of cesium are used for the $|d\rangle$ and $|e\rangle$ excited states, respectively. We set $\Omega_p = 0.01\gamma_e$, $\Omega_s = \gamma_e$, and $\kappa = 0.75\gamma_e$, assuming a 1 cm length HCPCF fiber cavity with 10^4 atoms. 135

6.9 (a) Three level scheme for optical switching where the insertion of a single switch photon (shown in purple) into the cavity mode alters $g_{eff} \rightarrow \sqrt{n_s+1}g_{eff}$, $\gamma_e \rightarrow \frac{\Gamma_e}{2} + n_s\kappa$ and $\gamma_s \rightarrow \frac{\Gamma_{sg}}{2} + \frac{\kappa}{2} + n_s\kappa$. (b) The transmission of the probe field is shown to be drastically affected by the presence of a single switch photon to create two distinct transmission states. 138

6.10 (a) Transmission ratio and (b) absolute value of the contrast as the number of switch photons is changed as well as the cavity decay rate. The optical depth is set to $OD \approx 36.9$, corresponding to about $\sim 10^4$ atoms in a 1cm long HCPCF cavity. The red dotted line represents the number of switch photons that will produce the maximum contrast possible for a given decay rate (Eq. 6.48). 141

6.11 (a) Transmission ratio and (b) contrast for an optical switch in a fiber cavity with varying decay rates and cavity lengths. The number of atoms is set to $N_a = 10^4$ ($OD \sim 37$) and the number of switch photons is set to $n_s = 1$. . . 142

6.12 (a) Optical switching scheme for a vacuum induced Raman absorption (VIRA) regime three level atom coupled to a cavity mode in the presence and absence of a switch photon, n_s. The two switching states are for zero switch photons in the cavity mode (blue) and one switch photon (purple). (b) Absorption plot of the VIRA switching scheme. The probe field is set on the VIRA resonance for zero cavity switch photons (green dashed line) resulting in a large absorption for $n_s = 0$, while a low absorption occurs for $n_s = 1$ which acts to shift the VIRA peak off resonant from the probe field. ($\Delta_c = 10\Gamma_e$, $\kappa = 0.1\Gamma_e$) 144

6.13 Transmission (a) contrast and (b) ratio for the VIRA-based optical switching scheme. A cavity length of 1 cm with 10^4 atoms in a cavity (OD$\sim$ 37) with a mode area diameter of 5.5μm is used for these calculations. 146

6.14 Transmission (a) contrast and (b) ratio for various cavity lengths which act to alter the coupling coefficient, g_{eff}, as well as the optical depth for a constant number of atoms set to 10^4, with $\kappa = 0.92\gamma_e$ and a mode diameter of 5 μm. The regions inside the red ellipses represent the parameter space that can simultaneously achieve relatively high values for both contrast and ratio. 147

Chapter 1

Introduction

The development of quantum mechanics initially led to a deeper understanding of nature at a fundamental level. Several key aspects of this theory drastically altered our philosophical picture of reality and challenged many preconceived notions in physics, such as the wave-particle duality, entanglement and the superposition principle. Amazingly, these concepts have since become vital in the development of many significant tools that have pushed the boundaries of our technological limits, such as the electronic transistor.

More recent research into quantum-based technologies have shown great promise for the advancement of a wide variety of fields such as metrology, imaging, simulation, sensing, cryptography and information science. In particular, quantum computation and quantum information processing heavily relies on these principles to provide quantum advantages over their classical counterparts, and it is in this vein that developing new devices exhibiting these quantum phenomena are valuable. Nonlinear optics can in fact provide a platform for the implementation of quantum logic gates towards a universal quantum computer [83, 19, 127, 27].

One such system that demonstrates these desired quantum phenomena are nonclassical states of light in the study of quantum optics. In order for photons to affect each other, however, there needs to be an effective interaction between them. Photons, of course, do not interact with each other, and instead matter can be used to act as a mediator between the photons which, in turn, produce effective photon-photon interactions. However, at the few photon level these nonlinearities can be realized with extremely strong light-matter interactions.

1.1 Motivations

The probability of a single photon interacting with a single atom can be characterized by the single atom optical depth, $p_{int} = \frac{\sigma_0}{A_{ph}}$, where σ_0 is the atomic absorption cross-section and A_{ph} is the area spot size of the photon with wavelength, λ. The resonant cross section of an atom is $\sigma_0 \sim \lambda^2$, while free-space focusing is diffraction limited such that in practise $A_{ph} \gg \lambda^2$, leading to very small interaction probabilities. The coupling of light to an ensemble of N_a atoms is instead proportional to the ensemble optical depth, $OD = N_a p_{int}$. However, free-space illumination is again plagued by the fact that tight focusing leads to short Rayleigh ranges which result in a small volume of interaction and reduced ensemble optical depths.

In order to prevent the limiting of ensemble optical depths, there are considerable efforts to couple ensembles to waveguides such as tapered optical nanofibers [75], photonic crystals [42], as well as hollow core fibers [40, 104, 79]. In particular, hollow-core photonic-crystal fibers (HCPCF) offer an excellent platform for enhancement of light-matter interactions, particularly when the matter takes the form of an atomic ensemble [19] such as a dilute atomic vapor. This is possible because the fiber geometry gives rise to a tight confinement of photons and their overlap with atoms over distances not limited by diffraction, while the hollow core allows introduction of atoms or molecules that would be incompatible with a solid-core fiber.

Optical nanowires can provide large single atom optical depths of $p_{int} \sim 0.15$ [113, 43] while the reported ensemble optical depths have reached $\sim 10^2$ [90]. Conversely, HCPCFs have not been shown to provide particularly large single atom optical depths ($p_{int} \sim 4 \times 10^{-3}$), however they can produce ensemble optical depths as high as $\sim 10^3$ [13, 84].

Over the last decade, HCPCFs loaded with room-temperature gases [41, 104, 98] and laser-cooled atoms [23, 6, 13] have been used in a number of experiments exploring the fundamental limits of non-linear optics at low light levels, such as all-optical switching [5], stationary light pulses [14], cross-phase modulation [112], and single-photon memory [100]. The hollow-core photonic-crystal fibers have propagation losses from < 250 dB/km for off-the-shelf fibers down to recently reported ~ 1 dB/km [88], which approaches the lowest losses reported for conventional solid-core fibers [73]. This gives hollow-core photonic-crystal fibers a significant advantage compared to other hollow-core waveguide platforms with a comparable cross-section and mode-field diameter, such as hollow-core anti-resonant reflection optical waveguides (ARROW) [122]. A cavity formed with dual-tapered reflectors has been recently demonstrated [12] using these on-chip hollow-core waveguides, where the reported losses for the fabricated structures are currently around 3 dB/cm. At the same

time, lithographical techniques developed recently for atom-chip applications [35] could be used to integrate the hollow-core fibers into on-chip platforms.

Further enhancement of the light-matter interaction inside hollow-core fibers filled with atomic gases, broadening the new horizons already opened by the HCPCF platform, could potentially be achieved by dispersion engineering of the hollow-core fiber or by incorporating a cavity into it. The goal of this would be to increase the probability of interaction between single photons and single atoms inside the fiber to as close as possible to unity [108, 19], while at the same time keeping the hollow core unobstructed to allow loading of atoms into the fiber.

For solid-core fibers, dispersion engineering and mirror integration can be achieved using fiber Bragg-gratings [80, 8] which are implemented by periodically modulating the refractive index of the fiber material, in particular, of the core. This task, however, is challenging for the hollow-core fiber, as the fiber core is empty and, furthermore, the fiber is designed with an effort to minimize the overlap between the propagating light and the glass material of the cladding.

High-finesse cavities have also been reported with reflective coatings deposited on the ends of a solid-core fiber piece [78]. Additionally, cavities in solid-core photonic-crystal fibers were earlier realized by pressing mirrors against the cleaved ends of a fiber section [49]. Unfortunately, sealing the face of a HCPCF with a multi-layer reflective coating or with a mirror would make it impossible to introduce gases into the fiber core after the cavity has been formed.

One of the main purposes of this thesis is to propose and experimentally implement fiber-based optical cavities which addresses these technical challenges of both using a hollow-core fiber to allow for the presence of atoms in the high field areas, as well as mirrors that leave the core unimpeded for the injection of atoms. We focus on two separate methods of implementing Fabry-Pérot mirrors. The first proposal is to incorporate Bragg gratings in a fiber segment by introducing modulated thin layers of resist coating the hollow-core walls which act to marginally alter the effective refractive index. This periodic pattern of the effective index as perceived by the fundamental fiber mode, can then result in Bragg reflection while still leaving the hollow-core accessible for the introduction of atoms.

The second realization of a Fabry-Pérot cavity integrated into a HCPCF relies on dielectric metasurfaces. Metallic and dielectric metasurfaces, formed by large two-dimensional arrays of nano-scale patterns, have been extensively explored in the past decade due to their capabilities to manipulate light in previously unimaginable ways [125, 1, 72]. Metasurfaces realized by perforating dielectric membranes, also known as photonic crystal (PC) slabs

[29] or high-contrast gratings [20], offer the additional advantage of being permeable by gases and liquids [57] and thus make an almost obvious choice as a technology for forming a cavity inside a HCPCF. In these cavities, the HCPCF provides tight transverse confinement of light to its hollow core, while the photonic crystal slabs acting as dielectric metasurface mirrors are mounted onto the ends of a fiber segment and provide longitudinal confinement of light along the axis of the fiber. One of the main advantages of this platform, as we will also explore in this work, is that such mirrors can be designed to be polarization-selective (polarization dichroic), which opens new opportunities for engineering atom-photon and photon-photon interactions.

1.2 Outline of Thesis

This thesis begins with basic background theory behind the nanophotonic structures explored in this research. Chapter 2 includes a brief overview and characterization of Fabry-Pérot cavities. We then explore the theoretical description of the two mechanisms of reflection utilized in the formation of the mirrors that form the fiber-based cavities in this work. The first being Bragg reflection and the photonic crystal bandgap effect in higher dimensions, and the second being Fano resonance by the means of guided resonances in a 2D photonic crystal membrane. Chapter 3 covers both the semi-classical and fully quantized description of an atom in a cavity and the various regimes of light-matter interaction. It also provides a derivation of Vacuum Induced Transparency (VIT) and the phenomenon of two photon absorption (TPA). The theoretical work done in Chapter 4 examines the possibility and required specification of a cavity incorporated into a HCPCF by the use of a unique formation of Bragg layers within the fiber. Chapter 5 presents the experimental realization of a PC membrane-based optical resonator within a HCPCF. The work done in Chapter 6 explores possible applications of such fiber-based cavities, specifically several novel schemes for single photon all-optical switching. The thesis concludes with Chapter 7, in which a summary of the work done is given and the possible future directions are discussed.

Chapter 2

Nanophotonics and Optics

In this chapter, the classical physics underlying the various nanophotonic structures utilized in this thesis will be discussed. We begin with a brief introduction and derivation of the properties of a simple planar Fabry-Pérot resonator. We then describe the reflectivity mechanism behind the different mirrors used for the fiber-integrated Fabry-Pérot cavities that we developed. There are generally three different types of mirrors available: metallic, Bragg (dieletric stack mirrors), and dielectric metasurfaces. The later two types of mirrors are employed in this work, and thus are the two that will be discussed in this chapter.

We first consider Bragg reflection as a 1D photonic crystal bandgap effect and determine the characteristic bandwidth and penetration depth. In addition, we apply these derivations to a 2D photonic crystal bandgap effect to provide intuition behind the means in which the HCPCFs can allow for the extremely low loss. This chapter concludes with a simple derivation of the last type of mirror. We show how the phenomenon of guided resonances in a dielectric metasurface (photonic crystal membrane) produce Fano resonances in the reflectivity spectrum of incident light that is perpendicular to the plane of the membranes.

2.1 Fabry-Pérot Cavity

A simple planar Fabry-Pérot cavity or etalon [102] is a device comprised of two parallel reflective mirrors with complex field reflectivities r_1 and r_2, and transmissivities t_1 and t_2, set apart from each other by a distance, d, as shown in Fig. 2.1a. We assume that the reflectivity and transmissivity are equal for both counter-propagating light. In order to

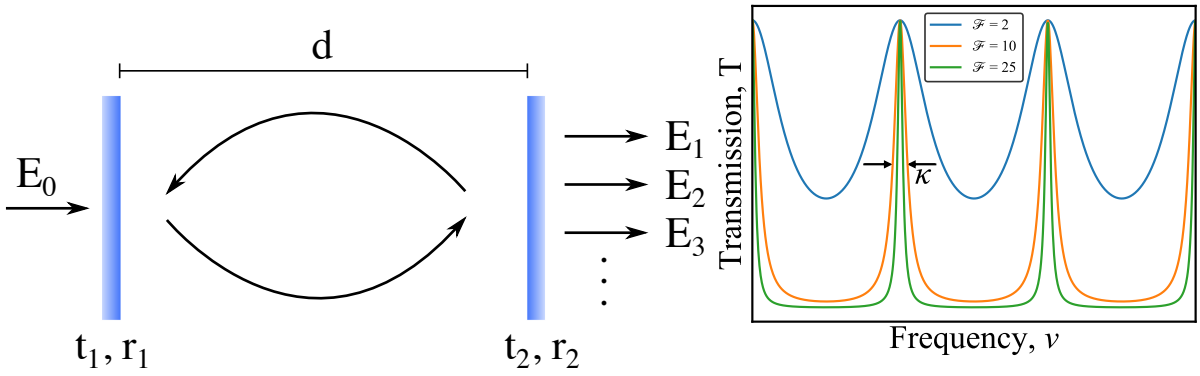

(a) (b)

Figure 2.1: (a) A Fabry-Pérot cavity, which is comprised of two parallel mirrors separated a distance, d, apart with reflectivities r_1 and r_2 and transmissivities t_1 and t_2, respectively. (b) Cavity transmission spectrum caused by the build-up of field that is transmitted through the cavity after each round trip. Multiple cavity decay rates (linewidths), κ, are plotted showing large finesse cavities possessing well resolved peaks with narrow linewidths.

calculate the transmission of the incident field, E_0, through the cavity at steady state, we must add the build-up of all the contributions of transmitted light occurring after n round trips, E_n. The field after each round trip will result in a total reduction in amplitude by a factor of $r_{rt} \equiv r_1 r_2 e^{-\alpha d}$ due to reflection from each mirror, as well as loss associated with the cavity medium with power attenuation, α. It should be noted that the *field* attenuation would be $\frac{\alpha}{2}$ and the round trip distance is $2d$, and thus a the attenuation of the field caused by the medium in one round trip is $\sim e^{\frac{\alpha}{2}2d} = e^{\alpha d}$. The field also obtains a relative phase shift of e^{i2kd} for each round trip. The resulting field that is transmitted, E_T, is thus expressed as

$$\begin{aligned} E_T &= E_0 t_1 t_2 + E_1 + E_2 + E_3 + \dots \\ &= E_0 t_1 t_2 + E_0 t_1 r_{rt} e^{i2kd} t_2 + E_0 t_1 (r_{rt} e^{i2kd})^2 t_2 + E_0 t_1 (r_{rt} e^{i2kd})^3 t_2 + \dots \\ &= E_0 t_1 t_2 \left[1 + r_{rt} e^{i2kd} + (r_{rt} e^{i2kd})^2 + (r_{rt} e^{i2kd})^3 + \dots\right] \\ &= \frac{E_0 t_1 t_2}{1 - r_{rt} e^{i2kd}} \end{aligned} \tag{2.1}$$

in which the last line makes use of the geometric series. The total transmission, T, for a particular frequency, ν,can then be calculated from Eq. 2.1 as

$$T = \left|\frac{E_T}{E_0}\right|^2 = \frac{T_{max}}{1 + \left(\frac{2\mathscr{F}}{\pi}\right)^2 \sin^2\left(\frac{\pi\nu}{\mathrm{FSR}}\right)} \tag{2.2}$$

where the cavity finesse is defined as

$$\mathscr{F} = \frac{\pi\sqrt{r_{rt}}}{1 - r_{rt}} \tag{2.3}$$

and the free spectral range (FSR) is given by

$$\mathrm{FSR} = \frac{c}{2d} \tag{2.4}$$

The maximum transmission available is thus

$$T_{max} = \frac{|t_1 t_2|^2}{(1 - r_1 r_2)^2} \tag{2.5}$$

which can simplify in the assumption that the two mirrors have identical reflectivity and transmissivity by the use of the Stokes relations and energy conservation for purely real field amplitudes ($|t|^2 = 1 - |r|^2$) to $T_{max} = 1$. Consequently, full transmission of light through the two parallel mirrors is allowed regardless of reflectivity (as long as the two mirrors have equal reflectivity). This is a result of complete destructive interference of the light in the backward reflected direction from the first mirror, and complete constructive interference in the forward transmitted direction after the second mirror.

The transmission spectrum of a Fabry-Pérot cavity (Eq. 2.2) is plotted in Fig. 2.1b, in which the FSR corresponds to the frequency spacing between resonant transmission peaks and the finesse characterizes the loss of the cavity represented by the broadening of the peaks. In order to find the full width half maximum of the resonant peaks, FWHM $= \frac{\kappa}{2\pi}$, (for κ defining the cavity linewidth) we can solve for the frequencies which result in an intensity of $T_{max}/2$. Thus by using Eq. 2.2, the condition

$$\left(\frac{2\mathscr{F}}{\pi}\right)^2 \sin^2\left(\frac{\pi\nu}{\mathrm{FSR}}\right) = 1 \tag{2.6}$$

must be met. Solving for the frequencies, up to an integer multiple of the free spectral range gives

$$\begin{aligned} \nu &= \pm\frac{\mathrm{FSR}}{\pi}\sin^{-1}\left(\frac{\pi}{2\mathscr{F}}\right) \\ &\approx \pm\frac{\mathrm{FSR}}{2\mathscr{F}} \end{aligned} \tag{2.7}$$

in which the second line uses the approximation of large finesse, which is a valid assumption due to the requirement that the peaks must be well resolved in order to define a width. Twice this frequency thus gives an expression for the full width half maximum

$$\text{FWHM} = \frac{\kappa}{2\pi} = \frac{\text{FSR}}{\mathscr{F}} \tag{2.8}$$

The broadening of the cavity resonant peaks is due to the fact that the imperfect mirrors will always allow light to leak out of the cavity and couple to the continuum of outside modes. The rate at which energy is lost from the cavity is also given by its linewidth, κ, which can easily be seen by performing an inverse Fourier transform of the Lorentzian resonant peaks of Eq. 2.2 to find the intra-cavity power, $P(t)$, corresponding to exponential decay over time

$$P(t) = P(0)e^{-\kappa t} \tag{2.9}$$

for some initial power, $P(0)$. Large finesse cavities are thus associated with a small cavity linewidth (or decay rate), as evident in Fig. 2.1b.

The average photon lifetime, τ_{ph}, can be found by

$$\begin{aligned} \tau_{ph} &= \int_0^\infty t \left(-\frac{d}{dt} \frac{N_{ph}(t)}{N(0)} \right) dt \\ &= \frac{1}{\kappa} \end{aligned} \tag{2.10}$$

in which the number of photons in the cavity, $N_{ph}(t)$, is proportionate to the power (see Eq. 2.9).

The average number of round trips, N_{rt}, that a photon will undergo will simply be the average lifetime in the cavity (Eq. 2.10) divided by the round trip time, $\tau_{rt} = \frac{2d}{c} = \frac{1}{\text{FSR}}$, resulting in

$$N_{rt} = \frac{\tau_{ph}}{\tau_{rt}} = \frac{\text{FSR}}{\kappa} \tag{2.11}$$

We see from Eq. 2.11 and Eq. 2.8 that the average number of round trips is related to the finesse of the cavity by

$$N_{rt} = \frac{\mathscr{F}}{2\pi} \tag{2.12}$$

Another important method of describing a Fabry-Pérot cavity is the Q factor, which is a parameter to characterize any general damped oscillator. It is defined as the ratio

between the total energy stored by the resonator to the dissipated energy per oscillation cycle caused by the damping.

$$Q = 2\pi \frac{\text{total stored energy}}{\text{energy loss per cycle}} \tag{2.13}$$

The relative energy loss rate compared to the total energy in the cavity is, of course, given by the cavity decay rate, κ (i.e. the cavity energy is exponentially decaying in time, as shown in Eq. 2.9, with a time constant of $\tau_{ph} = \frac{1}{\kappa}$). The relative energy lost per oscillation will thus be this decay rate times the optical period, T_{op}. The Q factor can consequently be expressed as

$$\begin{aligned} Q &= 2\pi \frac{1}{\kappa T_{op}} \\ &= \frac{w_0}{\kappa} \end{aligned} \tag{2.14}$$

in which the resonant optical angular frequency of the light is $w_0 = \frac{2\pi}{T_{op}}$.

Eq. 2.8 can be used to find the relationship between the finesse and Q factor

$$Q = q\mathscr{F} \tag{2.15}$$

where q is an integer such that the resonant optical frequency, ν_0, is an integer multiple of the FSR, $\nu_0 = q\text{FSR}$. This q integer is normally very large due to the length of practical cavities being much larger than optical wavelengths.

The Q factor for a simple Fabry-Pérot cavity with attenuation of the intra-cavity medium, α, can be determined by finding the power lost in one round trip of the light using Eq. 2.9 and Eq. 2.14

$$P(\tau_{rt}) = P(0)e^{-\kappa\tau_{rt}} = P(0)e^{-\frac{w_0\tau_{rt}}{Q}} \tag{2.16}$$

However, the reduction in power after one round trip is also given by the previously mentioned factor of the field reflectivities and attenuation squared, $r^2 \equiv (r_1 r_2 e^{-\alpha d})^2$. Defining the power reflectivities of $R_1 \equiv r_1^2$ and $R_2 \equiv r_2^2$ gives a relation

$$P(\tau_{rt}) = P(0)R_1 R_2 e^{-\alpha 2d} \tag{2.17}$$

Equating Eq. 2.16 and Eq. 2.17 and solving for the Q factor thus gives the final expression

$$Q = \frac{2w_0 d}{c(2\alpha d - \ln(R_1 R_2))} \tag{2.18}$$

using a round trip time of $\tau_{rt} = 2d/c$. If we assume a cavity medium without attenuation and with duplicate mirror reflectivities ($R_1 = R_2$), it can be seen that the behaviour of a Fabry-Pérot cavity can be fully characterized simply by two quantities (FSR and $\mathscr{F}$) from which all other relevant parameters (as discussed in this section) can be determined.

2.2 Bragg Reflection

Any structure with a dielectric constant (or refractive index) that exhibits a periodic pattern in space could be called photonic crystals (PC), in analogy to solid state crystal materials with a periodic lattice of potential. Electromagnetic waves that pass through such materials can display various interesting properties, such as Bragg reflection and holography. There are also many examples of photonic crystals that appear in nature. They are responsible for the diverse colours of many animals and insects such as different species of butterflies, beetles, and can even be found in the scales of some deep-sea fish [115].

The simplest example of a PC is a medium composed of two alternating layers of different materials called a dielectric stack or Bragg mirror, and is essentially a one-dimensional photonic crystal [121]. At each interface between the layers, light will experience Fresnel reflections due to the discontinuity in the refractive index. We sill show that when there are many layers, each resulting in Fresnel reflection and transmission, an exceptionally high reflectance can occur due to the interference of the light from the back-reflection off the many different interfaces in the medium. Interestingly, this effect can even persist when the indices of the two layers are very similar producing extremely weak Fresnel reflection at any given single interface.

We will explore the phenomenon of Bragg reflection by first deriving the general dispersion relation for Bragg layers and describe the optical stop bands that appear at particular frequencies of light. As shown in Fig. 2.2, we begin by defining two layers of refractive index n_1 and n_2 with thicknesses a and b, respectively. These layers are repeated for n times with a spatial period of $\Lambda = a + b$. Within each layer, there are incident and reflected electromagnetic waves travelling in the positive and negative z directions, respectively. The total electric field is simply the sum of these forward and backward propagating waves with complex amplitudes a_n and b_n, respectively, for the field in the layer with index n_1 and c_n and d_n, respectively, for the field in layer 2 at the n^{th} unit cell. We will assume the fields are perpendicular to the plane of the Bragg layers so the wavevectors in each layer type only have an z component, $k_1 = n_1 \frac{\omega}{c}$ and $k_2 = n_2 \frac{\omega}{c}$. The electric fields in each layer,

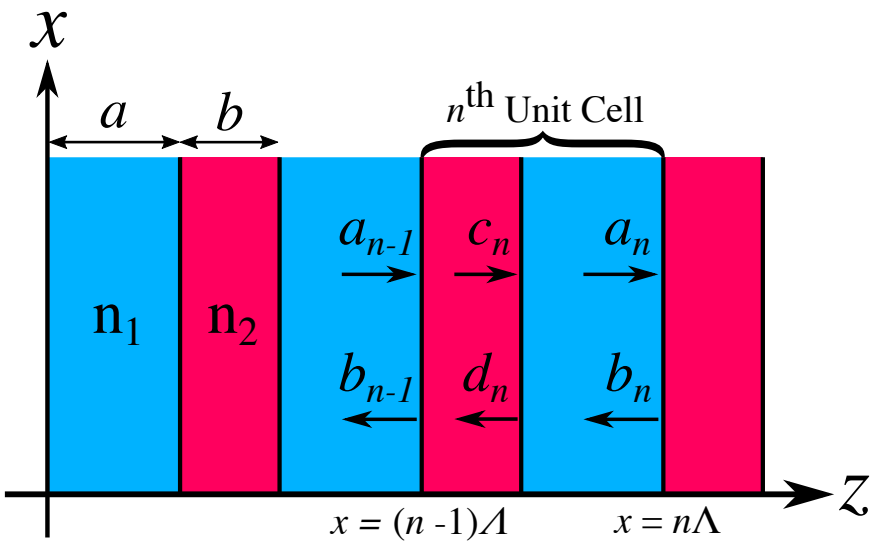

Figure 2.2: A Bragg medium consisting of two periodic layers with refractive indices n_1 and n_2 with thicknesses a and b, respectively. The unit-cell that repeated n times and has a period of $\Lambda = a + b$. The field amplitudes moving in the forward (backward) z direction in layer 1 and 2 are a_n (b_n) and c_n (d_n), respectively.

$E_{1n}(z)$ and $E_{2n}(z)$, are assumed to be oriented in the x direction and can be written as

$$\begin{aligned} E_{1n}(z) &= a_n e^{-ik_1(z-n\Lambda)} + b_n e^{ik_1(z-n\Lambda)}, \text{ for } n\Lambda - a < z < n\Lambda \\ E_{2n}(z) &= c_n e^{-ik_2(z-n\Lambda+a)} + d_n e^{ik_2(z-n\Lambda+a)}, \text{ for } (n-1)\Lambda < z < n\Lambda - a \end{aligned} \tag{2.19}$$

Two boundary conditions are used to ensure the fields are continuous and smooth over each interface between the layers at position z_L. The continuity boundary condition can be expressed as

$$E_{1n}(z_L) = E_{2n}(z_L) \tag{2.20}$$

where z_L represents the location of the position of the interface connecting the two field regions.

The second boundary condition requires that the field be smooth, and thus the derivatives of the field at each interface must be continuous. Alternatively, this boundary condition can be interpreted as demanding that the tangential magnetic field (oriented in the y direction in this case) also be continuous. The magnetic field is of course proportionate to the spatial derivative in the z direction of the electric field through Faraday's Law, giving

$$\left.\frac{\partial E_{1n}(z)}{\partial z}\right|_{z=z_L} = \left.\frac{\partial E_{2n}(z)}{\partial z}\right|_{z=z_L} \tag{2.21}$$

The two boundary conditions of Eq. 2.20 and 2.21 can be combined to create a 2×2 matrix formalism relating the complex field amplitudes of the fields in neighbouring layers. Evaluating the boundary conditions at the interface between layer 1 and 2 of the n^{th} unit cell ($z_L = n\Lambda - a$) gives

$$\begin{pmatrix} c_n \\ d_n \end{pmatrix} = I_{1\to 2} P_1 \begin{pmatrix} a_n \\ b_n \end{pmatrix} \tag{2.22}$$

and at the interface between layers 2 and 1 for the n^{th} and $(n-1)^{\text{th}}$ unit cells, respectively, in which $z_L = (n-1)\Lambda$ gives

$$\begin{pmatrix} a_{n-1} \\ d_{n-1} \end{pmatrix} = I_{2\to 1} P_2 \begin{pmatrix} c_n \\ d_n \end{pmatrix} \tag{2.23}$$

The matrix $I_{1\to 2}$ ($I_{2\to 1}$) is the well known transmission matrix from layer 1 to 2 (2 to 1) relating the field amplitudes on either side of an interface. It can be written in the form of the Fresnel transmission and reflection coefficients t_{12} and r_{12}, respectively, as

$$I_{1\to 2} = \frac{1}{t_{12}} \begin{pmatrix} 1 & r_{12} \\ r_{12} & 1 \end{pmatrix} = \frac{1}{2} \begin{pmatrix} 1 + \frac{k_2}{k_1} & 1 - \frac{k_2}{k_1} \\ 1 - \frac{k_2}{k_1} & 1 + \frac{k_2}{k_1} \end{pmatrix} \tag{2.24}$$

where

$$\begin{aligned} r_{12} &= \frac{k_1 - k_2}{k_1 + k_2} \\ t_{12} &= \frac{2k_1}{k_1 + k_2} \end{aligned} \tag{2.25}$$

for s polarized waves. The $I_{2\to 1}$ matrix is simply Eq. 2.24 with the layer 1 and 2 indices switched. The phase matrices P_1 and P_2 account for the phase accumulated across layers 1 and 2, respectively, and are given by

$$P_1 = \begin{pmatrix} e^{ik_1 a} & 0 \\ 0 & e^{-ik_1 a} \end{pmatrix} \tag{2.26}$$

and

$$P_2 = \begin{pmatrix} e^{ik_2 b} & 0 \\ 0 & e^{-ik_2 b} \end{pmatrix} \tag{2.27}$$

Substituting Eq. 2.22 into 2.23 we find that

$$\begin{pmatrix} a_{n-1} \\ b_{n-1} \end{pmatrix} = I_{2\to 1} P_2 I_{1\to 2} P_1 \begin{pmatrix} a_n \\ b_n \end{pmatrix} \tag{2.28}$$

The matrix multiplication can be performed in order to find a single transfer matrix connecting the incident and reflected field amplitudes a_{n-1} and b_{n-1}, respectively, to the corresponding amplitudes in the subsequent neighbouring unit-cell as

$$\begin{pmatrix} a_{n-1} \\ b_{n-1} \end{pmatrix} = \begin{pmatrix} A & B \\ C & D \end{pmatrix} \begin{pmatrix} a_n \\ b_n \end{pmatrix} \tag{2.29}$$

in which

$$\begin{aligned} A &= e^{ik_1 a}\left(\cos k_2 b + \frac{1}{2}i\left(\frac{k_2}{k_1} + \frac{k_1}{k_2}\right)\sin k_2 b\right) \\ B &= e^{-ik_1 a}\left(\frac{1}{2}i\left(\frac{k_2}{k_1} - \frac{k_1}{k_2}\right)\sin k_2 b\right) \\ C &= e^{ik_1 a}\left(-\frac{1}{2}i\left(\frac{k_2}{k_1} - \frac{k_1}{k_2}\right)\sin k_2 b\right) \\ D &= e^{-ik_1 a}\left(\cos k_2 b - \frac{1}{2}i\left(\frac{k_2}{k_1} - \frac{k_1}{k_2}\right)\sin k_2 b\right) \end{aligned} \tag{2.30}$$

It should be noted that this transfer matrix is unimodular, that is it has a determinant of one due to it describing the relationship between the fields in layers with equivalent index of refraction. Also the four matrix elements are related by $A = D^*$ and $B = C^*$, where the asterisk represents the complex conjugate.

The transfer matrix after N Bragg periods is simply found by taking the N^{th} power of the $ABCD$ matrix in Eq. 2.29. The reflection of such a Bragg mirror would be found by setting the final layer as have only propagating to the backward ($b_N = 0$), and so

$$\begin{pmatrix} a_0 \\ b_0 \end{pmatrix} = \begin{pmatrix} A & B \\ C & D \end{pmatrix}^N \begin{pmatrix} a_N \\ 0 \end{pmatrix} \tag{2.31}$$

for a forward and backward propagating initial wave amplitudes, a_0 and b_0, respectively. The reflectivity, R, is simply the square of ratio of backward to forward propagating electric field amplitudes waves at the initial layers,

$$R = \left|\frac{b_0}{a_0}\right|^2 \tag{2.32}$$

An analytical expression for the reflectivity can be found at the Bragg condition to simplify the transfer matrix after N periods, which results in

$$R(N) = \left|\frac{1 - \left(\frac{n_2}{n_1}\right)^{2N}}{1 + \left(\frac{n_2}{n_1}\right)^{2N}}\right|^2 \tag{2.33}$$

2.2.1 Band Structure

The treatment of electromagnetic wave propagation inside a periodically modulated media is analogous to the wave mechanics of electrons moving through a crystal lattice structure. Moreover, the mathematics of solid state band theory is equivalent to that of light in a periodically layered media. We will show that, as in solid state systems, a conduction gap (forbidden stop band) will occur in the energy (or frequency) versus wave number dispersion relation. As previously mentioned, Bragg layers are essentially one-dimensional dielectric lattice with period, Λ, such that

$$n^2(z+\Lambda) = n^2(z) \tag{2.34}$$

By the use of Bloch's theorem (or more generally, the Floquet theorem), the wave equation describing waves through a periodic medium give solutions for the electric field of the form

$$E_K(z) = u_K(z)e^{-iKz} \tag{2.35}$$

where $u_K(z)$ has the same periodicity as the crystal structure, such that

$$u_K(z+\Lambda) = u_K(z) \tag{2.36}$$

and K is the crystal wave number or Bloch wave number. The dispersion relation is then governed by the solutions for the allowed Bloch wave numbers.

Using the periodic boundary condition of Eq. 2.36 and keeping with the vector representation of the electric field amplitudes from the previous section, Eq. 2.35 can be written as

$$\begin{pmatrix} a_n \\ b_n \end{pmatrix} = e^{-iK\Lambda} \begin{pmatrix} a_{n-1} \\ b_{n-1} \end{pmatrix} \tag{2.37}$$

Thus, using the previously derived transfer matrix for the field amplitudes across one full period (Eq. 2.29 and 2.30), we can write

$$\begin{pmatrix} A & B \\ C & D \end{pmatrix} \begin{pmatrix} a_n \\ b_n \end{pmatrix} = e^{iK\Lambda} \begin{pmatrix} a_n \\ b_n \end{pmatrix} \tag{2.38}$$

This eigenvalue problem can thus be solved for the eigenvalues, $e^{iK\Lambda}$, as

$$e^{iK\Lambda} = \frac{1}{2}(A+D) \pm \{\frac{1}{4}(A+D)^2 - 1\}^{1/2} \tag{2.39}$$

using the fact that the determinant of the transfer matrix is one ($AD-BC=1$). Likewise, the eigenvectors corresponding to the eigenvalues in Eq. 2.39 can be solved for as

$$\begin{pmatrix} a_0 \\ b_0 \end{pmatrix} = \begin{pmatrix} B \\ e^{iK\Lambda} - A \end{pmatrix} \tag{2.40}$$

multiplied by an arbitrary constant. The final solutions for the Bloch waves in layer 1 can be found by combining the Bloch theorem (Eq. 2.35) with the field definitions of Eq. 2.19 giving

$$E_K(z) = u_K(z)e^{-iKz} = \left[(a_0 e^{-ik_1(z-n\Lambda)} + b_0 e^{ik_1(z-n\Lambda)})e^{iK(z-n\Lambda)}\right] e^{-iKz} \tag{2.41}$$

with the field amplitudes given by the eigenvectors in Eq. 2.40.

Since it can be seen from Eq. 2.30 that $A = D^*$, then $A + D$ is purely real. The dispersion relation can thus be found from the eigenvalues (Eq. 2.39) to be

$$\begin{aligned} K(\omega) &= \frac{1}{\Lambda}\cos^{-1}\left[\frac{1}{2}(A+D)\right] \\ &= \frac{1}{\Lambda}\cos^{-1}\left[\cos k_1 a \cos k_2 b - \frac{1}{2}\left(\frac{n_2}{n_1} + \frac{n_1}{n_2}\right)\sin k_1 a \sin k_2 b\right] \end{aligned} \tag{2.42}$$

where the wave numbers in each layer are $k_1 = n_1\omega/c = n_1 2\pi/\lambda$ and $k_2 = n_2\omega/c = n_2 2\pi/\lambda$ for a free-space optical wavelength of λ.

The solutions to this dispersion relation can be found in two regimes. In the regime in which $|\frac{1}{2}(A+D)| < 1$, the Bloch wave numbers are real, and thus correspond to solutions describing propagating Bloch waves. However, in the regime in which $|\frac{1}{2}(A+D)| > 1$, the Bloch wave numbers are instead complex with the form $K = m\pi/\Lambda + iK_i$, where m is an integer and K_i is the imaginary part of the Bloch wave number. These solutions represent Bloch waves that are evanescent in the Bragg media, resulting in incident light waves on the Bragg material boundary being reflected. The frequencies in which these solutions occur are the forbidden stop bands of the media dispersion diagram. The edges of the optical stop band occur when $|\frac{1}{2}(A+D)| = 1$.

Fig. 2.3 plots the Bloch dispersion relationship of Eq. 2.42, showing the optical stop band, when $\mathrm{Re}\{K\} = \pi/\Lambda$ with center frequency w_0 and bandwidth $\Delta\omega$. It should be noted that the dispersion relationship can also be used to find the group velocity, v_g, of the propagating light within the Bragg medium by $v_g = \frac{\partial\omega}{\partial k}$. Interestingly, we can also see from Fig. 2.3 that for a 1D Bragg grating the group velocity approaches zero at the stop band edges (corresponding to a Van Hove singularity).

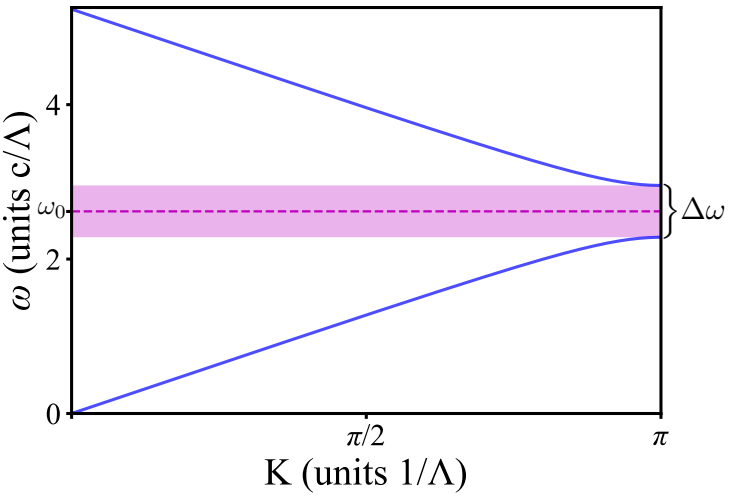

Figure 2.3: (a) Band diagram of a periodically layered medium comprised of two layers with index n_1 and n_2. The optical stop band is found at the Bragg condition of $\mathrm{Re}\{K\} = \pi/\Lambda$ with a center frequency of w_0 and bandwidth $\Delta\omega$ for the first stop band.

An approximate solution can be found for K within the stop band. First we let the Bloch wave number be complex with $\mathrm{Re}\{K\} = \pi/\Lambda$ such that

$$K\Lambda = \pi \pm ix \tag{2.43}$$

for a positive real number x. We define the center of the stop band to occur at frequency ω_0, in which we set

$$k_1 a = k_2 b = \frac{\pi}{2} \tag{2.44}$$

which is called the Bragg condition (or a quarter wave stack since $a = \frac{\lambda_0}{4n_1}$ and $b = \frac{\lambda_0}{4n_2}$).

We can also define a normalized frequency that is the difference from the center frequency as

$$y(\omega) = \frac{\omega - \omega_0}{c} n_1 a = \frac{\omega - \omega_0}{c} n_2 b \tag{2.45}$$

The general solution for the imaginary part of $K\Lambda$ as a function of frequency is found by substituting Eq. 2.45 and 2.43 into Eq. 2.42 (and using the identity $\cos(a_R + ia_I) = \cos a_R \cosh a_I - i \sin a_R \sinh a_I$ for a number with real and imaginary parts, a_R and a_I, respectively) to find

$$\cosh x = \frac{1}{2}\left(\frac{n_2}{n_1} + \frac{n_1}{n_2}\right)\cos^2 y(\omega) - \sin^2 y(\omega) \tag{2.46}$$

At the stop band edges, the Bloch wave number becomes purely real again and so we set $x = 0$ to obtain the upper and lower normalized frequencies

$$y_{\pm}(\omega_{\pm}) = \pm \sin^{-1} \frac{|n_2 - n_1|}{n_2 + n_1} \tag{2.47}$$

and thus the frequency bandwidth of the stop band, $\Delta\omega = \omega_+ - \omega_-$, is found to be

$$\begin{aligned} \Delta\omega &= \omega_0 \frac{4}{\pi} \sin^{-1} \frac{|n_2 - n_1|}{n_2 + n_1} \\ &\approx \omega_0 \frac{2}{\pi} \frac{\Delta n}{n_{avg}} \end{aligned} \tag{2.48}$$

where we used the approximation $|n_2 - n_1| \ll n_{1,2}$ in the last line, and defined the difference between the indices as $\Delta n = |n_2 - n_1|$ and the average index, $n_{avg} = \frac{n_2+n_1}{2}$.

We can also solve directly for x at the center frequency, w_0, by substituting Eq. 2.44 into the dispersion relation (Eq. 2.42). This reduces Eq. 2.42 to

$$\cos K\Lambda = -\frac{1}{2}\left(\frac{n_1}{n_2} + \frac{n_2}{n_1}\right) \tag{2.49}$$

at frequency w_0. Solving for x by substituting Eq. 2.43 into Eq. 2.49 gives

$$\begin{aligned} x_0 &= \left|\ln \frac{n2}{n1}\right| \\ &\approx \frac{2|n_2 - n_1|}{n_2 + n_1} = \frac{\Delta n}{n_{avg}} \end{aligned} \tag{2.50}$$

in which the last line is again found using the approximation $|n_2 - n_1| \ll n_{1,2}$. This means that the imaginary part of $K\Lambda$ will vary from zero at the band edges, $\omega_{\pm}$, to a maximum value of x_0 at ω_0 (Bragg condition) in which the Bloch wave number becomes

$$K_0 \approx \frac{1}{\Lambda}\left(\pi \pm i\frac{\Delta n}{n_{avg}}\right) \tag{2.51}$$

The general behaviour of the electric fields at the Bragg condition can be found using Eq. 2.51 and Eq. 2.35 giving

$$E_{K_0}(z) = u_{K_0}(z) e^{-i\frac{\pi}{\Lambda}z} e^{-\frac{1}{\Lambda}\frac{\Delta n}{n_{avg}}z} \tag{2.52}$$

This, of course, describes an evanescent wave that decays exponentially upon entry into the Bragg medium such that

$$E_{K_0}(z) \propto e^{-\frac{z}{z_p}} \tag{2.53}$$

with a characteristic penetration depth, z_p, of

$$z_p = \Lambda \frac{n_{avg}}{\Delta n} = \Lambda \frac{2}{\pi} \frac{\omega_0}{\Delta \omega} \tag{2.54}$$

2.2.2 2D Photonic Crystal Bandgap Effect

A structure that exhibits a two-dimensional translational symmetry, in which the material index (or dielectric, ϵ) is periodic in the x-y plane but homogeneous in the z direction, such that for a position in the lattice, $\vec{r}$,

$$\epsilon(\vec{r} + \vec{R}) = \epsilon(\vec{r}) \tag{2.55}$$

is called a two dimensional photonic crystal [54]. The dielectric pattern repeats over any linear combination of the primitive lattice vectors, $\vec{a}_1$ and $\vec{a}_2$, such that

$$\vec{R} = n_1 \vec{a}_1 + n_2 \vec{a}_2 \tag{2.56}$$

for integers n_1 and n_2.

One example of this type of structure would be a hexagonal (also called triangular) lattice of holes imprinted into a slab of dielectric material, as depicted in Fig. 2.4. Structures such as these can exhibit similar photonic crystal stop bands (sometimes called bandgaps) as found in the previous section on Bragg layers. The spectral location of the stop bands will depend on the geometrical parameters of the photonic crystal pattern including the lattice constant, a, thickness t, and hole radius, r, and will result in complete reflection for in-plane propagating modes.

The general dispersion relation can be found using Maxwell's equations (assuming a non-magnetic material with constant permeability, μ_0)

$$\begin{aligned} \nabla \times \vec{E} &= -i\omega\epsilon(\vec{r})\vec{E} \\ \nabla \times \vec{H} &= i\omega\mu_0\vec{H} \end{aligned} \tag{2.57}$$

for monochromatic electric and magnetic fields, $\vec{E}$ and $\vec{H}$, respectively, with time-dependence $e^{-i\omega t}$. By taking the curl of Faraday's law of induction and substituting in Ampère's Law, the following wave equation can be obtained for the electric field in the media

$$\nabla \times (\nabla \times \vec{E}) - \omega^2 \epsilon(\vec{r})\mu_0 \vec{E} = 0 \tag{2.58}$$

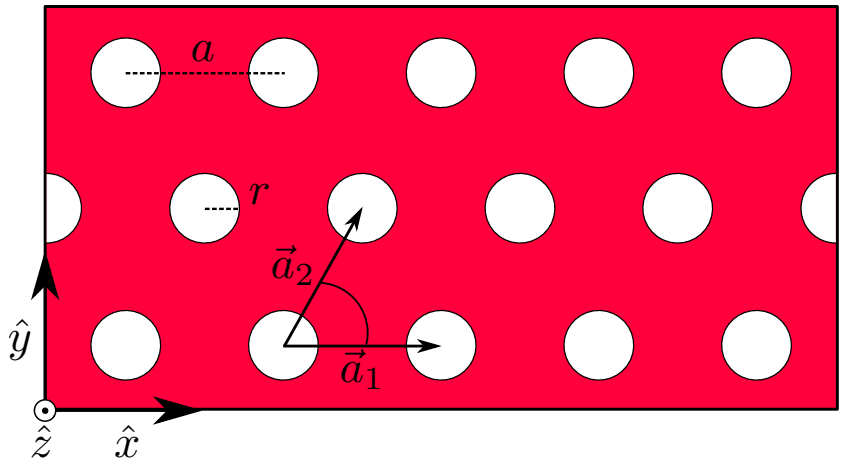

Figure 2.4: A 2D photonic crystal with a hexagonal (or triangular) pattern of holes in a dielectric material with lattice constant, a, and hole radius, r. The pattern is repeated for any linear combination of the primitive lattice vectors a_1 and a_2. Bandgaps (or stop bands) can occur in the dispersion relation for in-plane guided modes and thus can act as a reflective mirror allowing only evanescent waves to exist within the photonic crystal structure.

We can use the expression for the spatial Fourier transform of the electric field, $\vec{\mathcal{E}}(\vec{k})$, such that

$$\vec{E}(\vec{r}) = \iiint \vec{\mathcal{E}}(\vec{k}) e^{i\vec{k}\cdot\vec{r}} d^3k \tag{2.59}$$

and the discrete Fourier transform for the periodic dielectric constant with Fourier coefficients, $\epsilon(\vec{G})$,

$$\epsilon(\vec{r}) = \sum_{\vec{G}} \epsilon(\vec{G}) e^{i\vec{G}\cdot\vec{r}} \tag{2.60}$$

in which a general reciprocal lattice vector, $\vec{G}$, is any linear combination of primitive reciprocal lattice vectors, $\vec{b}_1$ and $\vec{b}_2$, such that

$$\vec{G} = m_1\vec{b}_1 + m_2\vec{b}_2 \tag{2.61}$$

for integers m_1 and m_2.

Substituting both Eq. 2.59 and Eq. 2.60 into Eq. 2.58 gives the dispersion relation

$$\vec{k} \times (\vec{k} \times \vec{\mathcal{E}}(\vec{k})) + \omega^2\mu_0 \sum_{\vec{G}} \epsilon(\vec{G})\vec{\mathcal{E}}(\vec{k} - \vec{G}) = 0 \tag{2.62}$$

The Bloch theorem still applies to the fields (as in Eq. 2.35), such that the solutions to the fields are of the form

$$\vec{E}_{\vec{K}}(\vec{r}) = u_{\vec{K}}(\vec{r})e^{-i\vec{K}\cdot\vec{r}} \tag{2.63}$$

where the spatial distribution is periodic ($u_{\vec{K}}(\vec{r}+\vec{R}) = u_{\vec{K}}(\vec{r})$).

Using the dispersion relation (Eq. 2.62) in combination with the Bloch theorem (Eq. 2.63), the propagation frequency as a function of the Bloch wave vector, $\vec{K}$, (band diagram) can be obtained. These Bloch vector solutions represent the allowed in-plane Bloch modes for the given PC pattern geometry in the dielectric material. In the same vein as the periodic Bragg layers, the dispersion relation can produce photonic bandgaps (stop bands) in which the solutions for the Bloch wave vectors become complex numbers. These solutions represent evanescent fields, and thus the light at frequencies within the stop band is unable to propagate in the medium and is reflected when incident upon such spatially periodic structures.

However, one of the main differences between a one-dimensional Bragg mirror and a two-dimensional photonic crystal is that the polarization of the light can play a large role. In a 2D PC slab, the in-plane guided modes (setting $k_z = 0$ for simplicity) can be separated into two distinct types. The first being transverse electric (TE) modes, which have magnetic fields that are perpendicular to the plane of the membrane ($\vec{H} = H_z\hat{z}$) with the electric field being completely in plane ($E_z = 0$). The other type is transverse magnetic (TM) modes in which the restraints on the magnetic an electric fields are reversed ($\vec{E} = E_z\hat{z}$ and $H_z = 0$). TE and TM modes can exhibit extremely different dispersion relations, with photonic bandgaps in distinct regions. Nevertheless, careful design of the PC pattern dimensions can allow for the bandgaps of both the TE and TM modes to overlap, resulting in a complete optical bandgap that occur for all polarizations.

Fig. 2.5a shows a band diagram for a 2D PC membrane (using Lumerical Mode Solutions) in a material of dielectric constant $\epsilon = 13$, and a hexagonal pattern of holes with a radius and lattice constant ratio of $\frac{r}{a} = 0.48$ for TE modes with $K_z = 0$. The Bloch vector directions are plotted with respect to the hexagonal reciprocal lattice directions of the irreducible Brillouin zone labelled Γ, M, and K as depicted in the inset. It is evident that there exists a frequency bandgap (shown as the shaded region) in which no waves can propagate in any direction.

Interestingly, the general behaviour of TE bandgaps is that they tend to occur for PC patterns that have connecting regions of high index, such as a thin grid of dielectric (dielectric veins). The TM bandgaps, conversely, appear for structures consisting of isolated regions of high index material (such as a lattice of dielectric columns).

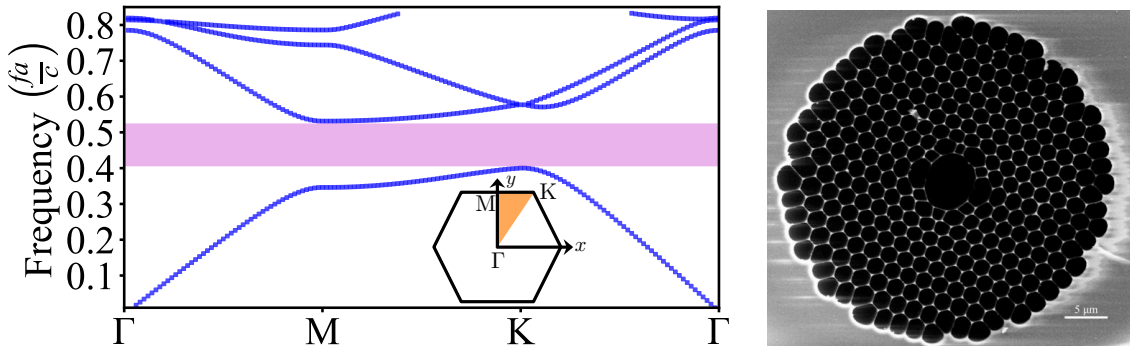

(a) (b)

Figure 2.5: (a) The band diagram of TE modes for a hexagonal lattice PC membrane with $\epsilon = 13$, $\frac{r}{a} = 0.48$ and $K_z = 0$ (found using Lumerical Mode Solutions software). The photonic bandgap is shown in the shaded area and the inset depicts the Bloch vector directions for the irreducible Brillouin zone. (b) An SEM image of a hollow core photonic crystal fiber (HCPCF) with a hexagonal PC pattern in the cladding that confines light to the center hollow core.

By using a triangular (or hexagonal) lattice of empty holes in a high index dielectric medium, such as the one shown in Fig. 2.4, both the requirements for TE and TM bandgaps can be met. The regions in the middle of the triangle of holes act as isolated high index regions that produce TM bandgaps, while the dielectric material is all still connected with thin bridges between the holes.

This is reason for the use of hexagonal patterns in the hollow core photonic crystal fibers that are utilized in this thesis. A cross-section of the HCPCF is shown in Fig. 2.5b, in which the fiber transversely confines light of all polarizations to the center hollow core region by the photonic crystal bandgap effect created from the surrounding triangular lattice of holes in the fiber material.

2.3 Photonic Crystal Membranes

This section will focus on the mechanism by which reflection can occur from incident light that is perpendicular to the plane of a photonic crystal pattern, as depicted in Fig. 2.6. This is in contrast to reflection of light incident in the plane of the PC slab due to the

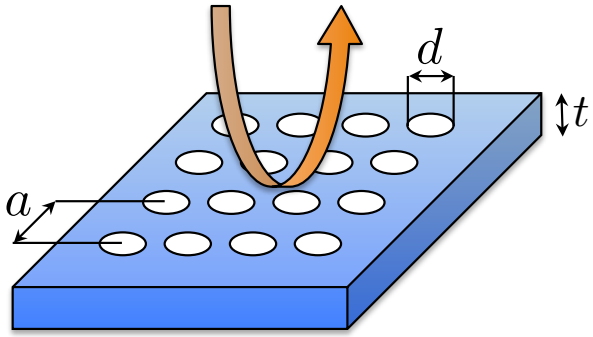

Figure 2.6: Incident light perpendicular to the plane of the PC membrane can be completely reflected for a PC membrane with a certain material index, lattice constant, a, hole diameter, d, (or radius, r) and membrane thickness, t.

photonic crystal bandgap effect, as discussed previously in Section 2.2.2.

In order to understand the mechanism of reflection for perpendicular incident light we must explore the different types of modes that can exist in a membrane with an embedded photonic crystal pattern. Fig. 2.7a shows a band diagram of TE (even) modes in a silicon membrane with a square lattice of holes of radius, $r = 0.2a$ and thickness, $t = 0.5a$ for the Bloch vector directions for the irreducible Brillouin zone, as shown in the inset. The line dividing the shaded yellow region and the non-shaded region is the light line for which $\omega = ck$.

The guided modes that exist from in-plane incident light represent modes under the light cone of the band diagram. These modes are trapped in the z direction (perpendicular to the plane of the membrane) by total internal reflection. In addition to these modes, guided resonances are also possible, which correspond to modes above the light cone (also called the leaky modes). Similar to the in-plane guided modes, the electromagnetic fields of the guided resonances are highly confined to within the PC slab.

However, in contrast to in-plane guided modes, guided resonances can couple to external fields in complex ways. Guided resonances with lower Q factors are very leaky and thus can couple strongly with the external fields, in contrast to extremely high Q resonances which are tightly confined to the membrane. For a particular wavelength of incident light, the design of the PC membrane can be tailored to cause complete destructive interference between particular guided resonances and the external fields in the forward direction, while allowing for constructive interference in the backward direction, thus producing a highly reflective surface.

A reflection spectrum of a 2D PC membrane can be seen in Fig. 2.7b, showing high reflectivity peaks at resonant frequencies. Each resonant peak in the spectrum corresponds to a particular guided resonant mode in the radiation region above the light cone. For example, the red dotted circle in Fig. 2.7a is the TE guided resonant mode (at perpendicular incident light, $k_x = k_y = 0$, represented by the Γ point) that causes for the high reflection peak in the red dotted circle shown in Fig. 2.7b.

The other TE modes evident in Fig. 2.7a have Q factors that are too large to couple to the external fields and thus do not produce a clear Fano resonance in the reflection spectrum of the PC film. The next higher order mode that has a low enough Q to produce a high reflection peak (the neighbouring peak to the resonance circled in red in Fig. 2.7b) happens to be a TM (odd) mode (only the TE modes are shown in the band diagram of Fig. 2.7a).

2.3.1 Fano Resonance in PC slabs

The first detailed theoretical analysis of guided mode resonances in a two-dimensional PC membrane was done by Fan et. al [29]. An intuitive explanation was found for the complicated reflection spectra that can be produced by PC membranes. This model describes the fields in the time domain and relies only on interference and conservation of energy arguments.

For incident light that is normal to the surface of the slab, there are two possible pathways light can take in order to transmit through the membrane. The first is the direct path through the membrane without coupling into guided resonances, and the second pathway is one in which the guided resonances are excited and subsequently decays slowly into free space. As alluded to above, these resonances can be thought of as cavity modes in the slab with relatively high Q factors. The total transmission will simply be the interference between these two direct and indirect pathways. Conversely, these same processes can of course be applied to the reflected fields as well.

The resonant peaks of reflection caused by the interference between a background (the direct pathway) and a resonant scattering process (the indirect pathway) are characteristically asymmetric. This interference effect is a type of Fano resonance similar to those found in some solid-state and atomic physics phenomena. The asymmetry of the Fano resonance peaks are due to the fact that the background pathway contributes field amplitudes that are continuous and slowly varying over frequency, while the guided resonances have amplitudes that change rapidly in magnitude and phase.

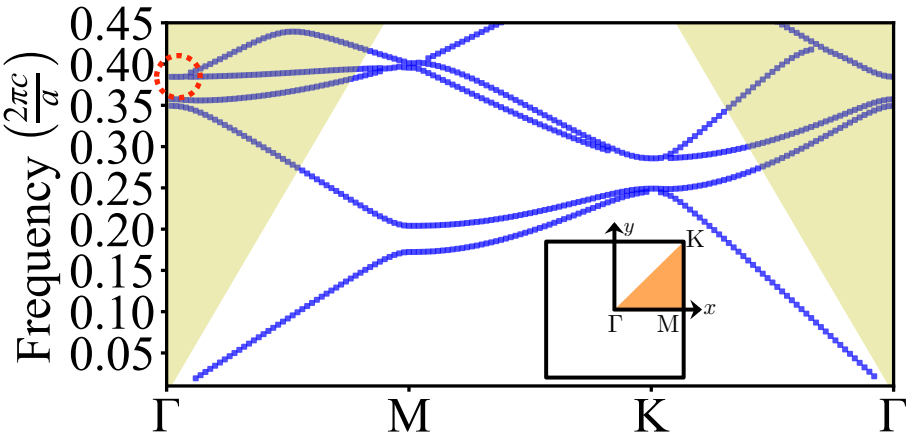

(a)

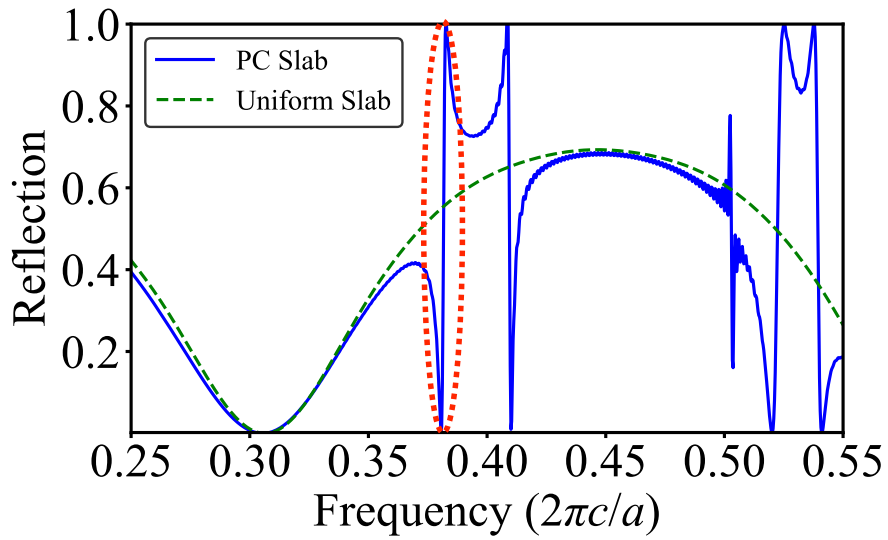

(b)

Figure 2.7: (a) Band diagram (for TE modes) of a silicon membrane with a square lattice PC pattern of hole radius, $r = 0.2a$, and film thickness, $t = 0.5a$, for Bloch vector directions in the irreducible Brillouin zone depicted in the inset. The yellow shaded region represents the radiation modes above the light cone ($\omega = ck$) where leaky modes (guided resonances) are possible. The non-shaded region are in-plane guided modes below the light cone. (b) Reflection spectrum of the 2D PC silicon membrane (solid blue line). The dashed green line shows the spectrum for a uniform film without PC holes with a refractive index found by averaging the holes and silicon material of the PC film. The dotted red circles in (a) and (b) represent the same low Q guided resonant mode. Both plots are produced by numerical simulations of the described PC membrane using Lumerical Solutions software.

These asymmetric Fano resonances of high reflection are clearly evident in the spectrum shown in Fig. 2.7b. The direct pathway produces the broad background peaks that are similar to a Fabry-Pérot spectrum. This is apparent from the spectrum of a uniform film without holes (with an averaged index of the silicon material and PC holes), as depicted as the dashed green line in Fig. 2.7b, in comparison with the background reflection of the pattern membrane spectrum (solid blue line). The direct pathway is thus responsible for this background spectrum of the PC film which acts to produce a Fabry-Pérot spectrum, while the presence of holes introduces the narrow resonant peaks that allow for large reflectivities. It is evident that the resonant peaks are characteristically asymmetric, with certain resonances possessing narrow linewidths allowing for the transmission to vary from 0% to 100% within a very short range of frequencies.

In order to find a single Fano resonant peak, we find the total field transmission and reflection amplitudes, t and r, respectively, by adding the contributions from the direct pathway, t_d and r_d, and the indirect pathway coupled to the particular resonant mode giving

$$\begin{aligned} t &= t_d + f\frac{\gamma}{i(\omega-\omega_0)+\gamma} \\ r &= r_d \pm f\frac{\gamma}{i(\omega-\omega_0)+\gamma} \end{aligned} \tag{2.64}$$

as a function of frequency, ω. The peaks corresponding to the indirect resonance pathways are modelled as a Lorentzian shape with center frequency, ω_0, peak linewidth, γ, and complex amplitude, f.

A Lorentzian shape is used because the guided resonances experience exponential decay out of the membrane over time on both the reflecting and transmitted sides, which has a Lorentzian spectrum in frequency space by taking the Fourier transform. The plus and minus signs are due to the different symmetries of the modes about the plane of the membrane. Odd modes represent a π phase difference between the fields leaking on either side of the membrane, while the even mode fields are in phase.

The peak amplitudes, f, can be determined using conservation of energy such that

$$|t|^2 + |r|^2 = 1 \tag{2.65}$$

We also note that since t_d and r_d are the transmission and reflection amplitudes of incident light through a uniform dielectric slab (without the PC holes), we must also require that

$$|t_d|^2 + |r_d|^2 = 1 \tag{2.66}$$

Using Eq. 2.65 and 2.66 with the total field amplitude coefficients of Eq. 2.64, the following constraint on the resonant peak amplitudes can be made

$$f = -\left(t_d \pm r_d\right) \tag{2.67}$$

Since r_d and t_d represent the background of the PC membrane spectra, as shown in Fig. 2.7b, they can be fitted to the general form of a uniform slab with an incident plane wave

$$\begin{aligned} r_d &= \frac{i\dfrac{k_{z0}^2 - k_{z1}^2}{2k_{z0}k_{z1}}\sin(k_{z1}z)}{\cos(k_{z1}z) - i\dfrac{k_{z0}^2 + k_{z1}^2}{2k_{z0}k_{z1}}\sin(k_{z1}z)} \\ t_d &= \frac{1}{\cos(k_{z1}z) - i\dfrac{k_{z0}^2 + k_{z1}^2}{2k_{z0}k_{z1}}\sin(k_{z1}z)} \end{aligned} \tag{2.68}$$

which can be derived from the transfer matrix method described in Section 2.2 using Eq. 2.24 - 2.28, assuming only a single layer. The wave numbers k_{z0} and k_{z1} represent the component of the wave vector perpendicular to the plane of the membrane in air and in the dielectric medium, respectively. The thickness of the membrane is set as z.

Using the correct linewidth and center frequency of the resonances, the spectra of the Fano resonances of the PC membranes can be reproduced using Eq. 2.68 and Eq. 2.67 in Eq. 2.64. This can be seen in Fig. 2.8, in which these equations are fitted to the first resonant peak found in the simulation results of Fig. 2.7b (circled with a red dotted line). The tow fitting parameters used are $\gamma = 1.122 \times 10^{-3} \times \frac{2\pi c}{a}$ and $\omega_0 = 0.3816 \times \frac{2\pi c}{a}$. It should be noted that the fitting of this peak clearly becomes poor at larger frequencies. This is caused by the fact that there is a nearby neighbouring (TM) resonant peak that slightly overlaps this fitted peak.

To summarize, the principal phenomenon of Fano resonances appear in the reflection and transmission spectra of a PC membrane by incident light that is perpendicular to the plane of the membrane. These resonances are caused by the interference of the background light of a direct pathway through the membrane with that of guided resonances confined to the dielectric slab. Thus, full reflection can occur even without the presence of a complete photonic crystal bandgap due to the leaky guided resonances coupling to the external field to create asymmetric Fano resonances.

Interestingly, as we will explore more in Section 5.7, these membranes can also be designed to have reflectivities that are polarization dependent by using a PC pattern with a

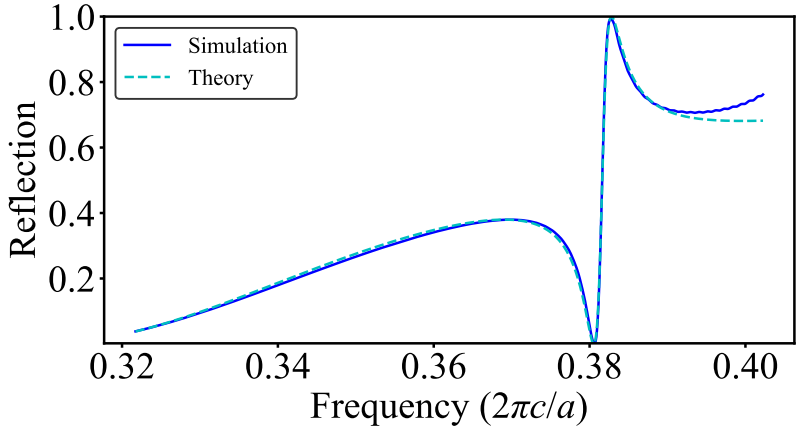

Figure 2.8: The first resonant peak of the silicon PC membrane simulated in Fig. 2.7b (circled in a red dotted line). The simulation results (shown as a solid blue line here) are fitted to Eq. 2.64 (using Eq. 2.68 and Eq. 2.67). This theoretical fit (shown as a dotted green line) uses fitting parameters of $\gamma = 1.122 \times 10^{-3} \times \frac{2\pi c}{a}$ and $\omega_0 = 0.3816 \times \frac{2\pi c}{a}$.

broken symmetry. The type of symmetry that is broken will dictate what type of polarization dependence the mirror will exhibit. For example, if the pattern instead consists of a lattice of rectangular holes rather than circular, this will allow for horizontal and vertically polarized light to be reflected differently, and can even be designed to completely transmit and reflect orthogonal polarizations for a particular wavelength of light [66].

Chapter 3

Light-Matter Interactions

In this chapter, we begin with a discussion of light-matter interactions. Specifically, we start by describing light propagation through a general medium. This leads into a brief review of a simple two level atom interacting with a classical electromagnetic field. We then introduce the interactions of a three level atom with multiple coupling fields, in particular the Λ-scheme configuration. This will include multi-photon processes such as electromagnetically induced transparency (EIT) [16, 45, 68] and two photon absorption (TPA) [82, 95].

We continue this chapter with the theoretical treatment of a single atom in a cavity, building on the concepts of an empty cavity, as reviewed in Chapter 2. This includes a summary of the various relevant coupling regimes between the atom and resonator that are possible, with their respective properties and applications considered. We then expand the theory to describe an ensemble of atoms in a cavity, and conclude with a treatment for three level atoms in a cavity resulting in vacuum induced transparency (VIT) [105, 106], a phenomenon that we will later utilize in our proposal for an all-optical switch controlled with a single photon.

3.1 Light-Matter Interaction in Free Space

In order to first describe light-matter interactions, we will begin by considering the propagation of classical light in a media. The electric, $\vec{E}$, and magnetic, $\vec{B}$, fields, of course,

obey Maxwell's equations (in the absence of free unbound charges or currents)

$$\begin{aligned}\vec{\nabla}\times\vec{E} &= -\frac{\partial\vec{B}}{\partial t}\\ \vec{\nabla}\times\vec{B} &= \frac{1}{c^2}\frac{\partial}{\partial t}\left(\vec{E}+\frac{1}{\epsilon_0}\vec{P}\right)\end{aligned} \tag{3.1}$$

for a macroscopic polarization of the medium, $\vec{P}$, which acts as a source term for the fields. The wave equation for the fields can be found by combining Eq. 3.1 together for a divergentless electric field (Gauss's law) while taking the appropriate time derivatives to give

$$\nabla^2\vec{E} - \frac{1}{c^2}\frac{\partial^2\vec{E}}{\partial t^2} = \frac{1}{\epsilon_0 c^2}\frac{\partial^2\vec{P}}{\partial t^2} \tag{3.2}$$

The wave equation is a second order differential equation in space and time, however, it can be reduced to a first order equation under the slowly varying envelope approximation (SVEA) [92]. We define a nearly monochromatic electric field with central frequency, ω_c, that has an envelop function, $\mathcal{E}$, that varies slowly over time and the propagation direction z, relative to the optical frequency period and wave vector, $k = \frac{\omega_c}{c}$, such that

$$\vec{E}(\vec{r},t) = \frac{1}{2}\vec{\mathcal{E}}(\vec{r},t)e^{i(kz-\omega_c t)} + c.c. \tag{3.3}$$

where $c.c.$ refers to the complex conjugate of the first term. Since we write the field in the form of Eq. 3.3, then the response of the medium allows for the atomic polarization density to be written as

$$\vec{P}(\vec{r},t) = \frac{1}{2}\vec{\mathcal{P}}(\vec{r},t)e^{i(kz-\omega_c t)} + c.c. \tag{3.4}$$

with a slowly varying amplitude, $\mathcal{P}$. The expressions for the electric field (Eq. 3.3) and polarization (Eq. 3.4) can be substituted into the wave equation (Eq. 3.2). Due to the slowly varying behaviour of the envelope functions, $\mathcal{E}$ and $\mathcal{P}$, we make the approximations

$$\begin{aligned}\omega_c\mathcal{P} &\gg \frac{\partial\mathcal{P}}{\partial t}\\ \omega_c\mathcal{E} &\gg \frac{\partial\mathcal{E}}{\partial t}\\ k\mathcal{E} &\gg \frac{\partial\mathcal{E}}{\partial z}\end{aligned} \tag{3.5}$$

which results in the reduced general SVEA wave equation for the envelop functions

$$\frac{\partial}{\partial z}\mathcal{E} + \frac{1}{c}\frac{\partial}{\partial t}\mathcal{E} = \frac{ik}{2\epsilon_0}\mathcal{P} \tag{3.6}$$

where we also assume, for simplicity, a plane wave field with no transverse spatial derivatives. In order to solve for the field we must find the polarization density, which is defined as the dipole moment per volume caused by an applied field. The proportionality constant between the polarization and the applied field, given the atoms respond linearly under a sufficiently weak field, is the susceptibility, χ, which can be written such that

$$\mathcal{P} = \chi \epsilon_0 \mathcal{E} \tag{3.7}$$

For the special case of a continuous wave field, in which the envelope function is constant over time ($\frac{\partial}{\partial t}\mathcal{E} = 0$), we can use Eq. 3.7 to obtain the simple differential equation

$$\frac{\partial}{\partial z}\mathcal{E} = \frac{ik\chi}{2}\mathcal{E} \tag{3.8}$$

This is trivially solved to find

$$\mathcal{E}(z) = \mathcal{E}_0 e^{i\frac{k\chi}{2}z} \tag{3.9}$$

with initial field amplitude, E_0. Substituting this solution for the envelop function, Eq. 3.9, back into the full equation for the field, Eq. 3.3, and setting the field in one direction, $\vec{E}(\vec{r}, t) = E(z, t)\hat{x}$, we find

$$E(z, t) = \frac{1}{2}\mathcal{E}_0 e^{i(\tilde{n}kz - \omega_c t)} + c.c. \tag{3.10}$$

for the plane continuous wave solution, where

$$\widetilde{n} = 1 + \frac{\chi}{2} \tag{3.11}$$

turns out to simply be the complex refractive index (for small susceptibility, $\chi \ll 1$). Since χ can in general be complex, there are two main effects from the media on the field that can occur. Exponential attenuation or amplification of the field power is a result of the imaginary component of χ, at a rate per distance, α, given by

$$\alpha = k \ \mathrm{Im}[\chi] \tag{3.12}$$

while the real part of χ is responsible for a phase shift as the pulse traverses the media, embodied by the real part of the refractive index of

$$n = 1 + \frac{\mathrm{Re}[\chi]}{2} \tag{3.13}$$

The effect of an atomic system on light can thus be characterized by the susceptibility of the atomic cloud. In order to relate χ to the atomic system we can first use again the definition of the polarization as the electric dipole moment per volume, (setting the polarization and dipole moment along the $\hat{x}$ direction)

$$\begin{aligned} P &= \frac{N_a}{V}\langle\mu\rangle \\ &= \frac{N_a}{V}\mu_{ge}\left(\rho_{eg}e^{-i\omega_c t} + c.c.\right) \end{aligned} \tag{3.14}$$

where N_a is the number of atoms, V is the volume, and $\langle\mu\rangle$ is the average electric dipole moment of a single atom. The last line is found using $\langle\mu\rangle = \mathrm{Tr}[\mu\rho]$, while the time dependence comes from converting to the Schrödinger picture. The dipole moment matrix element, $\mu_{ge} \equiv \langle g|\mu|e\rangle$, and density matrix element, $\rho_{eg} \equiv \langle e|\rho|g\rangle$ are found for the coherences between the atomic ground and excited state with a transition frequency close to the carrier frequency of the applied field.

Using Eq. 3.7 in Eq. 3.4, and comparing the negative and positive frequency components to Eq. 3.14, we find that

$$\chi = \frac{N_a}{V}\frac{\mu_{ge}}{\epsilon_0\mathcal{E}/2}\rho_{eg} \tag{3.15}$$

and thus the response of the field in the atomic cloud can be reduced to finding the atomic density matrix coherences, ρ_{eg}. We will show in the next two sections the derivations of these density matrix elements for both two level (Section 3.1.1) and three level atoms (Section 3.1.2).

3.1.1 Two Level Atom

Now that we have described the propagation of light through an atomic medium and the effect of the induced dipole moments on the field, we will now look at how the field, in turn, affects the atoms by causing coherences and driving transitions. This will be a semi-classical treatment, using quantized atomic energy levels interacting with a classical field, while in the later sections of this chapter we will use the fully quantized picture.

Under the assumption of a weak external coupling field that is nearly resonant to a single atomic transition, an atom may be approximated as a simple two level system. This ensures that populations of other atomic levels are negligible. As shown in Fig. 3.1, we denoted the ground and excited states as $|g\rangle$ and $|e\rangle$, respectively, which have an energy difference of $\hbar\omega_{eg}$. The atoms are illuminated by an external probe field that is nearly

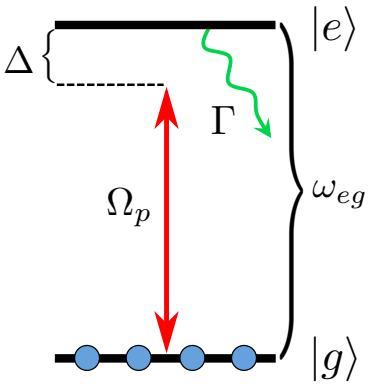

Figure 3.1: A two level atom excited by a weak external probe field with Rabi frequency, Ω_p, at a frequency detuning, Δ. The separation between the ground and excited state is ω_{eg}, and the spontaneous emission rate (natural linewidth) is Γ.

monochromatic with frequency, ω_p, with again a slowly varying envelop, $\mathcal{E}$, as previously defined in Eq. 3.3. We also define the detuning between the probe laser field and atomic transition energy as $\Delta \equiv \omega_p - \omega_{eg}$.

The Hamiltonian, H, describing this system is the summation of the internal atomic energy, H_A, and the interaction energy between the atom and field, H_{AF}. Using the dipole approximation, in which the atom is much smaller than the wavelength of the field, we have

$$\begin{aligned} H &= H_A + H_{AF} \\ H_A &= \hbar\omega_{eg}\sigma^\dagger\sigma \\ H_{AF} &= -\vec{\mu}\cdot\vec{E} \end{aligned} \tag{3.16}$$

with the ground state defined at zero energy. The raising and lowering atomic operators are $\sigma^\dagger = |e\rangle\langle g|$ and $\sigma = |g\rangle\langle e|$, respectively. We use the atomic dipole operator, $\vec{\mu} = -q\hat{r}$, with the fundamental charge, q, and electron position operator, $\hat{r}$. We can write the dipole operator in the basis of the bare energy eigenstates as

$$\vec{\mu} = \vec{\mu}_{ge}\left(\sigma + \sigma^\dagger\right) \tag{3.17}$$

noting that there is no permanent atomic dipole moment ($\langle e|\vec{\mu}|e\rangle = \langle g|\vec{\mu}|g\rangle = 0$) due to the spherical symmetry of the atom.

We can thus write the total Hamiltonian in the bare state energy eigenbasis with a

classical field using Eq. 3.16, Eq. 3.17 and Eq. 3.3 as

$$H = \hbar\omega_{eg}\sigma^\dagger\sigma - \hbar\frac{\Omega_p}{2}\left(\sigma + \sigma^\dagger\right)\left(e^{-i\omega_p t} + e^{i\omega_p t}\right) \tag{3.18}$$

where we define the Rabi frequency as $\Omega_p = \frac{\mu_{ge}\mathcal{E}}{\hbar}$. The expectation values of σ and $\sigma^\dagger$ have a time dependence of $e^{-i\omega_{eg}t}$ and $e^{i\omega_{eg}t}$, respectively, under the free evolution of the excited state atomic Hamiltonian (corresponding to a positive and negative frequency). This results in two terms that oscillate fast as $\sim e^{\pm i(w_p+w_{eg})t}$, and two cross terms that oscillate slowly as $\sim e^{\pm i(\omega_p-\omega_{eg})t}$. We can make the rotating wave approximation (RWA) under the assumption that $|\Delta| = |\omega_p - \omega_{eg}| \ll \omega_p + \omega_{eg}$, which means the fast oscillating terms can be set to an average of zero which acts to coarse-grain the dynamics over the short optical time scales to focus only on the slowly varying dynamics over long times. This is also under the assumption of a weak probe field, such that $\Omega_p \ll \omega_{eg}$.

It should be noted that this approximation necessarily accompanies our previous assumption of a two level atom. Both approximations ignore the far off resonance interactions with the other levels of the atom and consider only the near-resonant interaction of one excitation. If the detuning from the excited state becomes too large that the fast oscillating terms must be considered, and this would require us to have to also consider the couplings to other levels.

We see from Eq. 3.18 that after invoking the RWA we end up with the Hamiltonian

$$H = \hbar\omega_{eg}\sigma^\dagger\sigma - \hbar\frac{\Omega_p}{2}\left(\sigma e^{i\omega_p t} + \sigma^\dagger e^{-i\omega_p t}\right) \tag{3.19}$$

This Hamiltonian is, of course, still time dependent, which would produce state coefficients that are also time dependent, oscillating at optical frequencies. However, we can take advantage of the fact that these oscillations are phase-locked (on resonance), and so we may transform from the static lab frame to an appropriate rotating frame (laser frame) to ignore these fast oscillations. This transformation between general states in the lab frame, $|\psi\rangle = c_g|g\rangle + c_e|e\rangle$, with state coefficients, c_g and c_e, to a state in the rotating frame, $|\tilde{\psi}\rangle$, can be performed by applying a unitary operator, U, such that

$$|\tilde{\psi}\rangle = U|\psi\rangle \tag{3.20}$$

where

$$U = e^{i\omega_p t|e\rangle\langle e|} \tag{3.21}$$

The corresponding rotated Hamiltonian, $\tilde{H}$, can be then found using the correct transformation of

$$\tilde{H} = UHU^\dagger + i\hbar\frac{\partial U}{\partial t}U^\dagger \tag{3.22}$$

giving

$$\tilde{H} = -\hbar\Delta\sigma^\dagger\sigma - \hbar\frac{\Omega_p}{2}\left(\sigma + \sigma^\dagger\right) \tag{3.23}$$

as the final Hamiltonian that we will solve. We will use a tilde to indicate when an object is in the rotating frame.

This Hamiltonian encompasses the physics of the familiar Rabi oscillations between ground and excited states, as well as resulting new eigenstates that are not simply the bare energy eigenstates of the atomic Hamiltonian, but are instead the so-called dressed states. These concepts will again be relevant for the three level atom, as will be discussed in Section 3.1.2.

However, the phenomenon of decoherence (decay processes) in our system is not yet captured simply with the Hamiltonian in Eq. 3.23. This can be solved several ways, such as using the stochastic wave-function approach and phenomenologically introducing non-Hermitian damping terms to the Hamiltonian (with the proper normalization) [39].

Alternatively, in accordance with solving for the susceptibility as derived in the previous section, we will instead use the master equation approach for finding the density matrix elements. This is done using the quantum Liouville-von Neumann equation

$$\frac{\partial\tilde{\rho}}{\partial t} = -\frac{i}{\hbar}[\tilde{H}, \tilde{\rho}] + \Gamma\mathcal{L}[\sigma]\tilde{\rho} \tag{3.24}$$

where the spontaneous emission rate (natural linewidth) from the excited state to the ground state is Γ, and we ignored other extra dephasing processes. The Lindblad super-operators, $\mathcal{L}[\sigma]$, encompasses the dissipative processes, defined as

$$\mathcal{L}[\sigma]\tilde{\rho} \equiv \sigma\tilde{\rho}\sigma^\dagger - \frac{1}{2}(\sigma^\dagger\sigma\tilde{\rho} + \tilde{\rho}\sigma^\dagger\sigma) \tag{3.25}$$

Solving for the density matrix elements gives the optical Bloch equations

$$\begin{aligned}
\frac{\partial\rho_{ee}}{\partial t} &= -\Gamma\rho_{ee} - i\frac{\Omega_p}{2}(\tilde{\rho}_{eg} - \tilde{\rho}_{ge}) \\
\frac{\partial\rho_{gg}}{\partial t} &= -\frac{\partial\rho_{ee}}{\partial t} \\
\frac{\partial\tilde{\rho}_{eg}}{\partial t} &= -\left(\frac{\Gamma}{2} - i\Delta\right)\tilde{\rho}_{eg} - i\frac{\Omega_p}{2}(\rho_{ee} - \rho_{gg}) \\
\frac{\partial\tilde{\rho}_{ge}}{\partial t} &= \left(\frac{\partial\tilde{\rho}_{eg}}{\partial t}\right)^\dagger
\end{aligned} \tag{3.26}$$

where the diagonal density matrix elements are not altered when in the rotating frame.

The steady state solution to these coupled differential equations can be found by setting $\frac{\partial \tilde{\rho}}{\partial t} = 0$. We also approximate the atomic population as remaining mostly in the ground state due to our weak probe field assumption, thus setting $\rho_{gg} \approx 1, \rho_{ee} \approx 0$ to find

$$\tilde{\rho}_{eg} \approx \frac{i\Omega_p/2}{\frac{\Gamma}{2} - i\Delta} \tag{3.27}$$

for the diagonal density matrix element.

Substituting Eq. 3.27 into Eq. 3.15, as well as using the definition of the Rabi frequency ($\Omega_p = \frac{\mu_{ge}\mathcal{E}}{\hbar}$), we find the susceptibility to be approximately

$$\chi = \frac{N}{V}\frac{|\mu_{ge}|^2}{\epsilon_0 \hbar}\frac{i}{\frac{\Gamma}{2} - i\Delta} \tag{3.28}$$

We can write this expression in terms of the resonant cross section, $\sigma_0 = \frac{|\mu_{ge}|^2}{\hbar\epsilon_0 \frac{\Gamma}{2}} k_0$, as

$$\chi = \frac{N}{V}\frac{\sigma_0}{k_0}\frac{i\frac{\Gamma}{2}}{\frac{\Gamma}{2} - i\Delta} \tag{3.29}$$

Fig. 3.2a plots the real and imaginary parts of the susceptibility in Eq. 3.29. The absorption (imaginary part) is seen to exhibit a Lorentzian shape. The Lorentzian shape is simply characterized by the denominator, in which the real part provides the full-width half maximum (FWHM), Γ, and the imaginary part gives the centre resonance, $\Delta = 0$.

The behaviour of the field through an atomic medium of length, L, can be seen from the propagation of the field amplitude for a continuous plane wave (Eq. 3.9) and substituting Eq. 3.29 to find

$$\mathcal{E}(L) = \mathcal{E}_0 e^{-\frac{OD}{2}\frac{\frac{\Gamma}{2}}{\frac{\Gamma}{2} - i\Delta}} \tag{3.30}$$

where we have set the optical depth (for a constant atomic density) to be $OD = \frac{N}{V}\sigma_0 L$. It can be seen that on resonance the field intensity decays as the standard Beer-Lambert law

$$I = I_0 e^{-\frac{N}{V}\sigma_0 L} \tag{3.31}$$

The transmission, T, of the probe beam through the atomic medium is found using Eq. 3.30 through the relationship

$$T = \left|\frac{\mathcal{E}(z)}{\mathcal{E}_0}\right|^2 \tag{3.32}$$

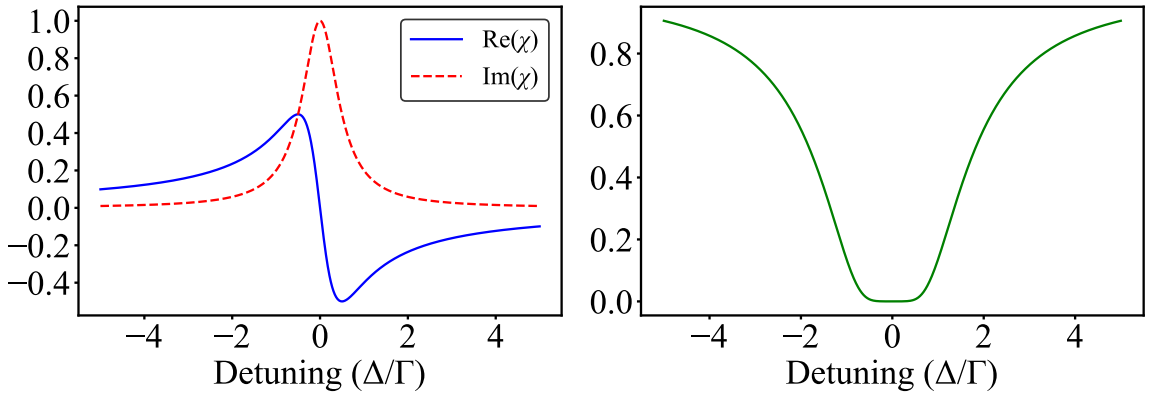

(a) (b)

Figure 3.2: (a) Normalized values for the real (solid blue line) and imaginary (dashed red line) parts of the susceptibility of a two level atom with a weak probe field (Eq. 3.29), representing the index of refraction and the attenuation, respectively. The absorption Lorentzian peak has a full-width half maximum of Γ. (b) Transmission of a weak probe field through a two level atomic medium (Eq. 3.32) with $OD = 10$.

Fig. 3.2b plots the transmission through an atomic cloud at varying probe field frequencies. This behaviour will be shown to be in contrast for certain three level schemes, as will be discussed in the next section.

3.1.2 Three Level Atom

We will now introduce a third level to the atom, $|s\rangle$, in a Λ scheme, as shown in Fig. 3.3. This third state is a metastable ground state, in which the $|g\rangle$-$|s\rangle$ is a dipole forbidden transition but separated with an energy difference of frequency ω_{gs}. In addition, to a probe field, Ω_p, coupling to the $|g\rangle$-$|e\rangle$ transition, we also apply a secondary control field at a frequency, ω_c, and Rabi frequency, Ω_c, to the $|s\rangle$-$|e\rangle$ transition. The presence of these additional pathways will result in new physical phenomena not present in the previous two level system due to quantum coherence and interference effects.

The Hamiltonian, under the RWA, again accounts for the internal atomic energy levels, as well as the interaction energy between the coupling fields and the atomic dipole transitions. We can invoke the RWA for each dipole interaction term separately by assuming that each of the probe and control fields are coupled only to one transition in the system.

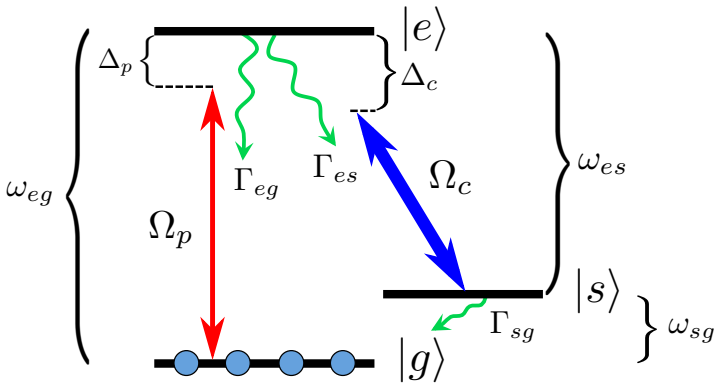

Figure 3.3: A three-level Λ scheme, with coupling probe and control Rabi frequencies, Ω_p and Ω_c, and detunings, Δ_p and Δ_c, respectively. Decay rates from the excited state to $|g\rangle$ and $|s\rangle$ are Γ_{eg} and Γ_{es}, respectively, while the metastable ground state decay is Γ_{sg}.

Setting the ground state to have zero energy, the Hamiltonian is

$$H = \hbar\omega_{eg}|e\rangle\langle e| + \hbar\omega_{sg}|s\rangle\langle s| - \hbar\frac{\Omega_p}{2}(\sigma_{ge}e^{i\omega_p t} + \sigma_{ge}^\dagger e^{-i\omega_p t}) - \hbar\frac{\Omega_c}{2}(\sigma_{se}e^{i\omega_c t} + \sigma_{se}^\dagger e^{-i\omega_c t}) \quad (3.33)$$

where we define the atomic operators, $\sigma_{ge} = |g\rangle\langle e|$, $\sigma_{ge}^\dagger = |e\rangle\langle g|$, $\sigma_{se} = |s\rangle\langle e|$, and $\sigma_{se}^\dagger = |e\rangle\langle s|$.

Similar to the two level case, we can transform this Hamiltonian into a rotating frame to eliminate the fast time dependence, focusing only on the slow evolution described by our dynamical equations. We do this by again by using a unitary operator, such that

$$U = e^{i\omega_p t|e\rangle\langle e| + i(\omega_p - \omega_c)t|s\rangle\langle s|} \quad (3.34)$$

Using Eq. 3.34 in Eq. 3.22, the transformed Hamiltonian is thus found to be

$$\tilde{H} = -\hbar\Delta_p|e\rangle\langle e| - \hbar(\Delta_p - \Delta_c)|s\rangle\langle s| - \hbar\frac{\Omega_p}{2}(\sigma_{ge} + \sigma_{ge}^\dagger) - \hbar\frac{\Omega_c}{2}(\sigma_{se} + \sigma_{se}^\dagger) \quad (3.35)$$

where the probe and control detunings are $\Delta_p = \omega_p - \omega_{eg}$ and $\Delta_c = \omega_c - \omega_{es}$, respectively.

We will again resort to the density matrix formalism to solve for the coherences in the presence of decay and dephasing, giving a master equation

$$\frac{\partial\tilde{\rho}}{\partial t} = -\frac{i}{\hbar}[\tilde{H}, \tilde{\rho}] + \Gamma_{eg}\mathcal{L}[\sigma_{ge}]\tilde{\rho} + \Gamma_{es}\mathcal{L}[\sigma_{se}]\tilde{\rho} + \Gamma_{sg}\mathcal{L}[\sigma_{gs}]\tilde{\rho} \quad (3.36)$$

We have introduced the natural decay rates between the $|e\rangle$-$|g\rangle$ and $|e\rangle$-$|s\rangle$ transitions as Γ_{eg} and Γ_{es}, respectively. This of course means the total linewidth of the excited state is $\Gamma_e \equiv \Gamma_{eg} + \Gamma_{es}$. Even though we have considered the $|s\rangle$-$|g\rangle$ transition as dipole forbidden, we will also included its decay rate, Γ_{sg}, in our dynamics, which we can later set as a relatively weak dissipative process. We will also ignore any additional dephasing or coherence relaxation processes, such as collisions.

Since we are solving for the density matrix coherences, we will look at the relevant equations obtained from the master equation (Eq. 3.36), the first being the coherence between $|e\rangle$ and $|g\rangle$,

$$\begin{aligned}\frac{\partial\tilde{\rho}_{eg}}{\partial t} &= -\left(\frac{\Gamma_e}{2} - i\Delta_p\right)\tilde{\rho}_{eg} - i\frac{\Omega_p}{2}(\rho_{ee} - \rho_{gg}) + i\frac{\Omega_c}{2}\tilde{\rho}_{sg} \\ &\approx -\left(\frac{\Gamma_e}{2} - i\Delta_p\right)\tilde{\rho}_{eg} + i\frac{\Omega_p}{2} + i\frac{\Omega_c}{2}\tilde{\rho}_{sg}\end{aligned} \tag{3.37}$$

where we again assume that we are illuminating the atomic system with a weak probe field, and thus the population is mostly in the ground state ($\rho_{gg} \approx 1$, $\rho_{ee} \approx 0$).

Since Eq. 3.37 depends on the coherence between the $|s\rangle$ and $|g\rangle$ states, we must look at the equation governing $\tilde{\rho}_{sg}$,

$$\begin{aligned}\frac{\partial\tilde{\rho}_{sg}}{\partial t} &= -\left(\frac{\Gamma_{sg}}{2} - i(\Delta_p - \Delta_c)\right)\tilde{\rho}_{sg} + i\frac{\Omega_c}{2}\tilde{\rho}_{eg} - i\frac{\Omega_p}{2}\tilde{\rho}_{se} \\ &\approx -\left(\frac{\Gamma_{sg}}{2} - i(\Delta_p - \Delta_c)\right)\tilde{\rho}_{sg} + i\frac{\Omega_c}{2}\tilde{\rho}_{eg}\end{aligned} \tag{3.38}$$

in which we drop the last term because it is proportionate to Ω_p as well as $\tilde{\rho}_{se}$, which itself is unpopulated to lowest order in Ω_p. This results in a term that has $\propto \Omega_p^2$ dependence, and can thus be ignored for a weak probe to lowest order.

We can solve for the system in steady state ($\frac{\partial\tilde{\rho}_{eg}}{\partial t} = 0$, $\frac{\partial\tilde{\rho}_{sg}}{\partial t} = 0$) by combing Eq. 3.37 and Eq. 3.38 to give

$$\tilde{\rho}_{eg} = -\frac{\Omega_p}{2}\frac{\Delta_p - \Delta_c + i\frac{\Gamma_{sg}}{2}}{(\Delta_p - \Delta_c + i\frac{\Gamma_{sg}}{2})(\Delta_p + i\frac{\Gamma_e}{2}) - \left(\frac{\Omega_c}{2}\right)^2} \tag{3.39}$$

Substituting Eq. 3.39 into Eq. 3.15, we find the susceptibility to be

$$\chi = \frac{N}{V}\frac{|\mu_{ge}|^2}{\epsilon_0\hbar}\frac{-(\Delta_p - \Delta_c + i\frac{\Gamma_{sg}}{2})}{(\Delta_p - \Delta_c + i\frac{\Gamma_{sg}}{2})(\Delta_p + i\frac{\Gamma_e}{2}) - \left(\frac{\Omega_c}{2}\right)^2} \tag{3.40}$$

We can rewrite Eq. 3.40 in terms of the resonance scattering cross section, σ_0, and collecting terms

$$\chi = \frac{N}{V}\frac{\sigma_0}{k_0}\frac{i\frac{\Gamma_e}{2}}{\frac{\Gamma_e}{2} - i\Delta_p + C} \tag{3.41}$$

where we define the term C as

$$C \equiv \frac{\left(\frac{\Omega_c}{2}\right)^2}{\frac{\Gamma_{sg}}{2} - i\Delta_{pc}} \tag{3.42}$$

using the definition $\Delta_{pc} \equiv \Delta_p - \Delta_c$ as the two photon detuning. It can be seen easily from Eq. 3.41 that the susceptibility of the two level system, Eq. 3.15, is reproduced exactly when we remove the control field by setting $\Omega_c = 0$ ($C = 0$).

We can again use the susceptibility to find the behaviour of the probe field amplitude through an atomic medium with optical density OD by substituting Eq. 3.41 into Eq. 3.9

$$\mathcal{E}(L) = \mathcal{E}_0 e^{-\frac{OD}{2}\frac{\frac{\Gamma_e}{2}}{\frac{\Gamma_e}{2} - i\Delta_p + C}} \tag{3.43}$$

3.1.3 Resonant Control ($\Delta_c = 0$): Electromagnetically Induced Transparency (EIT)

We first investigate the behaviour of this three level Λ scheme when the control field is on resonance ($\Delta_c = 0$) and the weak probe field frequency, Δ_p, is swept.

From Eq. 3.41 and 3.42, the susceptibility becomes

$$\chi(\Delta_c = 0) = \frac{N}{V}\frac{\sigma_0}{k_0}\frac{i\frac{\Gamma_e}{2}}{\frac{\Gamma_e}{2} - i\Delta_p + C} \tag{3.44}$$

with

$$C(\Delta_c = 0) = \frac{\left(\frac{\Omega_c}{2}\right)^2}{\frac{\Gamma_{sg}}{2} - i\Delta_p} \tag{3.45}$$

We can see that when the probe field detuning becomes large ($\Delta_p \gg \Omega_c, \Gamma_{sg}$), the susceptibility approaches that of the simple two level system, since $C \approx 0$. This means that the absorption is approximated as the normal two level Lorentzian shape for large probe detunings.

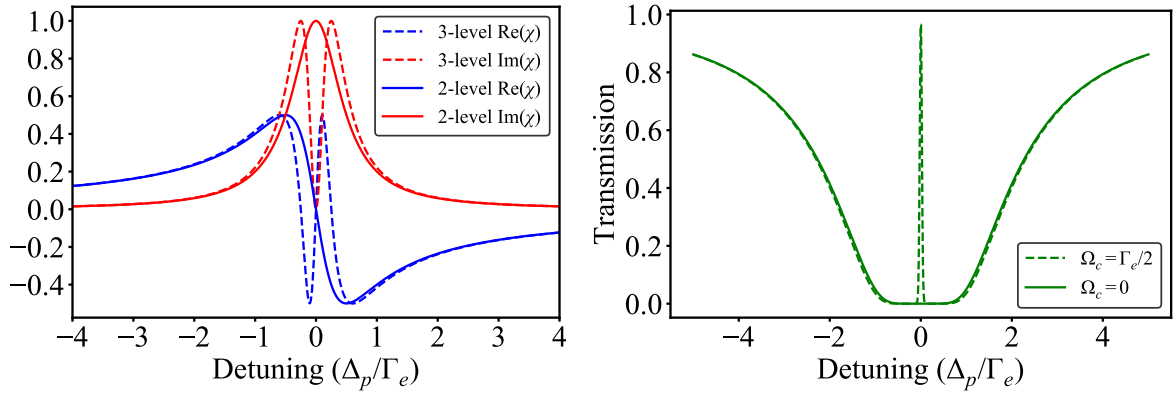

(a) (b)

Figure 3.4: (a) The normalized real and imaginary parts of the susceptibility of a two level atom ($\Omega_c = 0$) and three level atom ($\Omega_c = \frac{\Gamma_e}{2}$). (b) Transmission of a two and three level atom, with $OD = 10$.

However, when the probe detuning becomes on resonance as well ($\Delta_p = 0$), the susceptibility becomes purely imaginary since

$$\chi(\Delta_c = \Delta_p = 0) = \frac{N}{V}\frac{\sigma_0}{k_0}\frac{i\frac{\Gamma_e}{2}}{\frac{\Gamma_e}{2} + \frac{\Omega_c^2}{2\Gamma_{sg}}} \tag{3.46}$$

Remarkably, this absorption can become arbitrarily small for strong control fields and very weak metastable decay rate ($\Omega_c \gg \Gamma_{sg}$), which is easily achievable by choosing transitions between the two ground state to be dipole forbidden. This phenomenon is deemed electromagnetically induced transparency (EIT) [34], and thus leaves the probe field transparent to the atomic medium.

Fig 3.4a shows the susceptibility of both a two and three level system, while Fig. 3.4b shows the transmission. A large transmission peak is shown to occur on resonance, contrasting a normal two level system, which would exhibit a low transmission. This effect is also evident in Fig. 3.4a from the dip in the imaginary part (red dotted line) of the susceptibility.

The approximate width of this EIT transmission window can be found using the imag-

inary part of χ, ignoring any metastable decay rate ($\Gamma_{sg} = 0$), giving

$$\mathrm{Im}[\chi] = \frac{N}{V}\frac{\sigma_0}{k_0}\frac{\left(\frac{\Gamma_e}{2}\right)^2}{\left(\frac{\Gamma_e}{2}\right)^2 + (\Delta_p - \frac{(\Omega_c/2)^2}{\Delta_p})^2} \tag{3.47}$$

If we again make the approximation of a strong control field such that $\Omega_c \gg \Delta_p, \Gamma_e$,

$$\mathrm{Im}[\chi] \approx \frac{N}{V}\frac{\sigma_0}{k_0}\left(\frac{2\Gamma_e\Delta_p}{\Omega_c^2}\right)^2 \tag{3.48}$$

The transmission is given using Eq. 3.48

$$\begin{aligned} T &= e^{-\mathrm{Im}[\chi]k_0 L} \\ &\approx e^{-OD\left(\frac{2\Gamma_e\Delta_p}{\Omega_c^2}\right)^2} \end{aligned} \tag{3.49}$$

By setting $T = \frac{1}{2}$ we find the full-width half-maximum (FWHM) to be approximately

$$\Delta_{FWHM} \approx \sqrt{\frac{\ln 2}{OD}}\frac{\Omega_c^2}{\Gamma_e} \tag{3.50}$$

Interestingly, while the optical coherence, $\tilde{\rho}_{eg}$, can become vanishingly small, the coherence between the atomic ground states, $\tilde{\rho}_{sg}$, can remain finite with $\tilde{\rho}_{sg} \sim -\frac{\Omega_p}{\Omega_c}$. This intuitively indicates that the atomic coherence is involved in this physical process.

The Hamiltonian of the system (Eq. 3.35) can in fact be diagonalized to find its eigenstates. These eigenstates are of course no longer the bare atomic states due to the coupling terms, and instead will be a superposition of the different atomic states. A simple method to find the new ground state eigenstate is to rewrite the Hamiltonian at the two-photon resonance ($\Delta_p = \Delta_c \equiv \Delta$)

$$\tilde{H} = -\hbar\Delta|e\rangle\langle e| - \hbar\frac{\Omega_B}{2}(|B\rangle\langle e| + |e\rangle\langle B|) \tag{3.51}$$

in which we define

$$|B\rangle \equiv \frac{\Omega_p|g\rangle + \Omega_c|s\rangle}{\sqrt{\Omega_c^2 + \Omega_p^2}} \tag{3.52}$$

as the normalized bright state and

$$\Omega_B \equiv \sqrt{\Omega_c^2 + \Omega_p^2} \tag{3.53}$$

as the bright state Rabi frequency.

This transformed Hamiltonian shows transitions only between $|B\rangle$ and $|e\rangle$ with a coupling strength of Ω_B. The state orthogonal to this bright state is thus decoupled completely from the excited state and has an energy of zero. This so-called dark state, $|D\rangle$, satisfies $\langle B|D\rangle = 0$, and by invoking normalization we find

$$|D\rangle = \frac{\Omega_c|g\rangle - \Omega_p|s\rangle}{\sqrt{\Omega_c^2 + \Omega_p^2}} \tag{3.54}$$

Using this new dark/bright state energy eigenbasis, it can also be shown that the excited state can decay into both $|B\rangle$ and $|D\rangle$, however of course only $|B\rangle$ can be excited to $|e\rangle$. This results in coherent population trapping into the dark state, leaving all atoms in $|D\rangle$ at steady state.

When the system is in this dark state[2], the absorption vanishes, which as shown above, occurs for the two photon resonance condition ($\Delta_p = \Delta_c \equiv \Delta$), regardless of which single photon resonance, Δ, is chosen. This effect can even be interpreted as the quantum interference between the two pathways caused by Ω_p and Ω_c exciting to $|e\rangle$, which act to destructively interfere, resulting in the excited state being unpopulated.

Slow Light

In addition to EIT, another important phenomenon that occurs near resonance is the reduction in group velocity of the probe field. The group velocity is given by the dispersion relation, and if the real refractive index has a frequency dependence we can write

$$v_g = \frac{\partial\omega}{\partial k} = \frac{c}{n_g} \tag{3.55}$$

where we define the group index to be

$$n_g = n(\omega) + \omega\frac{\partial n}{\partial\omega} \tag{3.56}$$

for the real phase index, n, which depends on the real part of the susceptibility by Eq. 3.13.

We will investigate χ at a resonant control, $\Delta_c = 0$, and under a large control field, $\Omega_c \gg \Delta_p, \Gamma_{sg}$, giving

$$\chi \approx \frac{N}{V}\frac{\sigma_0}{k_0}\frac{\Gamma_e/2}{(\Omega_c/2)^2}(\Delta_p + i\Gamma_{sg}) \tag{3.57}$$

Again we can see how the absorption (imaginary part) tends to zero as $\frac{\Gamma_{sg}}{\Omega_c} \to 0$, allowing the probe to essentially experience a lossless media, in which a group velocity can be well defined.

As per Eq. 3.56, we take the derivative with respect to ω_p of the real part of χ (Eq. 3.57) and setting $n \approx 1 + \mathrm{Re}[\chi]/2$, we find

$$n_g \approx 1 + \frac{N}{V}\frac{\sigma_0 c \Gamma_e}{\Omega_c^2} \tag{3.58}$$

for the group index at a resonant probe field ($\Delta_p = 0$). Typical group index values can become very large, reducing the group velocity found from Eq. 3.55 to be

$$v_g \approx \frac{\Omega_c^2}{\frac{N}{V}\sigma_0 \Gamma_e} \tag{3.59}$$

This is consistent with Fig. 3.4a, which shows a large slope in the real part of the susceptibility around resonance that is not present for the two level system.

It should be noted, however, this analysis is only valid for when the pulse frequency bandwidth is within the EIT transmission window, given by Eq. 3.53, resulting in minimal field loss. As evident from Eq. 3.59 and Eq. 3.50, as the control power is reduced, the group velocity can become arbitrarily low, however the FWHM of the EIT window also decreases as $\Delta_{FWHM} \propto \frac{\Omega_c^2}{\Gamma_e}$.

A pulsed probe field will experience a compression in its length as it enters the atomic cloud. This is because as the pulse first enters the medium, the front of the cloud will initially experience a speed reduction from c to v_g, while the end of the pulse still travels at c. The length of the pulse will be compressed by a factor of $\frac{v_g}{c}$. However, the pulse field amplitude will remain a constant, and thus the total power in the field is also reduced by a factor of $\frac{v_g}{c}$. This somewhat counter-intuitive effect is a result of the coherence built up in the dark state (Eq. 3.54). The remaining energy from the original pulse is instead stored in this superposition of the ground state and metastable state [67]. Several notable demonstrations of slow light using EIT have been performed [56, 47], as well the complete stopping of a classical light pulse [64] and even storage of a single photon [28].

3.1.4 Off-Resonant Control ($\Delta_c \neq 0$): Two Photon Absorption

As we have seen in the previous section, EIT takes place at the two photon resonance condition ($\Delta_p = \Delta_c$), which can occur for any particular detuning of the fields. However, another

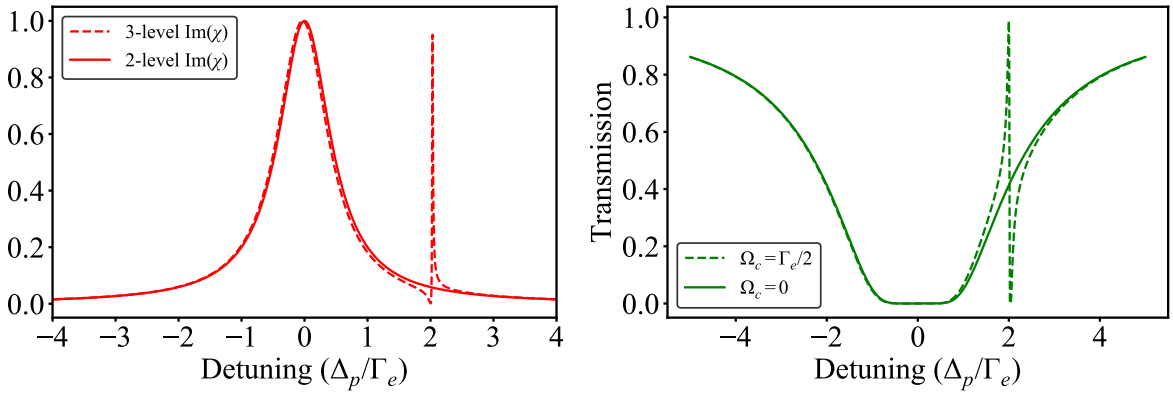

(a) (b)

Figure 3.5: Comparison of a two level system and a three level system with $\Delta_c = 2\Gamma_e$ and $\Omega_c = \frac{\Gamma_e}{2}$. (a) The normalized imaginary part of the susceptibility and the (b) transmission with $OD = 10$. The EIT resonance with large transmission is found at $\Delta_p^{EIT} = \Delta_c$, and the TPA resonance is found at $\Delta_p^{2ph} = \Delta_c + \frac{\Omega_c^2}{4\Delta_c}$.

interesting phenomenon called two-photon absorption (TPA) appears at large control field detunings. For a given $\Delta_c \gg \Gamma_e$, the spectrum of the probe field is usually characterized by a normal Lorentzian shape profile centred near the probe field resonance, $\Delta_p = 0$, but with an additional narrow absorption peak near the control field detuning, as shown in Fig 3.5. This secondary peak represents the dynamics for Raman absorption, and can be understood as the probe field causing a weak excitation to a virtual excited state, while simultaneously the strong control field acts to stimulate emission of light thereby transferring the atom into the metastable ground state $|s\rangle$.

We can explicitly investigate this behaviour by re-writing the susceptibility as

$$\begin{aligned}\chi &= \frac{N}{V}\frac{\sigma_0}{k_0}\frac{i\frac{\Gamma_e}{2}}{\frac{\Gamma_e}{2} - i\Delta_p}\left(1 - \frac{\left(\frac{\Omega_c}{2}\right)^2}{(\frac{\Gamma_{sg}}{2} - i\Delta_{pc})(\frac{\Gamma_e}{2} - i\Delta_p) + \left(\frac{\Omega_c}{2}\right)^2}\right) \\ &\equiv \chi_0 + \chi_1\end{aligned} \tag{3.60}$$

where the first term in the expression, χ_0, represents the simple two level Lorentzian absorption profile (Eq. 3.29) that we found in Section 3.1.1. The physics of the three level system are embedded in the second term, χ_1. In particular, this term gives a Fano resonance at the TPA condition for a large control and probe field detuning.

For the case of a large control field detuning, $\Delta_c \gg \Gamma_e$, and focusing only at the peak near the two photon resonance, $|\Delta_p - \Delta_c| \ll \frac{1}{2}(\Delta_p + \Delta_c)$, we can approximate the second term as

$$\chi_1 \approx \frac{N}{V}\frac{\sigma_0}{k_0}\frac{i\frac{\Gamma_{2ph}-\Gamma_{sg}}{2}}{\frac{\Gamma_{2ph}}{2} - i\Delta_{2ph}} \tag{3.61}$$

where again the real and imaginary parts of the denominator are related to the approximate FWHM and centre frequency, respectively, of the two photon absorption (TPA) peak as defined as

$$\Gamma_{2ph} \equiv \Gamma_{sg} + \Gamma_e \left(\frac{\Omega_c}{2\Delta_c}\right)^2 \tag{3.62}$$

and

$$\Delta_{2ph} \equiv \Delta_{pc} - \frac{\Omega_c^2}{4\Delta_c} \tag{3.63}$$

The centre of the TPA is at $\Delta_{2ph} = 0$ (also called Raman resonance), and thus the resonance condition for the TPA occurs when the probe field is at a frequency of

$$\Delta_p^{2ph} = \Delta_c + \frac{\Omega_c^2}{4\Delta_c} \tag{3.64}$$

It is worth noting there is a simple interpretation for the effective linewidth and resonant detuning of the TPA Raman transition. The strong control field acts to AC stark shift the $|s\rangle$ state by the amount $\omega_{AC} = \frac{\Omega_c^2}{4\Delta_c}$, and thus the Raman resonance condition becomes matching the probe detuning to the detuning of the control field relative to this AC stark shifted metastable state energy.

The linewidth of the TPA absorption peak, as seen in Eq. 3.62, is simply the addition of the two sources for transitions from the metastable state, $|s\rangle$, back to the ground state, $|g\rangle$. The first means by which this occurs is the natural decay of from $|s\rangle$ to $|g\rangle$, which has a linewidth of Γ_{sg}. The second source is by the control field acting to transfer atoms back to the ground state by scattering the atoms from $|s\rangle$. This scattering rate will be $R_{sc} = \Gamma_e \rho_{ee}$, in which the excited state population for a large detuning of the field is that of a two level system, $\rho_{ee} \approx \frac{\Omega_c^2}{4\Delta_c^2}$.

Fig 3.5a shows the normalized imaginary part of the susceptibility, in which the narrow TPA can been seen. It is evident from the transmission, shown in Fig. 3.5b, that there is still an EIT peak with large transmission at the two photon resonance condition ($\Delta_p^{EIT} = \Delta_c$), however there is also a nearby transmission dip at the TPA resonance condition (Eq. 3.64).

Another useful interpretation of this result is to look at the dressed state picture. The eigenstates of the system can be approximated in the large detuning limit, keeping only the highest order terms in $\frac{\Omega_c}{\Delta_c}$ to give the unnormalized eigenstates

$$\begin{aligned} |+\rangle &= |e\rangle - \frac{\Omega_c}{2\Delta_c}|s\rangle \\ |-\rangle &= |s\rangle + \frac{\Omega_c}{2\Delta_c}|e\rangle \end{aligned} \tag{3.65}$$

which can be thought of as a result of the control field dressing the $|e\rangle$ with $|s\rangle$.

The single photon probe field resonance represents the probe coupling between the $|g\rangle$ state and $|+\rangle$ state, giving an approximately two-level Lorentzian shape at $\Delta_p = 0$ with a linewidth of Γ_e, since $|+\rangle$ is mostly the $|e\rangle$ state in this limit. The TPA, alternatively, results from coupling between the $|g\rangle$ and $|-\rangle$ states at $\Delta_{2ph} = 0$ and has a width of approximately Γ_{2ph}.

3.2 Cavity Quantum Electrodynamics

We will now build on the discussion of light-matter interaction by inserting a two level atom into a cavity. The case of a two level atom excited in free space was discussed earlier in this chapter in Section 3.1.1, while in Section 2.1 we explored the physics of an empty cavity. By combining these concepts, we allow for the light to be confined to a small volume (as compared to a free space mode the size of the universe), increasing the effective field strength and enhancing the interaction with the atom in a field deemed cavity quantum electrodynamics (QED). One may also think of this enhancement as the photon passing by the atom many times as it bounces between the cavity mirrors, increasing its probability of interaction.

The next part of this chapter will be dedicated to determining the coupling between a two level atom and a cavity mode which we will describe first by introducing the Jaynes-Cummings Hamiltonian. However, the significance of coupling to a cavity mode (as compared to free space modes) is determined by the relative strengths between effects produced by the cavity field and the competing dissipative processes. We will discuss the different coupling regimes that are of importance to the work done in this thesis, and their different characteristics.

The chapter will conclude by considering an ensemble of atoms in a cavity resulting in the existence of collective states. These effects, together with the physics of a three level atom, can be used to understand vacuum induced transparency (VIT).

3.2.1 Jaynes-Cummings Hamiltonian

We previously have used a semi-classical treatment of light-matter interactions, in which the electromagnetic field is described classically, while the atom is quantized. If we now consider a two-level atom coupled to a single cavity mode, the field is instead quantized as well to provide a fully quantum picture of the system.

The total Hamiltonian will simply be the summation of the atomic energy term, H_a, the cavity photon energy term, H_c, the interaction energy term, H_{int},

$$H = H_a + H_c + H_{int} \tag{3.66}$$

in which

$$\begin{aligned} H_a &= \hbar\omega_{eg}\sigma^\dagger\sigma \\ H_c &= \hbar\omega_c a^\dagger a \\ H_{int} &= -\vec{\mu}\cdot\vec{E} \end{aligned} \tag{3.67}$$

where the cavity frequency, ω_c, is an integer value of the cavity free spectral range (FSR) such that $\omega_c = 2\pi n\text{FSR}$ ($n \in \mathbb{Z}$). We have ignored the vacuum energy of the cavity, and assumed that the atom only couples to a single cavity mode, which is valid for a system with a cavity frequency close to resonance with the atom ($|\omega_c - \omega_{eg}| \ll 2\pi\text{FSR}$).

The interaction term is again the dipole coupling energy ($-\vec{\mu}\cdot\vec{E}$), however we must now use the expression for the quantized electric field of the cavity, which is given by

$$\vec{E} = \vec{E}_0(ae^{i\vec{k}\cdot\vec{r}} + a^\dagger e^{-i\vec{k}\cdot\vec{r}}) \tag{3.68}$$

in which the cavity annihilation and creation operators for the cavity field mode are a and $a^\dagger$, respectively. The electric field amplitude corresponds to the vacuum energy ($\epsilon_0|E|^2 = \frac{\hbar\omega_c}{2}$), and is thus given by

$$\vec{E}_0 = \sqrt{\frac{\hbar\omega_c}{2\epsilon_0 V_{mode}}}\hat{e} \tag{3.69}$$

with a field polarization along $\hat{e}$ and mode volume of the field of

$$V_{mode} = \frac{\iiint \epsilon|E|^2 dV}{\max\{\epsilon|E|^2\}} \tag{3.70}$$

for a dielectric constant, ϵ, where the maximum value of $\epsilon|E|^2$ is used for normalization. We again use the dipole approximation, in which the spatial wavefunction of the electron

is much smaller than the wavelength of the cavity field. This results in $\vec{k} \cdot \vec{r} \ll 1$, and thus $e^{\pm i\vec{k}\cdot\vec{r}} \approx 1$.

Using the interaction energy from Eq. 3.67 with the quantized field and the dipole operator from Eq. 3.68 and Eq. 3.17, respectively, we find

$$H_{int} = -\hbar g(\sigma + \sigma^\dagger)(a + a^\dagger) \tag{3.71}$$

where we define the vacuum (or single-photon) Rabi frequency as

$$g \equiv \frac{\mu_{ge}}{\hbar}\sqrt{\frac{\hbar\omega_c}{2\epsilon_0 V_{mode}}} \tag{3.72}$$

The interaction energy can be simplified by again invoking the rotating wave approximation to ignore the non-energy conserving terms, σa and $\sigma^\dagger a^\dagger$, which are the terms with fast rotation at $\pm(\omega_{eg} + \omega_c)$ (as can be easily seen by converting into the interaction picture). We can then write the final Hamiltonian for cavity quantum electrodynamics (QED) systems, called the Jaynes-Cummings Hamiltonian,

$$H_{JC} = \hbar\omega_{eg}\sigma^\dagger\sigma + \hbar\omega_c a^\dagger a - \hbar g(\sigma^\dagger a + \sigma a^\dagger) \tag{3.73}$$

3.2.2 Dissipation

In most cavity QED models there are two major sources of dissipation which act to disrupt the coherent evolution of the atom-cavity field system, as shown in Fig. 3.6. We have already discussed each process in some detail in previous sections. The first decoherence process is spontaneous emission of the atom into a non-cavity mode (or free-space mode). This is of course characterized by the natural linewidth, or spontaneous emission rate, of the atom. The other process is the leakage of photons out of the cavity or absorption from the cavity medium, which happens at the cavity decay rate, κ.

As before, we can incorporate the decay processes into the evolution of the system by using the master equation approach, where we need only add the appropriate Lindblad superoperator terms to account for the atomic and cavity decay,

$$\frac{\partial\rho}{\partial t} = -\frac{i}{\hbar}[H_{JC}, \rho] + \Gamma_\perp\mathcal{L}[\sigma]\rho + \kappa\mathcal{L}[a]\rho \tag{3.74}$$

It should be noted that the non-cavity mode atomic decay rate, $\Gamma_\perp$, in Eq. 3.74 is the modified decay rate induced from the cavity. An open cavity is described by a simple

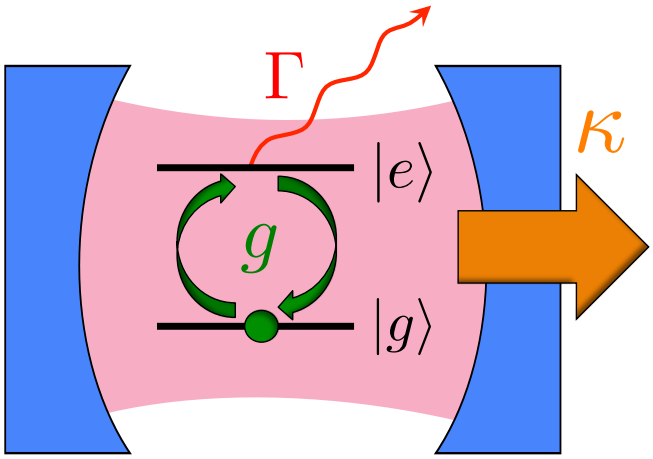

Figure 3.6: A two level atom interacting with a field in a cavity. The rate at which the atom coherently interacts with the cavity photons is the vacuum Rabi frequency, g. The two damping process are the atomic decay rate, Γ, which characterizes emission of photons into modes other than the cavity mode, and rate at which photons are leaked from the cavity, κ.

one-dimensional Fabry-Pérot etalon with a length much greater than the mode wavelength. This regime results in an atomic spontaneous emission rate similar to that of its free-space value because the atom can still interact and emit into the two orthogonal directions that are unconfined by the cavity.

However, a closed cavity is one in which light is confined in all three dimensions, and typically the cavity length is similar in size to the wavelength of light. These systems restrict the atom to interacting only with a limited number of modes, and thus the emission rate is greatly reduced from its free-space decay rate.

3.3 Coupling Regimes and Figures of Merit

As we have seen in the previous sections, there are essentially three parameters that govern the atom-light interaction strength. Each defines a time scale relevant to a process related to either coherence or decoherence in the system. The atom-photon coupling or vacuum Rabi frequency, g, is the rate at which atomic excitations and cavity photons are exchanged. The two important dissipative properties are the photon loss rate out of the cavity, κ, and the decay rate into non-cavity modes, $\Gamma_\perp$.

3.3.1 Strong Coupling

When the cavity and atom are near resonance and the cavity is made to not be leaky so that the dissipation processes are negligible, there can be a coherent exchange of energy similar to the free-space excitation of light with a two-level atom, as discussed in Section 3.1.1. The strong coupling regime is characterized by the coupling between the atom and photons being much faster than the irreversible processes of photons lost from the system, such that $g \gg \kappa, \Gamma_\perp$ [36]. This allows for the reversible process of the atom emitting a photon into the cavity and re-absorbing it before the photon can be lost.

In the strong coupling regime, the solutions for a cavity QED system can be found in the eigenbasis of the tensor product of bare atomic states and the Fock states of the photon. It can be seen from the Jaynes-Cummings Hamiltonian (Eq. 3.73), specifically the interaction terms, that the states $|e, n\rangle$ are coupled with $|g, n+1\rangle$, where we have written the atomic state in the first entry of the state, and the photon number as the second for a given integer n, representing the smallest number of photons in each manifold. This means that a state with no excitations, $|g, 0\rangle$, will not couple to any other state.

This convenient property will allow us to solve system by restricting the infinite Hilbert space to being spanned simply by $|e, n\rangle$ and $|g, n+1\rangle$. However, when dissipation is significant, the dynamics become more complicated as the atomic decay couples $|e, n\rangle$ with $|g, n\rangle$, and the cavity decay couples $|e/g, n+1\rangle$ with $|e/g, n\rangle$.

Fig. 3.7 shows the manifold of the eigenstates with and without the coupling between the atom and the cavity photon. The so-called dressed states, $|\pm\rangle$, are the new eigenstates of the coupled system, and can be found by diagonalizing the Jaynes-Cummings Hamiltonian (Eq. 3.73), giving

$$\begin{aligned} |+, (n)\rangle &= \cos\theta_n |e, n\rangle + \sin\theta_n |g, n+1\rangle \\ |-, (n)\rangle &= -\sin\theta_n |e, n\rangle + \cos\theta_n |g, n+1\rangle \end{aligned} \tag{3.75}$$

where we define

$$\tan 2\theta_n = -\frac{2g\sqrt{n+1}}{\Delta} \tag{3.76}$$

for the detuning, $\Delta \equiv \omega_c - \omega_{eg}$. The corresponding energies of the two dressed eigenstates, $E_\pm$, are

$$E_\pm = \frac{1}{2}\hbar\omega_{eg} + \hbar\left(n + \frac{1}{2}\right)\omega_c \pm \frac{\hbar}{2}\sqrt{4(n+1)g^2 + \Delta^2} \tag{3.77}$$

When the atom and cavity are exactly on resonance ($\Delta = 0$), the degeneracy of the bare states is broken at each excitation manifold and the dressed states become $|\pm\rangle =$

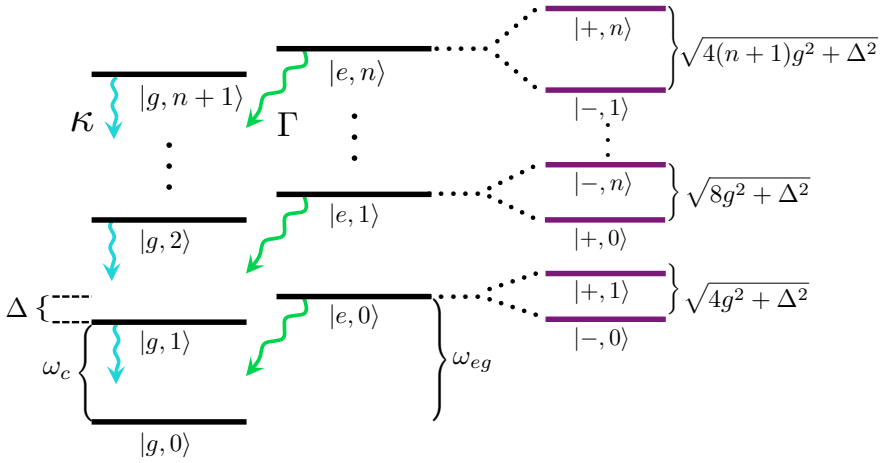

Figure 3.7: The left most ladders are the uncoupled bare states for a detuning between the atom and cavity frequencies, $\Delta = \omega_c - \omega_{eg}$. When the atom and cavity are strongly coupled, the new eigenstates are instead the dressed states.

$\frac{1}{\sqrt{2}}(|g,n+1\rangle \pm |e,n\rangle)$ with an energy splitting of $2\sqrt{n+1}g$. The dissipation in the system acts to give each of the dressed states a finite linewidth. Since the dressed states are a superposition state of excitations in the atom and the cavity, the effective linewidth is a combination of both the atom and cavity decay rate, giving $\Gamma_{eff} = n\kappa + \frac{\kappa+\Gamma_\perp}{2}$.

The dressed state picture gives us a new means of interpreting the strong coupling regime. When the condition $g \gg \Gamma_\perp, \kappa$ is met, the dressed state peaks can be resolved and the system undergoes weakly damped Rabi oscillations between atomic and cavity excitations. If this condition is not met, the linewidth of the peaks becomes so large that the splitting between the states are obscured and the system decays before it can undergo a single Rabi oscillation.

A state that does not begin in these dressed states (i.e. not a steady state), will instead undergo coherent oscillation between an excitation in the atomic state and an excitation in the cavity mode (a cavity photon). In particular, Rabi flopping will occur between the $|g,n+1\rangle$ and $|e,1\rangle$ states at a rate $2\sqrt{n+1}g$.

Interestingly, the oscillation of excitation between the atom and cavity mode can occur even in the absence of a cavity photon ($n = 0$). This effect can be interpreted as the vacuum fluctuations stimulating emission of the atomic excitation to produce a cavity photon, hence the name of the vacuum Rabi frequency for g. This coherent effect is the dominate evolution if the system is in the strong coupling regime, resulting in many of these oscillations before the photon is either lost through the cavity or the atom spontaneously

decays.

3.3.2 High Cooperativity

The most important parameter that characterizes a cavity QED system is called the single atom cooperativity, η, which is a dimensionless quantity defined as

$$\eta \equiv \frac{4g^2}{\kappa\Gamma_\perp} \tag{3.78}$$

A regime that is closely related to the strong coupling condition is deemed high cooperativity, where $\eta > 1$. This requirement is equivalent to the strong coupling regime when $\kappa = \Gamma_\perp$, however, it is a somewhat less stringent condition when $\kappa < \Gamma_\perp$ or $\kappa > \Gamma_\perp$, because the both decay rates need not be separately larger than the Rabi frequency, but instead their geometric average must be.

The strong coupling regime represents a system that has the splitting between the dressed state cavity resonances much larger than their linewidths and are thus the peaks are distinguishable. In contrast, the high cooperativity regime allows for the eigenstate modes to overlap within their linewidths, however destructive interference between the states can occur, which is what occurs in a classical EIT system and, more relevantly, to the VIT phenomenon that will be discussed in Section 3.5 [108].

Two closely related physically significant quantities that arise are the critical atom number, N_0, and the critical photon number, n_0, that represent the number of atoms and photons, respectively, that are required to alter the systems properties. They are given by

$$\begin{aligned} N_0 &= \frac{2\kappa\Gamma_\perp}{g^2} \\ n_0 &= b\frac{\Gamma_\perp^2}{2g^2} = \frac{4}{3}\frac{\Gamma_\perp^2}{g^2} \end{aligned} \tag{3.79}$$

where b is determined by the geometry of the cavity field profile. A uniform plane wave has $b = 1$, while $b = \frac{8}{3}$ when averaged over a standing wave Gaussian profile [58]. Specifically, the critical atom number is the number of atoms in the cavity required to induce a split in the cavity resonance peak, while the critical photon number is a measure of the photon number required to saturate the atoms.

Interestingly, it should be noted that the cooperativity is independent of the atomic species (i.e. does not depend of the dipole moment), and is instead purely a function of

the cavity features. This can be seen by assuming the non-cavity emission rate, $\Gamma_\perp$, will be the natural spontaneous emission rate,

$$\Gamma = \frac{w_{eg}^3 |\mu_{ge}|^2}{3\pi\epsilon_0 \hbar c^3} \tag{3.80}$$

which is valid for a one dimensional cavity where most emission directions are still free space modes. Using Eq. 3.80 together with the cavity decay rate and coupling constant formulas, Eq. 2.14 and Eq. 3.72, respectively, we find

$$\eta = \frac{3Q}{4\pi^2} \frac{\lambda^3}{V_{mode}} \tag{3.81}$$

or in terms of the finesse by Eq. 2.8,

$$\eta = \frac{3\mathscr{F}}{2\pi^2} \frac{\lambda^2}{A_{mode}} \tag{3.82}$$

for a mode area of the cavity, A_{mode}, and wavelength, λ.

We may also explore a more physical interpretation of the cooperativity by first expressing it in terms of the resonant cross section, $\sigma_0 = \frac{3\lambda^2}{2\pi}$, and the average number of round trips using Eq. 2.11,

$$\eta = 2\frac{\sigma_0}{A_{mode}} N_{rt} \tag{3.83}$$

Using the fact that the probability for an atom to absorb a photon for a single pass is $P_1 = \frac{\sigma_0}{A_{mode}}$, and the average number of times the photon will pass the atom is $N_{pass} = 2N_{rt}$ (since the photon bounces off the cavity mirrors and will pass by the atom twice for each round trip), we can also write

$$\eta = P_1 N_{pass} \tag{3.84}$$

Since the probability that the atom is *not* absorbed in a single pass is $1 - P_1$, the probability that the photon does *not* get absorbed after N_{pass} passes is simply $(1-P_1)^{N_{pass}}$. We can then write the probability that the photon *does* get absorbed, P_{abs}, after passing by the atom N_{pass} times is

$$\begin{aligned} P_{abs} &= 1 - (1 - P_1)^{N_{pass}} \\ &\approx 1 - e^{-P_1 N_{pass}} \\ &= 1 - e^{-\eta} \end{aligned} \tag{3.85}$$

where in the second line we used $\lim_{x\to 0}(1+x)^{\frac{1}{x}} = e$. This is valid for $P_1 \ll 1$, which for most cavity QED systems is true since the resonant cross section is on the order of optical wavelengths while the cavity mode areas are still macroscopic. Thus we can see from Eq. 3.85 that the cooperativity acts as an effective optical depth for a single atom in a cavity.

This strict condition of strong coupling can be extremely difficult to overcome in some systems with a single atom, where the cavity cannot be made to have a high enough finesse. Fortunately, the effective coupling becomes $\sqrt{N_a}g$ for N_a atoms interacting with the cavity photons, as we will see in Section 3.4. This allows systems that would otherwise have low single atom cooperativities, $\eta < 1$, to have a large collective cooperativity, $\eta_{coll} \equiv N_a\eta > 1$. This so-called bad cavity but high collective cooperativity regime is important in systems such as those exhibiting superradiance [77, 15].

3.3.3 Weak Coupling Regime

Cavity QED systems can be engineered and tailored to exhibit different effects depending on the relative strengths between the couplings and dissipative processes. In particular, the atomic decay rate can be drastically affected by the presence of a cavity, which is called the Purcell effect [85].

The weak coupling regime is characterized by the atom-cavity coupling strength being smaller than either the free space loss rate ($g < \Gamma_\perp$) or the cavity loss rate ($g < \kappa$). It should be noted that this regime would still allow for the cooperativity to be larger than unity. This limit means that the photons in the cavity are lost (either to non-cavity modes or leakage from the cavity) before they can undergo Rabi oscillations. Emission into the cavity is thus an irreversible process similar to emission into free space. We will investigate the alteration to the emission rate of the atom to produce an effective emission rate, Γ_{eff}. In the limit of weak coupling, the presence of the cavity has a relatively weak effect on the atom. This allows us to use perturbation theory in which the transition rate is given by Fermi's golden rule

$$\Gamma_{eff} = \frac{2\pi}{\hbar^2}|\langle e|H_{int}|g\rangle|^2\rho(\omega) \tag{3.86}$$

where $\langle e|H_{int}|g\rangle$ is the matrix element of the perturbative interaction energy, and $\rho(\omega)$ is the density of states per angular frequency.

For atoms in free space, the emitted photons have a quadratic density of states with frequency, and Eq. 3.86 can be used to reproduce the natural spontaneous emission rate of Eq. 3.80. However, the presence of the cavity can drastically modify the density of available sates that the atom can emit into, and thus alter its decay rate.

If we consider an atom with a transition frequency near a resonant frequency of a cavity, all other cavity modes may be ignored because they are far detuned from the atomic frequency. For this system, the atom is coupled a single cavity mode, which means the density of states for the cavity has a spectrum that can be represented as a Lorentzian peak centred on the resonant frequency, ω_c, and linewdith, κ. By normalizing the single Lorentzian peak with $\int_{\infty}^{-\infty} \rho(w)dw = 1$, we can write

$$\rho(w) = \frac{2}{\pi\kappa} \frac{(\kappa/2)^2}{(\omega - \omega_c)^2 + (\kappa/2)^2} \tag{3.87}$$

The interaction matrix element is found using the vacuum electric field, Eq. 3.69,

$$\begin{aligned} |\langle e|H_{int}|g\rangle|^2 &= |\langle e|\vec{\mu} \cdot \vec{E}|g\rangle|^2 \\ &= \mu_{eg}^2 \frac{\hbar\omega_{eg}}{2\epsilon_0 V_{mode}} \end{aligned} \tag{3.88}$$

where we have assumed the dipole moment is aligned with the electric field polarization.

Substituting Eq. 3.87 and Eq. 3.88 into Fermi's golden rule (Eq. 3.86) and evaluating the density of states at the atomic frequency, ω_{eg}, we find

$$\begin{aligned} \Gamma_{eff} &= \frac{2\mu_{eg}^2\omega_{eg}}{\hbar\epsilon_0 V_{mode}} \frac{1}{\kappa} \frac{(\kappa/2)^2}{(\omega_{eg} - \omega_c)^2 + (\kappa/2)^2} \\ &= \frac{4g^2}{\kappa} \frac{(\kappa/2)^2}{(\omega_{eg} - \omega_c)^2 + (\kappa/2)^2} \end{aligned} \tag{3.89}$$

We can now find the enhancement ratio, called the Purcell factor, $\mathcal{F}$, of the cavity-induced emission rate, Eq. 3.89, and the natural spontaneous emission rate, Eq. 3.80,

$$\begin{aligned} \mathcal{F} &\equiv \frac{\Gamma_{eff}}{\Gamma} \\ &= \frac{3Q}{4\pi^2} \frac{(\lambda_0/n)^3}{V_{mode}} \frac{(\kappa/2)^2}{(\omega_{eg} - \omega_c)^2 + (\kappa/2)^2} \end{aligned} \tag{3.90}$$

where we have used the Q factor of the cavity as $Q = \frac{\omega_c}{\kappa}$, for a refractive index, n, of the atomic media, and free space wavelength, λ_0.

When the cavity is set on resonance with the atomic frequency, $\omega_{eg} = \omega_c$, the effective decay in Eq. 3.89 becomes

$$\Gamma_{eff}(\omega_c = \omega_{eg}) = \frac{2\mu_{eg}^2 Q}{\hbar\epsilon_0 V_{mode}} = \frac{4g^2}{\kappa} \tag{3.91}$$

and the Purcell factor is

$$\mathcal{F}(\omega_c = \omega_{eg}) = \frac{3Q}{4\pi^2}\frac{(\lambda_0/n)^3}{V_{mode}} \tag{3.92}$$

The presence of a high Q cavity with a small mode volume on resonance can thus enhance the spontaneous emission rate of the atom ($\mathcal{F} > 1$) by effectively increasing the density of states that the atom can emit into.

When the frequencies of the cavity and atom are far off resonant from each other (called the dispersive regime, $|\Delta| = |\omega_{eg} - \omega_c| \gg \kappa$), we can approximate Eq. 3.90 as

$$\mathcal{F}(|\Delta| \gg \kappa) \approx \frac{3}{16\pi^2 Q}\frac{(\lambda_0/n)^3}{V_{mode}} \tag{3.93}$$

and the spontaneous emission rate of the atom is suppressed by high finesse cavities ($\mathcal{F} < 1$) because the density of states is greatly reduced.

Amazingly, it is shown that the spontaneous emission rate of an atom is not an intrinsic property, but rather dependent on the environment of the atom. Thus, cavity QED systems can be designed to not only enhance or suppress the spontaneous decay of the atom by either setting the cavity frequency on resonance with the atomic transition or far-detuned, respectively, but it can also be made coherent in the case of strong coupling Rabi oscillations.

3.4 Atomic Ensemble in a Cavity

We will now investigate the behaviour of the system when many atoms are introduced into the cavity and how collective effects may arise. The Hamiltonian describing a single cavity interacting with many atoms is called the Tavis-Cummings Hamiltonian [109]. It is built upon the Jaynes-Cummings Hamiltonian, in which the internal energy state of each atom must be summed, as well as each interaction energy between the atoms and the cavity mode, while ignoring any interactions between the atoms. Even though each atom may be identical, they may be in a region of different electric field strength (for example atoms in a Gaussian cavity mode), and thus could each have a different coupling to the cavity mode, g_j, resulting in

$$H_{TC} = \hbar\omega_{eg}\sum_j \sigma_j^\dagger\sigma_j + \hbar\omega_c a^\dagger a - \sum_j \hbar g_j(\sigma_j^\dagger a + \sigma_j a^\dagger) \tag{3.94}$$

This Hamiltonian can be approximately diagonalized by defining normalized collective state operators, Σ_{GE} and Σ_{EE}, [97, 105] such that

$$\begin{aligned}\Sigma_{GE} &\equiv \frac{1}{\sqrt{N_a} g_{eff}} \sum_j g_j \sigma_j \\ &= \Sigma_{EG}^\dagger\end{aligned} \tag{3.95}$$

for a number of atoms, N_a, and an effective average coupling constant,

$$g_{eff} \equiv \sqrt{\frac{\sum_j g_j^2}{N_a}} \tag{3.96}$$

representing the root mean square of the vacuum Rabi frequencies of the atomic ensemble, and

$$\begin{aligned}\Sigma_{EE} &\equiv \Sigma_{EG}\Sigma_{GE} \\ &= \frac{1}{N_a g_{eff}^2} \sum_{j,k} g_j g_k \sigma_j^\dagger \sigma_k\end{aligned} \tag{3.97}$$

Using the definition of these collective operators, we can re-write the Hamiltonian in Eq. 3.94 as

$$H = \hbar\omega_{eg}\Sigma_{EE} + \hbar\omega_c a^\dagger a - \hbar\sqrt{N_a} g_{eff}(\Sigma_{EG} a + \Sigma_{GE} a^\dagger) + \hbar\omega_{eg}\left(\sum_j \sigma_j^\dagger \sigma_j - \Sigma_{EE}\right) \tag{3.98}$$

Note that the last term is a result of the fact that $\Sigma_{EG}\Sigma_{GE} \neq \sum_j \sigma_j^\dagger \sigma_j$, and in fact represents the number of non-collective excitations.

We can also derive the symmetrically entangled collective state manifold by simply applying the collective excitation operator, Σ_{EG}, to the collective ground state, $|G\rangle \equiv |g_1, g_2, \ldots, g_{N_a}\rangle$, where each entry represents the different atoms in the ensemble. Each time the collective excitation operator is applied, it creates an entangled excitation, giving a total of N_e number of excitations, thus

$$\begin{aligned}|E^{N_e}\rangle &\equiv \frac{1}{\sqrt{N_e!}}(\Sigma_{EG})^{N_e}|G\rangle \\ &= \frac{1}{\sqrt{N_e!}(N_a g_{eff}^2)^{N_e}} \sum_{l_1,\ldots,l_{N_e}} \prod_{m=1}^{N_e} |g_1, \ldots, e_{l_1}, \ldots, e_{l_{N_e}}, \ldots, g\rangle\end{aligned} \tag{3.99}$$

If the number of excitations is much smaller than the total number of atoms, $N_e \ll N_a$, it can be shown that the collective operators have the commutation relations [105]

$$\begin{aligned}[\Sigma_{GE}, \Sigma_{EG}] &= 1 \\ [\Sigma_{GE}, \Sigma_{EE}] &= \Sigma_{GE} \\ [\Sigma_{EG}, \Sigma_{EE}] &= -\Sigma_{EG}\end{aligned} \tag{3.100}$$

in which the collective operators act exactly like harmonic annihilation and creation operators of excitations. Interestingly, this means that excitations of an ensemble of atoms acts like a quantum harmonic oscillator for a small number of excitations. These relations also indicate that if the ensemble is initially prepared in $|G\rangle$, the state will evolve only into superposition states of $|G\rangle$ and $|E^{N_e}\rangle$ for weak excitations, and will not couple to any non-collective state.

Using our definitions in Eq. 3.97 and Eq. 3.99 we can also find that

$$\sum_j \sigma_j^\dagger \sigma_j |E^{N_e}\rangle = N_e |E^{N_e}\rangle \tag{3.101}$$

and also

$$\Sigma_{EE} |E^{N_e}\rangle = N_e |E^{N_e}\rangle \tag{3.102}$$

which results in the last term in our Hamiltonian in the collective state representation (Eq. 3.98) to be equal to zero. Thus, the Hamiltonian in the collective state manifold for an ensemble of atoms with a small number of excitations can be written as

$$H = \hbar\omega_{eg}\Sigma_{EE} + \hbar\omega_c a^\dagger a - \hbar\sqrt{N_a} g_{eff}(\Sigma_{EG} a + \Sigma_{GE} a^\dagger) \tag{3.103}$$

There are two important qualitative properties that the collective states possess. The first is that the coupling strength between $|E_e^N\rangle$ and $|E_{N_e+1}\rangle$ increases as the number of excitations increase, since

$$\langle E^{N_e+1} | H_{int} | E^{N_e} \rangle = -\sqrt{N_a(N_e+1)} g_{eff} a^\dagger \tag{3.104}$$

This enhancement by $\sqrt{N_a}$ for a small number of excitations is the behaviour of superradiance, and these collective excitation states are the famous Dicke states for $N_e \ll N_a$ [26]. Superradiance occurs when an atomic ensemble spontaneously emit coherently into a single electromagnetic mode.

The other feature is that the collective states are resilient against loss of a single atom. Since the excitation is very weak such that $N_e \ll N_a$, if any given atom is lost and measured,

it will most likely be found to be in the ground state, preserving the entanglement of the rest of the ensemble.

The form of the Hamiltonian in Eq. 3.103 suggests that the properties of a weakly excited atomic ensemble coupled to a single cavity mode shows much of the same properties as a single atom in a cavity. The resonant case ($\omega_{eg} = \omega_c$) also shows a vacuum Rabi splitting of $2\sqrt{N_a}g_{eff}$, and the far-detuned system shows an AC stark shift of the cavity of $\frac{N_a g_{eff}^2}{\Delta}$. The main difference is that the single atom Rabi frequency is replaced with $g \rightarrow \sqrt{N_a}g_{eff}$, and thus the condition to see the Rabi splitting is reduced to $\sqrt{N_a}g_{eff} \gg \kappa, \Gamma_\perp$.

However, there is one main distinction between the behaviour of the collective state in a cavity as compared to a single atom. This comes from the fact that the single atom operators do not follow the commutation relations of a harmonic oscillators since $[\sigma, \sigma^\dagger] = \sigma_z \neq 1$, unlike the collective state operators. This results in an anharmonicity in the physics of a single atom coupled with a cavity, in which splitting between the resonances depend on the number of photons in the cavity, $2\sqrt{n+1}g$, as discussed in Section 3.3.

Conversely, the collective state manifold, under the assumption of small number of excitations, does indeed act like a harmonic oscillator, resulting in the eigenenergy splitting to be independent of the number of photons, and are simply a constant with number of atoms. Thus, a weakly excited atomic ensemble coupled to a cavity mode acts like two masses coupled by a spring, reacting the same no matter how strongly they are driven. The anharmonicity, however, returns when the system is strongly driven creating a large fraction of atoms in the excited state.

In the next section (Section 3.5), we will see that this nonlinearity in the photon number will be restored even with many atoms in the cavity. This is because we will treat the atoms as three-level systems such that the cavity will instead only couple to one atom at a time and effectively saturate the atom with a high finesse cavity.

3.5 Vacuum Induced Transparency (VIT)

We will now conclude this chapter by combining the previous sections to consider an ensemble of many three-level atoms inside a cavity. It has been shown how the interactions between the cavity mode photons and atoms are enhanced in the strong coupling regime. We can now explore the limit of no photons in the cavity mode to determine the effect of the vacuum field on the dispersive properties of the atomic ensemble. Chapter 6 will explore how the effects discussed in this section can be employed to develop a single-photon all-optical switch using several different schemes.

The previous sections have laid most of the mathematical foundation for these effects, in particular the phenomenon of Vacuum Induced Transparency (VIT), which is similar to EIT but with a few discrepancies such as in the group velocity delay. In EIT, the optical nonlinearities are induced by the strong classical control field, while in VIT the vacuum cavity mode can replace this classical field, creating the nonlinearities with the interaction of just a single photon with the atoms.

The initial predictions of VIT [31, 87] assumed a single atom in a cavity, rather than many atoms interacting with a single cavity probe field. However, these systems may be treated the same as long as the average number of photons scattered by the atoms in the cavity is much less than one.

In practice, this would be achieved by simply using a sufficiently weak probe to allow for only a single atomic excitation in the ensemble, within the relevant time scales. These processes can be somewhat counter-intuitive as there is only a single photon (at most) that is involved in the physics of a three-level scheme in which the interference between the simultaneous excitation of multiple pathways can, amazingly, still occur.

3.5.1 Hamiltonian and Master Equation

The Λ-type level scheme for a VIT system is shown in Fig. 3.8. A probe beam, Ω_p, is allowed to interact with the atoms through free space coupling the ground and excited states. The atoms are in a high-finesse cavity that has a resonance tuned near the transition between the metastable state and the excited state. Photons would be detectable through either the probe field mode or the cavity field mode.

The Hamiltonian for this system in the appropriate rotating frame under the RWA is given by

$$\tilde{H} = -\hbar\Delta_p \sum_j \sigma_{eg}^j \sigma_{ge}^j - \hbar(\Delta_p - \Delta_c) a^\dagger a - \sum_j \hbar g_j (\sigma_{es}^j a + \sigma_{se}^j a^\dagger) - \hbar \frac{\Omega_p}{2} \sum_j (\sigma_{eg}^j e^{i\vec{k_p}\cdot\vec{r}} + \sigma_{ge}^j e^{-i\vec{k_p}\cdot\vec{r}}) \tag{3.105}$$

This Hamiltonian is of course analogous to the previously discussed three-level system for EIT (Eq. 3.35), where we have again defined the probe detuning $\Delta_p \equiv \omega_p - \omega_{eg}$, cavity detuning (the 'c' now conveniently standing for 'cavity' instead of 'control'), $\Delta_c \equiv \omega_c - \omega_{es}$, and the general atomic raising/lower operators $\sigma_{ij} \equiv |i\rangle\langle j|$.

Rewriting the Hamiltonian in terms of the collective state operators we find

$$\tilde{H} = -\hbar\Delta_p \Sigma_{EE} - \hbar(\Delta_p - \Delta_c) a^\dagger a - \hbar g_{eff} (\Sigma_{ES} a + \Sigma_{SE} a^\dagger) - \hbar \frac{\sqrt{N_a}\Omega_p}{2} (\Sigma_{EG} + \Sigma_{GE}) \tag{3.106}$$

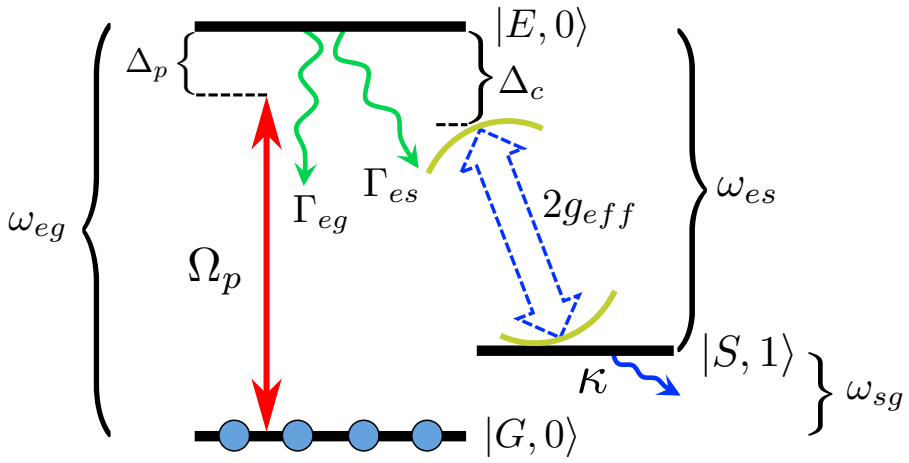

Figure 3.8: The single excitation manifold scheme for a three-level atomic ensemble in a cavity consists of the bipartite states $|E,0\rangle$, $|G,0\rangle$ and $|S,1\rangle$. A weak probe field with Rabi frequency Ω_p is coupled through free space to the $|E\rangle$-$|G\rangle$ atomic transition. The cavity mode is coupled to the $|S\rangle$-$|G\rangle$ with an effective vacuum Rabi frequency, g_{eff}, for the atomic ensemble, with cavity photons leaking at a rate κ.

using the definitions of

$$\begin{aligned}
\Sigma_{EG} &\equiv \Sigma_{GE}^{\dagger} \equiv \frac{1}{\sqrt{N_a}} \sum_j \sigma_{eg}^j e^{i\vec{k_p}\cdot\vec{r}} \\
\Sigma_{EE} &\equiv \Sigma_{EG}\Sigma_{GE} \\
\Sigma_{ES} &\equiv \Sigma_{SE}^{\dagger} \equiv \frac{1}{g_{eff}} \sum_j g_j \sigma_{es}^j
\end{aligned} \tag{3.107}$$

and

$$g_{eff} \equiv \sqrt{\frac{\sum_j g_j^2}{N_a}} \tag{3.108}$$

It can be seen from Eq. 3.106 that in this three level system, the effective coupling strength to the cavity mode is not enhanced to $\sqrt{N_a} g_{eff}$ from having many atoms in the cavity, unlike what we saw in the previous section for two level atoms in a cavity described by Eq. 3.103. This is because the cavity is instead coupled to the $|S\rangle$-$|E\rangle$ transition, which is left mostly unpopulated. The probe field photon, however, can excite any of the atoms in the sample, and so it can be thought of as having an increased probability of interacting with an atom. It is then only the single atom that has been excited by the probe photon

that can couple to the cavity, and so there is no cavity-atom enhancement by having many atoms in the sample.

We can further reduce the complexity of this Hamiltonian by only considering the so-called single excitation manifold. As we previously mentioned, the probe field is assumed to be weak such that less than a single photon interacts with the ensemble at once, thus restricting our Hilbert space to the bipartite sates of $|G,0\rangle$, $|E,0\rangle$, and $|S,1\rangle$, in which the first letter and second number indicates the atomic state and the cavity photon number, respectively. The Hamiltonian can then be considered a simple 3X3 matrix as

$$\begin{aligned}\tilde{H} =& -\hbar\Delta_p|E,0\rangle\langle E,0| - \hbar(\Delta_p - \Delta_c)|F,1\rangle\langle F,1| \\ &- \hbar g_{eff}(|E,0\rangle\langle S,1| + |S,1\rangle\langle E,0|) - \hbar\frac{\sqrt{N_a}\Omega_p}{2}(|E,0\rangle\langle G,0| + |G,0\rangle\langle E,0|)\end{aligned} \tag{3.109}$$

The resulting master equation is determined by considering the decay channels from the excited state to the two ground states, $\Gamma_e \equiv \Gamma_{es} + \Gamma_{eg}$, as well as introducing leakage of photons from the cavity mode at a rate κ. For simplicity we will ignore any decay between the two ground states in this treatment because the cavity decay rate in most systems will dominate the dissipation from the $|S,1\rangle$ state. The master equation, again analogous to that of the classical EIT system in Eq. 3.36, becomes

$$\frac{\partial\tilde{\rho}}{\partial t} = -\frac{i}{\hbar}[\tilde{H},\tilde{\rho}] + \Gamma_{eg}\mathcal{L}[\Sigma_{GE}]\tilde{\rho} + \Gamma_{es}\mathcal{L}[\Sigma_{SE}]\tilde{\rho} + \kappa\mathcal{L}[a]\tilde{\rho} \tag{3.110}$$

It should be noted that in this formalism of the master equation, probability is not preserved for the single excitation manifold. This is noticeable by the fact that $|S,1\rangle$ decays to $|S,0\rangle$ by the cavity leakage, which we do not consider in our manifold (as seen in Fig. 3.8). This is the same problem that arises when using the alternative approach of the stochastic wavefunction method, in which a non-hermitian Hamiltonian is used to account for the decay processes.

However, both the master equation and the stochastic wavefunction approach can be justified by use of perturbation theory under the assumption of a weak probe giving a small excited state population. The other main assumption we will make in order to validate our treatment is that the cavity decay rate out of the single excitation manifold from $|S,1\rangle$ to $|S,0\rangle$, which would represent non-conservation of probability, is much smaller than the coupling strength between $|E,0\rangle$ and $|S,1\rangle$ ($2g_{eff} \gg \kappa$), thus requiring us to operate in the strong coupling regime. Again we can then set the ground state probability to be approximately unity and the state can essentially be approximated as

$$|\psi\rangle \approx |G,0\rangle + c_E|E,0\rangle + c_S|S,1\rangle \tag{3.111}$$

with state coefficients c_E and c_S.

Mathematically the off-diagonal element density matrix equations found from the master equation, Eq. 3.110, become again equivalent to the classical EIT system, Eq. 3.37 and Eq. 3.38, with the substitutions $\Omega_c \to 2g_{eff}$, $\kappa \to \Gamma_{sg}$, and $\Omega_p \to \sqrt{N_a}\Omega_p$. The collective states are then also characterized by the effective cooperativity parameter $\eta_{eff} = \frac{4g_{eff}^2}{\kappa\Gamma_e}$.

The overall cooperativity also has a spatial dependence due to the mode profile of the field strength through the coupling constant, g_{eff}. Assuming a gaussian mode cross-sectional profile with an intensity width of σ_0 and a standing wave along the axis of the cavity, we can determine the spatial dependence in polar coordinates as

$$g(r,z) = g_{max}\cos(kz)e^{-\frac{r^2}{2\sigma_0}} \tag{3.112}$$

The effective coupling along the axis of the cavity, assuming a uniform distribution, is found by averaging over a period of the standing wave

$$\begin{aligned} g_{eff}^2 &= \frac{1}{N_a}\sum_j g_j^2(z) \\ &= g_{max}^2\frac{1}{\lambda}\int_{-\lambda/2}^{\lambda/2}\cos^2(kz)dz \\ &= \frac{1}{2}g_{max}^2 \end{aligned} \tag{3.113}$$

and thus the effective cooperativity becomes

$$\eta_{eff} = \frac{1}{2}\eta_{max} \tag{3.114}$$

at the centre of the Gaussian mode.

3.5.2 Transmission Spectrum

The alteration to the atomic response from the probe field is due to the coherent build up of the $|E,0\rangle$-$|F,1\rangle$ transition mediated by the cavity. As previously found, the dispersive properties of the atomic ensemble are governed by the susceptibility, with the real and imaginary parts being responsible for the phase accumulation and absorption, respectively. Similar to the discussion in Section 3.1, the susceptibility, χ, relates the induced polarization of the medium due to an applied electric field by Eq. 3.7. The polarization, $\mathcal{P}$, is

the total collective state dipole moment per volume, $\mathcal{P} = \frac{\langle \mu_{EG} \rangle}{V}$, where $\langle \mu_{EG} \rangle$ is the total collective state dipole moment. It is clear that

$$\chi = \frac{\langle \mu_{EG} \rangle}{V} \frac{1}{\epsilon_0 \mathcal{E}/2} \tag{3.115}$$

The collective state dipole can be found using Eq. 3.111 by

$$\begin{aligned} \langle \mu_{EG} \rangle &= \langle \psi | er | \psi \rangle \\ &= c_E^* c_G \langle E | qr | G \rangle + c_E^* c_S \langle E | qr | S \rangle + c.c. \\ &= \sqrt{N_a} (c_E^* c_G \langle e | qr | g \rangle + c_E^* c_S \langle e | qr | s \rangle + c.c.) \\ &= \sqrt{N_a} (\mu_{eg} \rho_{EG} + \mu_{es} \rho_{ES} + c.c.) \end{aligned} \tag{3.116}$$

with the electron charge, q, and single atom dipole moment $\langle \mu_{eg} \rangle$. The third line can be found using the single collective excitation state for identical coupling constants for each atom

$$\begin{aligned} \langle E | qr | G \rangle &= \frac{1}{\sqrt{N_a} g_{eff}} \sum_j g_j \langle g, \ldots, e_j, \ldots, g | qr | g, \ldots, g \rangle \\ &= \mu_{eg} \frac{\sum_j g_j}{\sqrt{N_a} g_{eff}} \\ &= \sqrt{N_a} \mu_{eg} \end{aligned} \tag{3.117}$$

Again by looking at the terms that oscillate with the correct frequency of the probe coupling only the $|E\rangle$-$|G\rangle$ transition, we find the susceptibility can be written as

$$\chi = \frac{\sqrt{N_a}}{V} \frac{\mu_{eg}}{\epsilon_0 \mathcal{E}/2} \rho_{EG} \tag{3.118}$$

and again becomes a problem of finding the off-diagonal collective density matrix elements.

The master equation (Eq. 3.110) can be solved under adiabatic evolution to reach steady state, which is valid for a weak probe compared to the cavity coupling, $\Omega_p \ll 2g_{eff}$. The mathematical details are identical to that found in Section 3.1.2, giving the density matrix element

$$\rho_{EG} = -\frac{\sqrt{N_a} \Omega_p}{2} \frac{\Delta_p - \Delta_c + i\frac{\kappa}{2}}{(\Delta_p - \Delta_c + i\frac{\kappa}{2})(\Delta_p + i\frac{\Gamma_e}{2}) - g_{eff}^2} \tag{3.119}$$

which can be substituted into Eq. 3.118 to find

$$\chi = \frac{N_a}{V}\frac{|\mu_{eg}|^2}{\epsilon_0\hbar}\frac{\Delta_p - \Delta_c + i\frac{\kappa}{2}}{g_{eff}^2 - (\Delta_p - \Delta_c + i\frac{\kappa}{2})(\Delta_p + i\frac{\Gamma_e}{2}))} \tag{3.120}$$

In order to characterize the behaviour of VIT using the single atom cooperativity parameter, $\eta = \frac{4g_{eff}}{\kappa\Gamma_e}$, we rewrite Eq. 3.120 as

$$\chi = \frac{OD}{kL}\frac{i\frac{\Gamma_e}{2}(\Delta_p - \Delta_c + i\frac{\kappa}{2})}{\frac{\Gamma_e}{2}(\Delta_p - \Delta_c + i(1+\eta)\frac{\kappa}{2}) - i\Delta_p(\Delta_p - \Delta_c + i\frac{\kappa}{2})} \tag{3.121}$$

using optical density, $OD = \frac{N}{V}\sigma_0 L$, for a sample of length, L, and resonant cross section, σ_0.

The transmission of the probe field at resonance, $\Delta_p = \Delta_c = 0$, is then simply

$$\begin{aligned} T &= e^{-\mathrm{Im}[\chi]kL} \\ &= e^{-\frac{OD}{1+\eta}} \end{aligned} \tag{3.122}$$

where the transmission is that of a modified effective optical depth, which becomes reduced as the coupling to the cavity is increased, creating a high transparency window. The system can be considered to be mostly in the dark state, but due to the dissipation out of the cavity it is not completely in the dark state.

The width of the transparency window, σ_{VIT}, can again be related to the figure of merit, η, by approximating the transmission near $\Delta_p \approx 0$ as a Gaussian shape with width for large optical depths, $OD \gg 1$ [34],

$$\sigma_{VIT} \approx \frac{(1+\eta)\kappa}{\sqrt{OD}} \tag{3.123}$$

Fig 3.9 shows the VIT transmission window for $\Delta_c = 0$, with a larger transmission occurring for larger coupling strengths. The width of the window is also seen to increase with the larger cooperativities.

3.5.3 Group Velocity and Pulse Width

As in the case of EIT, the group velocity can experience a large reduction due to the large dispersion in the transparency resonance window represented by a large derivative in the

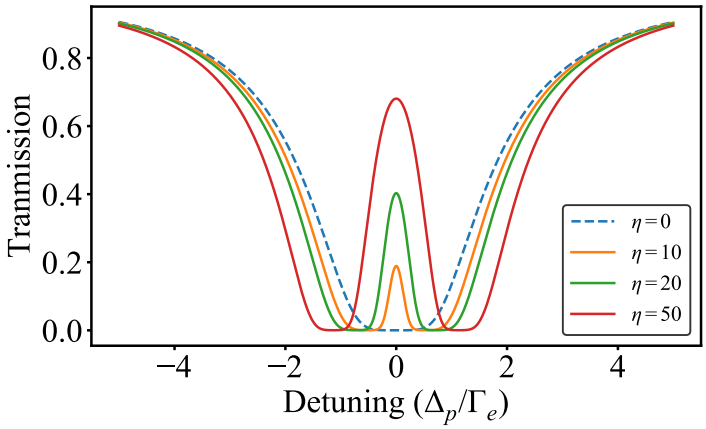

Figure 3.9: Transmission of the probe field at a cavity frequency resonant with the $|E\rangle$ - $|S\rangle$ transition ($\Delta_c = 0$) for various cooperativities resulting in vacuum induced transparency (VIT). The resonance probe transmission peak at $\Delta_p = 0$ increases in both amplitude and width for larger coupling strengths, in accordance with the behaviours of Eq. 3.122 and Eq. 3.123, respectively. The optical depth is set to $OD = 10$ and cavity decay rate as $\kappa = 0.1\Gamma_e$.

real part of the susceptibility. The extension of the result to a VIT system, however, has the remarkable implication that a pulse travelling through a medium coupled through free space can be slowed simply from the presence of a cavity encapsulating the medium.

We can again find the group velocity by

$$v_g = \frac{c}{n + \omega_p \frac{dn}{d\omega_p}} \tag{3.124}$$

where using Eq. 3.121 in relation to the real refractive index, $n = 1 + \frac{\mathrm{Re}[\chi]}{2}$, we find at resonance

$$\omega_p \frac{dn}{d\omega_p}\bigg|_{\Delta_p=\Delta_c=0} = \frac{OD}{L}\frac{\eta}{(1+\eta)^2}\left(\frac{1}{\kappa} + \frac{1}{\eta\Gamma_e}\right)c \tag{3.125}$$

Since the dispersion can be very large, $\omega_p \frac{dn}{d\omega_p} \gg 1$, we can approximate the group velocity in the limit of $g_{eff} \gg \kappa$,

$$v_g \approx \frac{\kappa L}{OD}\frac{(1+\eta)^2}{\eta} \tag{3.126}$$

The group velocity can become much smaller than the speed of light in a vacuum, $v_g \ll c$, which produces a group delay time, τ_d, for the pulse through the medium,

$$\begin{aligned}\tau_d &= \frac{L}{v_g} - \frac{L}{c} \\ &\approx \frac{L}{v_g} \\ &= OD\frac{1}{\kappa}\frac{\eta}{(1+\eta)^2}\end{aligned} \tag{3.127}$$

Interestingly, the delay time is independent on the actual length of the atomic medium, but simply on the OD. This delay time can intuitively be thought of as being caused by the photon being stored in the cavity. The average time spent in the cavity is $\frac{1}{\kappa}$ (Eq. 2.10), while the fraction of the photons that are in the cavity mode can be shown to be $\frac{\eta}{(1+\eta)^2}$ [108].

There is a practical issue that may arise, however, in these types of experiments, as we alluded to in Section 3.1.3. In order for the entire single photon pulse to be in a medium at once, it must have a spectrum that fits within the transparency window, and subsequently within the region of the large dispersive slope in the refractive index. The simplest way to analyse this problem is to assume a Gaussian-shaped envelope in the frequency domain with a spectral width equal to that of the transparency window (Eq. 3.123), thus the electric field is

$$E_p(\Delta_p) \propto e^{-\frac{\Delta_p^2}{2\sigma_{VIT}^2}} \tag{3.128}$$

which can then be Fourier transformed to find the time dependence of the pulse

$$E_p(t) \propto e^{-\frac{t^2}{2T_{VIT}^2}} \tag{3.129}$$

where the minimum pulse width in time that will still fit in the transparency window is thus

$$T_{VIT} = \frac{1}{\sigma_{VIT}} = \frac{\sqrt{OD}}{(1+\eta)\kappa} \tag{3.130}$$

This pulse width also represents the time scale in which the photon adiabatically constructs the dark state polariton with the atomic medium.

For large OD, we can find the ratio between the delay time and the minimum pulse time,

$$\frac{\tau_d}{T_{VIT}} = \frac{\sqrt{OD}}{2}\frac{\eta}{(1+\eta)} \tag{3.131}$$

This results in approaching a $\sqrt{OD}$ dependence for a system in the strong coupling regime, allowing the entire probe pulse to simultaneous fit into the atomic medium at once. However, it is evident that for $OD < 1$ the entire pulse cannot fit into the atomic cloud, no matter how strongly the atoms are coupled to the cavity (even for $\eta \gg 1$).

3.6 Validity of Approximations

In this section, and in the rest of this thesis, we utilize several assumptions when characterizing the actual physical system in order to find approximate solutions to otherwise unsolvable dynamical equations. This work considers the use of cold cesium atoms in all experiments, and thus we will discuss the validity each major approximation.

Most of the level selections employed would be within the D2 transitions, which have a minimum hyperfine splitting on the order of $\nu_{HF} \sim 100$ MHz. The natural linewidth of these transitions are $\Gamma \approx 2\pi \times 5.2$ MHz, which is of course much smaller than the level splittings, allowing for effective two or three level systems to be designed while neglecting any cross coupling to far off resonant levels. In addition, thermal excitations are also negligible since the cesium atoms are cooled to $\sim 10\mu$K, corresponding to $\nu_{thermal} = \frac{k_B T}{h} \approx$ 200kHz$\ll \nu_{HF}$.

In Sections 3.1 and 3.2 we had also discussed making the dipole approximation. This is valid for wavelengths much larger than the spatial extent of the electron wavefunction. Since the D2 transition wavelength is $\lambda_0 \sim 852$ nm and the dipole matrix element is $\sim 4.5ea_0$ (with a_0 as the Bohr radius) [101], we have $\lambda_0 \gg 4.5a_0$.

The final main approximate we have made is the rotating wave approximation (RWA), where we had dismissed the non-energy conserving terms, $a^\dagger \sigma_{ge}^\dagger$ and $a\sigma_{ge}$. We also saw that such terms rotate at a frequency of $\omega_0 + \omega$ (with ω as either the driving probe frequency or the cavity frequency, depending upon which context the RWA was made). Since the atomic frequency is $\omega_0 = 2\pi\frac{c}{\lambda_0} \approx 2\pi \times 3.52 \times 10^{14}$Hz. The relevant time scale that we are concerned with is usually at least on the order of the lifetime of the atomic excited state or longer, for which $\frac{1}{\Gamma} \sim 31$ns. Thus, these co-rotating terms are extremely fast ($\sim 10^7$ oscillations) with respect to the time scales we are exploring and so their effects can be considered to be averaged out to zero.

Chapter 4

Implementing Bragg Mirrors in a Hollow-Core Photonic-Crystal Fiber

The contents of this chapter are mostly based on the work published in Ref. [32]. One of the main goals of this thesis is to investigate and develop novel types of fiber-integrated cavities that will allow for the loading of atomic gases to enhance light-matter interactions. In this chapter we consider one such scheme for producing such a fiber-cavity, where we have numerically simulated the performance and requirements of the cavity, particular cavities that are incorporated into hollow core photonic crystal fibers (HCPCF).

The mirrors of the Fabry-Pérot cavity are formed by making Bragg reflectors, which were discussed in Section 2.2, in the fiber. We propose two separate methods to do so. Each method relies on periodically altering the effective index of the fiber cross section, as shown in Fig. 4.1. The interfaces between the different refractive indices result in Fresnel transmission and reflection of the propagating Gaussian mode supported by the fiber. Large reflectivities can occur by designing the thickness of the Bragg layers such that the reflected waves constructively interfere for a particular wavelength of light. These methods are somewhat related to realizations of Bragg gratings in photonic-crystal fibers reported in the past [99, 128], although these demonstrations were not done with hollow core fibers and resulted in complete filling of the photonic crystal region. Atoms could then be gravity loaded into the HCPCF, as we will describe in more detail in Chapter 5.

Our first method for forming Bragg layers (Figs. 4.2a and 4.2b) is based on coating the inner wall of the hollow core with a photoresist which is then exposed to an appropriate UV light interference pattern. The fiber core would then be flushed with resist developer to remove the unexposed resist, leaving behind a ribbed structure acting as a Bragg grating.

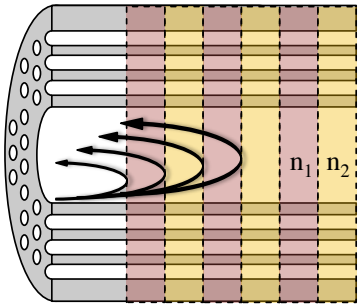

Figure 4.1: Bragg mirror formed in a hollow core photonic crystal fiber (HCPCF) by periodically altering the effective index along the optical axis of the fiber. The interference of a particular wavelength (Bragg condition) light reflected from each interface of the Bragg layers can cause for near unity reflection.

The reflectivites possible of the Bragg mirrors using this technique are presented in Section 4.3.1.

The initial coating of the hollow core with resist could possibly be obtained by the use of pressurized gas to eject resist loaded into the core. Adhesion of the resist to the core walls would allow for a thin film to remain, in which the film thickness would ideally be controllable by the variable pressure of the gas, the viscosity of the photoresist, and the solvent used. Alternatively, uniform thickness could be achieved through some type of evaporation technique, such as reported in [126], or through the use of chemical growth out of a solution.

In our second proposed method (Figs. 4.2c and 4.2d), one or more of the holes of the photonic crystal (PC) region are filled with UV sensitive epoxy. The fiber would again be exposed to a periodic light pattern to leave behind a periodic modulation of the refractive index of the injected epoxy. These results are presented in Section 4.3.2.

Both of these methods rely on selective filling of the holes of the photonic-crystal fiber. Such filling has, to some extent, been demonstrated previously [117, 53, 119, 24, 59], although refinement of these techniques will likely be needed. Alternatively, polymer cold-drawing reported by Shabahang *et al.* [93] may also provide a possible technique to produce high refractive index modulation in the fiber core.

The section begins by describing the simulation model for the HCPCF and the associated loss. We then describe in Section 4.2 the two theoretical methods in which we calculate the reflectivities of the Bragg mirrors. In the concluding sections we present the results of numerical simulations predicting the performance of these two types of Bragg

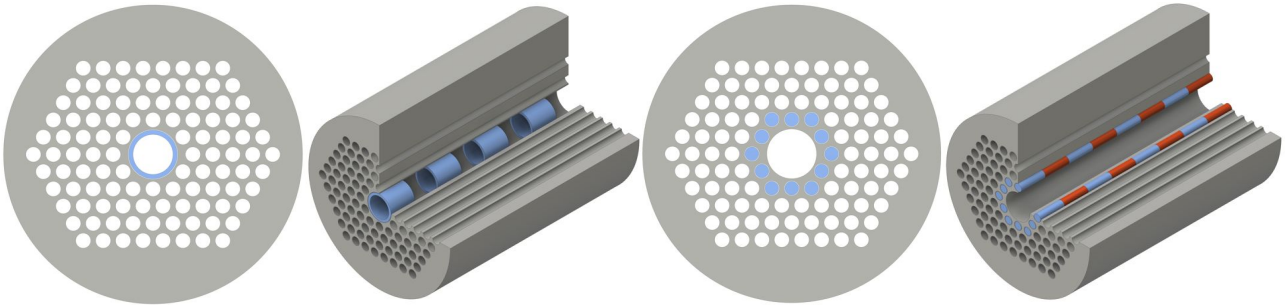

(a) (b) (c) (d)

Figure 4.2: The two proposed methods for integrating Bragg gratings into HCPCFs: (a) the cross section and (b) cutout of a HCPCF with a thin film of resist coating the hollow core. The (c) cross section and (d) cutout of a HCPCF with a UV-curable polymer selectively filled in the first layer of the photonic crystal holes.

gratings as mirrors integrated into a HCPCF to form a Fabry-Pérot cavity.

4.1 HCPCF Simulation Model

We start by implementing a fiber model using the Lumerical MODE Solutions software in which the field eigenmodes of the structure are solved to find its attenuation coefficient and effective index. We simulated two different models of the fiber, which are roughly based on HC-800-02 (Fig. 4.3a), a commercially available HCPCF from NKT Photonics guiding light [10]. We focused on this particular commercial fiber as it can guide wavelengths corresponding to transitions of alkali atoms, such as rubidium and cesium, whose vapors are commonly used to study non-linearities and quantum optics of low light levels.

The physics by which these fibers guide light has been previously discussed in Section 2.2.2. The 2D photonic crystal pattern in the cladding surrounding the core opens a photonic bandgap which allows for the trapping and guiding of the light in the empty hollow core for a particular bandwidth of frequencies.

The first model, shown in Fig. 4.3b and referred to as the circular hole model, employs an idealized circular shape for both the hollow core as well as the photonic crystal holes. It resembles one of the first demonstrations of a hollow-core fiber by Cregan *et al.* [25] in which light was guided by the photonic-bandgap effect in an air core and could be considered the simplest HCPCF shape.

The second model, shown in Fig. 4.3c and referred to as the hexagonal fiber model, is based on a theoretical rendering of a HCPCF [60] which has a twelve-sided core with alternately long and short sides arising when the glass nodes of the core are placed at uniform pitch and at the corners of each cladding hexagon. Shape-wise, the second model resembles relatively closely to the scanning electron microscope (SEM) image of the commercial fiber shown in Fig. 4.3a. The loss associated with the hexagonal hole model was found using a discretized picture of the fiber shown in Fig. 4.3c. The hollow core diameter was scaled to 6 μm, which resulted in a lattice pitch of $\sim 2.1\mu$m and a PC hole diameter of $\sim 2\mu$m. Minimal attenuation in this model occurred at a wavelength of 851 nm and all subsequent simulations for the fiber model are performed at this wavelength unless stated otherwise.

Although not exact, the hexagonal hole model of the fiber qualitatively reproduces the transmission properties of the commercial fiber (Fig. 4.3d), which has a minimal loss of $\sim$ 0.150 dB/m. The simulated hexagonal model (Fig. 4.3f), yields a minimum loss of $\sim$ 0.330 dB/m. Our simulation model has neglected any additional losses that may be caused by surface scattering and this higher loss arises from having fewer than 10 hole layers [10] surrounding the hollow core. While increasing the loss, this reduced number of hole layers allowed us to fit our simulation within our available computational resources. Since the light propagating through this model will experience larger attenuation compared to the actual fiber, we expect to obtain a conservative estimate on the performance of the fiber Bragg mirrors calculated in the later sections of this chapter.

The attenuation spectrum for the circular hole model (Fig 4.3e) was minimized by altering the lattice pitch of the triangular photonic crystal pattern, as well as the diameters of the PC holes and hollow core of the fiber, resulting in optimized dimensions roughly similar to HC-800-02 in which the pitch is specified as $2.3 \pm 0.1\mu$m and the hollow core diameter as $7.5 \pm 1\mu$m. In our circular model, the resulting optimized pitch was 2.3 μm, with a hole diameter of 2.174 μm and hollow core diameter of 6.386 μm. The minimum attenuation found occurred at a wavelength of 860 nm, producing a minimum loss of $\sim$ 1.78 dB/m.

Although the circular hole model leads to inferior mirrors compared to the hexagonal hole model, we included it to demonstrate that our methods can be applied to form mirrors in more than one design of a hollow-core photonic crystal fiber. For these reasons, this chapter will focus on the results from the hexagonal hole simulation model, and give only a summary of the results provided by the circular hole model in Section 4.4.

Perfectly matching layer (PML) boundary conditions were used for an eigenmode solver of size 23.6571 μm$\times$22.7641 μm, in order to simulate a symmetric region around the core. The number of mesh cells in this region were set at 2160 $\times$ 2160, so as to produce a

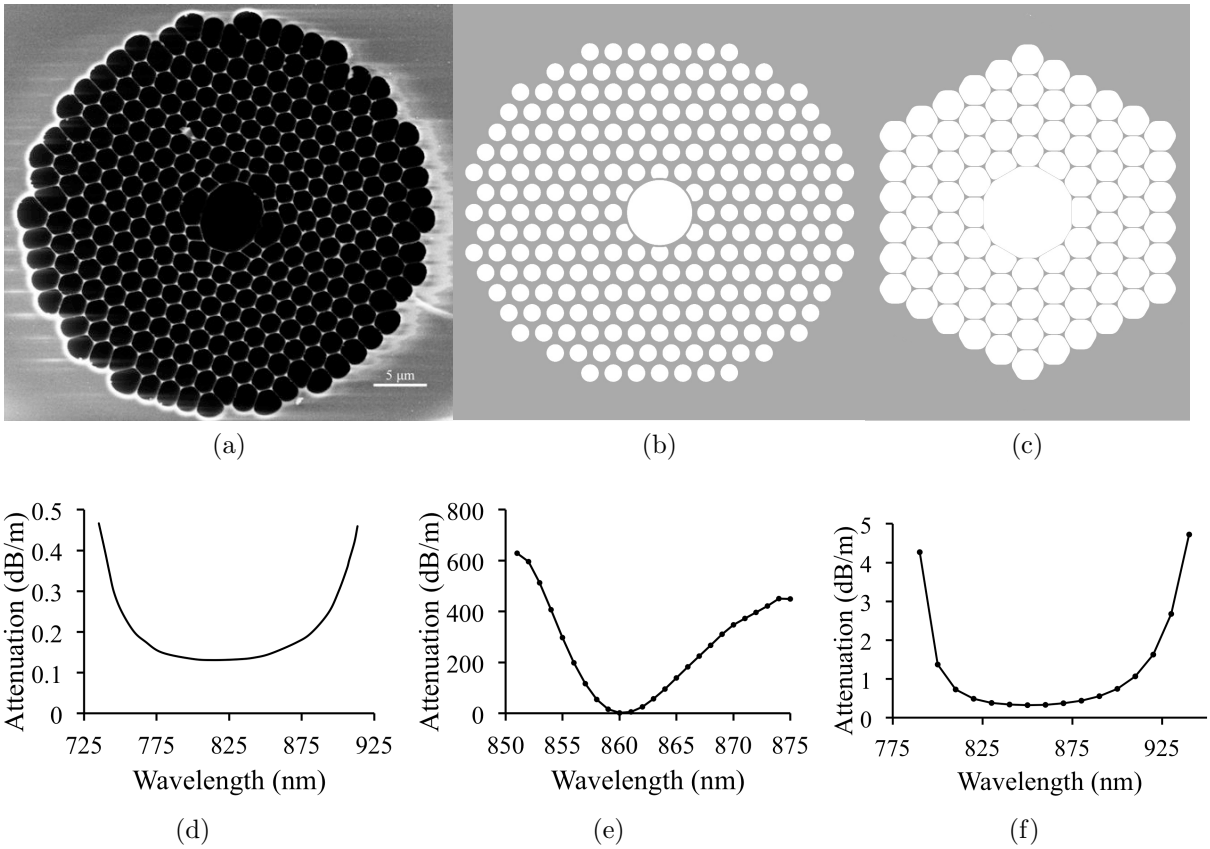

Figure 4.3: HCPCF cross sections: The (a) SEM picture of the HC-800-02 fiber. (b) The circular hole model and (c) hexagonal hole model [60] implemented to simulate the fiber structure (optimized lattice pitch, PC hole size and hollow core diameter not drawn to scale). Propagation attenuation in HCPCFs: (d) The manufacturer specification for HC-800-02 and the numerically simulated losses for the (e) circular hole model and (f) hexagonal hole model.

discretized simulation that highly resembles the actual fiber structures. The subsequent loss and effective index of the supported fundamental Gaussian mode can then be found.

Our simulations assume that the photoresist and UV epoxies that will coat the hollow core walls and fill the PC holes, respectively, are both continuous and homogeneous materials.

4.2 Theoretical Calculation of Bragg Reflectivity

As we have seen in Section 2.2, ideally for an infinite number of periods, a simple Bragg mirror would produce a reflectivity of 100% by Eq. 2.33 for wavelengths at the Bragg condition (Eq. 2.44), where the wavelength is four times the optical path length of each of the layers. In practice though, reflectivity will be reduced due to the loss associated with the fiber itself, as well as due to additional losses arising from the presence of the photoresist, which will partially disrupt the photonic-crystal waveguiding of the fiber.

The corresponding effective fiber loss reduces the reflectivity of the Bragg mirror as the light penetrates into the grating region. Two separate methods are used to estimate the attainable maximum reflectivity based on the fiber attenuation. The first method, which we refer to as the penetration depth method (PDM), uses the fact that the spatial distribution of the light within the bandgap of the Bragg mirror becomes exponentially decaying as the light enters the Bragg layers, as shown in Section 2.2.1. This behaviour is depicted in Fig. 4.4a.

We can then approximate the reduction in reflectivity as due to the loss that occurs for travelling twice the average penetration depth, z_p. This is a result of reflected light having travelled, on average, a total round trip of $2z_p$ due to propagation in and out of the Bragg mirror. The assumption of an infinite number of Bragg periods is still used, however the resulting approximate reflectivity, R, now becomes

$$R \approx e^{-2(\alpha_1 z_1 + \alpha_2 z_2)} \tag{4.1}$$

in which the two Bragg layer attenuation coefficients are α_1 and α_2, and the respective total travel distance in each layer is z_1 and z_2, such that $z_p = z_1 + z_2$. This approximation can be further refined by considering a sinusoidally varying function of the resist layer thickness that is likely to result from the interference lithography process, rather than a step function. However, it was found to give negligible corrections to the reflectivity values.

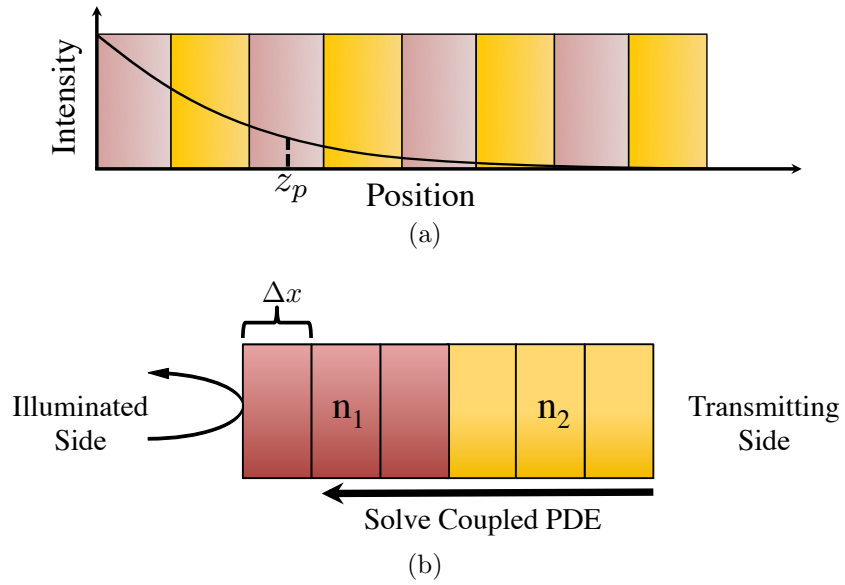

Figure 4.4: (a) The penetration depth method (PDM) method finds the reflectivity by accounting for the attenuation associated with propagation of the light into the lossy Bragg mirror to an average penetration depth, z_p. (b) The method of single expression (MSE) iteratively solves the coupled differential equations in Eq. 4.5 - 4.7 to find the reflectivity. The Bragg layers are discretized into Δx step sizes and the fields are solved for at the transmitted side and iterated towards the illuminated side.

The average penetration depth can be estimated using the results from Section 2.2.1, in which Eq. 2.54 gave

$$z_p = \Lambda \frac{n_{avg}}{\Delta n} \tag{4.2}$$

for a single Bragg period length, $\Lambda = a + b$, with the two Bragg layer lengths, $a = \frac{\lambda_0}{4n_1}$ and $b = \frac{\lambda_0}{4n_2}$.

Evidently the penetration depth depends on the refractive indices of the two Bragg layers, n_1 and n_2. We extract the effective indices from the numerical eigenmode simulations of the fiber cross sectional models, as discussed in the previous section. Simulations both with and without the presence of the resist are done, which act as the two respective Bragg layers. The above penetration depth expression is an approximation valid for small perturbations in the dielectric constant, which is the case here.

The second method for finding the reflectivities (calculations performed by Golam Bappi) also takes into account the absorption of the medium and is referred to as the

method of single expression (MSE) [4]. It utilizes the one dimensional Helmholtz equation,

$$\frac{d^2E_x(z)}{d^2z} + k_0^2\epsilon(z)E_x(z) = 0 \tag{4.3}$$

for an electric field, $E_x(z)$, through a medium with complex dielectric constant, $\epsilon(z)$, at position z with a free space wavenumber, k_0. For an inhomogeneous medium along the direction of propagation ($\vec{E} \perp \nabla\epsilon$), the general solution to Eq. 4.3 can be written as

$$E_x(z) = U(z)e^{i(wt-S(z))} \tag{4.4}$$

for a field amplitude, $U(z)$, and phase, $S(z)$. This form of the solution is an alternative to the common expression of the summation of two counter-propagating waves.

The general form for the electric field presented in Eq. 4.4 can be used to rewrite the Helmholtz equation (Eq. 4.3) in terms of the the amplitude and phase. We define the spatial derivative of the field amplitude as $Y(z)$ to obtain the set of coupled first order differential equations

$$\frac{dU(z)}{d(k_0z)} = Y(z) \tag{4.5}$$

$$\frac{dY(z)}{d(k_0z)} = \frac{P^2(z)}{U^3(z)} - Re[\epsilon(z)]U(z) \tag{4.6}$$

$$\frac{dP(z)}{d(k_0z)} = \mathrm{Im}[\epsilon(z)]U^2(z) \tag{4.7}$$

where $P(z) \equiv U^2(z)\frac{dS(z)}{d(k_0z)}$ is defined as a function proportionate to the power flow density or Poynting vector.

In order to impose boundary conditions for the problem we assume that the Bragg structure is defined for $0 < z < L$. The incident plane wave illuminates the structure from $z < 0$ to produce a forward travelling wave and a back reflected wave. The system is solved by beginning at the end of the Bragg structure where only a forward transmitted wave is present for $z > L$. We thus have the following boundary conditions at $z = L$,

$$\begin{aligned} U(L) &= E_T \\ Y(L) &= 0 \\ P(L) &= U(L)^2\sqrt{\epsilon_{sur}} \end{aligned} \tag{4.8}$$

for a transmitted wave amplitude, E_T, and dielectric constant of the surrounding media, ϵ_{sur}.

The set equations Eq. 4.5 - 4.7 are iteratively solved in discrete steps by numerical integration beginning at the transmitted side of the Bragg layers and proceeding toward the illuminated side, as displayed in Fig. 4.4b. The continuity of the functions over each interface between Bragg layers is retained by applying ordinary boundary conditions (as discussed in Section 2.2).

These normal boundary conditions imply that at the illuminated side ($z = 0$), the incident electric field can be written as

$$E_0 = \left| \frac{U^2(0)\sqrt{\epsilon_{sur}} + P(0) + iU(0)Y(0)}{2U(0)\sqrt{\epsilon_{sur}}} \right| \tag{4.9}$$

The reflectivity for a reflected field amplitude at the incident interface, E_R, can then be expressed as

$$R = \left| \frac{E_R}{E_0} \right|^2 = \left| \frac{U^2(0)\sqrt{\epsilon_{sur}} - P(0) - iU(0)Y(0)}{U^2(0)\sqrt{\epsilon_{sur}} + P(0) + iU(0)Y(0)} \right|^2 \tag{4.10}$$

and the transmission is as $T = |\frac{E_T}{E_0}|^2$.

4.3 Bragg Mirror Reflectivity Results

4.3.1 Coating Hollow Core Walls

The first approach we investigated for creating a Bragg grating along the axis of the fiber is based on coating the walls of the hollow core with a thin film of photoresist, as shown in Figs. 4.2a and 4.2b. The Bragg grating would be created by exposing the resist to a periodic interference pattern from a UV laser, such as from a Lloyd interferometer. The exposed sections of the resist film would then be flushed away by injecting resist developer into the fiber, which would produce a longitudinal variation of the fiber's effective refractive index.

Propagation attenuation in the fiber is greatly dependent on the film thickness of the resist. Figs. 4.5a and 4.5b shows the loss and effective propagation refractive index for various film thicknesses, respectively, using the hexagonal simulation model. The three different resist refractive indices explored were ~ 1.61, corresponding to photoresists such as AZ701 specifically, as well as 1.45 and 1.30 which act to span the region of possible resist indices in the hopes to observe a general trend.

Both methods for calculating the maximum reflectivities (PDM and MSE) of the fiber Bragg grating result in similar trends. Figs. 4.6a-4.6c show these reflectivity trends for

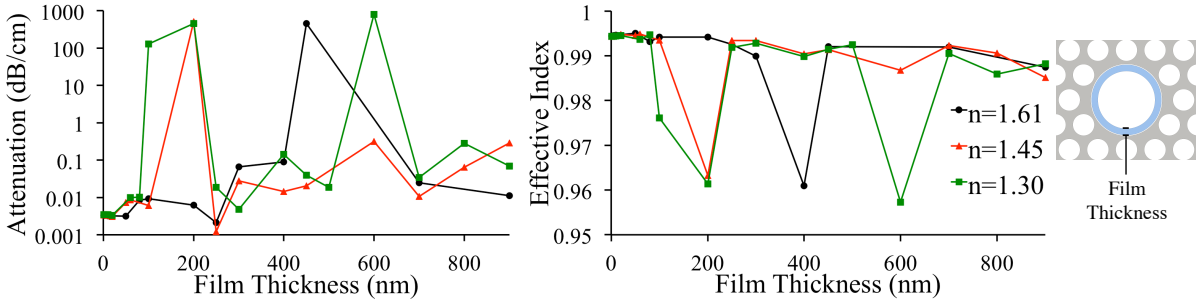

Figure 4.5: Simulation results for (a) attenuation and (b) effective refractive index in the fiber with a varying layer thickness of photoresist coating the inside walls of its hollow core, as shown in the inset. Results are obtained for the hexagonal hole model at a wavelength of 851 nm. Three different indices for the resist material were used: 1.61, 1.45 and 1.30. Simulations were done using a custom mesh size of $\sim$ 1.6 nm$\times$1.6 nm$\times$1.6 nm for the resist film in order to accurately model the relatively thin layer.

the hexagonal simulated model, although there are noticeable discrepancies between the calculated reflectivities obtained by the two methods for small thicknesses of the photoresist (1-5 nm). This is due to the extremely low effective index contrast between the Bragg layers that occurs when using these particular film thicknesses, which presents a challenge to the numerical implementation of MSE. Maximum reflectivities, using the hexagonal hole model, were found to occur using a 700 nm thick resist film (at all three resist indices) with a value of $> 99.99\%$.

To put this result in perspective, we can compare it to reflectivities potentially achievable by index modulation of just the silica material of the photonic crystal region. Such refractive index modulation of silica can be achieved, for example, by exposing the fiber to femtosecond laser pulses [50, 103]. The result can be up to $\sim 10^{-3}$ index change of the material and forming Bragg gratings in solid-core PCFs have been reported previously [37, 69]. Such index modulation of the glass material would result in only minor additional losses and would produce a relatively high maximum reflectivity value of $\sim 99.2\%$. However, to obtain such a high reflectivity based only on this low index modulation of the silica material, the number of Bragg periods required would be $\sim 10^5$ (corresponding to > 5.1 cm penetration depth) since the effective index contrast for the propagating mode would only be $\sim 10^{-5}$.

There is a similar effect when using an extremely thin layer of resist in the hollow

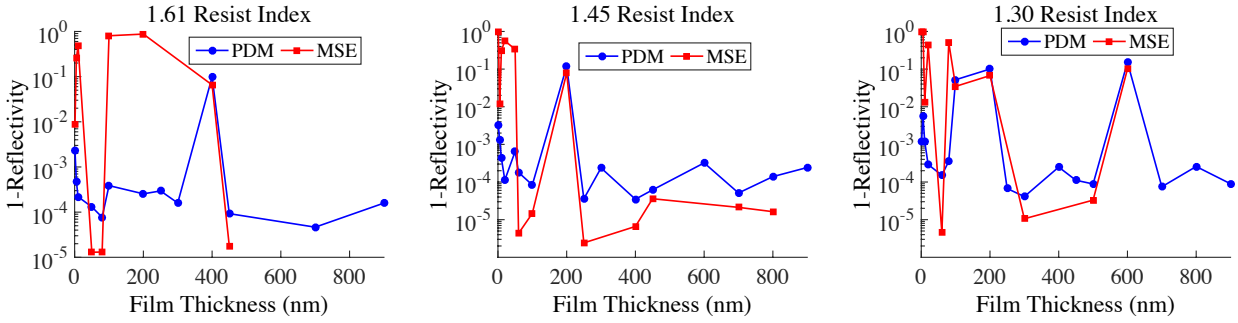

Figure 4.6: Maximum reflectivities for a Bragg mirror formed by periodic films of resist coating the hollow core. The three different material refractive indices used are (a) 1.61, (b) 1.45, and (c) 1.3 for the hexagonal hole model (note that 1-Reflectivity is plotted). The penetration depth method (PDM) calculates the reflectivity using Eq. 4.1 by accounting for the attenuation acquired as the light propagates an average penetration depth (Eq. 4.2) into the Bragg gratings. The method of single expression (MSE) is also used to analyze the grating reflectivity. Some of the reflectivity data points are absent for MSE because the numerical algorithm did not always converge to a finite value.

core. The reflectivity from these thinner films shown in Figs. 4.6a-4.6c can be quite large, however they suffer from the same consequence of inducing low index modulation in the fiber. This is in contrast to about $\sim 3 \times 10^2$ Bragg periods ($\sim$100 μm penetration depth) required for $> 99.99\%$ reflectivity using the 700 nm thick resist film coating the fiber core.

Consequently, large penetration depths will of course require longer mirrors to reach a given reflectivity. Additionally, if a pair of such mirrors is used to form a cavity within the fiber, the cavity mode volume would be larger for mirrors with larger penetration depth, which would in turn decrease the atom-field coupling strength in cavity quantum electrodynamics (QED) experiments [51], as we will discuss further in Section 4.5.

4.3.2 Selective Filling of Outer PC Holes

Another technique that could be used to modulate the effective index of the fiber in order to create a Bragg grating is to selectively fill the outer PC holes with a photo-sensitive polymer, as shown in Figs. 4.2c and 4.2d.

The disadvantage of this approach to fabricating Bragg gratings, however, is that the relatively smaller size of the PC holes ($\sim$1 μm) will likely prevent material from being removed by flushing the holes with a developer after exposure. Consequently, only the difference in index between the exposed and unexposed polymer can be relied on, rather than the absence of material (in contrast to the method described in the previous section). This results in a reduction of the effective index contrast for the propagating mode by about an order of magnitude compared to the previous method based on coating the walls of the hollow core with photoresist.

Filling the PC holes will thus require more Bragg periods in order to produce a given reflectivity (even in the absence of fiber loss) and a larger penetration depth will occur. Similar to coating the inner wall of the hollow core, the presence of material in the PC region will disrupt the finely-tuned bandgap effect and will increase propagation losses in the fiber.

For this technique, we investigate the use of a UV-curable epoxy (glue), in which a standing wave of UV light can be used to cure the glue in a periodic pattern, resulting in a modulated index of the material. The three indices we simulated are 1.62, which will imitate UV-glues such as Norland optical adhesives NOA162 epoxy, as well as 1.45, and 1.30 in order to again span the range of potential indices. Curing the epoxy is assumed to increase its refractive index by $\sim 2 \times 10^{-2}$.

Simulations are done as each hole is filled individually in a circularly consecutive pattern. Other filling sequences investigated were found to produce larger attenuations, however there may still exist an optimal manner in which to consecutively fill the holes but this is not further explored in this thesis. We present two implementations of this technique, one in which the first layer holes in the PC region (closest to the fiber core) are filled, and the other for when the second layer of holes are filled. Figs. 4.7a (4.7c) and 4.7b (4.7d) show the loss and effective index, respectively, associated with the number of filled holes in the first (second) layers of the PC region with uncured UV epoxy for the hexagonal hole model.

Figs. 4.8a and 4.8b show the maximum reflectivities calculated for the hexagonal hole model by filling the first and second layers of the PC region, respectively. These calculated reflectivities are obtained by combining the numerically calculated attenuation and effective index of the fiber with injected epoxy (cured and uncured) using the PDM and MSE as described in Section 4.2.

It can be seen that the two methods for determining the reflectivity are again relatively comparable for the hexagonal model simulation. The filled PC holes give a maximum reflectivity of $\sim$ 99.8% for the simulated model (using 1.30 uncured epoxy index and one

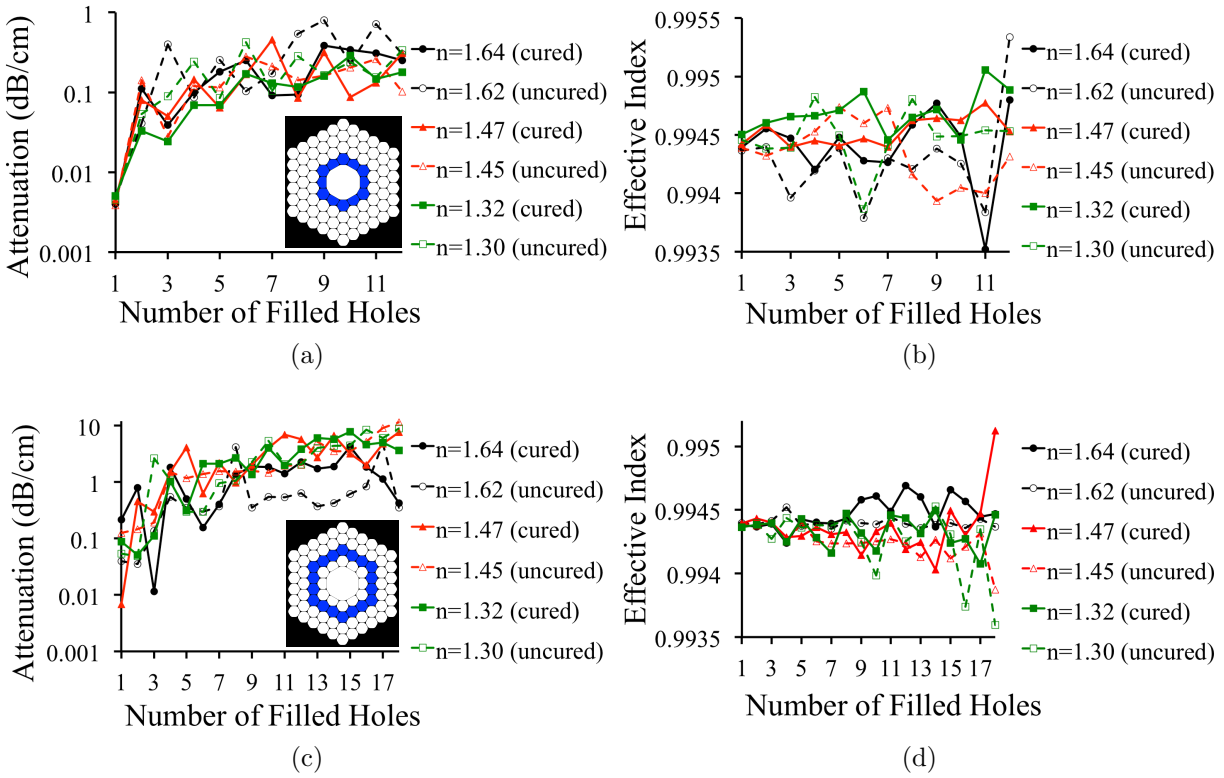

Figure 4.7: Simulation results for attenuation and effective refractive index in the fiber with the first or second layer of PC holes filled with epoxy: (a) and (b) show the simulation results for the filled first layer of PC holes using the hexagonal hole model. (c) and (d) show results for the filled second layer of PC holes. All simulations are performed at a wavelength of 851 nm. The 'hole number' signifies the number of filled holes in a clockwise direction. Three different indices for the uncured polymer material were used: 1.62 (representative of Norland NOA162 optical adhesive), 1.45 and 1.30.

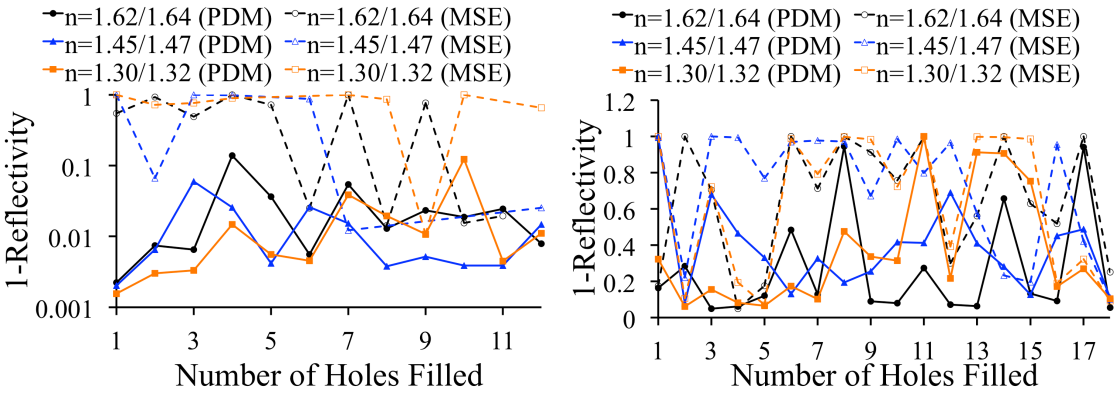

Figure 4.8: Maximum reflectivities for a Bragg mirror formed by periodic exposure of UV-curable epoxy selectively injected into the photonic crystal region. Hexagonal hole model is used for simulation when the (a) first and (b) second layers in the PC region are filled with modulated material. The three different material indices used for the uncured epoxy are 1.62, 1.45, and 1.30, while the cured epoxy indices are 1.64, 1.47, and 1.32. Both PDM and MSE reflectivity results are plotted.

hole filled in the first layer of the PC region). Reflectivities exceeding 99% appear to be achievable by filling one or two holes in the first ring with epoxy of either one of the three refractive indices we considered, while filling the holes in the second ring seems to result in reflectivities barely exceeding $\sim 90\%$.

Maximum reflectivities are observed to overall be lower when the Bragg layers are formed by filling the second layer, rather than the first layer, of PC holes. However, the maximum reflectivity for a mirror created by filling the PC holes is, in general, predicted to be substantially lower than when a resist film is added to the hollow fiber core.

This can be explained by the low effective index modulation and high attenuation of the Bragg layers caused by filling the PC holes. Disruption of the PC region reduces the fiber ability to trap light in the transverse direction, leading to larger losses. The differentiation between Bragg layers due only to the small difference in cured and uncured epoxy contributes to the extremely low index modulation of the mirror. This low effective index modulation also implies that a larger penetration, and thus mirror length, would be required to produce the given reflectivities caused by filled PC holes, as compared to a mirror created by modulation of a resist layer in the hollow core.

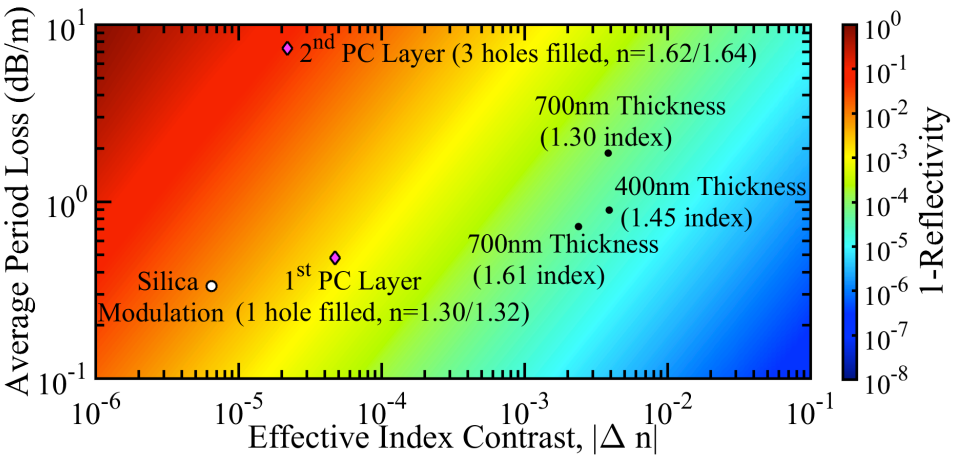

Figure 4.9: Maximum reflectivity of a lossy Bragg mirror for a range of effective refractive index contrast between layer pairs and average loss per unit length of the structure for the hexagonal hole model. Resist layer thicknesses that produced the highest reflectivities in the core coating method are marked in the plot (black circles), together with the points corresponding to the largest reflectivity predicted for the hole filling method (purple diamonds) for the corresponding number of holes filled. The reflectivity produced by Bragg layers formed by modulating the fiber silica material is also plotted (white dot).

4.4 Fiber Bragg Mirror Performance

The results of our numerical simulations of the hexagonal model are summarized and juxtaposed in Fig. 4.9, which shows the reflectivity of a Bragg mirror with lossy layers estimated using the PDM method to determine the total loss and resulting reflectivity. Here, $|\Delta n| = |n_2 - n_1|$ with $n_{1,2}$ being the values of the (complex) effective refractive index of each layer. Larger reflectivities naturally arise for lower attenuation in the layers, as well as larger index contrast because the penetration depth is reduced. The highest reflectivities predicted for the simulated fiber models is marked in the plots for both Bragg mirror approaches based on modulated resist coating the wall of the hollow core, as well as for the approach based on filing the crystal holes.

For comparison, the result arising from modulating the refractive index of only the silica material of the photonic crystal is identified as well (white dot). Unfortunately, introducing even small amounts of the photosensitive polymer into the fiber structure results in significant increase of the propagation loss. However, the increased contrast in effective refractive index between the grating layers seems to offer distinct advantages for

the mirror performance by require a fewer number of Bragg layers to produce a given reflectivity.

For the circular hole model, the highest reflectivity occurs by coating the hollow core with a resist thickness of 700 nm (at a resist index of 1.61), giving a reflectivity of $> 96\%$. In contrast, the filled PC holes instead give a maximum reflectivity of $\sim 44.4\%$ using the 1.30 uncured epoxy index and one hole filled in the first layer of the PC region. The number of Bragg periods required for the largest reflectivities occurring from coating the hollow core periodically is $\sim 2 \times 10^2$ Bragg periods (corresponding to $\sim 90\mu$m penetration depth).

Much like the hexagonal hole model results, the Bragg mirrors formed by modulation of the silica material itself using the circular hole model produce large reflectivities of $> 97\%$, however they again require a much larger number of Bragg periods of $\sim 2 \times 10^4$ (~ 0.9 cm penetration depth) since the effective index contrast between layers is greatly reduced.

Our reflectivity calculations can be further validated by bidirectional eigenmode expansion simulations solving Maxwell's equations in the frequency domain for a Bragg grating using the Lumerical software package. Figure 4.10a shows the simulated spectrum of the hexagonal hole model forming a Bragg grating with 100,000 periods for a resist coating thickness of 700 nm (and resist index of 1.61) of the hollow core walls. These simulations produce similar reflectivity values to those found using the penetration depth method (Fig. 4.6a) which relies on the plane-wave approximation of the light propagation in the structure. Additionally, this simulation predicts the range of frequencies reflected by this grating.

Note that for a low-contrast Bragg mirror such as discussed here, the mirror bandwidth, $\Delta\omega$, can also be easily estimated from the discussion in Chapter 2 using Eq. 2.48 in which

$$\Delta\omega \approx \omega_0 \frac{2}{\pi} \frac{\Delta n}{n_{avg}} \tag{4.11}$$

where ω_0 denotes the angular frequency of light resonant with the Bragg condition. Fig. 4.10b shows the bandwidth (Eq. 4.11) and corresponding penetration depth (Eq. 4.2) for a range of index contrast values that we expect to arise for a Bragg grating formed by the methods proposed here (using the hexagonal hole model). We can see from Figs. 4.9 and 4.10b that as the index modulation is increased, both the maximum reflectivity and the width of the bandgap increase, while the penetration depth decreases for an ideal Bragg mirror at a given average loss. At the same time, when loss in the fiber becomes more significant, the reflectivity can be reduced drastically, however the bandgap and penetration depth remain relatively constant.

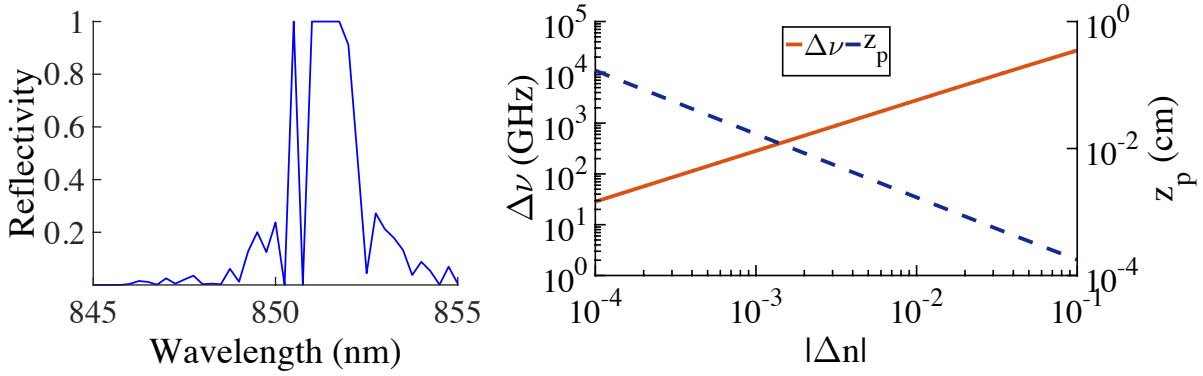

(a) (b)

Figure 4.10: (a) The simulated spectrum of a fiber Bragg grating using a 700nm thick resist (1.61 index) coating the hollow core walls for 100,000 periods. The maximum reflectivity is $\sim$ 99.9969%. (b) Estimated reflectivity bandwidth of the Bragg mirror (dashed blue, Eq. (4.11)) and corresponding penetration depth (solid orange, Eq. (4.2)) plotted against refractive index contrast between the layer pairs forming the mirror.

4.5 Fiber Bragg Cavity

If a cavity is formed from two of these Bragg mirrors placed in a simple Fabry-Pérot configuration, as depicted in Fig. 4.11a, we can define the distance between the two mirrors as the cavity spacer, L_{spacer}. The field between the Bragg mirrors is a constant Gaussian mode area profile supported by the HCPCF, however, as previously discussed, the field will decay exponentially along the optical axis as it enters the Bragg layers. Since the mirrors are no longer simple planar mirrors with a definite travel length of the light, the effective total length of this cavity can instead be defined as the spacer length plus twice the penetration depth (one for each of the two Bragg mirrors), $L_{eff} = L_{spacer} + 2z_p$.

While our calculations predict that a relatively high reflectivity can be achieved by modulating just the fiber material (e.g. by high intensity laser pulses), the benefit of using Bragg gratings formed by adding photosensitive material to the fiber structure is that the penetration depth, and thus the length of mirror required to achieve a given reflectivity, would be significantly smaller in this case. In addition to size-related advantages, a shorter mirror would allow tighter longitudinal confinement of light in a cavity formed by a pair of such mirrors, which is preferable for a number of applications, especially those related to cavity QED.

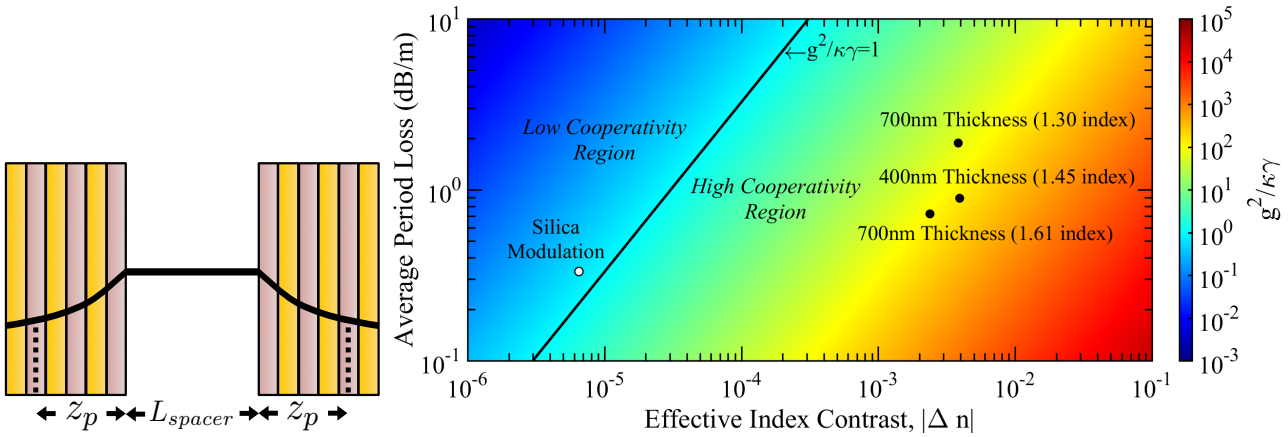

Figure 4.11: (a) A Fabry-Pérot cavity integrated into a HCPCF using two Bragg mirrors placed a distance L_{spacer} apart. The field along the optical axis of the fiber is shown as the black line, which experiences exponential decay when entering the Bragg layers with an average penetration depth of z_p, producing an effective length of the cavity as $L_{eff} = L_{spacer} + 2z_p$. (b) Cooperativity at varying effective index contrasts between Bragg layers and average attenuation per period. The thicknesses resulting in the largest cooperativity by coating the hollow core with resist (for each resist index) are plotted as black dots. The black line distinguishes the high and low cooperativity regimes. Bragg mirrors formed by modulating the fiber silica material is plotted as a white dot.

The benefits of using the types of Bragg mirrors discussed in this chapter are easily seen in Fig. 4.11b, where we have assume a planar cavity with the Q factor as Eq. 2.18. The black dots again represent the thicknesses of the hollow core coatings that resulted in the highest reflectivities (for each index) at their respective attenuations and index contrasts between Bragg layers. As in the previous section, the white dot is that of modulating the fiber material itself. We then plotted the calculated single atom cooperativity, η, with the solid black line separating the regions of high and low cooperativity. Since the cooperativity is proportional to $\eta \propto \frac{Q}{V_{mode}}$, as shown in Section 3.3.2, it is evident that a minimal mode volume is desirable, and thus we assume the limiting case of a zero cavity spacer. Evidently high cooperativity should be achievable employing Bragg layers formed using resist to coat the hollow core walls, while modulation of the silica material cannot reach this regime despite producing similar reflectivities.

The strong coupling regime is explored in Fig. 4.12 as a function of cavity spacer using

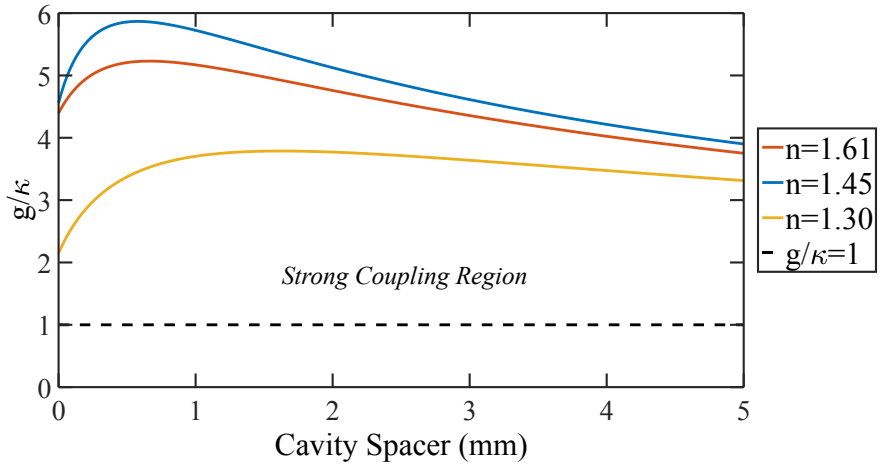

Figure 4.12: The thicknesses of the resist coating the inner walls of the hollow core that produce the highest reflectivity and cooperativity are again plotted here for each resist index discussed (for $n = 1.30, 1.45, 1.61$ we use resist thickness, $t = 700$nm, 400nm, 700nm, respectively). The strong coupling regime is defined as $\frac{g}{\kappa} > 1$ (since $g > \Gamma_\perp$ is the less stringent inequality). Forming Bragg layers by modulating the fiber silica material results in $\frac{g}{\kappa} \ll 1$ and so is not plotted.

cesium atoms, where we only plot $\frac{g}{\kappa}$ because $\frac{g}{\Gamma_\perp} > 1$ is easily satisfied for such systems. The Bragg mirrors using a modulation of the silica fiber material results in $\frac{g}{\kappa} \ll 1$ and thus is not plotted. The index resist index of 1.45 with a coating thickness of about 400 nm produces the greatest coupling at a cavity spacer of ~ 600 μm.

Interestingly, the presence of an optimal cavity length is because there are two competing effects that contribute to the strong coupling regime. For smaller cavity spacers, the photons will bounce off the mirrors more times per oscillation time, which may result in a higher loss due to the imperfect mirrors. However, the photons are of course confined to a smaller mode volume which acts to increase the coupling strength. Conversely, for larger cavity lengths, more time is instead spent traversing the cavity media (i.e. the fiber), which can have a relatively low attenuation compared to the loss through each mirror bounce.

4.6 Conclusions and Outlook

To summarize, two methods for fabricating reflective Bragg gratings in HCPCFs have been proposed and numerically simulated. The numerical simulations and subsequent reflectivity calculations performed for our fiber models predict a HCPCF-integrated Bragg mirror that has a maximum reflectivity of $> 99.99\%$ and that does not obstruct the hollow core. Both the high cooperativity and the strong coupling regimes seem to be possible using the Bragg mirrors discussed in the chapter. Given that our models used to simulate the fiber modes have propagation loss exceeding that of the manufacturer specifications, our calculations should represent a reasonable estimate of the achievable performance.

This Bragg reflection is possible despite the small overlap between the propagating mode confined to the hollow core and the grating itself. A relatively similar scenario occurs in other well-known photonic devices, such as distributed Bragg reflectors (DBR) which are used in certain diode lasers. In this case, the reflectors are formed by the periodic presence of material on the surface of a waveguide containing the diode to create Bragg mirrors which form the laser cavity, even though the overlap between the guided mode and the grating structure is again minimal [46].

Periodic coating of the inner wall of the hollow core of the fiber with photoresist appears to be the most promising way to produce a high reflectivity Bragg mirror and strong coupling cavity systems due to the relatively low loss and high index contrast between Bragg layers resulting from this approach, although finding techniques to deposit a photoresist layer of controllable thickness onto the core wall might present a challenge. On the other hand, creating Bragg layers by selectively filling the PC holes of the fiber with a periodically exposed UV-curable polymer results in a mirror with smaller contrast between its Bragg layers but the resist injection methods required for this have already been demonstrated [117, 53, 119].

While our calculations focused on a specific HCPCF model, we anticipate similar results for other photonic-bandgap HCPCFs. This work can be further extended by modelling these Bragg gratings for HCPCFs based on inhibited coupling between core and cladding modes, also known as 'kagome' fibers [10]. Given the distinctly different guiding mechanism in these fibers, it would be interesting to see the effects of polymer injection into the fibers' microstructure on propagation losses and effective refractive index.

We expect these mirrors to be utilized for novel devices, such as fiber-integrated lasers with atomic or molecular vapors serving as the gain medium, sensors, and frequency standards, as well as for fundamental studies of light-matter interactions.

Chapter 5

Fiber-integrated cavity based on photonic-crystal slab mirrors

The contents of this chapter are, in part, based on work published in Ref. [33]. In this chapter, we describe the design and fabrication of a tunable fiber-integrated cavity using photonic crystal membranes acting as mirrors, the physics of which is described in Section 2.3. The large reflectivities of these patterned membranes arises from the presence of internally guided resonance modes that are confined to the membrane by total internal reflection [29].

Light trapped in these resonances can leak out by coupling to external radiation modes. At particular resonant optical frequencies, the leaked light will interfere constructively in the backward direction and destructively in the forward direction with respect to the incident light [30], which can, under ideal conditions, result in a structure acting as a perfect mirror.

The PC mirrors are mounted onto a segment of HCPCF, as shown in Fig. 5.1, such that the full confinement of the light is provide by this photonic device to a relatively small volume in the hollow core. In addition, the loading of an atomic ensemble is possible by injection through the PC holes of the membranes and into the hollow core of the fiber.

Loading of an ensemble of cold atoms into these fiber-integrated cavity devices would be possible using the setup shown in Fig. 5.2. A magneto optical trap (MOT) is used to cool and trap cesium atoms to a spherical cloud inside a glass cell held at an ultra-high vacuum (UHV). Within the same glass cell, the fiber cavity is vertically oriented and mounted directly underneath the atomic cloud. The atoms are loaded into the fiber by

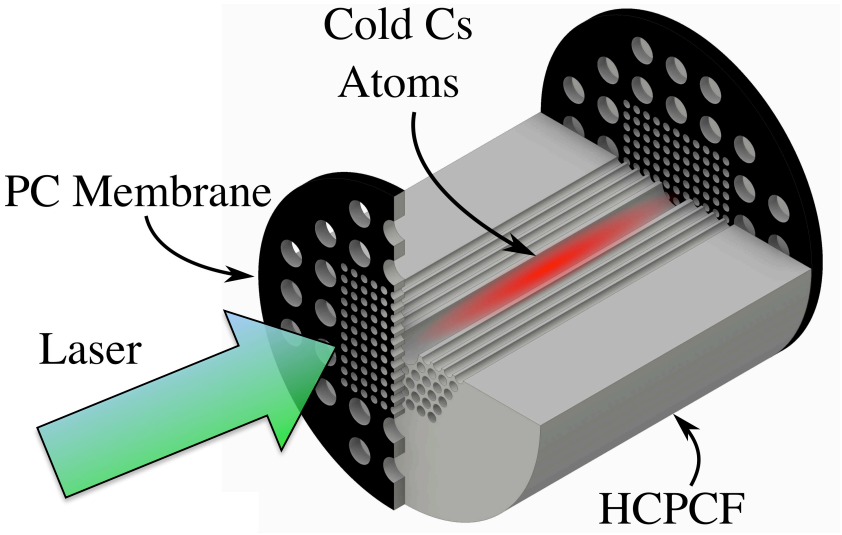

Figure 5.1: The HCPCF-integrated Fabry-Pérot cavity. The fiber serves as the cavity medium and confines light in the transverse direction, while a pair of dielectric metasurfaces (PC membranes) mounted on the ends of the fiber segment confine light longitudinally.

simply switching off the MOT, allowing the atoms to fall through the holes of the PC pattern and into the hollow core of the fiber due to gravity [6].

In addition, the atom loading efficiency can be increased by the presence of a red-detuned, magic wavelength dipole trap coupled through the fiber. The dipole trap acts to funnel the atoms into the hollow core during the loading process and helps to trap the atoms within the fiber to the centre of the core. The fact that the atoms are cooled to $\sim 10\mu$K not only acts to reduce Doppler broadening of the transitions, but also allows the atoms to be trapped by the relatively shallow dipole trap. Once the atoms are loaded into the fiber, the use of these optical tweezers will also reduce collisions with the walls of the hollow core and focus the atoms to the region of the core with the largest electric field amplitude, further increasing light-matter interactions. A magic wavelength dipole trap is used to eliminate the effect of AC stark shifts that would otherwise act to alter the transition frequency of the atoms. This speaks to one of the main reasons for the choice of cesium atoms over other alkali atoms. Apart from its larger mass which allows cesium to be cooled to lower temperatures, its transition wavelength of ~ 852 nm and magic wavelength of ~ 935 nm are close enough to each other to be both within the guiding bandwidth of commercially available HCPCF, which is not the case for other alkali atoms such as rubidium.

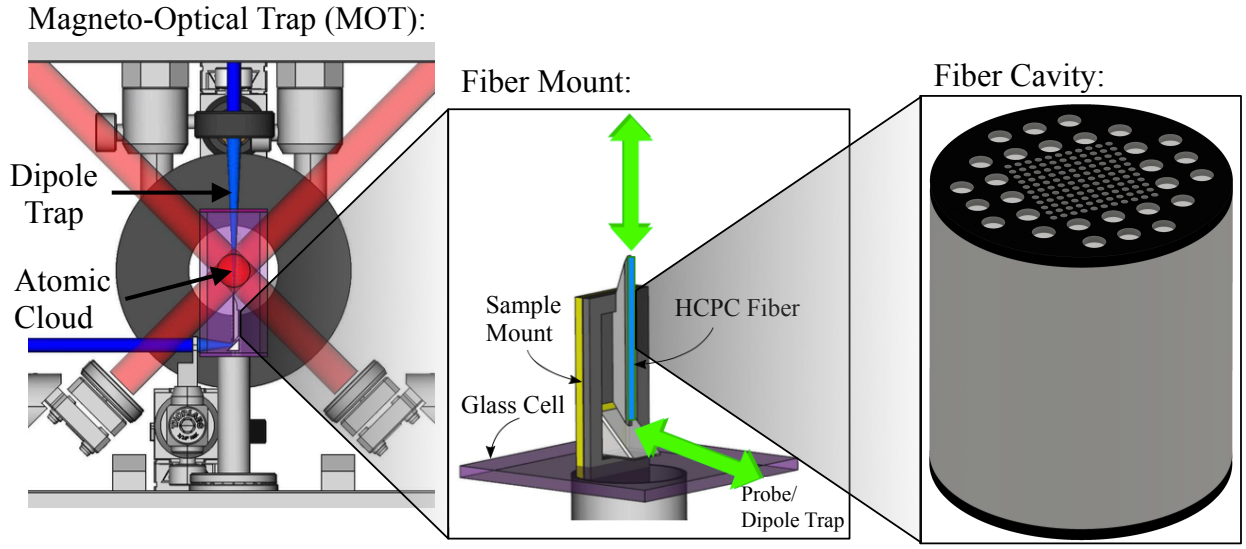

Figure 5.2: A magneto optical trap (MOT) would be used to load atoms into the fiber cavity. Atoms can be gravity-loaded by turning off the MOT system and letting the atoms be funnelled into the hollow core of the fiber using a magic wavelength dipole trap (blue beam) [Image credit: Chris Haapamaki].

We will begin this chapter by outlining the simulation efforts taken to achieve a highly reflective PC pattern design and the challenges involved. We then describe the nanofabrication procedure used to create the patterned membranes and the microassembly techniques used to mount the membranes onto the fibers to form a cavity. The membrane reflectivities and cavity spectrum are presented as well as a demonstration of tuning the resonance peaks by temperature control. We conclude the chapter with preliminary results of a polarization dependent cavity.

5.1 Photonic Crystal Membrane Simulations

The photonic-crystal membranes used here are designed and fabricated in silicon nitride (SiN). This material was chosen due to its low absorption at the target wavelength of 852nm for our cavities, as we plan to eventually use the cavities for experiments with laser-cooled cesium atoms at this transition wavelength. The reflection and transmission spectra of the membrane mirrors are determined by the membrane thickness, material refractive index, as well as type and dimensions of pattern used. The design can be adjusted for

other wavelengths or dielectric materials.

In order to find the combination of parameters that will produce broad-band, near-unity reflectivity at the desired wavelength, we employ finite difference time domain (FDTD) simulations using a commercial software package (Lumerical) to determine the spectrum of the photonic-crystal mirrors. While high reflectivity for a broad range of wavelengths may not be a necessary requirement for some applications, it should make it easier to maintain high reflectivity at the target wavelength if imperfections arising in the fabrication process end up shifting the structure's central wavelength.

We chose to use circular holes, which are somewhat easier to fabricate since they do not require any sharp features such as a square or rectangle. We also had originally explored simulating a hexagonal pattern of holes, however they did not produce very broad peaks in the reflectivity spectrum. We thus decided to instead utilize a simple square lattice of circular holes, in which three parameters dictate the full optical properties of the mirrors: lattice constant (hole pitch), a, hole radius, r, and thickness, t, of the silicon nitride film.

In previous studies [66], highly reflective broad band regions have been found using computationally more efficient techniques, such as transfer matrix methods, however these methods assume the light incident on the structure is a plane wave. Here, on the other hand, the light incident on the membrane will be the fundamental mode of the HCPCF, which has a nearly Gaussian profile with a waist size similar to the radius of the hollow core. In this work, we used HC-800-02 fiber available from NKT Photonics, which has a mode field diameter of $\sim 5.5\mu$m.

Fig. 5.3a shows the difference between the spectrum of a PC membrane assuming a plane wave source and a Gaussian source as the incident light. This illustrates that the reflective properties of the photonic-crystal membrane can be highly dependent on the transverse profile of the incident light, especially for the tightly-confined fiber-guided modes. This is because the reflective properties of the PC membranes are also dependent on the angle of incidence of the illuminating plane wave. In the Fourier domain, a Gaussian beam profile has a Gaussian profile of spatial frequencies, and thus is a combination of plane waves at varying incidence angles, producing a distinct spectrum compared to a single plane wave with normal incidence. It is the interference of these plane waves that ultimately produce the final reflectivity of the Gaussian beam.

As a result, our FDTD simulations have to simulate the whole mirror structure, as the translational periodicity and symmetries, which can be exploited to simplify the calculations for plane waves, are not available. This resulted in much larger computational requirements as the simulation region could not simply be a unit cell of the pattern. Instead, a $15\mu\text{m}\times15\mu\text{m}$ square simulation region was used to encompass the majority of the

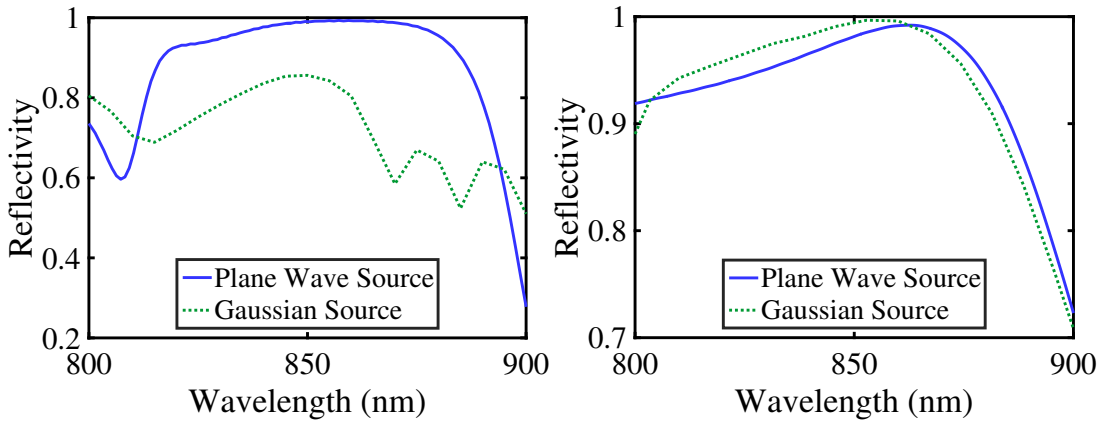

Figure 5.3: (a) FDTD simulation results of the reflectivity produced for light incident perpendicularly on a PC membrane with lattice constant a=819 nm, hole radius r=347 nm, and film thickness t=500 nm. A plane wave and a Gaussian beam (with 2.75 μm waist radius) experience significantly different reflectivities. (b) The simulated reflectivity spectra for plane wave and Gaussian beam with membrane parameters chosen to optimize the reflectivity for the 2.75 μm-waist Gaussian source with a=680 nm, r=297 nm, t=369 nm (material index used was 2.26).

Gaussian beam. This allowed for reasonable computational times without losing a large amount of power to the outer edges of the simulation region to approximately maintain energy conservation ($R + T \approx 1$).

We reduce simulation time by a factor of four by exploiting the four-fold symmetry of the beam shape and PC pattern by setting the minimum x and y boundaries to Symmetric boundary conditions, while the maximum x and y boundaries are set to perfectly matching layers (PML) that act to absorb any radiation exiting the simulation region. Nonetheless, given the larger computational requirements, we applied the Particle Swarm Optimization (PSO) algorithm provided in the Lumerical package to efficiently search the parameter space in order to maximize reflectivity.

Another major challenge in designing these PC patterns is keep the gap size of the material bridging the neighbouring holes (bridge size $= a - 2r$) large enough to ensure the structural stability of the membrane. If this bridge is to small, the membranes risk breaking or cracking during the fabrication procedure. We found that keeping this bridge size to be $\gtrsim$ 100 nm will allow for the membranes to retain the rigidity needed to survive

the various stresses that are present in fabrication process. However, a larger membrane thickness can potentially allow for smaller bridge sizes to be structurally stable.

A combination of parameters predicting a reflectivity $> 99.9\%$ at 852nm was found to consist of a 680 nm lattice constant, hole radius of 297 nm, and membrane thickness of 369 nm (Fig. 5.3b), in which both a Gaussian source as well as a plane wave source resulted in relatively high reflectivities. It was also found that the reflectivity was $> 99\%$ for Gaussian mode sizes with a waist radius $> 2\mu$m. However, given the multiple dimensions of the parameter space, other parameter combinations are likely to result in high reflectivities as well.

5.2 Fabrication of Fiber Cavity

5.2.1 PC Membrane Fabrication

We fabricate the photonic-crystal membranes using electron-beam lithography and dry etching. It should be noted that developing an effective and reproducible nano-fabrication procedure for these PC mirrors took the majority of the effort in making the optical devices described in this chapter. Our early attempts at developing a fabrication procedure involved using SiN films on Si wafer chips with a single square window leaving the SiN film free-standing. These were purchased from Norcada (NX5200E) which had an index of 2.11 at 852nm. Unfortunately, complications arose during the SiN etching procedure. The free-standing film was somewhat thermally isolated from the rest of the Si chip and so the SiN window was non-uniformly heated during the plasma etching causing for a variable etching rate of the SiN across the window.

Instead we decided to grow the SiN in-house using low-pressure chemical vapour deposition (LPCVD) on a 4 inch Si wafer producing a film with refractive index of 2.26 at 852 nm. The growing procedure is not completely uniform across the wafer and it is difficult to grow the SiN film to be exactly the correct thickness that the design requires. For these reasons, we grow the SiN films to be slightly thicker than the design thickness and simply etch each individual chip to the correct thickness. This also allowed us the possibility to fabricate designs at varying thickness without needing to grow an entire new film on a wafer.

We dice the 4 inch wafer into 8×8mm chips in which we can fabricate the PC pattern, while using a thick layer of PMMA on the SiN film ($\sim 1\mu$m) to act as a protective layer during the dicing process. The following procedure is how we fabricated the PC mirror templates onto an individual 8×8mm chip, which is summarized in Fig. 5.4a.

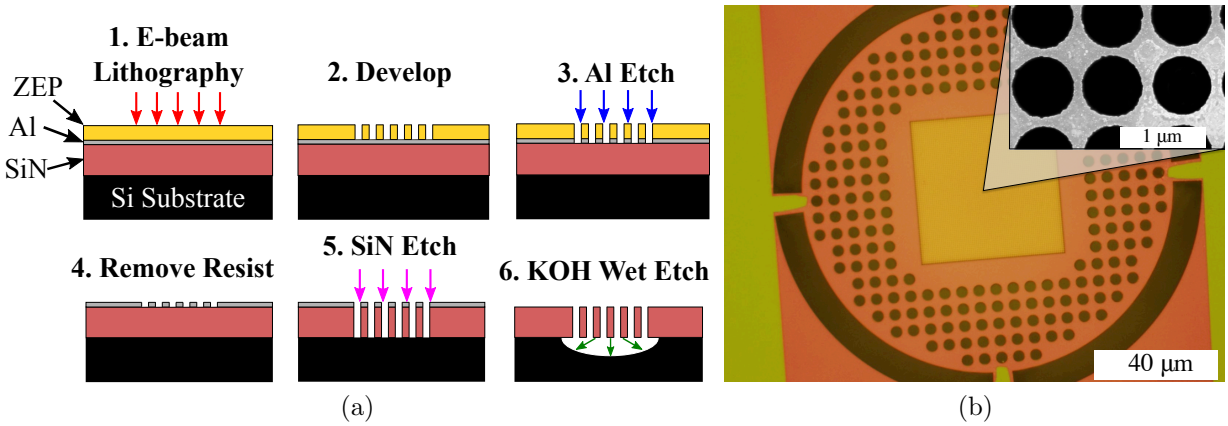

Figure 5.4: (a) Summary of the PC membrane fabrication process. E-beam lithography is used to create a pattern in ZEP520A resist, which is transfer to an Al hard mask followed by a SiN etch using RIE. The film is left free standing by undercutting the Si using a KOH wet etch. (b) The fabricated mirror template with the PC pattern that will be mounted onto the HCPCF tips to form a cavity. The inset shows a scanning electron microscope (SEM) image of the inner square of photonic crystal holes at the desired dimensions to produce maximum reflectivity at ∼852 nm.

1. **Remove PMMA**: The initial PMMA protective layer is removed by approximately 15 minutes of immersion in Remover PG at 80°C with sonication.

2. **Reactive Ion Etch**: The SiN film is etched to the design thickness using Reactive Ion Etching (RIE). The etch recipe uses a mixture of C_4F_8/SF_6 at 130/60 sccm, respectively, at 10 mTorr, 1000 W ICP RF power, and 30 W platen RF power. The platen temperature is set to 15°C. Before running the etching process on a sample, we condition the chamber by running the etch recipe for 45 minutes. The etch rate is determined by first etching the sample for 1 minute and measuring the film thickness before and after etching using filmetrics. Typical etch rates are 15-20 nm/min, which is then used to determine the total etch time required to etch the sample to the correct thickness.

3. **E-Beam Physical Vapour Deposition**: A 40 nm thick layer of aluminum is deposited onto the SiN film to act as a hard mask using e-beam evaporation.

4. **Spin Coat Resist**: We spin coat a 450nm thick layer of ZEP520A (Zeon Chemicals) positive e-beam resist onto the chip. A spin speed of 3000 rpm for 60 seconds is used

at a ramp rate of 3000 rpm/s. The chip is then baked for 2 minutes at 180°C.

5. **E-beam Lithography**: The hole pattern is written in the ZEP resist using e-beam lithography at 100 keV and developed using amyl-acetate for 90 seconds.

6. **Al Etching**: The e-beam pattern is transferred onto the aluminum mask using a two-step RIE process. The first step acts to break through any oxides formed and consists of a Cl_2/BCl_3 gas mixture at 10 sccm/40 sccm, respectively at 5 mTorr, 800W ICP power and 150W HF power for 8 seconds. The second step is designed to etch the Al and instead uses a Cl_2/BCl_3 gas mixture of 40 sccm/10 sccm, respectively, with a reduced HF power of 120 W for 10 seconds. We also include 50 sccm of N_2 in the recipe for both steps to reduce re-deposition of the Al by physical sputtering that can result in micro-masking effects by forming a passivation layer of aluminum nitride on the chamber walls [111].

7. **SiN Etch**: We again use RIE to now transfer the patterned template from the Al mask onto the SiN film by using the same SiN etching recipe as previously mentioned. A 1 minute etch is performed on a test SiN chip after the chamber is conditioned to measure the etch rate. The sample is then etched for the appropriate amount of time to achieve 150% of the film thickness.

8. **Remove E-beam Resist**: ZEP resist is removed by again exposing the chip to Remover PG immersed in an 80°C bath with sonication for $\sim$ 15 minutes.

9. **KOH Undercut**: We remove the underlying Si wafer substrate with a KOH wet etch, leaving the patterned silicon nitride structure as a free standing film. The KOH solution is set to 45% concentration and kept at 80°C and covered in order to prevent evaporation for long etch times. Typically the sample is kept in the KOH solution for $\sim$ 1 hour, followed by two 5 minute immersions in DI water for neutralization. Each neutralizing DI water bath is also held at 80°C to prevent the formation of crystals on the surface of the chip as the KOH is removed. Typically this is done by putting the three beakers (one KOH, two DI water) in a large water bath that is held at 80°C. After neutralization, the sample in put into two IPA solutions twice, for 5 minutes each, and gently dried from the side using N_2 gas. This is done to prevent the sample from breaking, which can become extremely delicate for certain pattern dimensions that leave only a small ($<$ 100nm) bridge of SiN material between holes. The sample is exposed to IPA prior to drying in an attempt to reduce the otherwise large surface tension of the surrounding DI water that would risk breaking the sample if immediately dried after the DI water exposure. The KOH etchant also

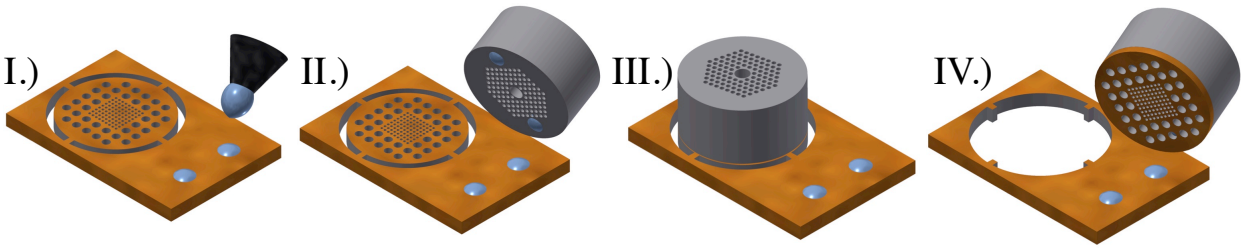

Figure 5.5: A diagram of the mounting technique, as described in the text.

acts to remove the Al hard mask. However, the samples that fabricated the templates onto the Norcada chips did not require KOH etch since they already had a window that left the SiN film free-standing. For these Norcada samples an Al wet etchant (Type A) is used instead to remove the Al hard mask after the SiN plasma etching.

We resorted to using a hard mask and a two-stage etching procedure because of the low selectivity between the etch rates of the ZEP and silicon nitride in the RIE process that would not allow us to etch through the entire SiN membrane before completely etching the ZEP mask. However, this may be avoided by using a thicker layer of e-beam resist, which is possible for thinner SiN membranes which require less etching.

Many alterations were made to the fabrication procedure in order to find a methodology that allowed for a reliable and repeatable recipe for producing the PC-patterned silicon nitride membranes. We summarize the various generations of samples in Appendix A to keep a record of the attempted processes and the issues that arose.

The final mirror template can be seen in Fig. 5.4b. The outer large trenches allow access to the underlying silicon wafer for the KOH solution to undercut the pattern, as well as to allow for easy removal of the mirror during the mounting procedure. The two dimensional lattice of PC holes is patterned in the central square of the structure shown and is large enough to cover the hollow core and photonic crystal regions of the fiber. The purpose of the larger holes surrounding the centre PC region is to aid in the presence of excess glue during the mounting of the membranes onto the fiber faces, which will be expanded upon in the next section.

5.2.2 Mounting Technique

We mount a pair of membranes onto the ends of a HCPCF segment using vacuum compatible UV-curable epoxy (Norland Optical Adhesive 88). The mounting technique is based

on the method developed by Shambat *et. al* [94]. It is summarized in Fig. 5.5 and consists of the following steps:

I. A sharp ($\sim 50\mu m$ diameter) tungsten probe is first used to deposit two small epoxy droplets near the mirror template. This is achieved by dipping the tip of the probe into a drop of epoxy and then tapping the tip onto the surface of the chip until droplets of the desired size are produced using a micromanipulator stage.

II. The fiber is then stamped onto a pair of the droplets, transferring the epoxy onto the glass cladding area of the cleaved face of one end of the HCPCF segment, again using a micromanipulator stage.

III. The HCPCF is then aligned and lowered onto the PC mirror template and the setup is flooded with UV light to cure the epoxy.

IV. The HCPCF is then retracted with the PC membrane attached. Depending on the intended application, the UV-curable epoxy can also be substituted by almost any two-component epoxy with a convenient curing time.

The trenches that form the edge of the template allow for easy separation of the structure from the remaining silicon nitride film thanks to the connecting narrow bridges. The large outer holes that surround the inner square of the photonic-crystal region allow the epoxy to leak through the film such that the membrane can sit flush against the fiber face. This also prevents excess epoxy from seeping into the PC region. Fig. 5.6 shows an SEM image of the PC membrane mounted onto the end of a HCPCF.

5.3 PC Membrane Reflectivity Measurements

Prior to mounting the PC membranes onto the fiber segment to form a cavity, the reflectivity of each fabricated template must be first measured. In Fig 5.7a we show the optical setup used to measure the reflectivity spectrum of each PC mirror. We used two methods of measuring the reflectivity: power measurements and cavity measurements, both of which are depicted in Fig. 5.7b showing a diagram of this reflectivity measurement setup, with the two methods differing by the optical pieces shown in the dashed boxes. We use a flip mirror to introduce a thermal white light source for imaging purposes with the use of another flip mirror directed to a CCD camera.

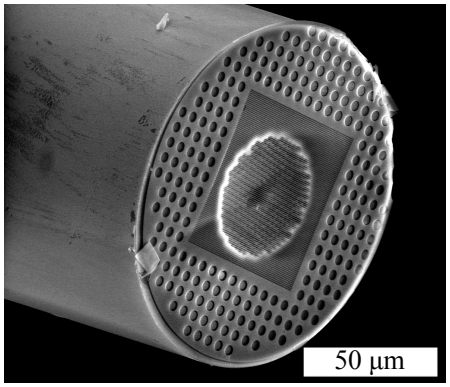

Figure 5.6: SEM image of the PC membrane attached to the tip face of a HCPCF segment. The centre square lattice of PC holes in the membrane covers the entire PC region of the underlying HCPCF.

For the power measurements, the sample is illuminated with either a laser or white light source by splitting the beam with a beam sampler and focusing through an objective where the reflected light is measured. The spot size is focused small enough to be completely localized within the PC region ($\sim 50 \times 50\mu$m). In order to obtain a spectrum using the laser source, a photodiode is used to measure the output power as the laser wavelength is stepped through in small increments. We also used a thermal white light source (and a supercontinuum source for later samples) in which we could obtain a one-shot measurement of the entire spectrum by using a spectrometer in place of the photodiodes.

For devices that were fabricated on the Norcada samples, we were also able to obtain a transmission spectra because of the presence of the complete window through the Si substrate, allowing us to collect the transmitted light. Since the power of the laser slightly fluctuates over time and at varying wavelengths, the measurements from the transmission and reflection photodiodes (A and B, respectively) are normalized to the power of the input light. This is done by taking a power measurement using an additional photodiode (C) placed at the transmitting side of the beam sampler (see Fig. 5.7b), and relating this power to the input power onto the membrane by calibrating it to the known splitting ratio of the beam sampler (as well as taking into account losses from the objective).

The second method for finding the reflectivity, as again depicted in Fig. 5.7b, was done by forming a cavity between the PC sample and a metallic mirror of known reflectance that is inserted behind the sample. The frequency of the input laser is swept as the reflectivity (photodiode B) is measured to obtain the characteristic Fabry-Pérot spectrum. The reflectivity for the PC mirror is found from fitting this spectrum using Eq. 2.2 for which

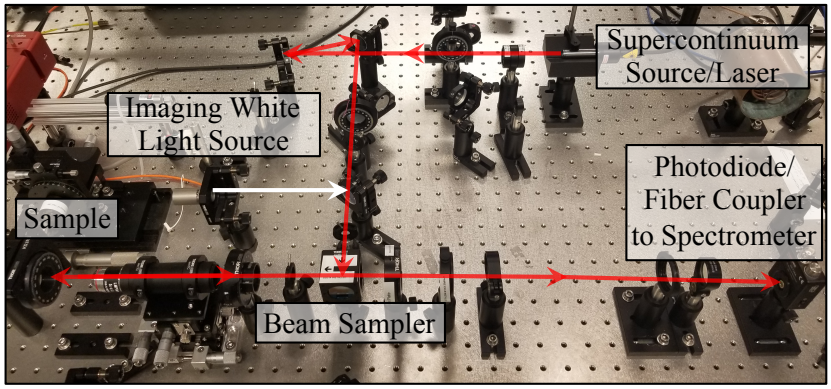

(a)

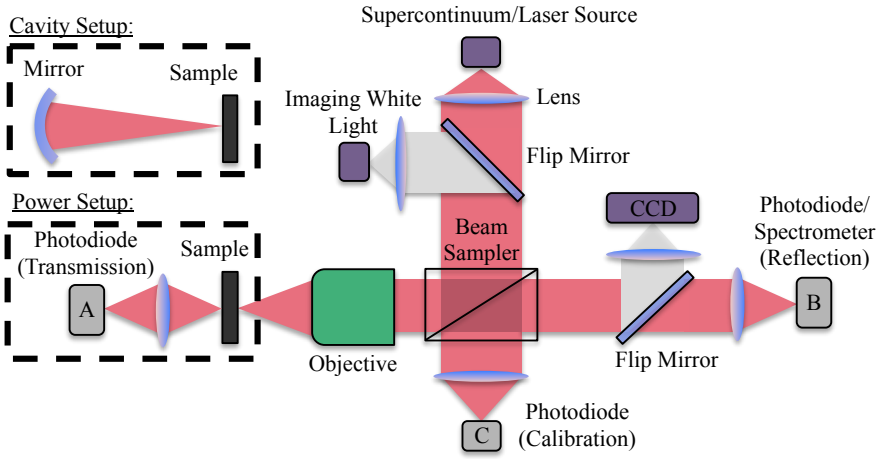

(b)

Figure 5.7: (a) Image of one of the versions of the reflectivity measurement optical setup. (b) Optical setup used to measure the transmission and reflectivity of the PC mirrors using power measurements and cavity measurements (shown in the dotted black boxes). Imaging of the sample is done using flip mirrors to introduce a white light source to illuminate the sample and a CCD camera is positioned to collect the reflected output light.

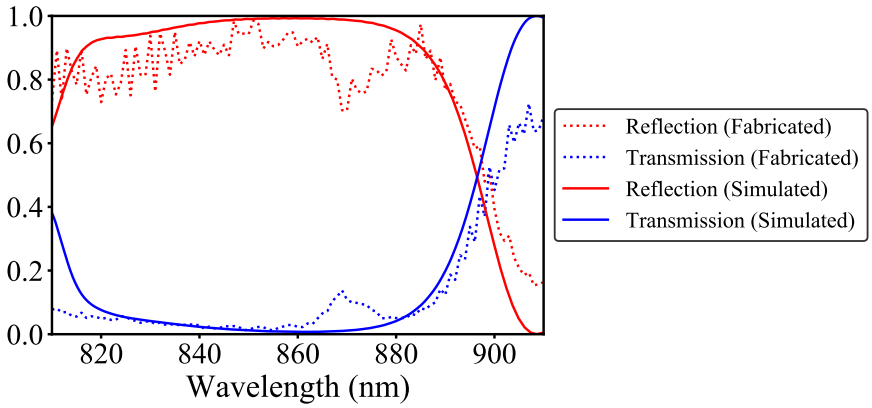

Figure 5.8: (a) Reflectivity of a PC pattern consisting of a square lattice of circular holes on Norcada samples (index 2.11) with thickness, $t = 500$ nm, lattice constant, $a = 817$ nm, radius, $r = 383$ nm using power measurements. The cavity measurements using a metallic mirror found a reflectivity of $\sim 92\%$ at 852 nm wavelength. Due to fluctuations in the laser power, the calibration is not stable and acts to create the noise seen in these reflectivity measurements.

$R_{cavity} = 1 - T_{cavity}$. However, since this method requires for the light to be transmitted through the sample to form the cavity with the metallic mirror, these measurements are only possible using samples that have an open window in the Si substrate (e.g. Norcada samples).

Fig. 5.8 shows the power measurements and simulation results for a PC membrane that was fabricated on a Norcada SiN sample with an index of 2.11. The cavity reflectivity measurements agreed with the power measurements, giving a reflectivity of $\sim 92\%$ at 852 nm. The spectrum seems to generally match the simulated results, however the overall reflectivity is lower. The dimensions of the fabricated PC pattern do not exactly match the desired design parameters, and so further refinement of the fabrication procedure may allow for higher reflectivities to be achieved.

However, the results of the simulations of the actual fabricated pattern dimensions still predicted larger reflectivities than were ultimately observed. A great deal of effort was directed towards determining the reasons for this non-negligible discrepancy. Unfortunately, we could not so far find satisfactory and conclusive answer to this question while pursuing several possible solutions. We initially investigated whether the silicon nitride film was absorptive, however we measured an insignificant amount of material attenuation using filmetrics and ellipsometry.

One of the main potential (and possibly the most likely) reasons for this loss in reflectivity, which will require further study, would be scattering either due to imperfections in the fabricated pattern or debris left on the samples. The Al mask seemed to leave the patterned holes with slightly coarse walls rather than smooth circles, as well as caused for non-uniformities and roughness of the film itself, even after removal of the mask. In addition, debris was commonly left on the chips from the metal etch and wet etching procedures. Due to the delicate nature of the films, cleaning of any debris from the samples (such as Piranha cleaning) proved to be difficult. In particularly, the membranes have a high risk of breaking after the wet etching process which leaves the films free-standing.

The other area that may result in discrepancy between measured and simulated results is the method of reflectivity measurement, which will also require additional inquiry. The initial results (such as in Fig. 5.8) utilized a Ti:sapphire laser to sweep over a frequency range and take power measurements with a photodiode. However, this laser suffered from power fluctuations over time and thus made calibration slightly unreliable. Later measurements used a supercontinuum source to provide a one shot measurement, nonetheless, calibrate to an initial input power was still not perfect. Another issue that arose during the reflectivity measurements was that the illuminating Gaussian spot size ($\sim 40\mu$m in diameter) may have been too large, allowing for some light to be scattered at the pattern edges. The low field at the outer edges of the pattern should have ideally minimized any loss of input power, especially in later samples that used a larger PC pattern size ($\sim 150\mu$m $\times 100\mu$m), which lead us to believe this conceivable concern should not have been a major issue.

5.4 Fiber-Integrated Cavity Measurements

After the PC membranes are mounted onto the HCPCF segment to form a cavity, its Fabry-Pérot spectrum must be measured. The fiber cavity was mounted onto a piece of silicon wafer with a lithographically defined clamping structure [70] and the transmission spectra was measured using the optical setup shown in Fig. 5.9a, which is similar to the setup that measured the PC reflectivities described in the previous section.

The light from a Ti:Sapph laser is aligned onto the fiber core using a 10$\times$ microscope objective and the transmitted light is coupled into a single mode fiber (SMF) before being detected by a photodiode. A 10$\times$ objective provides a coupling beam size that is close in size to the supported mode of the HCPCF. The SMF provides a spatial filter to remove any undesired higher order modes that may have been excited by the initial light coupling

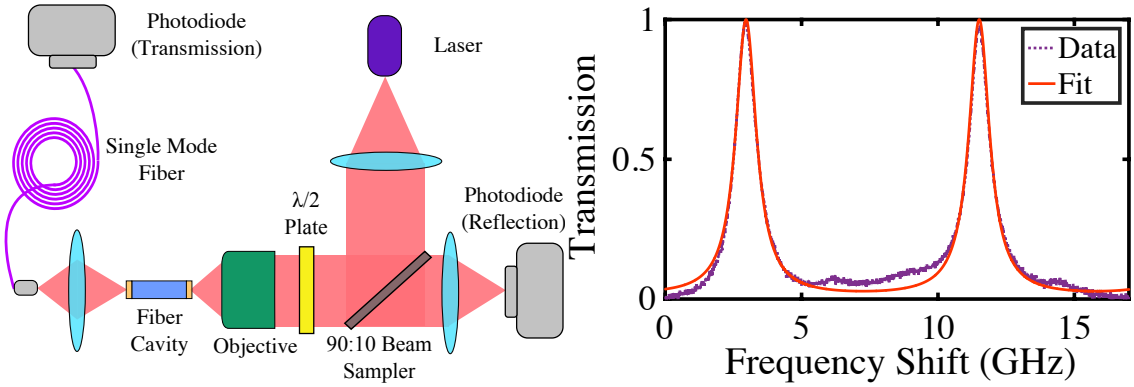

(a) (b)

Figure 5.9: (a) Optical setup used to measure the transmission and reflectivity spectrum of the fiber-cavity. (b) The transmission spectrum of the fiber-cavity found by scanning the input light frequency at a centre wavelength of 852nm. The normalized transmission data (purple dotted line) is fitted to Eq. 5.1 (orange solid line).

into the cavity so that the spectrum arising only from the fundamental mode of the fiber cavity can be observed.

In addition, a half-wave plate (HWP) is used to align the polarization of the input light with the slow and fast axis of the birefringent HCPCF. By rotating the polarization of the coupling light, the two fundamental modes of the fiber can be excited with varying contributions from both. Each mode produces distinct Fabry-Pérot peaks that overlap each other which are produced by the modes experiencing different propagation constants in the fiber. By matching the polarization of the light with the birefringent axis of the fiber, almost complete suppression of one of the polarization modes can be achieved, resulting in the observation of only a single set of Fabry-Pérot peaks, as shown in Fig. 5.9b, corresponding to one of the fundamental modes.

The fiber cavity transmission spectrum shown in Fig. 5.9b is plotted for frequency shifts with respect to 852 nm and can be fitted to the normalized transmission intensity, T, of a Fabry-Pérot resonator as discussed in Section 2.1:

$$T = \frac{I}{I_0} = \frac{1}{1 + \left(\frac{2\mathscr{F}}{\pi}\right)^2 \sin^2\left(\frac{\pi\nu}{FSR}\right)}, \tag{5.1}$$

where ν is the frequency of the incident light. The two fitting parameters that are determined from this spectrum are the finesse, $\mathscr{F}$, and the free spectral range, $FSR = \frac{c}{2nL}$,

where c is the speed of light, L is the length of the cavity, and n is the effective refractive index of the cavity medium. The finesse and the FSR then determine the quality factor of the resonator, $Q = \frac{\mathscr{F}}{FSR}\nu$ (Eq. 2.15).

In addition to quantifying the performance of our cavity, measuring the finesse also allows us to evaluate the power reflectivity, R, of the photonic-crystal mirrors. From Eq. 2.3 the finesse is determined by the round trip loss in the electric field, r, such that

$$\mathscr{F} = \frac{\pi\sqrt{r}}{1-r} \tag{5.2}$$

in which each round trip field loss is $r = \sqrt{R_1}\sqrt{R_2}e^{-\alpha d}$, for mirror power reflectivities, R_1 and R_2, cavity length, d, and propagation loss, α. Assuming identical mirrors, $R_1 = R_2 \equiv R$, and a round trip distance of twice the cavity length, the round trip loss becomes

$$r = Re^{-\alpha 2L} \tag{5.3}$$

For the case of the HC-800-02 fiber used to assemble the cavity, this loss is $\sim$ 150dB/km for wavelengths around 850nm. Using the fitted values for FSR and $\mathscr{F}$ from the cavity transmission spectrum, the reflectivities of the cavity PC mirrors can then be calculated using Eq. 5.2 and 5.3, as shown in Fig. 5.10a, giving a maximum $R \sim 76\%$ at 845nm.

The reflectivities of our fabricated PC membranes were significantly below the design prediction. The fabricated PC pattern sizes were a ≈680 nm, r ≈260 nm, and t ≈363 nm, while the optimal design was found to be a=680 nm, r=297 nm, t=369 nm for an input Gaussian beam of 2.75μm waist radius. Refinements to our fabrication procedure should allow us to produce mirrors with much higher reflectivities and, consequently, cavities with increased finesse, as reflectivities exceeding 99% have been demonstrated [22], albeit for mirrors designed for beams with larger waist of $\sim$ 50μm. The currently fabricated mirrors form fiber cavities with maximum $\mathscr{F} \approx 12$ and Q-factor of about 5×10^5 (Fig. 5.10b). In Section 5.6 we will discuss the particular cavity performances and that would be required for various coupling regimes.

5.5 Cavity Tuning

Fig. 5.11b shows tuning of our cavity by changing its temperature. As the temperature is altered, the thermal expansion and contraction of the fiber material which acts to modify the effective length of the cavity, which of course dictates the free spectral range of the resonant peaks. Since a given resonant peak, ν_0 is simply an integer, q, of the FSR

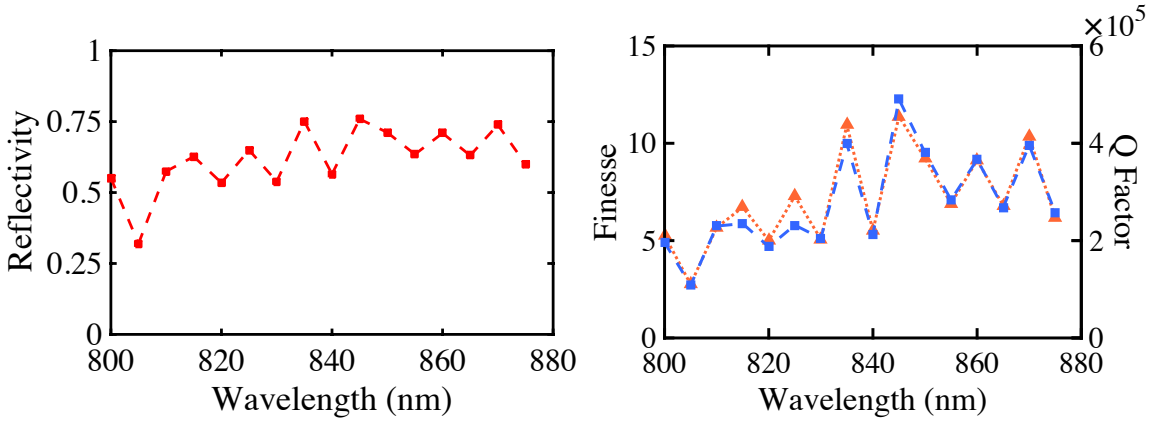

(a) (b)

Figure 5.10: (a) The reflectivity of the individual PC mirrors on the fiber tips extracted from the transmission spectrum fit. The parameters of the PC membrane measured from its SEM image were a ≈680 nm, r ≈260 nm, and t ≈363 nm. (b) Finesse (orange triangles) and Q factor (blue squares) of the fiber-cavity for a range of wavelengths. The finesse and FSR are found by fitting Eq. 5.1 to the cavity transmission spectrum and the Q factor is then found using the relationship $Q = \frac{\mathscr{F}}{FSR}\nu$.

($\nu_0 = q$FSR), the shift in this resonant peak frequency, $\Delta\nu_0$, between two cavity lengths, L and L', is then

$$\Delta\nu_0 = q\frac{c}{2}\left(\frac{1}{L} - \frac{1}{L'}\right) \tag{5.4}$$

For this measurement, the silicon wafer piece holding the fiber cavity was mounted onto a thermoelectric element. As the cavity temperature is changed, the thermal expansion changes the length of the HCPCF, L, by about 5-10 nm per °C, causing the cavity resonances to shift by $\Delta\nu_0 \sim 0.2$ GHz per °C at the measured optical frequency ranges. In practical applications, the cavity can thus either be stabilized by keeping it at a specific temperature or locked to a reference frequency using temperature tuning as part of the feedback loop.

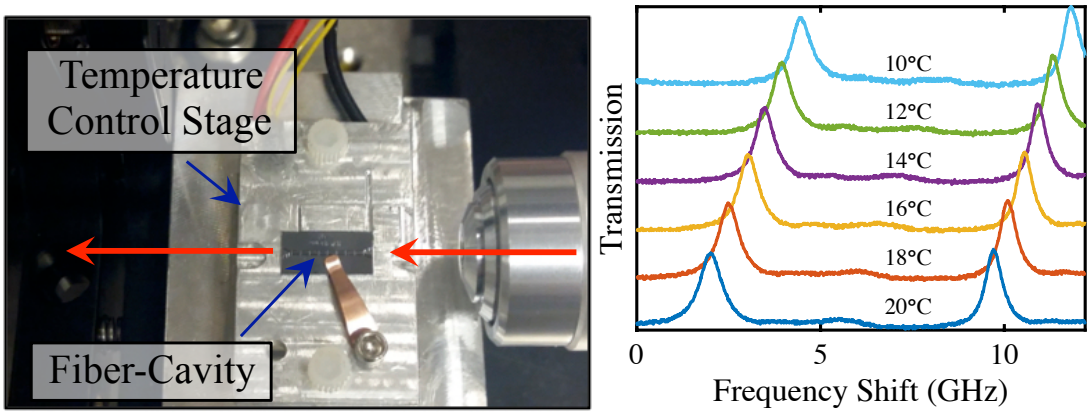

(a) (b)

Figure 5.11: (a) A temperature stage is used to tune the temperature of the fiber cavity which acts to shift the resonant Fabry-Péro peaks. The red arrows represent the coupling input light from the objective into the fiber cavity. (b) Normalized transmission spectrum of the cavity at varying temperatures. The resonant peaks are shifted ~ 0.2 GHz per °C.

5.6 PC Membrane-Based Cavity Regimes

As discussed in Section 3.3, two important coupling regimes are the strong coupling and high cooperativity regimes. Unfortunately, the fabricated fiber cavities discussed in the previous sections of this chapter do not yet meet the criteria to be in either of these regimes. In Figs. 5.12a we plot the cooperativity, $\eta = \frac{4g^2}{\kappa\Gamma}$, at varying PC mirror reflectivities and cavity lengths. From Eq. 3.81, we can see that the cooperativity is species independent and these calculations hold for coupling to any atom in a cavity system.

Additionally, the coupling strength is affected by the mode volume and thus the cooperativity becomes inversely proportionate to the mode volume ($\eta \propto \frac{1}{V_{mode}}$). It can be seen that as the cavity length is decreased, the cooperativity becomes larger, and a minimum PC mirror reflectivity of ~ 0.996 is required to reach high cooperativity, $\eta > 1$. The current fiber cavity devices produce a cooperativity of $\eta \sim 10^{-2}$, which of course does not meet the high cooperativity requirement. However, our current MOT setup allows for a loading efficiency of atoms into a HCPCF of about $N_a \sim 10^4$ atoms, and so in theory, our cavity may be able to reach the collective cooperativity regime in which $N_a\eta \sim 10^2 \gg 1$ which may allow for our system to exhibit certain phenomena such as superradiance.

Fig. 5.12b indicates the region in which the strong coupling regime is possible with these

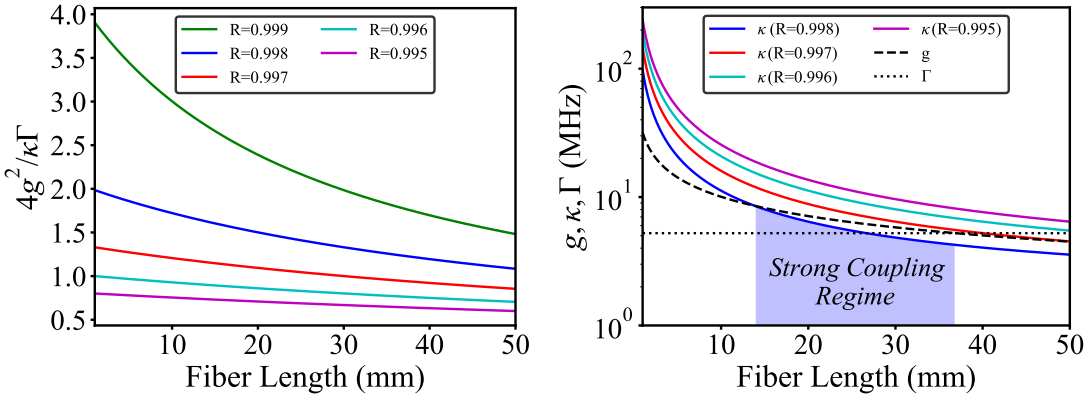

(a) (b)

Figure 5.12: (a) Single atom cooperativity for the fiber cavities discussed in this chapter with varying lengths. High cooperativity occurs for $\frac{4g^2}{\kappa\Gamma} > 1$. (b) Plot showing the relationship between g, κ, and Γ at varying cavity lengths for cesium atoms in a fiber cavity. Strong coupling regime occurs for $g > \kappa, \Gamma$, which is depicted as the shaded blue region for a mirror reflectivity of 0.998. Mirror reflectivities lower than this cannot reach the strong coupling regime, regardless of cavity length. [44]

fiber cavity devices. Remarkably, for a given PC membrane reflectivity (which determines the cavity decay rate), the strong coupling regime is only achievable for a certain range of cavity lengths. Similar to the results found in Section 4.5, this effect is caused by contesting effects as the cavity length is altered. At smaller lengths, the cavity has a smaller mode volume allowing larger coupling constants, however photons are lost through the larger number of bounces off the non-unity mirrors per time. Larger lengths, on the other hand, instead attributes the photon a larger portion of time traversing the fiber, which can have a relatively low attenuation compared to a single reflection off a PC membrane.

The blue shaded region depicts the strong coupling regime for a mirror reflectivity of 0.998, which approximately represents the lower limit of reflectivity that is required to allow for strong coupling, as evident by the plot where both $g > \kappa$ and $g > \Gamma$. This slightly more stringent condition compared to the requirements for high cooperativity is of course again not possible with the currently fabricated fiber cavity that have only $\sim 80\%$ effective PC mirror reflectivities. However, recently it has been demonstrated that PC membranes can be fabricated with a reflectivity of ~ 0.9995 [22], and so with improved fabrication techniques both the high cooperativity as well as the strong coupling regimes

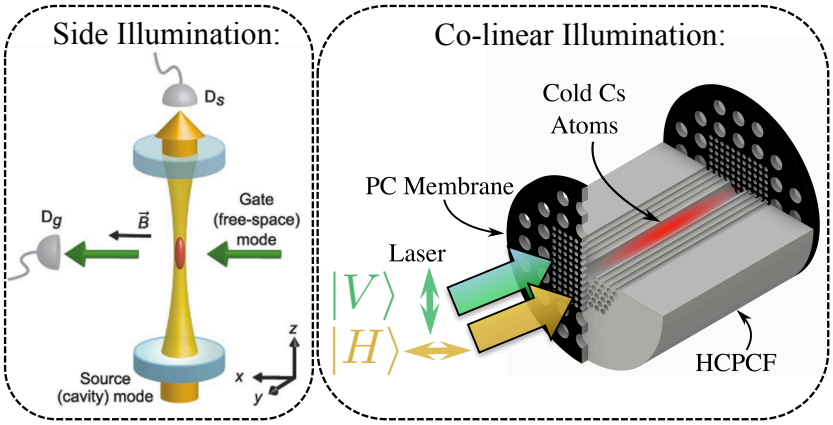

Figure 5.13: Previous cavity systems require the free space and cavity illumination signals to be perpendicular to each other, resulting in side illumination of the atomic cloud along the low optical depth axis [Image source: [21]]. The co-linear illumination scheme provided by the polarization dependent fiber-integrated cavity can allow for both the free space and cavity sources to be sent along the high optical depth axis of the atomic ensemble by setting the correct polarization of the each signal.

may be possible in these devices.

5.7 Polarization-Selective Membranes

As alluded to earlier in this chapter, another main beneficial feature of using photonic crystal membranes as mirrors is that they can be designed to be polarization-selective (i.e. completely reflective for one polarization of input light and fully transmissive for the orthogonal polarization). This allows for all light signals (e.g. probe and gate photons) to be sent along the optical axis of the fiber, and all interactions with the atoms can be set to occur either within a cavity or effectively in free space simply by choosing the appropriate polarization of the input light. This geometry provides a means of co-linear illumination in which all input sources are sent along the longitudinal axis of the atomic cloud and thus will have largest optical depth. This is in contrast to other cavity systems such as Bohnet et al. [15] and Chen et al. [21], as illustrated in Fig. 5.13. These systems require the free space illumination to be perpendicular to the axis of high optical depth of the cloud, and thus reduce the total optical depth achieved for the signal illuminated from the side.

In order to create a polarization-selective spectrum, the type of broken symmetry that

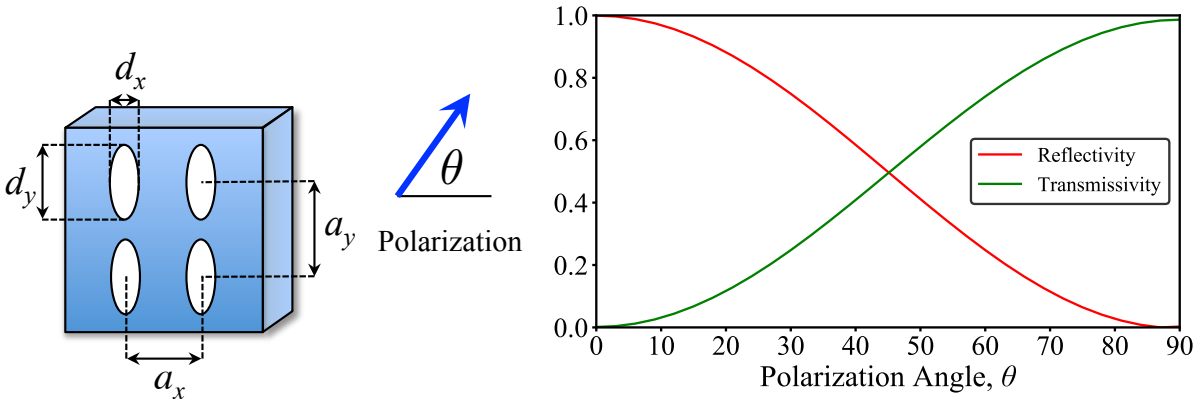

(a) (b)

Figure 5.14: (a) Unit cell of a polarization-selective photonic crystal pattern. The linear symmetry is broken by using a rectangular lattice and elliptical holes. (b) FDTD simulations show complete transmission and complete reflectivity at orthogonal linear polarizations using a plane wave source ($a_x = 781$ nm, $a_y = 560$ nm, $d_x = 504$ nm, $d_y = 396$ nm).

the PC pattern exhibits needs to reflect the type of polarization dependence. For example, if the mirror is to be selective for right and left handed circular polarization, the PC pattern needs to break chiral symmetry. In this work, we develop a mirror that has linear polarization selectivity, and thus the PC pattern must break x/y symmetry. We decided to employ a pattern composed of a rectangular lattice (instead of a square lattice) of elliptical holes (instead of circular holes), as shown in Fig. 5.14a.

This pattern, of course, has a larger number of degrees of freedom than the previously discussed symmetric pattern (non-polarization selective), and so again optimization algorithms were used to find pattern dimensions that maximized the difference in reflectivities at orthogonal polarizations. Using a plane wave source, it is possible to design a mirror with near unity reflectivity and transmission for orthogonal polarizations, as shown in Fig. 5.14b. Unfortunately, using a Gaussian mode source can again drastically alter the spectrum of the PC membranes, requiring a more extensive effort to find parameters that act to have a large polarization selectivity by again using particle swarm optimization algorithms.

Similar to the fabrication challenges previously discussed, one main requirement for these patterns to be practical to fabricate is to set a lower limit for the material bridge

size between two neighbouring holes. If this bridge size is too small, the membranes risk breaking during the fabrication procedure. Given this restrained parameter space, we obtained a heuristic result that gave a polarization dependence with a Gaussian source while keeping the dimension ratios reasonable. The optimal pattern dimensions found were for a membrane thickness of $t = 342$ nm, x and y lattice constants of $a_x = 676$ nm and $a_y = 444$ nm, respectively, and x and y hole diameters of $d_x = 430$ nm and $d_y = 364$ nm, respectively, giving a reflectivity of $> 99\%$ and $\sim 11\%$ at the two orthogonal polarizations.

5.7.1 Polarization Dependent Reflectivity Measurements

To fully characterize the spectrum of the polarization-selective PC membranes, it is not merely enough to take an absolute reflectivity, as is the case for the non-polarization dependent mirrors. Instead, we need to find each of the four Jones matrix elements describing the input and output x/y polarization intensities, $I_{in,x/y}$ and $I_{out,x/y}$, respectively. The Jones matrix acts to relate the input intensities to the output reflected intensities such that

$$\begin{bmatrix} I_{out,x} \\ I_{out,y} \end{bmatrix} = \begin{bmatrix} R_{xx} & R_{xy} \\ R_{yx} & R_{yy} \end{bmatrix} \begin{bmatrix} I_{in,x} \\ I_{in,y} \end{bmatrix} \tag{5.5}$$

It can be seen from the definition in Eq. 5.5 that each Jones matrix element has a different physical meaning. The R_{xx} and R_{yy} elements represent the direct coupling for an input polarization to the reflected output of the same polarization state. Conversely, R_{xy} and R_{yx} represent the cross coupling between the two polarization states that describes the amount of the reflected polarization that is orthogonal to the input polarization state. A perfectly polarization-selective mirror will thus have Jones matrix elements of $R_{xx} = R_{xy} = R_{yx} = 0$ and $R_{yy} = 1$.

Each of the Jones matrix elements can be measured using the optical setup shown in Fig. 5.15a. We define the z direction as the axis of propagation of light, the x direction as in the plane of the figure, and the y direction as perpendicular to the plane of the figure. The source light, either from a laser of supercontinuum source, is initially polarized in the x direction and half-wave plate (HWP) A is then used to control of the input light polarization. The light can be set to be polarized in either the x or y by setting the angle of the HWP, with respect to the x direction, to 0° or 45°, respectively (since of course the HWP will rotate the polarization of light twice this angle).

To measure each polarization of light, an x polarized filter is used in which HWP B controls which polarization of light is measured by the photodiode by again using the

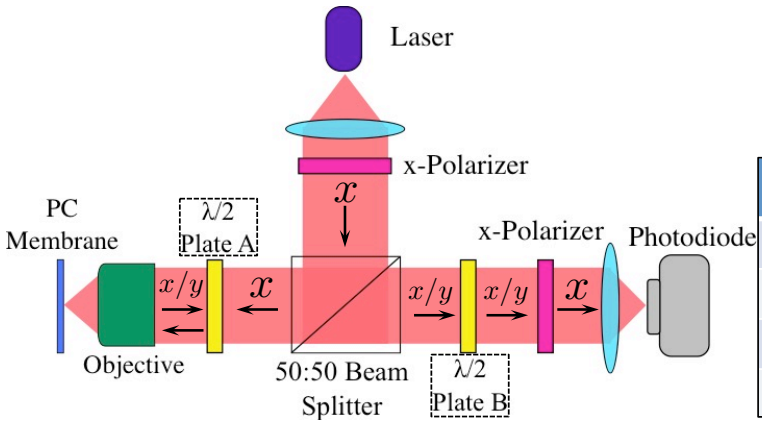

(a)

$\lambda/2 : A$	$\lambda/2 : B$	Measure
0°	0°	R_{xx}
0°	45°	R_{yx}
45°	0°	R_{yy}
45°	45°	R_{xy}

(b)

Figure 5.15: (a) Optical setup used to measure the four Jones matrix elements in Eq. 5.5. Half-wave plate A is used to set the polarization of the input light and half-wave plate B sets the polarization of the measured reflected light. (b) A summary table of the four settings of the half-wave plates A and B and the corresponding Jones matrix element that is measured.

appropriate setting of either 0° or 45°. The table in Fig. 5.15b provides a summary of the HWP settings used to measure the corresponding Jones matrix elements. It should be noted that if HWP A is set to 45°, it will rotate the input light to y polarized, but will also again rotate the x and y polarized reflected light to y and x, respectively. This is why the HWP B set to 0° would then measure the y polarized reflected light, and the x polarized reflected light will be measured with HWP B set to 45°.

The fabricated polarization dependent PC membrane shown in Fig. 5.16a had approximate pattern dimensions of $t = 342$ nm, $a_x = 676$ nm, $a_y = 444$ nm, $d_x \approx 396$ nm, and $d_y \approx 352$ nm. Primarily, the hole diameters are the main parameters that are not the exact optimal pattern dimensions that were found using the FDTD simulations due to fabrication challenges as previously discussed. However, there is still a large polarization dependence as found by the measured Jones matrix elements shown in Fig. 5.16b, using a supercontinuum white light source. The maximum extinction coefficient of $\frac{R_{yy}}{R_{xx}} \approx 23$ was found to be at a wavelength of 820 nm.

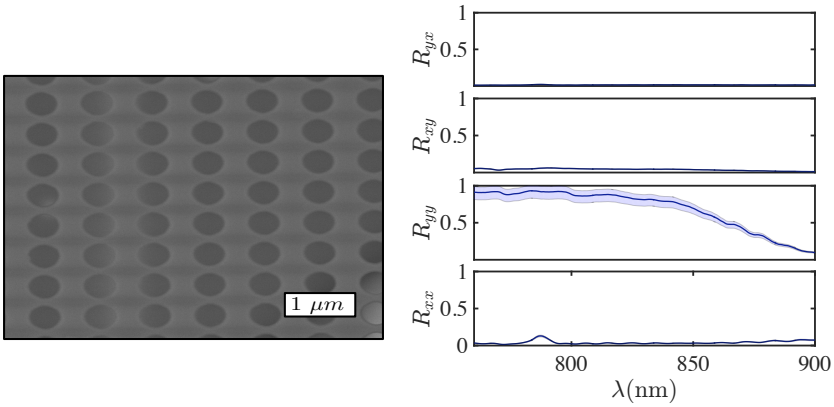

(a) (b)

Figure 5.16: (a) SEM image of a rectangular lattice of elliptical PC pattern resulting in a polarization selective mirror (with pattern dimensions $t = 342$ nm, $a_x = 676$ nm, $a_y = 444$ nm, $d_x \approx 396$ nm, and $d_y \approx 352$ nm). (b) Jones matrix elements for the fabricated polarization dependent PC mirrors. The largest extinction ratio was found to be $\frac{R_{yy}}{R_{xx}} \approx 23$ at 820 nm (with $R_{yy} \approx 93$ and $R_{xx} \approx 4$).

5.7.2 Mounting Polarization-Selective Mirrors

The construction of a polarization dependent fiber-integrated cavity using the fabricated asymmetric PC patterned membranes poses several additional challenges when mounting the PC mirrors to the fiber segments. Mainly, the axis of the two PC mirrors must be aligned with each other, as well as with the birefringent axis of the HCPCF. This slight birefringence in the fiber is a result of the asymmetric patterning of the PC region in the cladding of the fiber, as well as any additional external stresses that may be applied to the fiber, such as that from the various mechanism that hold the fiber to the sample chip (e.g. the clamping structures or epoxy droplets).

A preliminary procedure was used to mount the polarization dependent mirrors to the fiber while addressing these new alignment concerns. The first step is to determine the angle of the birefringent axis of the HCPCF, which was done using the optical setup shown in Fig. 5.17. The input light that is coupled to the fundamental mode of the HCPCF segment is initially polarized horizontally in the plane of the figure. HWP A is now used to rotate the input light to a given angle, 2θ, with respect to the horizontal plane of the figure (thus the axis of the HWP is set to θ). HWP B is then also set to an angle of θ such that it would rotate the light from 2θ back to the horizontal x direction in the absence of

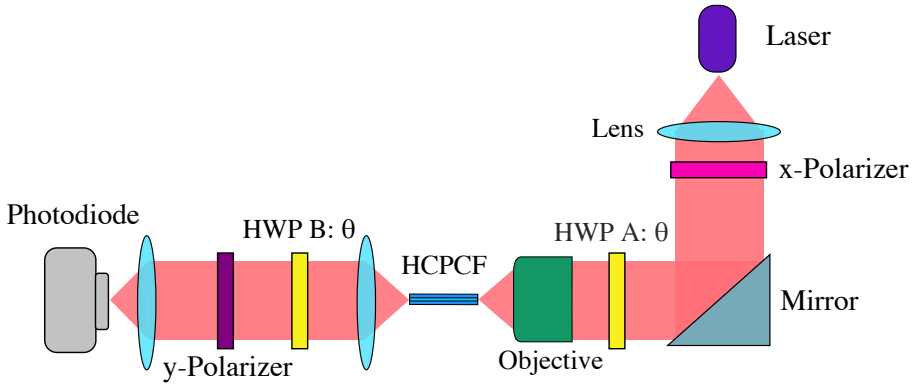

Figure 5.17: Optical setup used to measure the birefringent axis of the HCPCF. Both half-wave plates A and B are set to an angle of θ with respect to the horizontal and rotated until the power at the photodiode is minimized, thereby determining the angle of either the slow or fast axis in the fiber.

the HCPCF. This output light is then passed through a polarizer oriented in the vertical y direction perpendicular to the plane of the figure with the power being measured by a photodiode.

When the coupled light into the HCPCF is not polarized to either the slow or fast axis of the fiber, the output light from the fiber will be elliptically polarized, and thus some fraction of the total power will be measured by the photodiode. However, when the polarization of the coupling light is set to either the slow or fast axis of the fiber, the output light will be linearly polarized and at the same initial angle as the input light (assuming the axis does not rotate appreciably in the length of the fiber segment). HWP B will then act to rotate this light back to the horizontal and thus the power measured by the photodiode after the polarizer will be minimal. The birefringent axis is the then found by stepping through different θ angles until the power measured at the photodiode is minimized at θ_{min}, indicating that the axis of the fiber is at an angle of $2\theta_{min}$.

Each mirror must then be mounted with respect to the measured angle of birefringence in the fiber. The method does not distinguish which axis of the fiber that was found, slow or fast. However, the PC mirrors only need to be aligned to one of the birefringent axis of the fiber and thus this information is not required. The mounting of the polarization dependent mirrors is done by attaching the chip with the fabricated PC templates to a rotation mount. The entire template is simply rotated to the appropriate angle with respect to the HCPCF axis before performing the mounting procedure previously described in Section 5.2.2 for each of the two cavity PC mirrors.

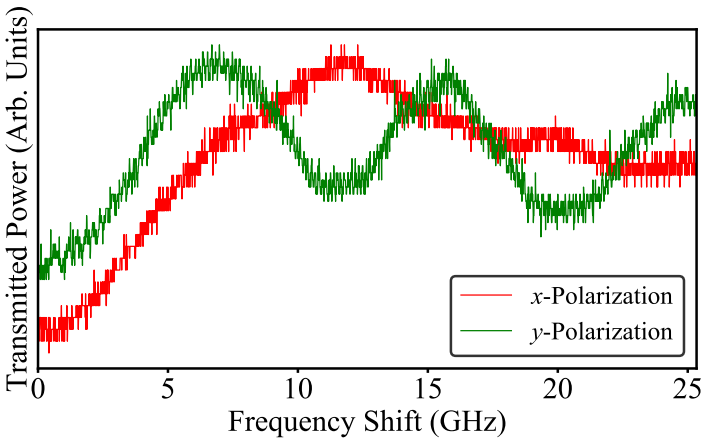

Figure 5.18: Spectrum of a polarization-selective fiber-integrated cavity using asymmetric PC patterned membranes acting as mirrors. Background noise is still included as the signal is not filtered through a single mode fiber.

5.7.3 Preliminary Polarization-Selective Fiber-Cavity

Two separate polarization dependent PC mirrors were mounted onto a HCPCF segment, as discussed in the previous section. We show here only preliminary data of the resulting polarization-selective cavity in Fig. 5.18. It is clear that there is a dependence on the transmission based on the input polarization. This is shown through the fact that there are several Fabry-Pérot peaks present in the transmission of the y-polarized light, while the peaks are mostly absent for the orthogonal x-polarization. However, this data is still noisy and the background power was not filtered by coupling the transmitted light into a single mode fiber (SMF) to eliminate other higher order modes that may be excited.

Fitting the Fabry-Pérot spectrum again to Eq. 5.1 we find that the effective reflectivity of each of the cavity mirrors is $\sim 30\%$. This is of course much lower than the measured reflectivities of the membranes before being mounted on the fiber (Fig. 5.16b). This drastic drop in effective reflectivity may, at least in part, be accounted for by the fact that the mirrors were not perfectly aligned to each other, and in fact were $\sim 3^\circ - 6^\circ$ misaligned. In addition, the mirrors themselves were also not aligned with the birefringent axis of the fiber, which would result in partial cross coupling into the transmissive polarization each round trip. In order to achieve a higher finesse and greater polarization selection in the cavity these alignment issues in the mounting procedure must be resolved.

5.8 Conclusion and Future Work

In conclusion, we have demonstrated a novel type of fiber-integrated cavity created by attaching a pair of perforated photonic membranes acting as dielectric metasurface mirrors to the tips of a HCPCF piece. As the holes can allow injection of gases into the fiber, we expect this cavity to open paths to a broad range of exciting new applications. Even with the currently demonstrated relatively low finesse of ∼12, the cavity can be used to improve the performance of fiber-integrated gas lasers [74] and frequency references [116].

The tight confinement of photons over macroscopic distances in the HCPCF cavity, not available in confocal cavities, could potentially enable novel regimes of the recently demonstrated super-radiant lasers [15] and spin-squeezing measurements [62, 52], as well as offer an alternative to tapered fibers in exploring multi-mode strong-coupling cavity quantum electrodynamics (cavity QED) systems [91].

While not yet confirmed through numerical simulations, the membrane should allow the loading of laser-cooled atoms into the HCPCF. One area that will require further investigation is the effect of the Casimir-Polder potential that acts to attract the atoms to the walls of the PC holes as they fall through the holes. We show a one-dimensional plot of this $-\frac{C_4}{r^4}$ potential (with $C_4 = 8.2 \times 10^{-56} Jm^4$ [63, 120]) in Fig. 5.19 across a single PC hole with a radius of 250 nm, in which the blue shaded regions indicates the silicon nitride walls. It is evident that this force may become important near the walls of the PC holes, however, since the atoms will have a downward velocity as they approach the holes they may be able to escape this potential. A full numerical simulation of the atoms falling through the membrane will need to be performed in order to fully characterize the loading efficiency through such perforated membranes. Atoms passing through a PC membrane with a hole radius of 170 nm has recently been demonstrated [61], suggesting our proposed scheme of loading atoms through the membranes and into the HCPCF is plausible.

With improved reflectivities of the fabricated membranes, a cavity with high single-photon cooperativity [107] could be realized in the very near future [7] and pave the way toward tantalizing new studies combining coherent control techniques of light propagation, such as slow light and light storage, with cavity QED phenomena in atomic ensembles. This fiber-based cavity also allows for the potential of on-chip integration by the use of lithographically fabricated mechanical structures forming fiber couplers [70].

Our preliminary data showing a dependence of the cavity spectrum on the polarization of the input demonstrates the potential for a polarization-selective fiber-integrated cavity using asymmetric PC mirrors [66, 20]. Before these cavities can be fully realized, the challenges of mounting the mirrors with the correct orientation with respect to each other

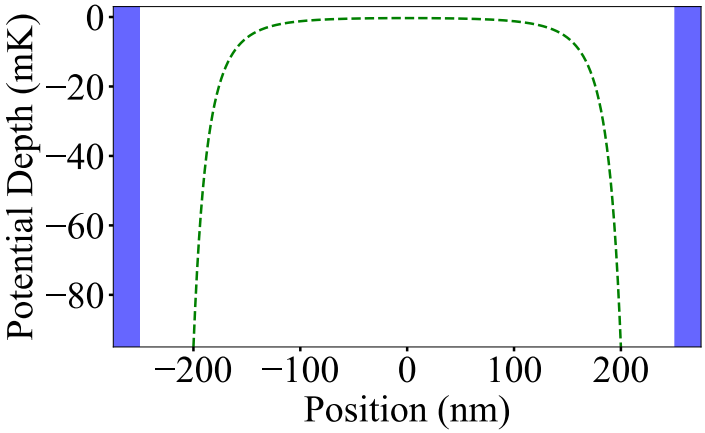

Figure 5.19: Plot of the attractive Casimir-Polder potential across a single photonic crystal hole of radius 250 nm. The walls of the silicon nitride membrane are shown as the blued shaded region. We use a $-\frac{C_4}{r^4}$ potential from the dielectric surface with $C_4 = 8.2\times10^{-56} Jm^4$ from [63, 120].

and the birefringent axis of the HCPCF must first be addressed in a controllable and repeatable way. Future efforts to solve these problems may be to incorporate the mounting technique directly with the optical coupling scheme used to find the slow and fast axis of the fiber. By positioning the PC membranes freely near the end of a fiber segment, the reflected light from the fibers may be monitored as the PC membranes are rotated in order to determine the optimal angle for attaching the mirrors.

In addition to this work, we have also successfully designed and fabricated mirrors sensitive to the left/right handedness of circularly polarized input light. This work could also lead to forming a free space cavity that have circular polarization-selectivity.

A polarization selective cavity, such as the ones discussed in this chapter, may be used to implement vacuum-induced transparency (VIT) [106] in a high-optical-depth ensemble or to improve the performance of the recently demonstrated all-optical transistor controlled by a single photon [21] by simplifying its geometry and allowing the 'gate' and 'source' fields to both propagate along the axis of the cavity. Novel schemes for optical switching that may be implemented in such a cavity will be discussed in the next chapter.

Chapter 6

All-Optical Single Photon Switching

The focus of this chapter will be on the specific applications of a cavity QED system for the purpose of all-optical single photon switching. These devices could provide seamless integration with existing telecommunication networks to allow for optical computation and communication. The speed and efficiency of classical computation in such systems could potentially be enhanced by the use of optical transistors, by enabling faster signals and by the avoidance of resistive heating [71]. In addition, if the limit of single photon switching can be reached, further applications can be found in quantum information, computation and key distribution protocols [17].

Electromagnetically induced transparency (EIT) has previously been utilized to demonstrate all-optical switching with a few hundred photons [5]. Cavity QED systems have also been able to demonstrate $\sim 20\%$ two-photon attenuation [38, 106, 114] and have performed switching of the cavity transmission with a single atom [110]. More recently, a single photon gate optical switch has been shown using a four-level scheme [21].

One possible avenue for creating optical switching is to use high finesse cavities to facilitate the nonlinearities that are required to produce the effective photon-photon interactions between gate and source. In that spirit, the theoretical work done here could potentially be applied to any type of cavity that can reach the strong coupling regime. However, as we will see, the polarization dependent PC membrane fiber-cavities in Chapter 5 make them particularly suited for the photonic switches discussed here, assuming they can be fabricated with a high enough finesse.

There are two main types of optical switches that will be discussed in this chapter. We begin by describing a four-level atom scheme with a switching field that controls the transmission of probe photons acting as a source field for the optical transistor. The later

sections will describe a simple three-level scheme with a vacuum coupling cavity, with the switching of a free-space probe field provided by the insertion of a single photon into the cavity mode. These schemes can be easily integrated into the polarization dependent fiber-cavities discussed in this thesis by setting all probe and switch fields that do not require the presence of a cavity to the polarization that is transparent to the PC mirrors, and the orthogonal polarization will provide the vacuum cavity mode required for the switching scheme. The main benefit of such a system is that the probe and switch fields can all be sent along the longitudinal axis of the cloud within the hollow core of the fiber, allowing for a high optical depth (as opposed to other systems requiring side illumination of the atomic cloud).

6.1 Four-Level Optical Switching Scheme

The four-level system that we will describe is shown in Fig. 6.1a, where we have two metastable ground states, $|g\rangle$ and $|s\rangle$, and two excited states, $|e\rangle$ and $|d\rangle$. The bipartite states are expressed by atomic excitation and number of cavity excitations (number of photons in the cavity mode). A weak probe field and switch field with Rabi frequency, Ω_p and Ω_s, respectively, are applied to the transitions as shown. The natural decay rates between states $|i\rangle$ to $|j\rangle$ are Γ_{ij}. A single empty cavity mode, a, is used to couple the $|s\rangle$-$|e\rangle$ transition, with a cavity decay rate of κ. The frequencies, ω_k, of the fields and cavity mode are detuned from their respectively coupled transition frequencies, ω_{ij}, by $\Delta_k \equiv \omega_k - \omega_{ij}$.

We will show that the weak probe field transmission can be controlled by the presence (or absence) of the switch field in an N-type scheme, as shown in Fig. 6.1b. Previous optical switches have utilized a similar four level switching scheme [5], however they suffer from using a strong classical control field coupling the $|s\rangle$-$|e\rangle$ transition to act as a bias. Our scheme replaces this classical field with a vacuum cavity mode to allow for a truly single photon gate transistor without the need for a bias power.

Following a formalism similar to the one introduced in Section 3.4, we again use an ensemble of N_a atoms, with the definition of the collective state operators (Eq. 3.107) and effective coupling constant (Eq. 3.108). In the RWA the Hamiltonian becomes

$$\begin{aligned} H =& \hbar\omega_{eg}\Sigma_{ee} + \hbar\omega_{sg}\Sigma_{ss} + \hbar\omega_{dg}\Sigma_{dd} + \hbar\omega_c a^\dagger a \\ & - \hbar g_{eff}(\Sigma_{es}a + \Sigma_{se}a^\dagger) - \hbar\frac{\sqrt{N_a}\Omega_p}{2}(\Sigma_{eg}e^{-i\omega_p t} + \Sigma_{ge}e^{i\omega_p t}) - \hbar\frac{\Omega_s}{2}(\Sigma_{ds}e^{-i\omega_s t} + \Sigma_{sd}e^{i\omega_s t}) \end{aligned} \tag{6.1}$$

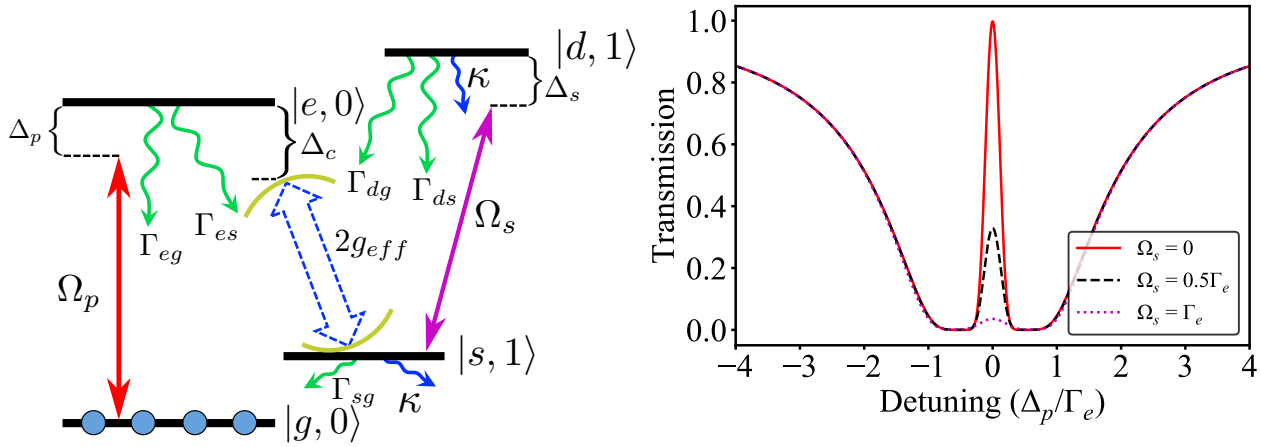

Figure 6.1: (a) Four level scheme used for optical switching of the weak probe field, Ω_p, by controlling the switching field, Ω_s. A cavity mode is set to near resonance to $|s\rangle$ and $|e\rangle$ transition with a coupling constant, g_{eff}, eliminating the need for biasing the switch with a strong control field. The decay rate between states $|i\rangle$ to $|j\rangle$ is Γ_{ij}. (b) Transmission of the probe field at different switch field powers. ($OD = 10$, $2g_{eff} = \Gamma_e$, $\Delta_p = \Delta_c = \Delta_s = 0$, $\Gamma_h = \Gamma_e$)

If we again restrict ourselves to the low excitation manifold shown in Fig. 6.1a (since we assume a weak probe), and transform into the appropriate rotating frame, the total Hamiltonian for this four level system can be written as

$$\begin{aligned}\tilde{H} =& -\hbar\Delta_p|e,0\rangle\langle e,0| - \hbar\Delta_{pc}|s,1\rangle\langle s,1| - \hbar\Delta_{pcs}|d,1\rangle\langle d,1| - \hbar g_{eff}(|e,0\rangle\langle s,1| + |s,1\rangle\langle e,0|) \\ &- \hbar\frac{\sqrt{N_a}\Omega_p}{2}(|e,0\rangle\langle g,0| + |g,0\rangle\langle e,0|) - \hbar\frac{\Omega_s}{2}(|h,1\rangle\langle s,1| + |s,1\rangle\langle h,1|)\end{aligned} \tag{6.2}$$

where $\Delta_{pc} \equiv \Delta_p - \Delta_c$ and $\Delta_{pcs} \equiv \Delta_p - \Delta_c + \Delta_s$.

The dissipation can be incorporated into the system through use of the master equation, where

$$\frac{\partial\tilde{\rho}}{\partial t} = -\frac{i}{\hbar}[\tilde{H},\tilde{\rho}] + \Gamma_{eg}\mathcal{L}[\Sigma_{ge}]\tilde{\rho} + \Gamma_{es}\mathcal{L}[\Sigma_{se}]\tilde{\rho} + \Gamma_{ds}\mathcal{L}[\Sigma_{sd}]\tilde{\rho} + \Gamma_{dg}\mathcal{L}[\Sigma_{gd}]\tilde{\rho} + \kappa\mathcal{L}[a]\tilde{\rho} \tag{6.3}$$

In this treatment we will ignore any decay between the metastable states, which is valid under the assumption that the decay from the $|s,1\rangle$ state is dominated by the cavity decay, $\kappa \gg \Gamma_{sg}$.

We can again find the transmission of the probe field through an atomic cloud with length, L, and optical depth, OD, from the susceptibility for a collective state (Eq. 3.118), which depends on the off-diagonal density matrix element, $\tilde{\rho}_{eg}$. Using the steady state solution ($\frac{\partial \tilde{\rho}}{\partial t} \approx 0$) of Eq. 6.3 and assuming a weak probe such that $\Omega_p \ll 2g_{eff}, \Omega_s$ and $\rho_{ee} = \rho_{ss} = \rho_{dd} \approx 0$, $\rho_{gg} \approx 1$, we find

$$\chi_{Nscheme} = \frac{OD}{k_0 L} \frac{i\gamma_e}{\gamma_e - i\Delta_p + C} \tag{6.4}$$

where, similar to Section 3.1.2, we define

$$C \equiv \frac{g_{eff}^2}{\gamma_s - i\Delta_{pc} + S} \tag{6.5}$$

and

$$S \equiv \frac{\left(\frac{\Omega_s}{2}\right)^2}{\gamma_d - i\Delta_{pcs}} \tag{6.6}$$

with the decays defined as $\gamma_e \equiv \frac{\Gamma_e}{2}$, $\gamma_s \equiv \frac{\Gamma_{sg}}{2} + \frac{\kappa}{2}$, and $\gamma_d \equiv \frac{\Gamma_d}{2} + \frac{\kappa}{2}$ (with $\Gamma_d \equiv \Gamma_{dg} + \Gamma_{ds}$, $\Gamma_e \equiv \Gamma_{eg} + \Gamma_{es}$).

It should be noted that in this treatment we have ignored any extra dephasing processes and considered only the spontaneous emission rates. To include other homogeneous broadening effects, such as from collisions, we include an additional term to the master equation in Eq. 6.3 of the form $\gamma_h^{ij}\mathcal{L}[\sigma_z^{ij}]\tilde{\rho}$, where γ_h^{ij} is the extra dephasing decay rate and σ_z^{ij} is the Pauli Z operator for a given $|i\rangle$-$|j\rangle$ transition. This has the effect of replacing $\frac{\Gamma_{ij}}{2} \rightarrow \frac{\Gamma_{ij}}{2} + \gamma_h^{ij}$ in our above equations for the susceptibility (Eq. 6.4-6.6).

6.1.1 Resonant Case

For the optical switch that we will discuss here, we set both the probe and switch fields, as well as the cavity mode, in resonance with their respective transitions, $\Delta_p = \Delta_c = \Delta_s = 0$. The susceptibility in Eq. 6.4 then becomes

$$\chi(\Delta = 0) = \frac{OD}{k_0 L} \frac{i\gamma_e}{\gamma_e + C(0)} \tag{6.7}$$

with

$$C(0) \equiv \frac{g_{eff}^2}{\gamma_s + \frac{\Omega_s^2}{4\gamma_d}} \tag{6.8}$$

This resonant case reproduces the purely imaginary susceptibility of the normal VIT and classical EIT results in Eq. 3.46 and Eq. 3.121, with the substitution $C(0) = \frac{g_{eff}^2}{\gamma_s} \rightarrow \frac{g_{eff}^2}{\gamma_s + \frac{\Omega_s^2}{4\gamma_d}}$. Thus we can see that the presence of the switch acts as an additional decoherence channel to interrupt the EIT coherent quantum interference process.

In order to quantify the performance of the optical switch we can introduce two different (but similar) figures of merit. We may investigate the behaviour of the transmission switching ratio, $q \equiv \frac{T_0}{T_s}$, as well as the switching contrast, $c \equiv T_0 - Ts$, where T_s is the transmission of the probe field in the presence of a switch field, and T_0 is the transmission without the switch. In the following sections we will discuss various systems and the characteristics required to maximize these two figures of merit.

Switching Ratio

The transmission with the switch field off results in a transmission (similar to EIT) of

$$T_0 = \exp\left\{-OD\frac{\gamma_e}{\gamma_e + \frac{g_{eff}^2}{\gamma_s}}\right\} \tag{6.9}$$

where we can solve for the required vacuum Rabi frequency

$$g_{eff}^2 = -\gamma_s\gamma_e\left(\frac{OD}{\ln T_0} + 1\right) \tag{6.10}$$

The presence of the switch field will alter the transmission to

$$T_s = \exp\left\{-OD\frac{\gamma_e}{\gamma_e + \frac{g_{eff}^2}{\gamma_s + \frac{\Omega_s}{4\gamma_d}}}\right\} \tag{6.11}$$

which can be solved for the required switching field power (which is $\propto \Omega_s^2$) given a particular T_0 by rearranging Eq. 6.11 and substituting Eq. 6.10 to give

$$\Omega_s^2 = 4\gamma_s\gamma_d\left(\frac{\frac{OD}{\ln T_0} + 1}{\frac{OD}{\ln T_s} + 1} - 1\right) \tag{6.12}$$

Thus we can find the ratio between the powers of the switch field and cavity coupling strength using Eq. 6.12 and Eq. 6.10

$$\frac{\Omega_s^2}{g_{eff}^2} = 4\frac{\gamma_d}{\gamma_e}\frac{OD\ln q}{(OD+\ln T_s)(OD+\ln T_0)} \tag{6.13}$$

where we have introduced the transmission ratio, $q \equiv \frac{T_0}{T_s}$. It is worth noting that the above ratio is independent of the metastable decay rate, γ_s. If we use a large optical depth, $OD \gg \ln T_0, \ln T_s$, we can approximate the above expression as

$$\frac{\Omega_s^2}{g_{eff}^2} \approx 4\frac{\gamma_d}{\gamma_e}\frac{\ln q}{OD} \tag{6.14}$$

to obtain a general trend that a larger optical depth requires a lower switch field power for a given switching ratio.

Switching Contrast

The contrast between switching transmissions, $c \equiv T_0 - T_s$, has a slightly different behaviour as a function of the optical depth than the switching ratio. As we will see, there is actually an optimal optical depth for which the switching contrast will be maximized. To find this we simply take the derivative of the contrast with respect to optical depth. To simplify things, let us first define the transmissions with the switch field off and on, T_0 and T_s, respectively, as

$$T_0 = e^{-OD\cdot A_0} \tag{6.15}$$

where

$$A_0 \equiv \frac{\gamma_e}{\gamma_e + \frac{g_{eff}^2}{\gamma_s}} \tag{6.16}$$

and

$$T_s = e^{-OD\cdot A_s} \tag{6.17}$$

where

$$A_s \equiv \frac{\gamma_e}{\gamma_e + \frac{g_{eff}^2}{\gamma_s + \frac{\Omega_s^2}{4\gamma_d}}} \tag{6.18}$$

We can then take the derivative of the contrast as

$$\begin{aligned}\frac{dc}{d(OD)} &= \frac{d}{d(OD)}\left(e^{-OD\cdot A_0} - e^{-OD\cdot A_s}\right) \\ &= -A_0 e^{-OD\cdot A_0} + A_s e^{-OD\cdot A_s}\end{aligned} \tag{6.19}$$

Setting Eq. 6.19 equal to zero and rearranging we find the OD that will optimize the contrast as

$$OD_{max} = \frac{\ln \frac{A_0}{A_s}}{A_0 - A_s} \tag{6.20}$$

Using Eq. 6.20 we can solve for the maximum contrast as

$$\begin{aligned} c_{max} &= e^{-OD_{max} \cdot A_0} - e^{-OD_{max} \cdot A_s} \\ &= \frac{A_0}{A_s}^{\frac{A_0}{A_s - A_0}} \left(1 - \frac{A_0}{A_s}\right) \end{aligned} \tag{6.21}$$

We can see from Eq. 6.18 that as the switch field becomes strong ($\Omega_s \gg \kappa, g_{eff}$) then $A_s \approx 1$ and the OD that maximizes the contrast asymptotes to a constant

$$OD_{max} \approx \frac{\ln A_0}{A_0 - 1} \tag{6.22}$$

More importantly, it is clear from Eq. 6.21 that in this limit,

$$c_{max} \approx A_0^{\frac{A_0}{1 - A_0}} (1 - A_0) \tag{6.23}$$

If we also assume that the lifetime of the metastable state is very long, such that $\Gamma_{sg} \ll \kappa$, then $\gamma_s \approx \frac{\kappa}{2}$ and we can rewrite Eq. 6.16 in terms of the cooperativity as

$$A_0 \approx \frac{1}{1 + \eta_{eff}} \tag{6.24}$$

and thus the maximum optical depth and contrast become

$$OD_{max} \approx \frac{1 + \eta_{eff}}{\eta_{eff}} \ln(1 + \eta_{eff}) \tag{6.25}$$

and

$$c_{max} \approx \frac{1}{1 + \eta_{eff}}^{\frac{1}{\eta_{eff}}} \left(1 - \frac{1}{1 + \eta_{eff}}\right) \tag{6.26}$$

respectively.

We can make further simplifications if we assume our cavity system is deeply in the strong coupling regime such that $\eta_{eff} \gg 1$, thus we find from Eq. 6.25 and Eq. 6.26 that

$$OD_{max} \approx \ln \eta_{eff} \tag{6.27}$$

and

$$c_{max} \approx 1 - \frac{1}{\eta_{eff}} \tag{6.28}$$

which of course will approach unity at this optimal optical depth.

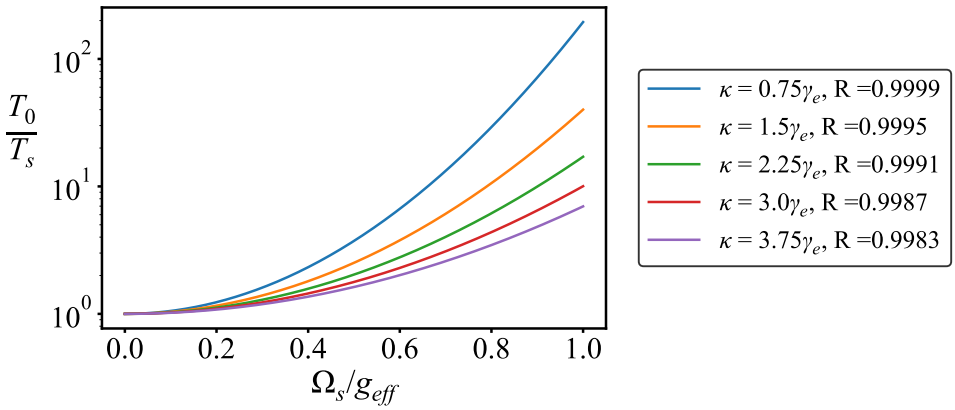

Figure 6.2: Transmission switch ratio as a function of the switch Rabi frequency normalized to the cavity vacuum Rabi frequency (Eq. 6.14). We use the D_2 cesium transition ($\mu = 1.7138 \times 10^{-29}$ Cm) at a wavelength of 852 nm. Varying cavity decay rates, κ, shown with the resulting mirror reflectivity required to produce the given decay rate. The number of atoms are set to 10^4 corresponding to an optical depth of 36.9. The fiber loss is $\sim$ 150 dB/m with a core radius of 3.5 μm and Gaussian mode radius of 2.75 μm, and the length of the fiber is set to 1 cm. $\Gamma_e = \Gamma_d = 2\pi \times 5.2$ MHz.

6.2 Semiclassical: Continuous Probe and Control Switch

We will begin investigating the behaviour of the four level switch by considering the simplest system in which we apply continuous plane wave probe and switch fields. Although the schemes discussed in this chapter could be employed in a variety of cavity QED systems, we will represent the relevant results for the type of system employed our research group. Specifically, we use the D_2 transition of cesium atoms ($\Gamma_e = 2\pi \times 5.2$ MHz) that can be cooled to a $\sim$10 μK temperature, with the $|g\rangle$-$|e\rangle$ state as the $F = 3 \rightarrow F' = 3$, and the $|s\rangle$-$|d\rangle$ state as the $F = 4 \rightarrow F' = 4$.

The cavities that we will perform the following calculations for are the fiber-integrated resonators discussed in Chapter 4 and 5. The HCPCF that we use has a loss of $\sim$ 150 dB/m attenuation at the wavelength of 852 nm, with a core radius of 3.5 μm and a Gaussian mode radius of 2.75 μm. For simplicity, we will set the cavity length, L, to 1 cm unless otherwise stated. Such a system results in a vacuum Rabi frequency of $g_{eff} \approx 2\pi \times 8.6$ MHz.

The approximate switch transmission ratio is plotted in Fig. 6.2 as a function of the

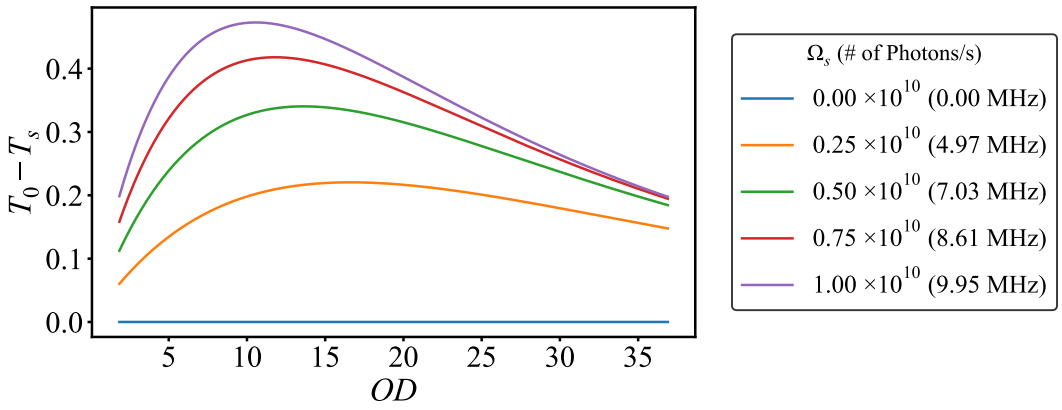

Figure 6.3: Transmission contrast at varying optical depths. The maximum contrast occurs at a particular optical depth for each given switch power (given in both units of photons per second and MHz). The decay rate is set to $\kappa = \gamma_e$ and $L = 1$cm, $\Gamma_e = \Gamma_d = 2\pi \times 5.2$ MHz.

switch-to-cavity coupling constant, $\frac{\Omega_s}{g_{eff}}$, as determined by Eq. 6.14. The number of atoms is set to $N_a = 10^4$, which is approximately the number of atoms that has been successfully loaded into a HCPCF using a magic wavelength dipole trap [6, 123, 124], and corresponds to an optical depth of $OD = 36.9$. The transmission ratio is plotted for different values of the cavity decay rate, given the attenuation of the fiber. The reflectivity of the cavity mirrors that produce the given decay rate is also shown. The ratio, of course, increases with a larger switch power, however, a minimal switch power would be ideal in order to require less photons.

The other major figure of merit, switch transmission contrast, exhibits more interesting behaviour, as discussed in the previous section. Fig. 6.3 shows the transmission contrast as a function of the optical depth at a fixed cavity decay rate of $\kappa = \gamma_e$. Various switch powers are also plotted and shown in units of the number of photons per second. It is clear that the contrast actually is maximized at a particular optical depth, derived in the previous section in Eq. 6.20, which occurs at a larger OD as the power is decreased.

The optical depth that maximizes the contrast and the resulting maximum contrast at this optimal optical depth are shown in Fig. 6.4a and 6.4b, respectively, as a function of the switch field power at various cavity decay rates. Interestingly, as the cavity becomes more lossy, the optimal optical depth is reduced, and of course the maximum contrast achievable is lowered as well. These extra decay mechanisms act as decoherence for the

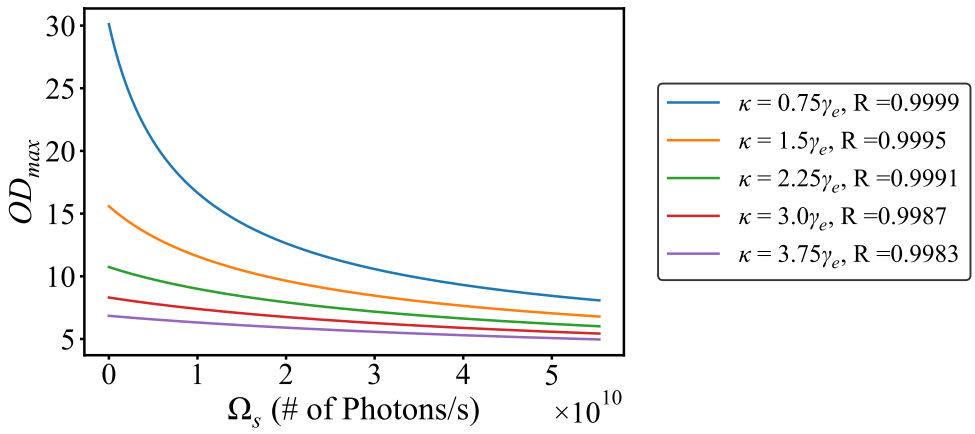

(a)

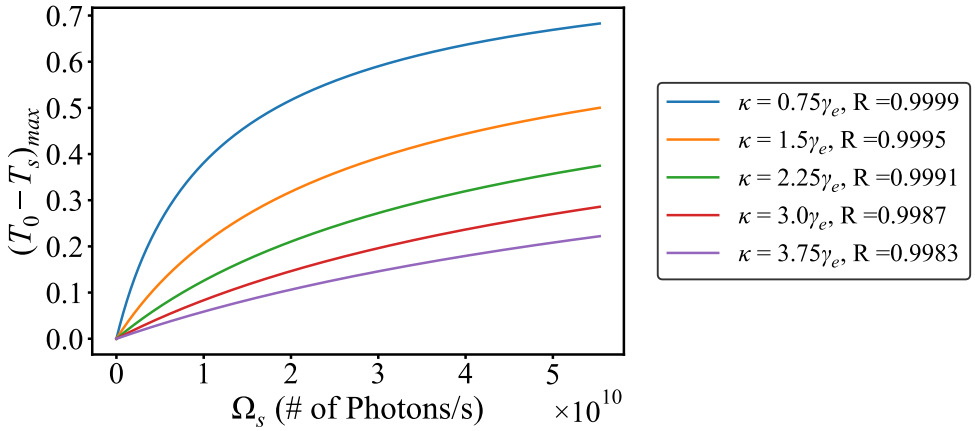

(b)

Figure 6.4: (a) Optimal optical depth that allows for the (b) maximum contrast between on and off switch states for a range of switch field powers. Each are plotted at different cavity decay rates and respective mirror reflectivities ($L = 1$cm, $\Gamma_e = \Gamma_d = 2\pi \times 5.2$ MHz).

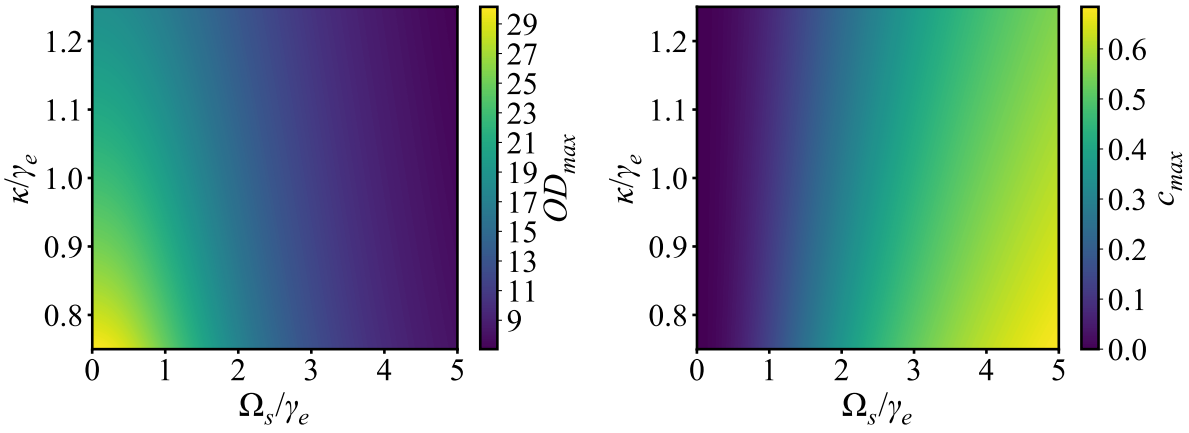

(a) (b)

Figure 6.5: (a) Optical depth required to produce the (b) maximum contrast at varying cavity decay rates, κ, and switch field strengths, Ω_s.

VIT phenomenon, which causes for the transmission without the presence of the switch to decrease.

The presence of an optimal optical depth can also have a relatively simple physical interpretation from two competing effects between the on and off switch positions. For a given switch power, an optical depth that is too small will not act to absorb enough of the probe light, and thus will have a larger T_s. However, when the optical depth is too large, the VIT must have very large coherences in order to create transparency, and thus T_0 is decreased. With very large switch fields, we see from Fig. 6.4a and 6.4b that the optimal optical depth and maximum contrast, respectively, asymptotically approach constant values described by Eq. 6.25 and 6.26. For completeness, we also solved the system without the underlying assumptions of steady state or a weak probe field by numerically solving the full coupled differential master equation (Eq. 6.3). The analytical results of this section only begin to diverge from the numerical solution (without approximations) for a probe field $\Omega_p > 0.1\gamma_e$.

6.2.1 Quasi-Continuous Wave Switch

If we are now assuming that the probe is a weak (potentially single photon) pulse, there is another important factor that must be considered: the group velocity. As we have seen in

Section 3.5.3, a VIT system produces a large dispersion on resonance and thus a reduction in the group velocity. When the switch field is on, the normal VIT dispersion and resulting group velocity is altered, however it can still be greatly reduced for a relatively weak switch field.

As we have seen in the previous section, high switch powers are needed for large switching ratios and contrasts. However, the goal is to minimize the number of switch photons required for a given switch performance. We can quantify the total number of switch photons required by simply assuming it is a quasi-continuous plane wave source, in which it is only turned on during the time it takes the probe pulse to traverse the atomic cloud with this reduced group velocity. Thus we effectively assume a perfect a square wave pulse for the switch field which has a constant power when turned on.

Assuming this quasi-continuous switch field we will investigate the switching process, for simplicity, by restricting the analysis to using the contrast as the primary figure of merit. Fig. 6.5a and 6.5b shows the optical depth that produces the largest contrast and the maximum contrast achievable, respectively for varying cavity decay rates and switch fields.

We find the group velocity of the probe pulse, v_g^p, plotted in Fig. 6.6a, using Eq. 3.124 by taking the derivative of the susceptibility of the four level system (Eq. 6.4). As mentioned, the group velocity is greatly reduced for low switch powers, as shown in the plot, and is slightly dependent on the cavity decay rate.

However, it is also clear that at a switch field of $\Omega_s \approx 2.5\gamma_e$ the group velocity of the probe diverges to infinity. This is a mathematical consequence that as the switch field is increased, the dispersion relation transitions from a positive slope to a negative slope. On resonance, the phase index is $n = 1$, and there exists a switch field power that causes for $\omega_p \frac{\partial n}{\partial \omega_p} = -1$, thus causing the group index to become zero, $n_g = 0$. It should be noted that we plot the absolute value of the group velocity, and in fact the group velocity is actually negative for switch powers greater than this resonance value. These complications are avoided by again considering only the low switch field powers.

Next we use the group velocity of the probe field to determine the number of switch photons, N_s, required by assuming that Ω_s is turned on for a time equal to the time it takes the probe pulse to travel the length of the atomic cloud. Fig. 6.6b shows these results, where the low switch powers used naturally require a low number of switch photons. Interestingly, a low number of switch photons is also required near the point in which the group velocity is divergent. This is due to the fact that as the group velocity of the probe becomes large, the transit time of the atomic cloud can become extremely low, and thus the switch field is only on for a short period of time, reducing the total number of photon

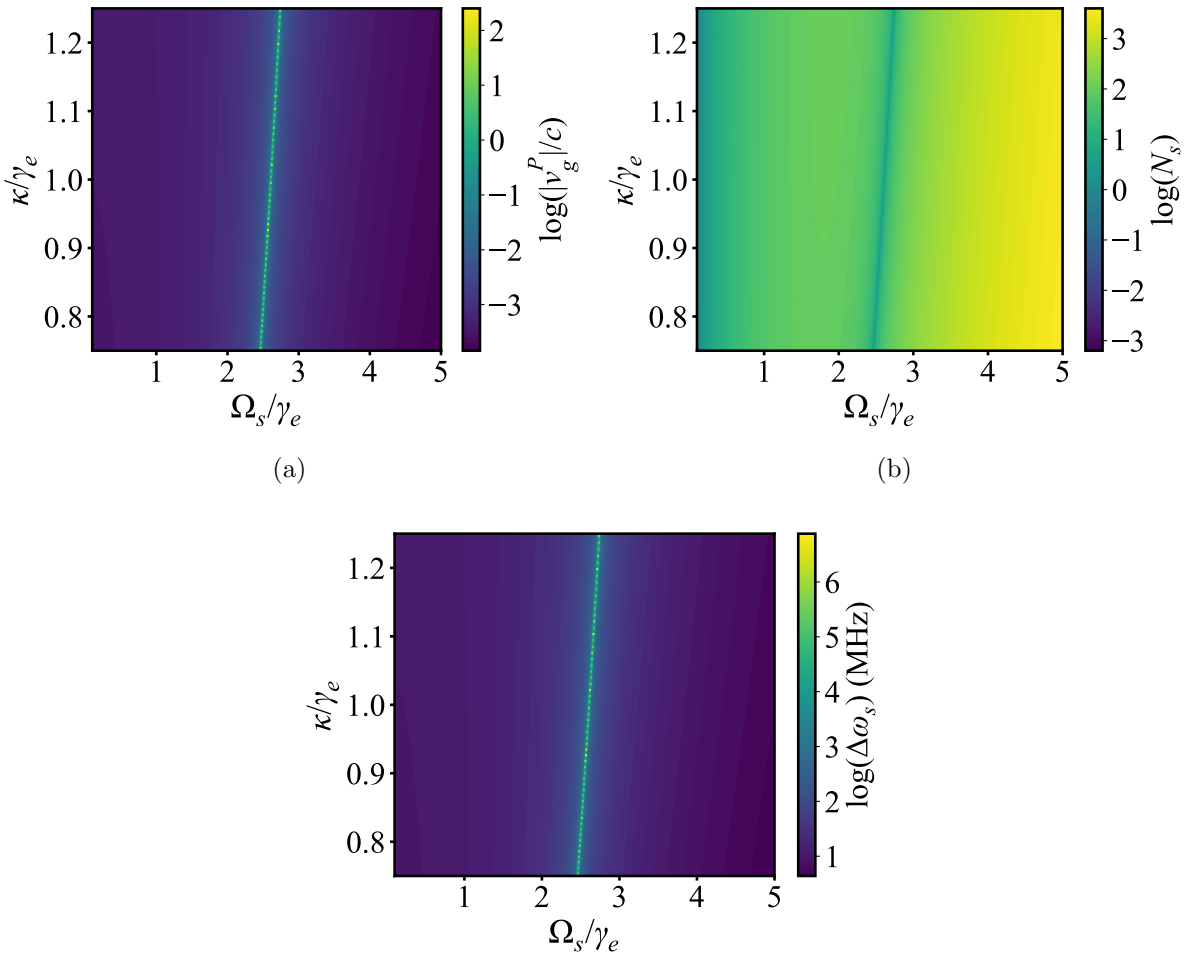

Figure 6.6: (a) Group velocity of the probe pulse as a function of the switch field and cavity decay rate. It should be noted that we plot the magnitude of the group velocity, as the dispersion relation for large switch powers creates a negative group velocity. (b) Number of switch photons required for a quasi-continuous source that is assumed to be turned on for only as long as the transit time of the probe pulse of the atomic cloud. (c) Frequency width of the switch field square pulse with a width in time equal to the transit time of the probe pulse.

required.

Naively, one may initially propose that using a switch field power near this divergent group velocity point would be optimal to use in a switch. However, there are issues that arise when considering switch fields that produce these large probe group velocities and thus extremely short transit times. The first issue occurs from considering the switch field only being on for a short period of time (effectively a narrow square wave pulse). By the Fourier transform, the frequency width of the switch becomes very large.

This effect is evident in Fig. 6.6c, where we have plotted the frequency bandwidth of these switch field square pules. Again at the divergent group velocity switch field power we see that the frequency spectrum also becomes divergent. This becomes problematic when the bandwidth becomes comparable to the frequency difference between the nearest neighbouring atomic states as cross coupling to these states may occur, which for the D_2 line hyperfine transitions in cesium is on the order of ~ 100 MHz. Ideally, the bandwidth of the switch pulse would be smaller than the linewidth of the atomic level, which is on the order of ~ 10 MHz.

In addition to this consideration, a large probe group velocity means that the full probe pulse may not fit into the atomic ensemble at once, and instead the head of the pulse may exit the cloud before the tail end of the pulse can enter. If we narrow the probe pulse too much in time, the bandwidth of the pulse may even become larger than the transparency window, as explored in Section 3.5.3, and undesired absorption of the probe may occur.

6.3 Pulsed Probe and Control Switch

In order to treat the system in a more realistic manner, we will now consider both the switch and probe fields as pulses. This would allow for the switch field to not be at full strength the entire time that the probe field traverses the cloud. The switch field could instead be allowed to travel with the probe pulse with a shorten pulse width in time requiring fewer photons.

However, the additional challenge that this treatment introduces is that the interaction between the atoms with both the switch and probe field simultaneously requires the respective pulses to overlap. Thus, for an efficient switch, it is desirable to engineer the system in such a way as to match the switch pulse and probe pulse group velocities.

As discussed in the previous sections, the four-level N-type scheme results in a reduced group velocity of the probe field. Unfortunately the weakness of the probe field means that

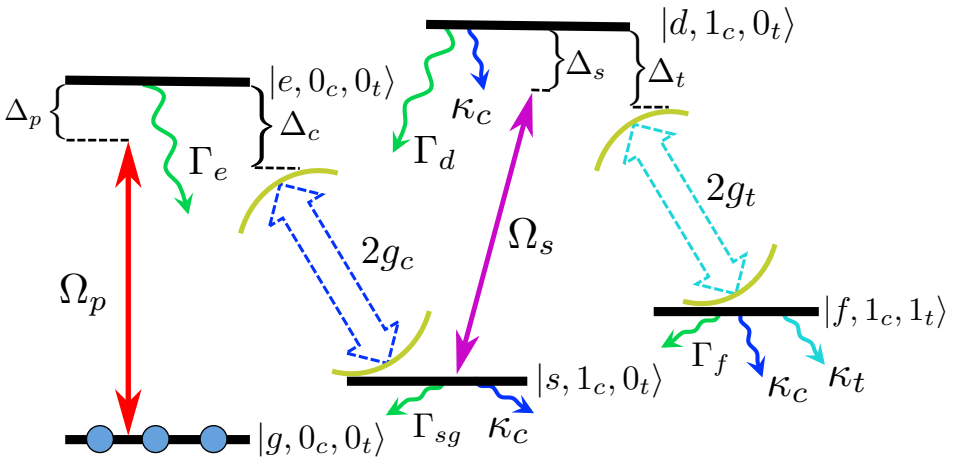

Figure 6.7: A five level M-type scheme that can be used to tune the group velocity of the switch field, Ω_s, by altering the detuning of the tuner cavity mode, Δ_t. ($\Gamma_d \equiv \Gamma_{dg}+\Gamma_{ds}+\Gamma_{df}$, $\Gamma_e \equiv \Gamma_{eg}+\Gamma_{es}+\Gamma_{eg}$, $\Gamma_f \equiv \Gamma_{fs}+\Gamma_{fg}$)

there is little population in the $|s\rangle$ state, and so the group velocity of the switch pulse is only marginally affected. In the following sections we will discuss two separate possible schemes to alter the switch group velocity until it is the same as the probe pulse.

6.3.1 M-Scheme Group Velocity Matching

The scheme discussed in this section is similar to that proposed by Ottaviani et al. [81]. We introduce a third metastable ground state, $|f\rangle$, where a tuner field can be applied to the $|f\rangle$-$|d\rangle$ transition in an M-type scheme, as shown in Fig. 6.7. However, rather than introducing an additional source, which would require additional photons, we can eliminate this need by instead using again a cavity mode to drive this transition. In fact, we can even utilize the same cavity that drives the $|e\rangle$-$|s\rangle$ transition by simply setting a separate cavity resonant frequency tuned near ω_{df}. Such a scheme would restrict the maximum amount of detuning possible for these modes to $\frac{FSR}{2}$, as a larger detuning would begin to become resonant to the neighbouring Fabry-Pérot peak.

This five level scheme can be thought of as two Λ-type EIT schemes together, one from the $|g\rangle$-$|e\rangle$-$|s\rangle$ transitions, and the other from $|s\rangle$-$|d\rangle$-$|f\rangle$ transitions, which can allow for slow light of both the probe and switch fields. We define the tuner cavity mode drive frequency as ω_t. As we will show, the group velocity of the switch field can be tuned by altering the detuning, $\Delta_t \equiv \omega_t - \omega_{df}$, of the tuner field.

We can build onto the system master equation of the N-scheme in Section 6.1 to determine the behaviour of an M-scheme. By adding the interaction energies of the tuner field and the internal energy of the additional $|f\rangle$ state, and again moving into the appropriate rotating frame, we find the system Hamiltonian to be

$$\begin{aligned}\tilde{H} = &-\hbar\Delta_p|e,0_c,0_t\rangle\langle e,0_c,0_t| - \hbar\Delta_{pc}|s,1_c,0_t\rangle\langle s,1_c,0_t| \\ &-\hbar\Delta_{pcs}|d,1_c,0_t\rangle\langle d,1_c,0_t| - \hbar\Delta_{pcst}|f,1_c,1_t\rangle\langle f,1_c,1_t| \\ &-\hbar g_c(|e,0_c,0_t\rangle\langle s,1_c,0_t| + |s,1_c,0_t\rangle\langle e,0_c,0_t|) - \hbar\frac{\sqrt{N_a}\Omega_p}{2}(|e,0_c,0_t\rangle\langle g,0_c,0_t| + |g,0_c,0_t\rangle\langle e,0_c,0_t|) \\ &-\hbar\frac{\Omega_s}{2}(|h,1_c,0_t\rangle\langle s,1_c,0_t| + |s,1_c,0_t\rangle\langle h,1_c,0_t|) - \hbar g_t(|d,1_c,0_t\rangle\langle f,1_c,1_t| + |f,1_c,1_t\rangle\langle d,1_c,0_t|)\end{aligned} \tag{6.29}$$

where we define $\Delta_{pcst} \equiv \Delta_p - \Delta_c + \Delta_s - \Delta_t$, and the effective control and tuner cavity mode coupling constants as $g_c \equiv \frac{\mu_{es}}{\hbar}\sqrt{\frac{\hbar\omega_c}{2\epsilon_0 V_{mode}}}$ and $g_t \equiv \frac{\mu_{fd}}{\hbar}\sqrt{\frac{\hbar\omega_t}{2\epsilon_0 V_{mode}}}$, respectively. We have again restricted the Hilbert space of the system to the lowest excitation manifold. The states are expressed using the notation as the first entry indicating the atomic excitation level, and the second and third entries as the control cavity mode ($|g\rangle$-$|e\rangle$ transition) and tuner cavity mode ($|f\rangle$-$|d\rangle$ transition) photon number, respectively.

The master equation is determined by the Hamiltonian in Eq. 6.29 such that

$$\begin{aligned}\frac{\partial\tilde{\rho}}{\partial t} = -\frac{i}{\hbar}[\tilde{H},\tilde{\rho}] &+ \Gamma_{eg}\mathcal{L}[\Sigma_{ge}]\tilde{\rho} + \Gamma_{es}\mathcal{L}[\Sigma_{se}]\tilde{\rho} + \Gamma_{ef}\mathcal{L}[\Sigma_{fe}]\tilde{\rho} \\ &+ \Gamma_{ds}\mathcal{L}[\Sigma_{sd}]\tilde{\rho} + \Gamma_{dg}\mathcal{L}[\Sigma_{gd}]\tilde{\rho} + \Gamma_{df}\mathcal{L}[\Sigma_{fd}]\tilde{\rho} \\ &+ \kappa_c\mathcal{L}[a_c]\tilde{\rho} + \kappa_t\mathcal{L}[a_t]\tilde{\rho}\end{aligned} \tag{6.30}$$

using again the notation of Section 6.1 for the decay rates between states. For generality, the cavity decay rates for the control mode (a_c) and tuner mode (a_t) are set as κ_c and κ_t, respectively. We will again ignore any natural spontaneous emission between any of the metastable ground states since the cavity decay rates will be the most dominant sources of decoherence from these states, $\kappa \gg \Gamma_{sg}, \Gamma_{fs}, \Gamma_{fg}$.

By solving the above master equation in the steady state, weak probe approximation, the susceptibility is found to be (using Eq. 3.118)

$$\chi_{Mscheme} = \frac{OD}{k_0 L}\frac{i\gamma_e}{\gamma_e - i\Delta_p + C} \tag{6.31}$$

where we define

$$
\begin{aligned}
C &\equiv \frac{g_c^2}{\gamma_s - i\Delta_{pc} + S} \\
S &\equiv \frac{\left(\frac{\Omega_s}{2}\right)^2}{\gamma_d - i\Delta_{pcs} + T} \\
T &\equiv \frac{g_t^2}{\gamma_f - i\Delta_{pcst}}
\end{aligned}
\tag{6.32}
$$

with $\gamma_e \equiv \frac{\Gamma_{eg}}{2} + \frac{\Gamma_{es}}{2} + \frac{\Gamma_{ef}}{2}$, $\gamma_s \equiv \frac{\Gamma_{sg}}{2} + \frac{\kappa_c}{2}$, $\gamma_d \equiv \frac{\Gamma_{dg}}{2} + \frac{\Gamma_{ds}}{2} + \frac{\Gamma_{df}}{2} + \frac{\kappa_c}{2}$ and $\gamma_f \equiv \frac{\Gamma_{fg}}{2} + \frac{\Gamma_{fs}}{2} + \frac{\kappa_c}{2} + \frac{\kappa_t}{2}$.

As in previous sections, the group velocity is dependent on the dispersion relation of the susceptibility, specifically the derivative of the susceptibility, $\frac{\partial \chi}{\partial \omega}$. By using Eq. 6.31 in Eq. 3.124, the group velocity of the probe field can be found. In addition, using Eq. 3.124 as the definition of group velocity, we can solve for the switch pulse group velocity by numerically solving the steady state solution of master equation for the M-level scheme (Eq. 6.30) to determine the density matrix element $\tilde{\rho_{ds}}$ and its derivative.

However, since the switch field group velocity is altered due to the interaction of atoms in the $|s\rangle$ state, we cannot simply assume $\rho_{gg} \approx 1$, $\rho_{ee} = \rho_{dd} = \rho_{ss} = \rho_{ff} \approx 0$ in the weak field approximation. Instead, we must keep the lowest order Taylor expanded terms to introduce a small population in the other metastable ground states. The expanded state populations become

$$
\begin{aligned}
\rho_{gg} &= \left| 1 - \frac{\left(\frac{\Omega_p}{2}\right)^2 + g_c^2}{2|\delta_p \delta_{cp} - g_c^2|^2} \right|^2 \\
\rho_{ee} &= \left| \frac{\Omega_p}{2} \frac{\delta_{cp}(g_t^2 - \delta_{pcs}\delta_{cpst}) + \left(\frac{\Omega_s}{2}\right)^2 \delta_{pcst}}{\delta_A} \rho_{gg} \right|^2 \\
\rho_{ss} &= \left| -\frac{\Omega_p}{2} g_c \frac{g_t^2 - \delta_{pcs}\delta_{pcst}}{\delta_A} \rho_{gg} \right|^2 \\
\rho_{dd} &= \left| -\frac{\Omega_p}{2} g_c \frac{\Omega_s}{2} \frac{\delta_{pcst}}{\delta_A} \rho_{gg} \right|^2 \\
\rho_{ff} &= \left| -\frac{\Omega_p}{2} g_c \frac{\Omega_s}{2} g_t \frac{1}{\delta_A} \rho_{gg} \right|^2
\end{aligned}
\tag{6.33}
$$

where we define

$$\begin{aligned}
\delta_p &= -\Delta_p - i\gamma_e \\
\delta_{pc} &= -\Delta_{pc} - i\gamma_s \\
\delta_{pcs} &= -\Delta_{pcs} - i\gamma_d \\
\delta_{pcst} &= -\Delta_{pcst} - i\gamma_f \\
\delta_A &= [\delta_p\delta_{pc} - g_c^2][\delta_{pcs}\delta_{pcst} - g_t^2] - \delta_p\delta_{pcst}\left(\frac{\Omega_s}{2}\right)^2
\end{aligned} \tag{6.34}$$

We again calculate the group velocity tuning for an atomic cloud of cesium atoms, however, if we assume a 1 cm length cavity giving a FSR = 1.5 GHz, then we cannot use the separate hyperfine levels of the D_2 line (as in Section 6.2). This is because the difference in the energy levels is less than the FSR, since we require the excited states to be resonant with two separate cavity modes. Instead, we can set the $|d\rangle$ state as a hyperfine level in the D_2, while the D_1 line can be used for the $|e\rangle$ state, with a transition wavelength $\sim$ 894.6 nm. The requirement of three distinct metastable ground states can be achieved with the application of a uniform magnetic field to Zeeman split the $6^2S_{1/2}$ states.

Fig 6.8 shows the detuning of the tuner cavity mode required to match the group velocities of the probe and switch pulses in this system, where we have set $\Delta_p = \Delta_c = \Delta_s = 0$. We also have chosen $\Omega_s = \gamma_e$ and set $\kappa = 0.75\gamma_e$, which corresponds to a fiber-integrated cavity with mirror reflectivity R $\approx$ 0.9999. It is evident that the group velocities can indeed be matched by tuning the tuner cavity to $\Delta_t \sim -1.23\gamma_e$. However, it is also clear that this resonant phenomenon is incredibly sensitive to tuner cavity detuning, and thus the precision required may be difficult to implement in practical systems.

6.3.2 Bragg Grating Slow Light

An alternative method for engineering a system that will match the group velocities of the probe and switch fields is by utilizing Bragg dispersion within the cavity. This is simply achieved by modulating the effective refractive index of the cavity medium. One way to perform this modulation was described in Chapter 4, where the hollow core walls of the fiber are coated with a periodic modulation of resist to alter the effective cross-sectional refractive index. In that work, the fiber Bragg layers were designed to be highly reflective mirrors by tuning the periodicity of the resist modulation to allow for the desired frequency of the cavity (e.g. the atomic transition frequency) to be within the photonic bandgap. Two such Bragg sections would then be applied to opposite ends of a fiber segment to form the Fabry-Pérot cavity.

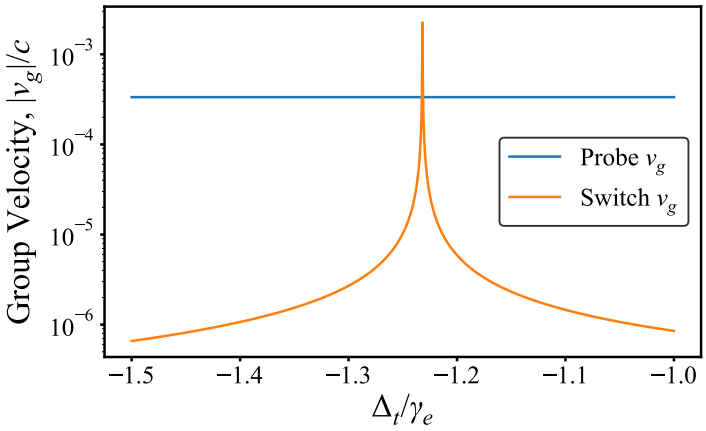

Figure 6.8: Group velocities of the probe and switch pulses when altering the tuner cavity detuning, Δ_t, while keep $\Delta_p = \Delta_c = \Delta_s = 0$. The D_2 and D_1 lines of cesium are used for the $|d\rangle$ and $|e\rangle$ excited states, respectively. We set $\Omega_p = 0.01\gamma_e$, $\Omega_s = \gamma_e$, and $\kappa = 0.75\gamma_e$, assuming a 1 cm length HCPCF fiber cavity with 10^4 atoms.

Alternatively, to allow for slow light in this optical switching scheme these Bragg layers would need to be present along the entire fiber (rather than just the end segments), and the operational frequency would instead be set to be outside of the bandgap, although near the bandgap edge. Regardless of the technical details of the cavity system used, in general, any Bragg modulation of the cavity medium refractive index can allow for slow light.

These Bragg layers need to be designed to operate at a frequency slightly outside of the bandgap because, firstly, we of course require the light to be allowed to propagate within the medium, and secondly, the highly dispersive effects near the bandgap edge acts to slow the light pulse, as briefly discussed in Section 2.2.1. From the definition of group velocity, $v_g = \frac{\partial w}{\partial k}$, we can see from the bandgap diagrams in Chapter 2 (such as Fig. 2.3) that as the frequency approaches the bandgap edge, $\omega \to \omega_\pm$, then $\frac{\partial w}{\partial k} \to 0$. By adjusting the periodicity of the Bragg layers the group velocity of the switch pulse could potentially by tuned to match that of the probe field.

As we will see, there is a major advantage for using Bragg dispersion to slow light rather than an additional VIT scheme (M-scheme), as suggested in the previous section. For so-called structural slow light, which deals with the dispersion resonances created by the structure and geometry of a spatially dependent refractive index, the electric field, and thus intensity, can become enhanced as the pulse is squeezed in space when entering into the medium.

In the case of this structural slow light, such as that produced by the Bragg dispersion, as the pulse enters the Bragg medium it is compressed along the optical axis in space (but not in time) as it slows, resulting in an enhanced electric field within the pulse. The origins of this enhancement can be understood as the result of the addition of the both the forward and backward propagating waves contributing to the total electric field strength at a given location.

Conversely, material slow light, which is a result of the resonance associated in a media with a frequency dependent refractive index (but spatially uniform), does not allow for electric field enhancement [18]. As we alluded to in Section 3.1.3, the phenomenon of slow light in a general EIT system results in the partial transfer of energy from the pulse to the atomic coherent dark state superposition (polariton), and the electric field in the pulse is not altered as it enters the atomic media.

We can find the structural slow light enhancement in the case of a sinusoidally varying index modulation, $n(z) = n_0 + n_1 \cos(2\kappa_0 z)$, where $\kappa_0 = \frac{\pi}{\Lambda}$ is the Bragg condition for a spatial index period of Λ. This is done by solving for the envelope fields for the forward, E_F, and backward, E_B, travelling waves with the coupled equations [18, 118]

$$\begin{aligned} \frac{\partial E_F}{\partial z} + \frac{1}{v}\frac{\partial E_F}{\partial t} &= i\kappa E_B e^{2i\Delta\beta z} \\ \frac{\partial E_B}{\partial z} - \frac{1}{v}\frac{\partial E_B}{\partial t} &= -i\kappa E_F e^{-2i\Delta\beta z} \end{aligned} \tag{6.35}$$

where $\kappa \equiv n_0 n_1 \omega_0$ is called the coupling strength at the center Bragg frequency $\omega_0 = k_0 c/n_0$. The wavenumber mismatch is $\Delta\beta = n_0\frac{\Delta}{c}$ for $\Delta = \omega - \omega_0$ and $v = \frac{c}{n_0}$ is the background group velocity.

In principle, these coupled equations can be solved for an incident pulse of a particular shape with the total field in the medium being $E = E_B + E_F$. The steady state solution of Eq. 6.35 can in fact be found analytically to be

$$\begin{aligned} E_F(z) &= E_0 \frac{\gamma\cosh(\gamma(z-L)) + i\frac{\Delta}{v}\sinh(\gamma(z-L))}{\gamma\cosh(\gamma L) - i\frac{\Delta}{v}\sinh(\gamma L)} \\ E_B(z) &= -iE_0 \frac{\kappa\sinh(\gamma(z-L))}{\gamma\cosh(\gamma L) - i\frac{\Delta}{v}\sinh(\gamma L)} \end{aligned} \tag{6.36}$$

for an incident electric field, E_0, where $\gamma \equiv \sqrt{\kappa^2 - (\Delta/v)^2}$ which can be used to find the total energy stored, U, from the volume-average of the time-averaged energy density, $u = \frac{1}{2}n^2\epsilon_0(|E_B|^2 + |E_F|^2)$, as

$$U = U_0 \frac{(\kappa/\gamma)^2\tanh(\gamma L)/(\gamma L) - (\Delta/\gamma v)^2\mathrm{sech}^2(\gamma L)}{1 + (\Delta/\gamma v)^2\tanh^2(\gamma L)} \tag{6.37}$$

where $U_0 = \frac{1}{2}\epsilon_0 n_0^2 |E_0|^2 AL$ is the average total energy in the background material. We can now use this field enhancement to reduce the amount of initial switch photons needed to produce a given contrast, since the switch pulse will have an increased intensity within the atomic medium as it interacts with the probe field.

Taking the results of the previous sections, it is clear that various aspects of the system need to be considered to find an optimal switch setting. We desire a minimal number of switch photons to produce a large contrast. By matching the group velocities of the probe and switch using structural slow light, this can be achieved. Using structural slow light, rather than material slow light, can further reduce the required number of photons due to field enhancement with the medium.

However, the pulses need to also have a bandwidth that will fit into the VIT window. If we chose an input $\Omega_s \sim 2\gamma_e$, we find a relatively low number of photons required per pulse, as well as an acceptable bandwidth (as seen from Fig. 6.6c), but a maximum contrast that is about ~ 0.4 (Fig. 6.4b) depending on the losses of the cavity. As we will see in the following sections, these switching performances can be greatly improved by using instead a simple three-level system rather than the four-level scheme.

6.4 Three-Level Switching Scheme

The work presented in this chapter has so far involved a four-level scheme that uses a switching field that is resonant on the fourth state. The main issues with such a scheme is that it is difficult to match the group velocities of the switch and probe fields, however, even if the pulses can be matched, a relatively substantial amount of photons are required for the switching process to produce, at maximum, only a moderate amount of contrast for our given fiber-cavities.

In the rest of this chapter, we will discuss another type of switching scheme that is based only on a three-level system, which can address both the problems of group velocity matching as well as the strict condition of applying only a single switch photon to produce a relatively high contrast. In general, these issues are overcome by instead driving the cavity mode with a single switch photon in order to alter the nonlinear properties of the system. It can be shown that a single switch photon can be efficiently loaded into the cavity mode by pulse shaping the input photon. The most efficient pulse shape is the time reversal of a photon leaking from the cavity by exponential decay with decay constant, κ, i.e. an exponentially growing pulse with a κ growth constant [65, 3].

This can also allow the photon to be trapped within the cavity for at least as long as

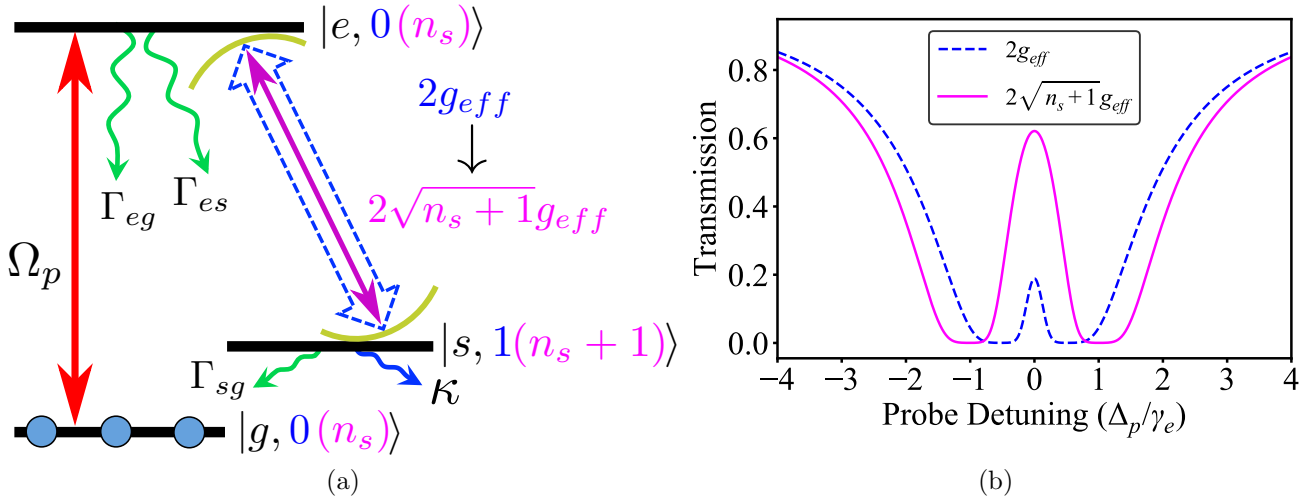

Figure 6.9: (a) Three level scheme for optical switching where the insertion of a single switch photon (shown in purple) into the cavity mode alters $g_{eff} \rightarrow \sqrt{n_s+1}g_{eff}$, $\gamma_e \rightarrow \frac{\Gamma_e}{2} + n_s\kappa$ and $\gamma_s \rightarrow \frac{\Gamma_{sg}}{2} + \frac{\kappa}{2} + n_s\kappa$. (b) The transmission of the probe field is shown to be drastically affected by the presence of a single switch photon to create two distinct transmission states.

the transit time of the probe field. In such as case, the group velocity of the probe and switch no longer need to be matched, instead the lifetime of the cavity photon simply needs to be longer than the transit time of probe pulse, which would be possible assuming low enough decay rates needed to reach the strong coupling regime.

The following sections will discuss two ways of accomplishing this type of switch, the first is when the cavity mode is set on resonance and the second is when it is set far off resonance, the later of which will prove to be a much more versatile method for producing larger contrasts and ultimately will be the superior switching scheme that is explored in this chapter.

6.4.1 On-Resonance Cavity Mode: VIT Switch

Fig. 6.9a shows a switching scheme with only three levels the probe field and cavity set on resonance to the $|g\rangle - |e\rangle$ and $|s\rangle - |e\rangle$ transitions, respectively. A single switching photon is inserted into the cavity to modify the resonant transmission of the weak probe field, as shown in Fig. 6.9b. We can see the reason for this effect by looking at the Hamiltonian (on-resonance) for a single manifold with, for generality, n_s number of switch photons in

the cavity,

$$\tilde{H} = -\hbar\sqrt{n_s+1}g_{eff}(|E,n_s\rangle\langle S,n_s{+}1|{+}|S,n_s{+}1\rangle\langle E,n_s|){-}\hbar\frac{\sqrt{N_a}\Omega_p}{2}(|E,n_s\rangle\langle G,n_s|{+}|G,n_s\rangle\langle E,n_s|) \tag{6.38}$$

where again the dynamics are determined from the master equation of Section 3.5.1

$$\frac{\partial\tilde{\rho}}{\partial t} = -\frac{i}{\hbar}[\tilde{H},\tilde{\rho}] + \Gamma_{eg}\mathcal{L}[\Sigma_{GE}]\tilde{\rho} + \Gamma_{es}\mathcal{L}[\Sigma_{SE}]\tilde{\rho} + \Gamma_{sg}\mathcal{L}[\Sigma_{SG}]\tilde{\rho} + \kappa\mathcal{L}[a]\tilde{\rho} \tag{6.39}$$

The solution to the master equation will reproduce the previously discussed equations for the susceptibility, except that the cavity coupling strength will be replaced with $g_{eff} \to \sqrt{n_s+1}g_{eff}$, and the coherence decay terms must be modified such that $\gamma_e = \frac{\Gamma_e}{2} \to \frac{\Gamma_e}{2}+n_s\kappa$ and $\gamma_s = \frac{\Gamma_{sg}}{2}+\frac{\kappa}{2} \to \frac{\Gamma_{sg}}{2}+\frac{\kappa}{2}+n_s\kappa$. We find the susceptibility (for general detunings) thus to be

$$\chi = \frac{OD}{k_0L}\frac{i\frac{\Gamma_e}{2}}{\gamma_e - i\Delta_p + C} \tag{6.40}$$

keeping the definition of optical depth as $OD = \frac{N}{V}\frac{|\mu_{eg}|^2}{\hbar\epsilon_0\Gamma_e/2}k_0L$, and with

$$C \equiv \frac{(n_s+1)g_{eff}^2}{\gamma_s - i\Delta_{pc}} \tag{6.41}$$

Similar to Section 6.1.1 we can again find the transmission in the absence and presence of the switch photon, T_0 and T_s, respectively, from Eq. 6.40 as

$$T_0 = e^{-OD\cdot B_0} \tag{6.42}$$

where we define

$$B_0 \equiv \frac{\Gamma_e/2}{\gamma_e(0) + \frac{g_{eff}^2}{\gamma_s(0)}} \tag{6.43}$$

and

$$T_s = e^{-OD\cdot B_s} \tag{6.44}$$

with

$$B_s \equiv \frac{\Gamma_e/2}{\gamma_e(n_s) + \frac{(n_s+1)g_{eff}^2}{\gamma_s(n_s)}} \tag{6.45}$$

where we recognize that both $\gamma_e(n_s)$ and $\gamma_s(n_s)$ are functions of the switch photon number.

As per the analysis in the previous sections of this chapter, we have identified two relevant figures of merit in assessing the performance of these optical switches: the transmission ratio, q and contrast, c such that

$$q = \frac{T_0}{T_s} \tag{6.46}$$

and

$$c = T_0 - T_s \tag{6.47}$$

The transmission ratio at varying number of switch photons is plotted in Fig. 6.10a for an optical depth again corresponding to 10^4 atoms in our system, and a cavity decay of $\kappa \sim 0.75\gamma_e$ corresponds to a mirror reflectivity of $R \sim 0.9999$ for the fiber integrated cavities of Chapter 4 and 5. Fig. 6.10b shows the absolute value of the contrast between the transmissions.

For a lower number of switch photons, it is clear that a low decay rate is desirable. Large cavity decay rates result in a decreased transmission ratio because it acts as a decoherent term that reduces the VIT phenomenon and thus both T_s as well as T_0 are decreased, and the ratio between the two can even become $q < 1$. However, the transmissions can become arbitrarily small while still producing a large ratio.

It can be seen from Fig. 6.10 that the certain values of the number of switch photons and cavity decay rates result in $c = 0$ and $q = 1$ ($T_s = T_0$). When a switch photon is added, there are two competing effects that contribute to the resulting transmission. The coupling strength to the cavity is increased, which allows for a larger transmission, however this is also an increase in the decay processes which act to decrease the transmission. For low decay rates and number of switch photons, $T_0 > T_s$ while for larger decay rates and switch photon numbers $T_s > T_0$.

Interestingly, there is a number of switch photons that will allow for an optimal contrast for a given cavity decay rate, which is plotted as the dotted red line in Fig. 6.10b. We can obtain a simple analytical form for this by setting $\frac{\partial c}{\partial n_s} = 0$ and solving for n_s, giving

$$n_s^{max} = -\frac{\alpha}{\kappa} + \frac{g_{eff}}{\kappa^2}\sqrt{\kappa^2 - \alpha\kappa} \tag{6.48}$$

where we define $\alpha = \Gamma_{sg}/2 + \kappa/2$.

Ideally, the optical switch will operator with only a single switch photon, and from these calculations we find maximum contrast of only ~ 0.125 with the current fiber-cavity device. However, one of the device parameters that we have not yet altered is the cavity length. Since $g_{eff} \propto \frac{1}{\sqrt{V_{mode}}}$, changing the length of the fiber will affect the coupling strength to

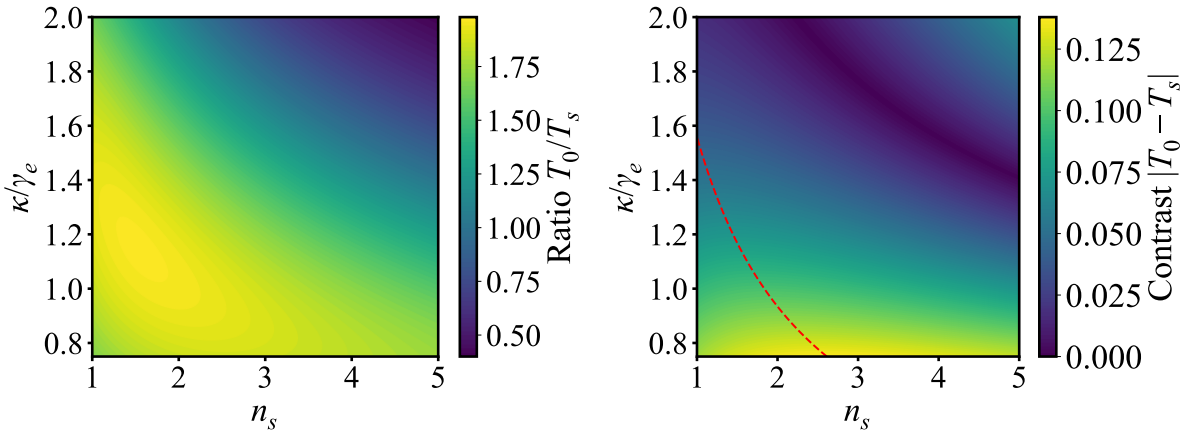

(a) (b)

Figure 6.10: (a) Transmission ratio and (b) absolute value of the contrast as the number of switch photons is changed as well as the cavity decay rate. The optical depth is set to $OD \approx 36.9$, corresponding to about $\sim 10^4$ atoms in a 1cm long HCPCF cavity. The red dotted line represents the number of switch photons that will produce the maximum contrast possible for a given decay rate (Eq. 6.48).

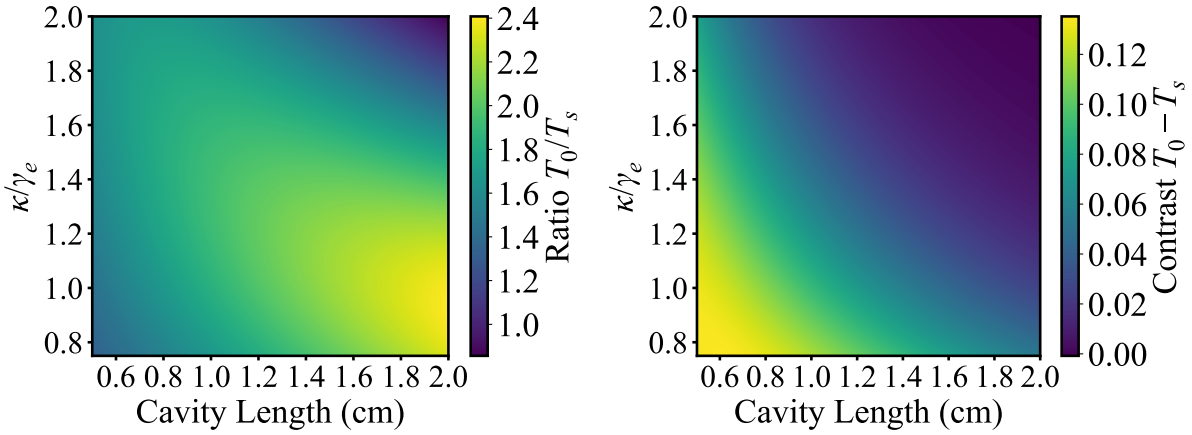

(a) (b)

Figure 6.11: (a) Transmission ratio and (b) contrast for an optical switch in a fiber cavity with varying decay rates and cavity lengths. The number of atoms is set to $N_a = 10^4$ ($OD \sim 37$) and the number of switch photons is set to $n_s = 1$.

the cavity mode. If the density of the atomic cloud within the cavity is kept constant, then the optical depth of the medium will scale linearly with length. We chose to set the number of atoms, rather than density, as a constant because the number of trapped atoms within the MOT cloud before loading into a fiber-cavity is relatively constant.

Fig. 6.11a and 6.11b show the transmission ratio and contrast at different cavity lengths with a constant number of atoms set to 10^4 with the use of only a single switch photon. For relatively low cavity loss rates, the ratio benefits from a larger cavity volume, however, the contrast is reduced. The combination of these results indicates that both the total transmissions of both states of the switch are being reduced for larger mode volumes due to the decrease in coupling strengths.

The on-resonance three level VIT switching scheme presented in this section can merely produce a maximum contrast of ~ 0.125 and ratio ~ 2.4, suggesting that a different scheme will need to be developed to allow for enhanced contrast and ratios. As we will see in the next section, more favourable performances can potentially be obtained by instead setting the cavity to the far off-resonance case.

6.4.2 Off-Resonance Cavity Mode: VIRA Switch

The final section of this chapter will be dedicated to describing the most promising method for producing a single-photon optical switch using an atomic medium in a resonator. Similar to the previous section, we use a simple three level scheme with the vacuum cavity mode coupled to the empty atomic transition [89, 96, 9], as shown in Fig. 6.12a. However, the cavity and probe photons are set to the far off-resonant regime, where the physics of two-photon absorption, as discussed in Section 3.1.4, are relevant.

In this system, the strong control field is again replaced by a vacuum cavity mode, and thus the narrow two-photon absorption peak of the classical field system is instead induced by the vacuum mode in a process we deem Vacuum Induced Raman Absorption (VIRA). The probe photon is stimulated by the vacuum in a Raman transition to the metastable $|s\rangle$ state.

The switching scheme is employed by setting the probe frequency on resonant with this VIRA peak for a given cavity detuning, Δ_c, as shown by the green dot vertical line in Fig. 6.12b. The large absorption (imaginary part of susceptibility) corresponds to a low transmission of the probe photons. When a single switch photon is loaded into the cavity, the effective coupling is again affected in which $2g_{eff} \rightarrow 2\sqrt{n_s+1}g_{eff}$ and the excitation manifold is also increased. This acts to shift the VIRA peak such that the probe field is no longer on the absorption resonance and thus becomes highly transmissive through the atomic cloud.

This dispersive switching scheme benefits from the fact that the VIRA peak can be a very narrow resonance which can be shifted by the presence of even a single switch photon. This allows for a very large alteration in the absorption even if the resonant peak shift is minimal. We can see this easily from the approximated VIRA peak position for the probe detuning (for a given switch photon number, n_s) as

$$\Delta_p^{VIRA}(n_s) = \Delta_c + \frac{(n_s+1)g_{eff}^2}{\Delta_c} \tag{6.49}$$

which can be thought of as the VIT resonance ($\Delta_p = \Delta_c$) but instead with respect to the AC stark shifted metastable $|s\rangle$ state by an amount $\frac{(n_s+1)g_{eff}^2}{\Delta_c}$. The effective width of the VIRA peak can similarly be found as

$$\Gamma_{VIRA}(n_s) = 2\gamma_s + 2\gamma_e\frac{(n_s+1)g_{eff}^2}{\Delta_c^2} \tag{6.50}$$

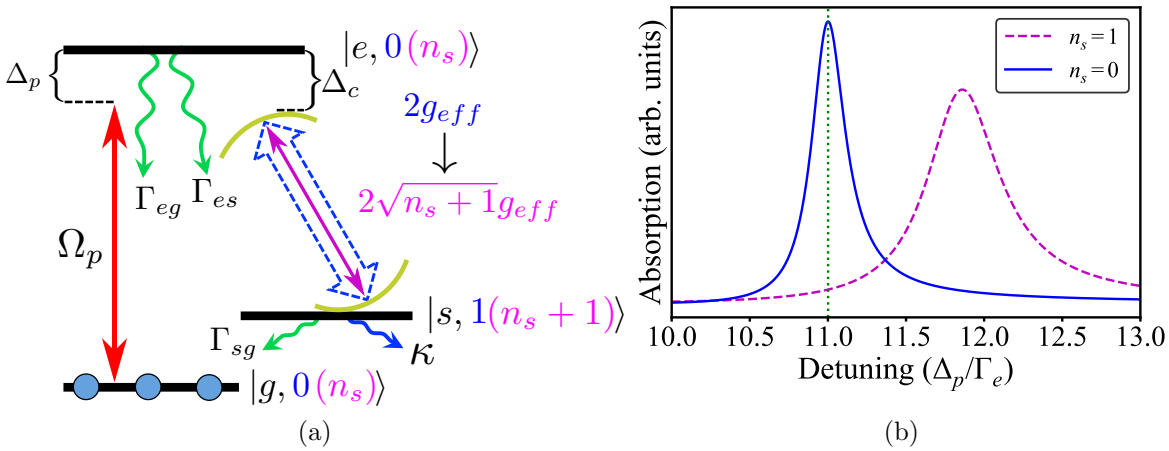

Figure 6.12: (a) Optical switching scheme for a vacuum induced Raman absorption (VIRA) regime three level atom coupled to a cavity mode in the presence and absence of a switch photon, n_s. The two switching states are for zero switch photons in the cavity mode (blue) and one switch photon (purple). (b) Absorption plot of the VIRA switching scheme. The probe field is set on the VIRA resonance for zero cavity switch photons (green dashed line) resulting in a large absorption for $n_s = 0$, while a low absorption occurs for $n_s = 1$ which acts to shift the VIRA peak off resonant from the probe field. ($\Delta_c = 10\Gamma_e$, $\kappa = 0.1\Gamma_e$)

The scattering cross section, σ_{VIRA} of this absorption can be shown (from Eq.3.61 with the appropriate substitutions for a vacuum control field) to be

$$\sigma_{VIRA} = \sigma_0 \frac{\gamma_e \frac{(n_s+1)g_{eff}^2}{\Delta_c^2}}{\gamma_s + \gamma_e \frac{(n_s+1)g_{eff}^2}{\Delta_c^2}} \tag{6.51}$$

with the coherent decay rates, γ_e and γ_s, as defined in the previous section. Interestingly, as $\gamma_s \to 0$, this secondary off-resonant absorption peak can approach the same attenuation as the normal two-level on-resonant absorption peak, but it of course has a much narrower linewidth (Eq. 6.50).

The requirement for a large transmission contrast and ratio will thus be that the VIRA resonant shift created by the presence of the switch photon is much larger than the linewidth

of the VIRA peak, such that for one switch photon

$$\begin{aligned} \Delta_p^{VIRA}(1) - \Delta_p^{VIRA}(0) &\gg \Gamma_{VIRA}(1) \\ \frac{g_{eff}^2}{\Delta_c} &\gg 2\gamma_s + 2\gamma_e \frac{2g_{eff}^2}{\Delta_c^2} \end{aligned} \tag{6.52}$$

Naturally, for a negligible cavity loss rate and metastable linewidth we find from Eq. 6.52 that this requirement is simply $\Delta_c \gg 2\Gamma_e$. This means there is, in general, a minimum cavity detuning we require for a good switch, however as the detuning becomes too large such that $\Delta_c \gg \gamma_e, g_{eff}$, the effective cross section (Eq. 6.51) is reduced giving smaller absorptions and thus there is a (non-trivial) optimal cavity detuning that will maximum the switching performance.

The other main requirement for such a practical switch to operate is that the cavity detuning in which the cavity operates at cannot be larger than half of the free spectral range of the cavity. This is because the driving cavity mode, unlike a classical driving source, has multiple resonant peaks and thus each Fabry-Pérot peak can, in principle, couple to the atomic transition.

For this work we are only considering the coupling to the nearest peak, but this results in the limitation that as $|\Delta_c| > \frac{1}{2}$FSR, the neighbouring resonant peak will then begin to couple to the atomic resonance. The fiber-integrated cavities developed in Chapter 5 have a length of $\sim$ 1cm for an FSR $\sim$ 15 GHz, well within the limit for the cavity detunings considered here.

Transmission Contrast and Ratio

As discussed in the previous sections, the transmission contrast and ratio are the figures of merit that we will consider in this work. Fig. 6.13a and 6.13b show the contrast and ratio, respectively, for this VIRA-based optical switching scheme for a general cavity with a mode area of the hollow core fibers used in this work (diameter of 5.5μm) with decay rates, κ, for 10^4 atoms in a 1 cm length cavity. It is evident that the contrast and ratio can be relatively large for a small cavity decay rate, which can be achieved for some systems.

However, the fiber cavities developed in this thesis are limited by the intrinsic attenuation associated with the HCPCF. It has been recently shown that photonic crystal membranes can be fabricated to achieve a reflectivity of $R \sim 0.9995$[22]. This corresponds to a minimum cavity loss rate to be $\kappa_{min} \sim 0.92\gamma_e$, resulting in a maximum switching contrast of ~ 0.17.

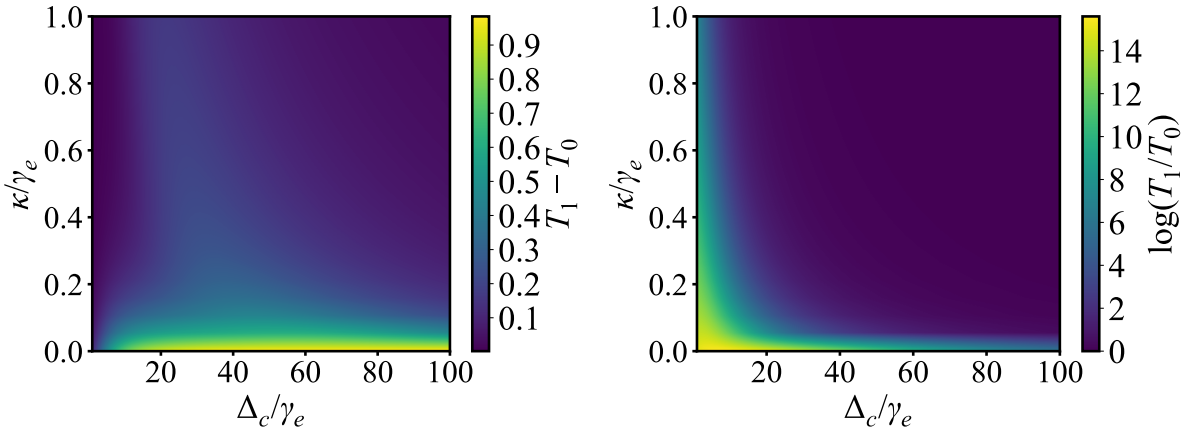

(a) (b)

Figure 6.13: Transmission (a) contrast and (b) ratio for the VIRA-based optical switching scheme. A cavity length of 1 cm with 10^4 atoms in a cavity (OD$\sim$ 37) with a mode area diameter of 5.5μm is used for these calculations.

In addition to finding the optimal cavity detuning, the coupling strength can also be altered by again simply changing the length of the cavity to affect the cavity mode volume. We plot the switching contrast and ratio different cavity lengths for various cavity detunings at $\kappa = 0.92\gamma_e$ in Fig. 6.14a and 6.14b, respectively. The observed trends become non-trivial because in addition to tuning the cavity coupling rate, g_{eff}, adjusting the cavity length will also affect the total optical depth (assuming a constant number of atoms are still loaded).

Interestingly, the transmission contrast and ratio seem to exhibit somewhat complimentary behaviour in certain regions. The transmission ratio is largest for small cavity detunings, while large contrast require slightly increased values for the cavity detuning. This is because at small detunings the transmission becomes drastically reduced due to the overlap between the absorption peaks of the two switching states, causing the ratio between the transmissions of the two states to become extremely large.

However, there exists a region (red outlined region in Fig. 6.14) that allows for a moderately large contrast and ratio of ~ 0.7 and $\sim 10^7$, respectively for cavity lengths of $\sim$ 1mm. It should be noted that these values can become much larger if it is feasible to make fiber-cavities with a length much smaller than 1 mm, although this would introduce new technical challenges and the current mounting method described in Section 5.2.2 would

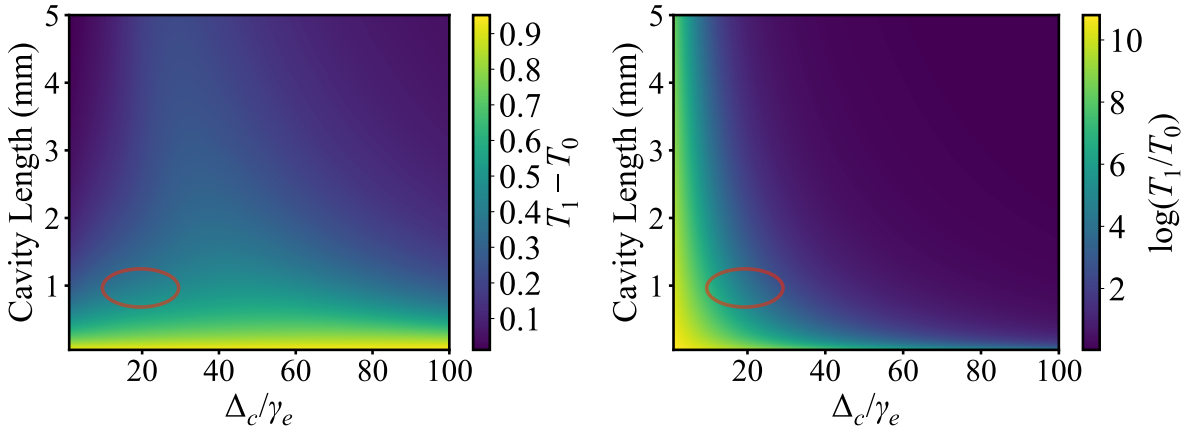

(a) (b)

Figure 6.14: Transmission (a) contrast and (b) ratio for various cavity lengths which act to alter the coupling coefficient, g_{eff}, as well as the optical depth for a constant number of atoms set to 10^4, with $\kappa = 0.92\gamma_e$ and a mode diameter of 5 μm. The regions inside the red ellipses represent the parameter space that can simultaneously achieve relatively high values for both contrast and ratio.

need to be heavily modified. In general, this switching scheme can potentially lead to much larger contrast and ratios in other cavity systems that have a reduced cavity loss rate, such as free space cavities.

6.5 Conclusion

We have explored all-optical switching schemes in both a four-level and and a three-level system. The use of the coupling vacuum cavity mode to the atomic system means that a strong classical bias field is no longer required, as is the case in previously demonstrated optical switching schemes. The four-level switches, however, suffer from complications when using pulsed fields due to the difficulties in matching the group velocities of the switch and probe pulses. These schemes also, in general, require many switch photons and have low transmission contrast and ratios.

The described three-level switching schemes provide much larger switching contrast and ratios by using a far-detuned cavity mode Raman transition. They also eliminate the need to match group velocities by instead inserting a single photon into the cavity mode in order to switch the atomic medium from being highly absorptive to highly transmissive.

This particular optical switching process is naturally suited for a device such as the polarization-selective fiber-integrated cavities discussed in Chapter 5. The probe field can be sent along the longitudinal axis of the atomic cloud to allow for high optical depths by setting photons to the polarization that is transmissive to the PC mirrors allowing for interaction with the atoms in effectively free space. The switching photons are then sent at the orthogonal highly reflective polarization to be inserted into the cavity mode. However, it should be noted that in our fiber cavity systems, the cavity loss rate is limited by the attenuation of the HCPCF media. Conversely, in other cavity systems with much lower cavity decay rates, the VIRA-based switching scheme discussed here may produce a much larger contrast and ratio than we reported for our fiber cavity devices.

Such an optical switch can even be useful in other applications such as quantum non-demolition experiments [76]. The presence of a single photon in the cavity mode can be determined simply by monitoring the transmission of the probe field. Other applications may also include single-photon phase gates [86] by taking advantage of the large dispersions that occur at the VIT and VIRA resonance peaks.

Chapter 7

Conclusions and Outlook

7.1 Summary

The work presented in this thesis demonstrates novel techniques for developing unique optical resonators that may facilitate the enhancement of light-matter interactions. This is enabled by the tight confinement provided by the small mode area of the fundamental mode supported by hollow core photonic crystal fibers (HCPCF). The other main feature of the mirrors used to make these fiber-based cavities is that the hollow core is also left unobstructed to allow for the loading of an atomic ensemble into the cavity. This research can be summarized into three main projects:

1. A fiber-integrated cavity is shown to be possible using Bragg mirrors at each end of the fiber segment. In order to modulate the effective refractive index to form a Bragg reflector, a thin layer of material (e.g. resist) may be used to coat the inner core walls and modulated periodically along the axis of the fiber. We show that such a device is indeed possible to reach the strong coupling regime by finely tuning the thickness of this coating layer.

2. We successfully demonstrated a novel type of fiber-integrated resonator in which highly reflective photonic crystal membranes are designed, fabricated, and mounted onto a fiber segment to form a Fabry-Pérot cavity within the fiber. It is also shown that these photonic crystal membranes can be made to have a large polarization dependence which may be used to produce a polarization-selective cavity, permitting all light signals to be sent along the high optical depth axis of the atomic ensemble.

3. Several unique schemes for establishing a single-photon all-optical switch are discussed and explored by replacing a strong control bias field with a vacuum cavity mode. We find that a scheme involving the far off-resonant Raman transitions enabled by a vacuum cavity mode can allow for large transmission contrasts and ratios of a signal probe using a single photon injected into the cavity mode as a switch. The implementation of such a scheme would benefit from the use of the polarization-selective fiber-integrated cavities that are developed in this work.

7.2 Future Directions

Each of the above separate projects offer various avenues that may be explored in future work. The obvious next steps in progressing the project involving the development of a fiber cavity formed using Bragg layers within the fiber is to fabricate such a device. We briefly discussed the possibility of using a pressure sensitive technique to eject resist through the hollow core of the fiber to controllably dispense a thin coating of material on the core walls. Once this is accomplished, interference lithography implemented with two properly angled ultraviolet laser beams illuminating the fiber from the side may be used to create a standing wave interference pattern to periodically develop the resist, after which the hollow core may be flushed with developer to leave regularly spaced rings of resist. Admittedly this fabrication procedure may require a substantial development to achieve the needed high degree of controllability and repeatability.

There are two main areas of advancement for the fiber-integrated cavities formed with PC mirrors. The first means of improvement is to fabricate the PC membranes to produce higher reflectivities. One obvious path forward may be to alter the fabrication procedure, such as employing critical point drying after the KOH wet etch in order to reduce the risk of breaking or cracking the membranes during drying as well as to leave a cleaner surface devoid of any debris.

The other possibility is to develop a more resilient and effective design for the PC pattern. This would include finding dimensions that will produce a high reflectivity with broader tolerance in the acceptable pattern dimensions, since the exact desired sizes can be difficult to fabricate precisely. In addition, parameter dimensions that leave larger bridges of material will act to structurally strengthen the membrane to further prevent any breaking and cracking of the film. One possible route forward may be to use spatially variable pattern dimensions across the film, such as a radially dependent lattice constant and/or hole size. This may even address the difficulties in making a pattern that is highly reflective for an input Gaussian mode shape.

Further development of the polarization dependent fiber cavities using asymmetric PC mirrors also provides a rich medium for possible technical advancement. Again efforts may be made to possibly design and fabricate the PC mirrors to have a larger polarization selectivity. However, the more immediate improvement needs to be in finding a more reliable and accurate means of mounting these membranes to the fiber faces with the correct alignment with respect to each PC mirror axis as well as to the fiber birefringent axis. One potential approach that such a mounting process may utilize would be to actively monitor the power of coupled light through the fiber that is reflected back from the PC mirror while rotating the mirror itself until the reflected light has the correct polarization and the power is maximized.

Once either the Bragg mirror-based or PC mirror-based fiber cavities are fabricated with the required specifications to allow for large nonlinearities at the few photon level, there are several interesting experiments that may be carried out by loading cold cesium atoms into the cavities from the MOT system using the gravity loading technique discussed in Chapter 5. Primarily, as discussed in Chapter 6, a polarization dependent fiber cavity that can reach the strong coupling may be used for an efficient single photon switch.

Unfortunately, the current fiber-based cavities using PC membranes do not yet have a high enough finesse to reach the strong coupling regime and are instead in the weak coupling and low cooperativity regimes, $\frac{g^2}{\kappa\gamma} \ll 1$. Nonetheless, several interesting effects can be demonstrated with cavities occupying these regimes. One such phenomenon is superradiance and specifically, superradiant lasing within the cavity. These experiments require low cooperativity, in which our device has $\frac{g^2}{\kappa\gamma} \sim 10^{-2}$, as well as collective cooperativity, $N_a \frac{g^2}{\kappa\gamma} \gg 1$, which may be possible with the previously demonstrated loading of $N_a \sim 10^4$ cesium atoms into a HCPCF with our MOT system.

It should be conceded that such a loading efficiency may be somewhat optimistic as the consequence of have a perforated membrane partially obstructing the entrance to the hollow core will most likely be to reduce the total number of atoms loaded. However, the exact impact of this complication remains to be determined and would require further investigation. It would also be beneficial to examine the cavity QED system in more depth, such as how the dipole trap beam shape will be modified as it passes through the PC membranes. Moreover, other possible means to increase the previously shown number of atoms loaded by our MOT setup may be explored. For example, increasing the dipole trap depth by using larger powers or near red-detuned frequencies may increase loading efficiencies, as well as forming larger initial MOT clouds with optimal trapping settings.

These fiber-based cavities discussed in this thesis were all specifically designed to be utilized with laser-cooled cesium atoms to create large optical nonlinearities. At the same

time, there are other applications which can benefit from cavities integrated into hollow-core fibers. One example of such an application would be fiber-integrated gas lasers that can be formed by filling these cavities with room-temperature gas. For example, a cavity designed for a wavelength of $\sim$ 1500 nm, where the transition frequencies of acetylene molecules can be found, would be a platform for fiber-integrated lasers in the telecom S- and C- bands [41, 55, 74]. Similarly, these cavities could be used to enhance the operation of the recently demonstrated ultraviolet light sources based on plasma generated inside large-diameter hollow-core fibers through RF discharge in Xenon gas [11, 48].

References

[1] A. Arbabi, Y. Horie, M. Bagheri, and A. Faraon. Dielectric metasurfaces for complete control of phase and polarization with subwavelength spatial resolution and high transmission. *Nature Nanotechnology*, 10:937–943, 2015.

[2] E. Arimondo. V coherent population trapping in laser spectroscopy. *Progress in Optics*, 35:257–354, 1996.

[3] M. Bader, S. Heugel, A. L. Chekhov, M. Sondermann, and G. Leuchs. Efficient coupling to an optical resonator by exploiting time-reversal symmetry. *New Journal of Physics*, 15:0–10, 2013.

[4] H. V. Baghdasaryan, T. M. Knyazyan, T. H. Baghdasaryan, B. Witzigmann, and F. Roemer. Absorption loss influence on optical characteristics of multilayer distributed bragg reflector: wavelength-scale analysis by the method of single expression. *Opto-Electronics Review*, 18(4):438–445, 2010.

[5] M. Bajcsy, S. Hofferberth, V. Balic, T. Peyronel, M. Hafezi, a. S. Zibrov, V. Vuletic, and M. D. Lukin. Efficient all-optical switching using slow light within a hollow fiber. *Physical Review Letters*, 102(20):1–4, 2009.

[6] M. Bajcsy, S. Hofferberth, T. Peyronel, V. Balic, Q. Liang, a. S. Zibrov, V. Vuletic, and M. D. Lukin. Laser-cooled atoms inside a hollow-core photonic-crystal fiber. *Physical Review A*, 83(6):1–9, 2011.

[7] G. Bappi, J. Flannery, R. Al Maruf, and M. Bajcsy. Prospects and limitations of bottom-up fabricated hollow-core waveguides. *Optical Materials Express*, 7:148, 2017.

[8] Y. O. Barmenkov, D. Zalvidea, S. Torres-Peiró, J. L. Cruz, and M. V. Andrès. Effective length of short fabry-perot cavity formed by uniform fiber bragg gratings. *Optics Express*, 14:6394–6399, 2006.

[9] O. Bechler, A. Borne, S. Rosenblum, G. Guendelman, O. E. Mor, M. Netser, T. Ohana, A. Aqua, N. Drucker, R. Finkelstein, Y. Lovsky, R. Bruch, D. Gurovich, E. Shafir, and B. Dayan. A passive photonatom qubit swap operation. *Nature Physics*, 14(October), 2018.

[10] F. Benabid and P. J. Roberts. Linear and nonlinear optical properties of hollow core photonic crystal fiber. *Journal of Modern Optics*, 58:87–124, 2011.

[11] G. Benabid, F. Gerome, B. Debord, and M. Alharbi. Kagome PC fiber goes to extremes for ultrashort-pulse lasers. *Fiber for Fiber Lasers*, 2014.

[12] Mohammad H Bitarafan and Ray G Decorby. 3-D microcavitites in on-chip hollow waveguides using cutoff-based mirrors. 18(24):24917, 2017.

[13] F. Blatt, T. Halfmann, and T. Peters. One-dimensional ultracold medium of extreme optical depth. *Optics letters*, 39(3):446–449, 2014.

[14] F. Blatt, L. S. Simeonov, T. Halfmann, and T. Peters. Stationary light pulses and narrowband light storage in a laser-cooled ensemble loaded into a hollow-core fiber. *Physical Review A*, 94:1–9, 2016.

[15] J. G. Bohnet, Z. Chen, J. M. Weiner, D. Meiser, M. J. Holland, and J. K. Thompson. A steady-state superradiant laser with less than one intracavity photon. *Nature*, 484:79, 2012.

[16] K.-J. Boller, A. Imamoğlu, and S. E. Harris. Observation of electromagnetically induced transparency. *Physical Review Letters*, 66(20):2593, 1991.

[17] D. Bouwmeester, A. Ekert, and A. Zeilinger. *The physics of quantum information*. Springer, 2000.

[18] R. W. Boyd. Material slow light and structural slow light: similarities and differences for nonlinear optics. *JOSA B*, 28(12):A38–A44, 2011.

[19] D. E. Chang, V. Vuletić, and M. D. Lukin. Quantum nonlinear optics — photon by photon. *Nature Photonics*, 8(9):685–694, 2014.

[20] C. J. Chang-Hasnain and W. Yang. High-contrast gratings for integrated optoelectronics. *Advances in Optics and Photonics*, 4:379–440, 2012.

[21] W. Chen, K. M. Beck, R. Bücker, M. Gullans, M. D. Lukin, H. Tanji-Suzuki, and V. Vuletić. All-optical switch and transistor gated by one stored photon. *Science*, 341:768, 2013.

[22] Xu Chen, Clément Chardin, Kevin Makles, Charles Caër, Sheon Chua, Rémy Braive, Isabelle Robert-Philip, Tristan Briant, Pierre-François Cohadon, Antoine Heidmann, T. Jacqmin, and S. Deleglise. High-finesse fabry-perot cavities with bidimensional si3n4 photonic-crystal slabs. *Light: Science & Applications*, 6(1), 2017.

[23] C. Christensen, S. Will, M. Saba, G. Jo, Y. Shin, W. Ketterle, and D. Pritchard. Trapping of ultracold atoms in a hollow-core photonic crystal fiber. *Physical Review A*, 78, 2008.

[24] C. M. B. Cordeiro, E. M. dos Santos, C. H. Brito Cruz, C. J. de Matos, and D. S. Ferreiira. Lateral access to the holes of photonic crystal fibers – selective filling and sensing applications. *Opt. Express*, 14(18):8403–8412, Sep 2006.

[25] R. F. Cregan, B. J. Mangan, J. C. Knight, T. A. Birks, P. St. J. Russell, P. J. Roberts, and D. C. Allan. Single-mode photonic band gap guidance of light in air. *Science*, 285(5433):1537–1539, 1999.

[26] R. H. Dicke. Coherence in spontaneous radiation processes. *Physical Review*, 93(1):99, 1954.

[27] P. Domokos, J.-M. Raimond, M. Brune, and S. Haroche. Simple cavity-qed two-bit universal quantum logic gate: The principle and expected performances. *Physical Review A*, 52(5):3554, 1995.

[28] M. D. Eisaman. Md eisaman, a. andré, f. massou, m. fleischhauer, as zibrov, and md lukin, nature (london) 438, 837 (2005). *Nature (London)*, 438:837, 2005.

[29] S. Fan and J. Joannopoulos. Analysis of guided resonances in photonic crystal slabs. *Physical Review B*, 65(23), 2002.

[30] S. Fan, W. Suh, and J. D. Joannopoulos. Temporal coupled-mode theory for the Fano resonance in optical resonators. *Journal of the Optical Society of America. A, Optics, Image Science, and Vision*, 20(3):569–572, 2003.

[31] J. E. Field. Vacuum-rabi-splitting-induced transparency. *Physical Review A*, 47(6):5064, 1993.

[32] J. Flannery, G. Bappi, V. Bhaskara, O. Alshehri, and M. Bajcsy. Implementing bragg mirrors in a hollow-core photonic-crystal fiber. *Optical Materials Express*, 7:1198, 2017.

[33] Jeremy Flannery, Rubayet Al Maruf, Taehyun Yoon, and Michal Bajcsy. Fabry-Perot Cavity Formed with Dielectric Metasurfaces in a Hollow-Core Fiber. *ACS Photonics*, 2017.

[34] M. Fleischhauer, A. Imamoglu, and J. Marangos. Electromagnetically induced transparency: Optics in coherent media. *Reviews of Modern Physics*, 77(2):633–673, 2005.

[35] R. Folman, P. Kruger, J. Schmiedmayer, J. Denschlag, and C. Henkel. Microscopic atom optics: From wires to an atom chip. *Advances in Atomic, Molecular and Optical Physics*, 48(C):263–356, 2008.

[36] M. Fox. *Quantum optics: An Introduction*, volume 15. OUP Oxford, 2006.

[37] L. B. Fu, G. D. Marshall, J. A. Bolger, P. Steinvurzel, E. C. Mägi, M. J. Withford, and B. J. Eggleton. Femtosecond laser writing bragg gratings in pure silica photonic crystal fibres. *Electronics Letters*, 41(11):638–640, 2005.

[38] I. Fushman, D. Englund, A. Faraon, N. Stoltz, P. Petroff, and J. Vučković. Controlled phase shifts with a single quantum dot. *science*, 320(5877):769–772, 2008.

[39] C. W. Gardiner, A. S. Parkins, and P. Zoller. Wave-function quantum stochastic differential equations and quantum-jump simulation methods. *Physical Review A*, 46(7), 1992.

[40] s. Ghosh, A. R. Bhagwat, C. K. Renshaw, S. Goh, A. L. Gaeta, and B. J. Kirby. Low-light-level optical interactions with rubidium vapor in a photonic band-gap fiber. *Physical Review Letters*, 97(2):023603, 2006.

[41] S. Ghosh, J. E. Sharping, D. G. Ouzounov, and A. L. Gaeta. Resonant optical interactions with molecules confined in photonic band-gap fibers. *Physical Review Letters*, 94(9):093902, 2005.

[42] A. Goban, C.-L. Hung, S.-P. Yu, J. D. Hood, J. A. Muniz, J. H. Lee, M. J. Martin, A. C. McClung, K. S. Choi, D. E. Chang, O. Painter, and H. J. Kimble. Atom–light interactions in photonic crystals. *Nature Communications*, 5:3808, 2014.

[43] B. Gouraud, D. Maxein, A. Nicolas, O. Morin, and J. Laurat. Demonstration of a memory for tightly guided light in an optical nanofiber. *Physical Review Letters*, 114(18):180503, 2015.

[44] C. M. Haapamaki, J. Flannery, G. Bappi, R. Al. Maruf, S. V. Bhaskara, O. Alshehri, T. Yoon, and M. Bajcsy. Mesoscale cavities in hollow-core waveguides for quantum optics with atomic ensembles. *Nanophotonics*, 2016.

[45] S. E. Harris, J. E. Field, and A. Imamoğlu. Nonlinear optical processes using electromagnetically induced transparency. *Physical Review Letters*, 64(10):1107, 1990.

[46] G. Hasnain, K. Tai, L. Yang, Y. H. Wang, R. J. Fischer, J. D. Wynn, B. Weir, N. K. Dutta, and A. Y. Cho. Performance of gain-guided surface emitting lasers with semiconductor distributed bragg reflectors. *IEEE journal of quantum electronics*, 27(6):1377–1385, 1991.

[47] L. V. Hau, S. E. Harris, Z. Dutton, and C. H. Behroozi. Light speed reduction to 17 metres per second in an ultracold atomic gas. *Nature*, 397(6720):594, 1999.

[48] O. H. Heckl, C. R. E. Baer, C. Kränkel, S. V. Marchese, F. Schapper, M. Holler, T. Südmeyer, J. S. Robinson, J. W. G. Tisch, F. Couny, P. Light, F. Benabid, and U. Keller. High harmonic generation in a gas-filled hollow-core photonic crystal fiber. *Applied Physics B: Lasers and Optics*, pages 369–373, 2009.

[49] S. M. Hendrickson, T. B. Pittman, and J. D. Franson. Microcavities using holey fibers. *Journal of Lightwave Technology*, 25(10):3068–3071, 2007.

[50] K. Hirao and K. Miura. Writing waveguides and gratings in silica and related materials by a femtosecond laser. *Journal of Non-Crystalline Solids*, 239(1):91–95, 1998.

[51] C. J. Hood, H. J. Kimble, and J. Ye. Characterization of high-finesse mirrors: Loss, phase shifts, and mode structure in an optical cavity. *Physical Review A*, 64:033804, 2001.

[52] O. Hosten, N. J. Engelsen, R. Krishnakumar, and M. A. Kasevich. Measurement noise 100 times lower than the quantum-projection limit using entangled atoms. *Nature*, 529:505–508, 2016.

[53] Y. Huang, Y. Xu, and A. Yariv. Fabrication of functional microstructured optical fibers through a selective-filling technique. *Applied Physics Letters*, 85(22):5182–5184, 2004.

[54] J. D. Joannopoulos, R. D. Meade, and J. N. Winn. *Photonic Crystals: Modling the Flow of Light*. Princeton University Press, 1995.

[55] A. M. Jones, A. V. V. Nampoothiri, A. Ratanavis, T. Fiedler, N. V. Wheeler, F. Couny, R. Kadel, F. Benabid, B. R. Washburn, K. L. Corwin, and W. Rudolph. Mid-infrared gas filled photonic crystal fiber laser based on population inversion. 19(3):399–402, 2011.

[56] M. M. Kash, V. A. Sautenkov, A. S. Zibrov, L. Hollberg, G. R. Welch, M. D. Lukin, Y. Rostovtsev, E. S. Fry, and M. O. Scully. Ultraslow group velocity and enhanced nonlinear optical effects in a coherently driven hot atomic gas. *Physical Review Letters*, 82(26):5229, 1999.

[57] O. Kilic, M. J. F. Digonnet, G. S. Kino, and O. Solgaard. Miniature photonic-crystal hydrophone optimized for ocean acoustics. *The Journal of the Acoustical Society of America*, 129:1837–1850, 2011.

[58] H. J. Kimble. Strong Interactions of Single Atoms and Photons in Cavity QED. *Physica Scripta*, T76(1):127, 1998.

[59] B. T. Kuhlmey, B. J. Eggleton, and D. K. C. Wu. Fluid-filled solid-core photonic bandgap fibers. *Journal of Lightwave Technology*, 27(11):1617–1630, Jun 2009.

[60] J. Laegsgaard and P. J. Roberts. Dispersive pulse compression in hollow-core photonic bandgap fibers. *Optics express*, 16(13):9628–9644, 2008.

[61] M. Lee, J. Kim, W. Seo, H.-G. Hong, Y. Song, R. R. Dasari, and K. An. Three-dimensional imaging of cavity vacuum with single atoms localized by a nanohole array. *Nature communications*, 5:3441, 2014.

[62] I. D. Leroux, M. H. Schleier-Smith, and V. Vuletić. Implementation of cavity squeezing of a collective atomic spin. *Physical Review Letters*, 104:073602, 2010.

[63] Y.-J. Lin, I. Teper, C. Chin, and V. Vuletić. Impact of the casimir-polder potential and johnson noise on bose-einstein condensate stability near surfaces. *Physical Review Letters*, 92(5):050404, 2004.

[64] C. Liu, Z. Dutton, C. H. Behroozi, and L. V. Hau. Observation of coherent optical information storage in an atomic medium using halted light pulses. *Nature*, 409(6819):490, 2001.

[65] C. Liu, Y. Sun, L. Zhao, S. Zhang, M. M. T. Loy, and S. Du. Efficiently loading a single photon into a single-sided fabry-perot cavity. *Physical Review Letters*, 113(3):1–5, 2014.

[66] V. Lousse, W. Suh, O. Kilic, S. Kim, O. Solgaard, and S. Fan. Angular and polarization properties of a photonic crystal slab mirror. *Optics Express*, 12(8):1575–82, apr 2004.

[67] M. D. Lukin and A. Imamoğlu. Controlling photons using electromagnetically induced transparency. *Nature*, 413, 2001.

[68] J. P. Marangos. Electromagnetically induced transparency. *Journal of Modern Optics*, 45(3):471–503, 1998.

[69] C. Martelli, J. Canning, N. Groothoff, and K. Lyytikainen. Strain and temperature characterization of photonic crystal fiber bragg gratings. *Optics Letters*, 30(14):1785–1787, 2005.

[70] R. Al Maruf and M. Bajcsy. On-chip splicer for coupling light between photonic crystal and solid-core fibers. *Appl. Opt.*, 56(16):4680–4684, Jun 2017.

[71] D. A. B. Miller. Are optical transistors the logical next step? *Nature Photonics*, 4(1):3, 2010.

[72] J. P. Balthasar Mueller, N. A. Rubin, R. C. Devlin, B. Groever, and F. Capasso. Metasurface polarization optics: Independent phase control of arbitrary orthogonal states of polarization. *Physical Review Letters*, 113901:1–5, 2017.

[73] K. Nagayama, M. Kakui, M. Matsui, T. Saitoh, and Y. Chigusa. Ultra-low-loss (0.1484 db/km) pure silica core fibre and extension of transmission distance. *Electronics Letters*, 38(20):1168–1169, 2002.

[74] A. V. V. Nampoothiri, A. M. Jones, C. Mao, N. Dadashzadeh, B. Baumgart, Y. Y. Wang, M. Alharbi, T. Bradley, N. Campbell, F. Benabid, B. R. Washburn, K. L. Corwin, and W. Rudolph. Hollow-core optical fiber gas lasers (HOFGLAS): a review [Invited]. *Optical Materials Express*, 2(7):948–961, 2012.

[75] K. P. Nayak, M. Sadgrove, R. Yalla, F. Le Kien, and K. Hakuta. Nanofiber quantum photonics. *Journal of Optics*, 20(7):073001, 2018.

[76] G. Nogues, A. Rauschenbeutel, S. Osnaghi, M. Brune, J. M. Raimond, and S. Haroche. Seeing a single photon without destroying it. *Nature*, 400(6741):239, 1999.

[77] M. A. Norcia, M. N. Winchester, J. R.K. Cline, and J. K. Thompson. Superradiance on the millihertz linewidth strontium clock transition. *Science Advances*, 2(10):37–40, 2016.

[78] E. Obrzud, S. Lecomte, and T. Herr. Temporal solitons in microresonators driven by optical pulses. *arXiv*, page 1612.08993v1, 2016.

[79] s. Okaba, T. Takano, F. Benabid, T. Bradley, L. Vincetti, Z. Maizelis, V. Yampol'Skii, F. Nori, and H. Katori. Lamb-dicke spectroscopy of atoms in a hollow-core photonic crystal fibre. *Nature Communications*, 5:4096, 2014.

[80] A. Othonos. Fiber Bragg gratings. *Review of Scientific Instruments*, 68(12):4309–4341, 1997.

[81] C. Ottaviani, S. Rebi, D. Vitali, and P. Tombesi. Cross phase modulation in a five level atomic medium : semiclassical theory. *The European Physical Journal D*, 296:281–296, 2006.

[82] D. A. Oulianov, I. V. Tomov, A. S. Dvornikov, and P. M. Rentzepis. Observations on the measurement of two-photon absorption cross-section. *Optics Communications*, 191(3-6):235–243, 2001.

[83] T. Pellizzari, S. A. Gardiner, J. I. Cirac, and P. Zoller. Decoherence, continuous observation, and quantum computing: A cavity qed model. *Physical Review Letters*, 75(21):3788, 1995.

[84] T. Peters, T. P. Wang, A. Neumann, L. S. Simeonov, and T. Halfmann. Stopped and stationary light at the single-photon level inside a hollow-core fiber. *arXiv preprint arXiv:1906.05771*, 2019.

[85] E. M. Purcell and H. C. Torrey. Proceedings of the american physical society. *Phys. Rev*, 69(11-12):674–674, 1946.

[86] A. Rauschenbeutel, G. Nogues, S. Osnaghi, P. Bertet, M. Brune, J. M. Raimond, and S. Haroche. Coherent operation of a tunable quantum phase gate in cavity qed. *Physical Review Letters*, 83(24):5166, 1999.

[87] P. R. Rice and R. J. Brecha. Cavity induced transparency. pages 587–588. Springer, 1996.

[88] P. Roberts, F. Couny, H. Sabert, B. Mangan, D. Williams, L. Farr, M. Mason, A. Tomlinson, T. Birks, J. Knight, and P. St. J . Russell. Ultimate low loss of hollow-core photonic crystal fibres. *Optics Express*, 13(1):236–244, 2005.

[89] S. Rosenblum, A. Borne, and B. Dayan. Analysis of deterministic swapping of photonic and atomic states through single-photon Raman interaction. *Physical Review A*, 033814:1–11, 2017.

[90] C. Sayrin, C. Clausen, B. Albrecht, P. Schneeweiss, and A. Rauschenbeutel. Storage of fiber-guided light in a nanofiber-trapped ensemble of cold atoms. *Optica*, 2(4):353–356, 2015.

[91] P. Schneeweiss, S. Zeiger, T. Hoinkes, A. Rauschenbeutel, and J. Volz. Fiber ring resonator with a nanofiber section for chiral cavity quantum electrodynamics and multimode strong coupling. *Optics Letters*, 42(1):85–88, Jan 2017.

[92] M. O. Scully and M. S. Zubairy. *Quantum Optics*. Cambridge University Press, 1997.

[93] S. Shabahang, G. Tao, Joshua J. Kaufman, Y. Qiao, L. Wei, T. Bouchenot, A. P. Gordon, Y. Fink, Y. Bai, R. S. Hoy, and A. F. Abouraddy. Controlled fragmentation of multimaterial fibres and films via polymer cold-drawing. *Nature*, 534(7608):1–24, 2016.

[94] G. Shambat, J. Provine, K. Rivoire, T. Sarmiento, J. Harris, and J. Vučković. Optical fiber tips functionalized with semiconductor photonic crystal cavities. *Applied Physics Letters*, 99(19):191102, 2011.

[95] Y. R. Shen. Quantum statistics of nonlinear optics. *Physical Review*, 155(3):921, 1967.

[96] I. Shomroni, S. Rosenblum, Y. Lovsky, O. Bechler, G. Guendelman, and B. Dayan. All-optical routing of single photons by a one-atom switch controlled by a single photon. *Science*, 345(6199):542–546, 2014.

[97] J. Simon. *Cavity QED with atomic ensembles*. Harvard University, 2010.

[98] A. D. Slepkov, A. R. Bhagwat, V. Venkataraman, P. Londero, and A. L. Gaeta. Generation of large alkali vapor densities inside bare hollow-core photonic band-gap fibers. *Optics Express*, 16:18976, 2008.

[99] H. R. Sørensen, J. Canning, J. Lægsgaard, K. Hansen, and P. Varming. Liquid filling of photonic crystal fibres for grating writing. *Optics Communications*, 270(2):207–210, 2007.

[100] M. R. Sprague, P. S. Michelberger, T. F. M. Champion, D. G. England, J. Nunn, X.-M. Jin, W. S. Kolthammer, a. Abdolvand, P. St. J. Russell, and I. a. Walmsley. Broadband single-photon-level memory in a hollow-core photonic crystal fibre. *Nature Photonics*, 8(4):287–291, 2014.

[101] D. A. Steck. Cesium D Line Data. available online at http://stech.us/alkalidata. (revision 2.1.4, 23 December 2010).

[102] D. A. Steck. *Classical and Modern Optics*. available online at http://steck.us/teaching, 2016.

[103] K. Sugioka and Y. Cheng. Femtosecond laser processing for optofluidic fabrication. *Lab on a Chip*, 12(19):3576–3589, 2012.

[104] T. Takekoshi and R. J. Knize. Optical guiding of atoms through a hollow-core photonic band-gap fiber. *Physical Review Letters*, 210404:3–6, 2007.

[105] H. Tanji. 2011.

[106] H. Tanji-Suzuki, W. Chen, R. Landig, J. Simon, and V. Vuletić. Vacuum-induced transparency. *Science*, 333:1266, 2011.

[107] H. Tanji-Suzuki, I. D. Leroux, M. H. Schleier-Smith, M. Cetina, A. Grier, J. Simon, and V. Vuletić. Interaction between atomic ensembles and optical resonators: Classical description. *Advances in Atomic, Molecular and Optical Physics*, 60:201, 2011.

[108] H. Tanji-Suzuki, Ian D. Leroux, M.H. Schleier-Smith, M. Cetina, A.T. Grier, J. Simon, and V. Vuletić. Interaction between Atomic Ensembles and Optical Resonators: Classical Description. *Advances in Atomic, Molecular and Optical Physics*, 60:201–237, 2011.

[109] M. Tavis and F. W. Cummings. Exact solution for an n-moleculeradiation-field hamiltonian. *Physical Review*, 170(2):379, 1968.

[110] R. J. Thompson, G. Rempe, and H. J. Kimble. Observation of normal-mode splitting for an atom in an optical cavity. *Physical Review Letters*, 68(8):1132, 1992.

[111] A. M. Vadiraj. High Frequency readout scheme for Graphene based NEMS. (July), 2012.

[112] V. Venkataraman, K. Saha, and A. L. Gaeta. Phase modulation at the few-photon level for weak-nonlinearity-based quantum computing. *Nature Photonics*, 7:138–141, 2013.

[113] E. Vetsch, D. Reitz, G. Sagué, R. Schmidt, S. T. Dawkins, and A. Rauschenbeutel. Optical interface created by laser-cooled atoms trapped in the evanescent field surrounding an optical nanofiber. *Physical Review Letters*, 104(20):203603, 2010.

[114] T. Volz, A. Reinhard, M. Winger, A. Badolato, K. J. Hennessy, D. L. Hu, and A. Imamoğlu. Ultrafast all-optical switching by single photons. *Nature Photonics*, 6(9):605, 2012.

[115] P. Vukusic and J. R. Sambles. Photonic structures in biology. *Nature*, 424(6950):852, 2003.

[116] C. Wang, N. V. Wheeler, C. Fourcade-Dutin, M. Grogan, T. D. Bradley, B. R. Washburn, F. Benabid, and K. L. Corwin. Acetylene frequency references in gas-filled hollow optical fiber and photonic microcells. *Applied Optics*, 52:5430–5439, 2013.

[117] Y. Wang, C. R. Liao, and D. N. Wang. Femtosecond laser-assisted selective infiltration of microstructured optical fibers. *Optical Express*, 18(17):18056–18060, Aug 2010.

[118] H. G. Winful. The meaning of group delay in barrier tunnelling: a re-examination of superluminal group velocities. *New Journal of Physics*, 8(6):101, 2006.

[119] L. Xiao, W. Jin, M. Demokan, H. Ho, Y. Hoo, and C. Zhao. Fabrication of selective injection microstructured optical fibers with a conventional fusion splicer. *Optics Express*, 13(22):9014–9022, Oct 2005.

[120] A.-C. Yan, A. Dalgarno, and J. F. Babb. Long-range interactions of lithium atoms. *Physical Review A*, 55(4):2882, 1997.

[121] P. Yeh. *Optical Waves in Layered Media*. John Wiley & Sons, 1988.

[122] D. Yin, H. Schmidt, J. P. Barber, and A. R. Hawkins. Integrated arrow waveguides with hollow cores. *Optics Express*, 12(12):2710–2715, 2004.

[123] T. Yoon and M. Bajcsy. Laser-cooled cesium atoms confined with a magic-wavelength dipole trap inside a hollow-core photonic-bandgap fiber. *Physical Review A*, 99:023415, Feb 2019.

[124] Y. Yoon, Z. Ding, J. Flannery, F. Rajabi, and M. Bajcsy. Monitoring raman emission through state population in cold atoms confined inside a hollow-core fiber. *Optics Express*, 27(13):17592–17600, Jun 2019.

[125] N. Yu and F. Capasso. Flat optics with designer metasurfaces. *Nature Materials*, 13:139, 2014.

[126] J. Zhang, C. Con, and B. Cui. Electron beam lithography on irregular surfaces using an evaporated resist. *ACS Nano*, 8(4):3483–3489, 2014.

[127] S.-B. Zheng and G.-C. Guo. Efficient scheme for two-atom entanglement and quantum information processing in cavity qed. *Physical Review Letters*, 85(11):2392, 2000.

[128] G. Zito and S. Pissadakis. Holographic polymer-dispersed liquid crystal bragg grating integrated inside a solid core photonic crystal fiber. *Optics Letters*, 38(17):3253–3256, 2013.

APPENDICES

Appendix A

Fabrication Variants of Photonic Crystal Membranes

The following table summarizes the main alterations made to the various fabrication procedures and the different approaches taken throughout this work. Slight variations of the process were required for particular PC pattern dimensions and type of sample used. A noteworthy example being the need for KOH undercut etching for the in-house grown SiN films which have a Si substrate, while the Norcada samples already have free-standing SiN films and thus do not require undercutting.

Generation #	Mask	SiN Thickness	Substrate	Notes
1	ZEP	500 nm	Free-standing film (Norcada, refractive index = 2.11)	PC parameters used for optimizing reflectivity of plane wave source. (a = 817 nm, r = 347 nm). Broke after plasma etching.
2	ZEP	500 nm	Free-standing film (Norcada, refractive index = 2.11)	PC parameters used for optimizing reflectivity of Gaussian wave source. (a_x = 742 nm, a_y = 533 nm, r = 191 nm). Etched through ZEP before fully through SiN film.
3	ZEP	500 nm	Free-standing film (Norcada, refractive index = 2.11)	PC parameters used for optimizing reflectivity of Gaussian wave source. Films broke after final DI rinse (holes too large after plasma etching).
4	ZEP	500 nm	Free-standing film (Norcada, refractive index = 2.11)	Used thicker ZEP mask (2×300 nm = 600 nm). Sample again etched mask before etching entire SiN film. Etching selectivity not large enough between ZEP and SiN.
5	ZEP/Al	500 nm	Free-standing film (Norcada, refractive index = 2.11)	Used Al hard mask to increase selectivity. Samples broke during Al wet etch when spraying with neutralizing DI water.
6	ZEP/Al	500 nm	Free-standing film (Norcada, refractive index = 2.11)	Samples destroyed after SiN plasma etching. RF power too high (50 W RF). White precipitate formed during Al etch, and Al mask cracked after trying to clean with acetone/IPA.
7	ZEP/Al	500 nm	Free-standing film (Norcada, refractive index = 2.11)	Used 30 W RF power for plasma etching. Sample destroyed after Al dry etch (only outer edges of window broke). Possibly performed the Al dry etch for too long.
8	ZEP/Al	500 nm	Free-standing film (Norcada, refractive index = 2.11)	Used 30 W RF power and 2000 ICP power for plasma etching. Used tapered hole size on edge of PC pattern to allow for structural support. Sample broke after removing ZEP.

Generation #	Mask	SiN Thickness	Substrate	Notes
11	ZEP/Cr	500 nm	Free-standing film (Norcada, refractive index = 2.11)	Used chrome as hard mask and did only 125% of the total etch time during the SiN plasma etch (instead of normally 150%). Not all patterns properly developed after the e-beam exposure. Sample broke after SiN plasma etch.
12	ZEP/Cr	500 nm	Free-standing film (Norcada, refractive index = 2.11)	Did not stir during the e-beam developing of the PC pattern. Chrome etch did not properly etch through.
13	ZEP/Al	500 nm	Free-standing film (Norcada, refractive index = 2.11)	Used PMMA to glue sample onto carrier wafer for SiN etching, but baked at 90°C instead of 180°C to avoid re-flowing the ZEP mask. Al mask cracked, potentially from bending due to adhesion of films to the gel pack used as the chip container.
14	ZEP/Al	500 nm	Free-standing film (Norcada, refractive index = 2.11)	Used plastic containers rather than gel pack as a chip container. Using 125% of total SiN plasma etch time. First sample to be not destroyed after the entire fabrication process. Precipitates still found on the samples after the Al dry etch. The holes were smaller than the design size (fabricated $r = 330$ nm, design was for $r = 347$ nm).
15	ZEP/Al	500 nm	Free-standing film (Norcada, refractive index = 2.11)	Used N_2 in the Al dry etch, which acted to eliminate the precipitates formed during the process. The SEM performed after developing the pattern caused for irregularities in the pattern and the film broke during the Al wet etch.
16	ZEP/Al	500 nm	Free-standing film (Norcada, refractive index = 2.11)	Used incorrect Raith file of the PC pattern for the e-beam lithorgraphy.

Generation #	Mask	SiN Thickness	Substrate	Notes
17	ZEP/Al	500 nm	Free-standing film (Norcada, refractive index = 2.11)	The PC holes are designed for a plane wave source ($a = 817$ nm, $r = 347$ nm). Reflectivity results are shown in Fig. 5.8, in which reflectivities of $\sim 99\%$ are predicted, but only $\sim 92\%$ are measured. Difficulties arose while removing chip from Si carrier wafer and so we decided not to use PMMA to glue the chip to the wafer.
18	ZEP/Al	500 nm	Free-standing film (Norcada, refractive index = 2.11)	Reset software hole sizes to compensate for the reduced hole size that was previously fabricated. Used white paste for gluing sample to carrier wafer, instead of PMMA, which previously caused issues. Only patterns near the edge of the SiN window produce smooth holes that are near the correct design size. Debris left on the sample, possibly from the white paste used to glue the chip to the carrier wafer.
19	ZEP/Al	500 nm	Free-standing film (Norcada, refractive index = 2.11)	After developing the e-beam resist, no pattern was visible. The ZEP possibly did not adhere to the chip when spin coating because the chips are older and may have accumulated a thin film of water on the surface. Fabricated elliptical holes that are polarization-selective.
20	ZEP/Al	500 nm	Free-standing film (Norcada, refractive index = 2.11)	Determined that the plasma etch rate of the SiN is different for regions in the middle of the SiN window than near the edges. Sample broke during transfer out of cleaning beaker.
21	ZEP/Al	430 nm	Si (In-house SiN, refractive index = 2.26)	Cleaned sample with asher. Fabricated PC holes with $a = 800$ nm, $r \approx 300$ nm (for a design of $r = 340$ nm). Simulated reflectivity should be $R \sim 93\%$ for a Gaussian source. Measured reflectivity is near this predicted value, but the calibration measurements caused for a large amount of noise.

Generation #	Mask	SiN Thickness	Substrate	Notes
22	ZEP/Al	369 nm	Si (In-house SiN, refractive index = 2.26)	Fabricated PC holes for $a = 680$ nm, and $r \sim 260$ nm (designed pattern for $r = 297$ nm). SiN films were mounted onto HCPCFs and the resulting spectra were used in our published work in *ACS Photonics* (2018) 5, 2, 337-341. Mirror reflectivities are predicted to be $> 99\%$, however the measured results when mounted onto the fiber were $R \sim 80\%$. Small precipitates formed after the initial RIE to etch the SiN film to desired thickness.
23	ZEP/Al	369 nm	Si (In-house SiN, refractive index = 2.26)	Performed an O_2 plasma cleaning after the initial etch of the SiN to the correct thickness. Dose test for JEOL to find the correct dose needed for the given resist thickness for the optimized parameters for Gaussian source (same parameters as Generation 22). Larger PC holes were destroyed because the ZEP film possibly obtained moisture why the chips were diced.
24	ZEP/Al	369 nm	Si (In-house SiN, refractive index = 2.26)	Performed another dose test using JEOL and baked the ZEP resist again to release moisture. PC holes were $r \sim 295$ nm (with a designed $r = 297$ nm). Reflectivity measured was only $R \sim 90\%$, while the simulations show it should be $R \sim 99\%$. Tried illuminating sample with $4\times$ and $10\times$ objective, but the different spot sizes both produced the same reflectivity results.
25	ZEP/Al	369 nm	Si (In-house SiN, refractive index = 2.26)	Fabricated a much larger region of the PC pattern to investigate if the spot size of the beam is too large and power is being lost to the outer regions where the PC holes are absent. The calibrated dose used was 315 $\mu C/cm^2$. Again there is small black precipitates that form after the initial SiN etch to thin the film thickness, which are possibly caused by the Al hard mask.

Generation #	Mask	SiN Thickness	Substrate	Notes
26	ZEP	163 nm	Si (In-house SiN, refractive index = 2.26)	Fabricated the PC pattern from [22] ($t = 163$ nm, $a = 676$ nm, $r = 239$ nm, which are scaled to give large reflection at 852 nm). Tried using O_2 plasma to clean the sample from the black precipitates after the initial thinning of the SiN film, however the precipitates were not removed. Performed EDS on these precipitates and determined they were pillar structures but still composed of SiN.
27	ZEP	163 nm	Si (In-house SiN, refractive index = 2.26)	Again fabricated $t = 163$ nm, $a = 676$ nm, $r = 239$ nm. Measured reflectivity peak near 900 nm wavelength with $R \sim 95\%$, which matches the simulation results for a Gaussian wave. Used white light source and optical spectrum analyser for the reflectivity measurements and so the noise fluctuations are much less than the laser frequency scan previously used. Mounted these membranes onto a HCPCF and found that the effective reflectivity dropped to $R \sim 66\%$.
28	ZEP	184 nm	Si (In-house SiN, refractive index = 2.26)	Fabricated an optimized parameter set using a Gaussian source but a much thinner film ($t = 184$ nm, $a = 681$ nm, $r = 299$ nm). Did not use Al mask, tried ising a thick ZEP mask instead. Cracks were formed on the ZEP mask after developing, and the films broke after KOH wet etching.
29	PMMA	430 nm	Si (In-house SiN, refractive index = 2.26)	Tried to eliminate the need for Al mask, which may cause for micromasking, by using thick layer of PMMA to mask the SiN etch (ZEP cannot be spun thick enough). Performed new dose test for PMMA, however doses used were much too small and did not produce large enough holes.

Generation #	Mask	SiN Thickness	Substrate	Notes
30	PMMA	430 nm	Si (In-house SiN, refractive index = 2.26)	Again performed a dose test for PMMA resist (a = 790 nm, r = 320 nm). The features in the spectrum match the simulations, however the maximum reflectivity measured ($R \sim 85\%$) did not match the simulated results ($R \sim 95\%$). Large amount of debris was present on the sample of plasma etching.
31	PMMA	430 nm	Si (In-house SiN, refractive index = 2.26)	Fabricated large regions of PC holes to accommodate a large white light illuminating spot size. Measured reflectivity ($R \sim 95\%$) still much lower than the predicted results ($R \sim 99\%$).
32	PMMA	430 nm	Si (In-house SiN, refractive index = 2.26)	Repeated Generation 31, however we used critical point drying (CPD) to reduce risk of breaking, but debris was still left on the sample after drying.
33	PMMA	430 nm	Si (In-house SiN, refractive index = 2.26)	Repeated Generation 32, we also performed a double clean for the plasma etching to reduce resputtering of the thick PMMA mask. Membranes broke during CPD.
34	PMMA	430 nm	Si (In-house SiN, refractive index = 2.26)	Repeated Generation 33, although we instead used a shorter conditioning time (5 minutes) of the plasma etching chamber to try to reduce resputtering of mask. Debris was still present after this SiN etch. Reflectivities are again measured to be low ($R \sim 90\%$).

Generation #	Mask	SiN Thickness	Substrate	Notes
35	ZEP	342 nm	Si (In-house SiN, refractive index = 2.26)	Fabricated polarization-selective membranes (t = 342 nm, r_x = 215 nm, r_y = 182 nm, a_x = 3676 nm, a_y = 444 nm). Used ZEP again because the SiN film thickness was thin enough to not require a thick e-beam mask. No re-sputtering problem occurred, suggesting that the thick PMMA used in the previous samples caused for this re-sputtering onto the film during the plasma etching. Simulated results were $R \sim 99\%$ and $R \sim 11\%$ at the two orthogonal linear polarizations. We measured the reflectivity to be $R \sim 94\%$ and $R \sim 4\%$ at orthogonal polarizations.